SHAPE PRESERVING CONVERSION REACTION OF SILICEOUS STRUCTURES USING METAL HALIDES: PROPERTIES, KINETICS, AND POTENTIAL APPLICATIONS

A Dissertation
Presented to
The Academic Faculty

by

Samuel Shian

In Partial Fulfillment
of the Requirements for the Degree
Doctor of Philosophy in the
School of Materials Science and Engineering

Georgia Institute of Technology
December 2008

SHAPE PRESERVING CONVERSION REACTION OF SILICEOUS STRUCTURES USING METAL HALIDES: PROPERTIES, KINETICS, AND POTENTIAL APPLICATIONS

Approved by:

Dr. Ken H. Sandhage, Advisor
School of Materials Science & Engineering
Georgia Institute of Technology

Dr. Robert L. Snyder
School of Materials Science & Engineering
Georgia Institute of Technology

Dr. Joe K. Cochran
School of Materials Science & Engineering
Georgia Institute of Technology

Dr. Sankar Nair
School of Chemical & Biomolecular Engineering
Georgia Institute of Technology

Dr. Meilin Liu
School of Materials Science & Engineering
Georgia Institute of Technology

Date Approved: August 22, 2008

To my loving mom, Hernawati

my late father, Albert T.L. Shansiang,

and

my dearest friend, Daria

ACKNOWLEDGEMENTS

I would like to sincerely express my gratitude to my advisor, Professor Kenneth H. Sandhage for his guidance and support. It has been my privilege to work with him, whose patience, hardworking, and profound knowledge set an example for me and will continue to influence the rest of my life. I also would like to thank my committee members, Professor Robert L Snyder, Professor Meilin Liu, Professor Joe K. Cochran and Professor Sankar Nair for their valuable suggestions and discussions. I would like to thank my lab mates, Dr. Gul Ahmad, Shawn M. Allan, Dr. Zhihao Bao, Dr. Ye Cai, Dr. Benjamin C. Church, Dr. Matthew B. Dickerson, Eric Ernst, Dr. Yunnan Fang, Dr. Michael Haluska, Christopher Gaddis, Phillip D. Graham, David W. Lipke, Dr. Yajun Liu, Helena Rick, Dr. Michael R. Weatherspoon, Dr. Sehoon Yoo, and Dr. Yunshu Zhang. It was fun to work with you guys!

This work would never been accomplished without the support and prayers of my family, especially my mom. My sister, Eunice, has been particularly helpful during my stay here in US. I thank God for providing me with a dearest friend, Daria Theodora, who has been brightening my days, giving me encouragement, and willing to help me.

This research was supported by the Air Force Office of Scientific Research (Dr. Joan Fuller and Dr. Hugh DeLong, program managers).

TABLE OF CONTENTS

LIST OF TABLES

Page

LIST OF FIGURES

Page

LIST OF SYMBOLS

χ^2	Goodness of fit
δ	Thickness of the external $TiOF_2$ layer
ε	Lennard-Jones parameter: energy of molecular interaction
ϕ	Octahedra tilt angle
κ	The Boltzmann Constant
2θ	Diffraction angle in Bragg-Brentano geometry
ρ	Molecular density
σ	Conductivity; Collision diameter
τ	Time constant
Ω	Collision integral for molecular diffusion
a	Lattice parameter
C	Concentration, correlating constant as in Sherwood's equation
c	Lattice parameter,
Da	The Damköhler number
D_e	Effective diffusion coefficient
d	Diameter
G	Conductance
I	Amount of current
J_A	Molar flux of A
k"	First-order chemical reaction rate constant
k_g	Mass transfer coefficient

M	Correlating constant as in Sherwood's equation
N_A	Number of moles of A
N_{Bo}	Number of moles of B at time t=0
N_{Bt}	Number of moles of B at time t
P_{ethanol}	Vapor pressure of ethanol
p^o	Equilibrium partial pressure at standard condition
qV_s	Schottky barrier height
r	Radius
Re	The Reynolds number
R_{exp}	The expected profile R-value
$R_{\text{weighted profile}}$	The weighted profile R-value
S	Sensitivity
Sc	The Schmidt number
Sh	The Sherwood number
t	Time
V	Volume
V_s	Schottky barrier potential
X	The extent of the reaction
x	Atomic coordinate
z	Volume ratio between product and reactant

SUMMARY

Diatoms (*Bacillariophyta*), provide examples of living organisms or bio-machines that have the capability of producing very complex shapes through self-assembly, may be utilized in potential microdevices, and may play an important role in nanotechnology. The recently invented BaSIC process has opened a route for such utilization, that is the chemistry of the diatom frustule may be modified from silica. A number of BaSIC reactions have been developed in order to convert diatom frustules, or generally speaking any promising 3-D microscale silica structures, into numerous different compositions. This dissertation reports the BaSIC reaction of halide gases (i.e., TiF_4, ZrF_4, and $ZrCl_4$) with 3-D silica structures, (i.e., diatom frustules, silicified direct-write assembly scaffolds, and Stöber silica spheres). Additionally, potential applications of the converted titania diatom frustules (i.e., as a fast micron-sized ethanol sensor, and as a pesticide hydrolyzing agent) are also demonstrated.

A two-step gas-solid displacement process has been successfully shown to generate zirconia diatom frustule replicas without a loss of the original frustule shape (i.e., the cylinder shape of *Aulacoseira* diatom frustules). The successful conversion of silica structures into anatase replicas with feature preservation at the scale of ~100 nm has been demonstrated through the work on the *Corethron criophilum* diatom spines. Reaction temperature played a critical role for the shape preservation. Certain atmospheric conditions were also required during the oxygenation ($TiOF_2$ to TiO_2) process to avoid structural distortion. An ethanol sensor, based on a single TiO_2-converted diatom frustule, has been successfully fabricated. This sensor exhibited a more rapid response to the ethanol concentration change compared to other sensors reported in

the literature, and was able to detect at least 100 ppm of ethanol in air. Significant enhancements of the rate of hydrolysis of pesticide-like compounds were observed in the presence of F-doped anatase TiO_2-converted diatom frustules.

X-ray powder diffraction data and Rietveld analyses have been successfully used to characterize the crystal structure, and the temperature-induced phase transformation (from the room temperature hexagonal $R\bar{3}c$ structure to the higher temperature cubic *Pm3m* structure) of polycrystalline $TiOF_2$ that was synthesized through metathetic reaction of silica with TiF_4(g). To analyze the kinetics of reaction of silica with titanium tetrafluoride gas, a novel HTXRD reaction chamber was developed. The combination of the HTXRD conversion data, the analyses of microstructural evolution, and the analyses of nitrogen physisorption data have suggested that the kinetics of the reaction of Stöber silica spheres with titanium tetrafluoride gas could be modeled by assuming the existence of 2 kinetic regimes. The initial kinetic regime followed chemical reaction control, while the second kinetic regime followed mass transport control through a $TiOF_2$ layer of constant thickness. The total reaction time was influenced by the initial size of the silica spheres and the TiF_4 partial pressure.

CHAPTER 1: INTRODUCTION

1.1 Diatom Frustules

Certain living organisms, or bio-machines, have the capability of producing inorganic structures with very complex shapes through self-assembly. The construction of such structures is achieved using a DNA blueprint that controls all aspects of the organism. One of the amazing features of certain bio-machines is the ability to replicate complex shape structures faithfully in accordance to their master DNA blueprint. In certain single cell organisms, their rapid rate of reproduction results in a massive number of daughter cells in a relatively short time. Diatoms (*Bacillariophyta*), one example of such microorganisms, form an astounding variety ($10^4 – 10^5$) of uniquely-shaped silica microshells (frustules). Upon close inspection, the frustules not only consist of simple

Table 1.1. Typical chemical composition of diatomaceous earth deposits. Source: Dicalite Corp.

	Natural (%)	Calcined (%)
SiO_2	86.8	91.0
Al_2O_3	4.1	4.6
Fe_2O_3	1.6	1.9
CaO	1.7	1.4
MgO	0.4	0.4
Ignition loss	1.6	0.3
Undetermined	0.8	0.4

basic shapes, like spheres or cylinders, but also possess regular, periodic nanostructures. For example, the frustule of the *Aulacoseira* diatom species, contains rows of tiny, periodically spaced pores (~150 nm); the *Corethron Criophilum* diatom species form 100 nm thick spines with triangular cross sections.

Diatomaceous earth (also referred as diatomite or kieselguhr) is obtained from the siliceous remains of diatoms. It occurs as a lightweight, porous, and permeable sedimentary deposit of fine aggregate structure whose chemical composition is primarily silica. However, numerous other minor elements may also be present[1], as seen in Table 1.1. Mined diatomaceous earth has been used for filtration[2,3], filler materials, pesticides (malathion substitute)[4], catalyst supports [5], chromatography sorbents[6], and other applications. Gomes *et al*. investigated the mixture of diatomite with titania and niobia for dielectric properties to be used in ceramic capacitors[7].

Potential uses of diatoms in nanotechnology (e.g., gel filtration, biosensors, immunoisolation, microfabrication) have been discussed by Parkinson and Gordon[8]. They proposed that by utilizing the self-assembly ability of diatom cell cultures, the resulting frustule structures can be used as cheap masks for conventional micromachining. With recent progress in complete genome sequencing of one diatom species[9], the genetic manipulation of diatom frustule shapes for specific device applications seems plausible in the near future.

1.2 The BaSIC Process

Three-dimensional chemical conversion of biological structures is a new and attractive approach for producing complex 3-D microscale structures. The primary advantage is the potential capability for mass producing 3-D microdevices with tailored chemistries at low cost. Current approaches for fabricating 3-D microdevices, which tend

to depend on the 2-D layer-by-layer stacking of planar shapes, require relatively expensive tools and are quite time consuming.

The BaSIC process has been developed to chemically tailor complex shape diatom frustules[10]. BaSIC, which stands for **B**ioclastic **a**nd **S**hape-preserving **I**norganic **C**onversion, enables tailoring of the diatom chemistry, which is limited naturally to silica, into other, different chemistries while maintaining the original structure. Three approaches for altering the chemistry of silica-based diatom frustules have been successfully demonstrated: i) gas/silica displacement reaction methods; ii) conformal coating methods; and iii) a combination of the displacement reaction and conformal coating methods. The first approach has been used to convert SiO_2 frustules into replicas comprised of MgO (via an oxidation-reduction displacement reaction with Mg(g))[11] or TiO_2 (via a metathetic displacement reaction with TiF_4(g))[12]. Silica frustules have been converted into polymer or ZrO_2 replicas with the second approach[13,14], while continuous $BaTiO_3$ coatings have been applied to MgO-bearing frustule replicas[15] using the third approach. Recent research progress demonstrated that the BaSIC process could also be used to obtain non-oxide diatom frustule replicas, such as porous silicon[16] or boron nitride[17].

The BaSIC process has provided ways to utilize the unique diatom structures in various potential applications. Sensors made from a single titania diatom have shown excellent response, in terms of conductivity change, upon exposure to ethanol vapor. Catalysts consisting of converted anatase diatom frustules have shown substantially higher effectiveness for hydrolyzing organophosporous esters (pesticide compounds) compared to commercial 10 nm spherical anatase particles[18].

The BaSIC method, when combined with genetically engineered bio-structures, could prove to be a powerful manufacturing approach. Once the knowledge of manipulating diatom DNA to control the frustule shape is known, an almost unlimited

range of frustule 3-D shapes may then available for conversion to different chemistries, and then be used for devices. However, even without DNA manipulation, an estimated hundred thousand distinct diatom shapes currently exist[8,19,20], and many such structures may potentially be used for specific applications.

1.3 Scope of Research

The work reported in this dissertation is focused on the metathetic reactions that produce ZrO_2 and TiO_2 replicas with more emphasis given to the latter. The conversion of silica-based diatom frustules into nanocrystalline zirconia replicas, via the use of gas/solid displacement reactions, is demonstrated in Chapter 2. The rest of the chapters address several aspects of gas/solid reactions that produce TiO_2. Chapter 3 demonstrates the feasibility of the reactive conversion process to fabricate 3-D titania structures from both natural (*Corethron criophilum* spines) and synthetic templates (direct write assembly). The next two chapters report potential applications of TiO_2 *Aulacoseira* frustules; Chapter 4 investigated the use of single titania frustule for use in a sensitive and fast response ethanol sensor, while Chapter 5 investigated the use of batch of titania frustules for accelerated hydrolysis of organophosphorous ester compounds. In Chapter 6, the crystal structure and thermally induced phase transformation of $TiOF_2$ that was synthesized through gas/solid reaction is analyzed using high-temperature XRD. Chapter 7 describes the design of a sealed, but X-ray transparent chamber that can be used to analyze the kinetics of $TiF_4(g)/SiO_2(s)$ reaction. Later in Chapter 8, the experimentally-measured and modeled kinetics for the $TiF_4(g)/SiO_2(s)$ reaction are reported.

CHAPTER 2: Shape-Preserving Chemical Conversion of Silica-Based Diatom Frustules into Zirconia

The research presented in this chapter has been reported in the following publication:

Shian, S.; Cai, Y.; Weatherspoon, M. R; Allan, S. M.; Sandhage, K. H.; *J. Am. Cer. Soc.* 2006, 89, 694

2.1 Introduction

Zirconium dioxide or Zirconia is one of the most studied ceramic materials due to its attractive chemical, electrical, thermal, optical, and mechanical properties[21,22]. Zirconia-based ceramics have been used in many applications ranging from industrial applications (such as gas sensors, gas separators, catalysts and catalyst supports, refractories, cutting tools, and high-temperature electrodes and heating elements.)[23-25], to biomedical applications (such as dental restorations and implants)[26,27], and to consumer applications (such as jewelry as a diamond substitute and a radio frequency transparent electronics case)[21,28]. Such a wide range of applications has led to a significant global effort to produce intricate three-dimensional (3-D) shapes and finely (submicron) featured microscale zirconia-based structures [24,29-35]. Current ceramic microfabrication methods, which are based on the buildup of 2-D patterned layers (e.g., micro-stereolithography, ink jet printing, co-firing of stacked ceramic tapes) [36-40], are still facing a significant challenge to produce complex-shape 3-D zirconia microstructures in large quantities and at low manufacturing cost.

The diatom is an example of a micro-organism that is capable of replicating complex 3-D silica microstructures under ambient (marine or freshwater) conditions in a

precise manner (through species-specific genetic control) and at a massive rate of reproduction[41,42], greatly exceeding the capabilities of current synthetic (man-made) microfabrication processes. The estimated 10^4–10^5 extant diatom species provide a diverse selection of frustule morphologies for use in various applications[8,19,20]. Converting the composition of the frustules while preserving the shapes would tremendously increase the number of potential applications. Recent work has demonstrated that zirconia frustule replicas may be generated by coating silica frustules with a thin, sol–gel-derived film and then removing the underlying silica through selective dissolution[13]. While such a sol–gel approach may be used to produce frustule replicas with a variety of chemistries, alkoxide-based precursors tend to be relatively expensive. In this chapter, we set out to demonstrate that 3-D silica-based diatom frustules may be converted into nanocrystalline zirconia replicas through a series of shape-preserving gas/solid displacement reactions with lower-cost reactants.

2.2 Experimental Procedures

2.2.1 Direct Conversion Method

Cylindrical *Aulacoseira* diatom frustules (obtained in the form of diatomaceous earth) and ZrF_4 powder (99% pure, Advanced Research Chemicals Inc., Catoosa, OK) were placed in two separate nickel crucibles, with molar ZrF_4:SiO_2 ratio within the crucibles was varied from 0.36:1 to 3.6:1 in different experiments. The crucibles were loaded inside a nickel alloy tube (5.1 cm diameter, 20.3 cm long, Inconel Alloy 600, CG Metals, Duluth, GA) that was then welded shut within an argon atmosphere glovebox (Model Omni-Lab, Vacuum Atmosphere, Hawthorne, CA) maintained at an oxygen partial pressure below 0.1 ppm. The sealed ampoules were then heated at 5°C/min to a fixed temperature in the range of 250°–800°C and held at this temperature for 2 h, and

then allowed to cool to room temperature. The specimens were extracted after the tubes were cut open.

2.2.2 Two-step Displacement Reaction Method

An oxidation–reduction reaction with magnesium gas was first used to convert the silica frustules into magnesia-based replicas. A metathetic reaction with zirconium tetrachloride gas was then used to convert the magnesia replicas into zirconia. For the first step, magnesia-based replicas of *Aulacoseira* frustules were prepared by S. Allan and M. Weatherspoon in the following manner:

A steel reaction tubes (20 cm long by 2.5 cm in dia., McMaster Carr, Atlanta, GA) was crimped and TIG welded shut on one end. Magnesium flakes were then added to this end of the tube and a slight crimp was placed 8 cm from the welded end of the tube to prevent mixing of the reactants. The silica diatom frustules were thinly spread inside of a custom built steel boat (constructed from metal foil 8 cm long by 2 cm wide) and placed at the opposite end of the steel tube. This end of the tube was then crimped and welded shut in air. The as-prepared reaction vessels were then thrust into the hot zone of the furnace (900°C) and held for 1.5 h to allow for magnesium vaporization and reaction with the silica frustules. After cooling and extraction from the reaction tube, the MgO-based replicas were then exposed to a 0.49M NaOH solution at 60°C for 3 h to selectively dissolve residual silicon from the magnesia.

At the second reaction step, MgO diatom replicas and anhydrous $ZrCl_4$ powder (99.9% pure, Advanced Research Chemicals Inc.) were loaded into two separate nickel crucibles. The molar ratio of $ZrCl_4$:MgO placed within the crucibles was chosen to be 0.52:1, 0.86:1, or 1.2:1. The two crucibles were then placed inside a nickel alloy tube (5.1 cm diameter, 20.3 cm long, Inconel Alloy 600, CG Metals) that was welded shut within an argon atmosphere glovebox. The sealed ampoules were then heated at 5°C/min to

650°C and held at this temperature for 2 h. After cooling to room temperature, the sealed tubes were cut open and the reacted diatom frustules were withdrawn. The reacted frustules were then immersed and stirred (100 rpm) for 1 h in de-ionized water heated to 90°C. The frustules were then removed from the water with vacuum-assisted filtration.

2.2.3 Characterization

Scanning electron microscopy (SEM) (LEO-1530, Zeiss Germany) was used to analyze the morphology of the reacted samples. The elemental composition and crystalline phase of the frustules was studied with energy dispersive X-ray (EDX) detector (Oxford, England) attached to the SEM and X-ray diffractometer (Panalytical, Amelo, The Netherlands), respectively. Electron transparent cross-sections of the converted samples were examined by Dr. Y. Cai (Georgia Institute of Technology) with a transmission electron microscope (JEOL 4000FX, Tokyo, Japan) operated at 400 kV.

2.3 Results and Discussion

2.3.1 Direct Conversion Method

The direct conversion method is an analogue to the conversion of diatom frustules into titanium oxyfluoride[12], in which ZrF_4 gas was directly reacted with *Aulacoseira* diatom frustules shown in Figure 2.1a to produce zirconium oxyfluoride replicas. No reaction was detected within 2 h at temperature of 350°C or below, and at higher temperatures, for all starting molar ZrF_4:SiO_2 ratios examined, the silica frustules were found to disintegrate. Figure 2.1b shows a partially disintegrated frustule and Figure 2.1c shows relatively large, faceted crystallites, typically found at a distance from the location of the disintegrated frustules. EDX analysis in Figure 2.1d indicates that these

crystallites contained Zr, F, and O, which was consistent with a zirconium oxyfluoride compound[43].

The frustule disintegration, and concurrent formation of Zr–O–F-bearing crystals away from the frustule surfaces, suggested that the silica had reacted to form an oxygen-bearing vapor species (e.g., $Si_2OF_6(g)$, or $SiOF_2(g)$) that migrated away from the frustule surface and then reacted further with $ZrF_4(g)$ to form the Zr–O–F-bearing crystals. Such vaporization and crystal formation may have proceeded through the following reactions:

$$3ZrF_4(g) + 2SiO_2(s) \Rightarrow 3ZrOF_2(s) + Si_2OF_6(g) \quad (1)$$

$$Si_2OF_6(g) + ZrF_4(g) \Rightarrow ZrOF_2(s) + 2SiF_4(g) \quad (2)$$

A similar type of reactive frustule disintegration, and faceted Ti–O–F crystal formation away from the frustules, was observed upon exposure of diatom silica frustules to $TiF_4(g)$ at temperatures in the range of 500°–700°C and at TiF_4:SiO_2 molar ratios in excess of 4.9:1[44]. The occurrence of such disintegration under all of the reaction conditions examined indicated that a different reaction path was needed in order to generate zirconia frustule replicas.

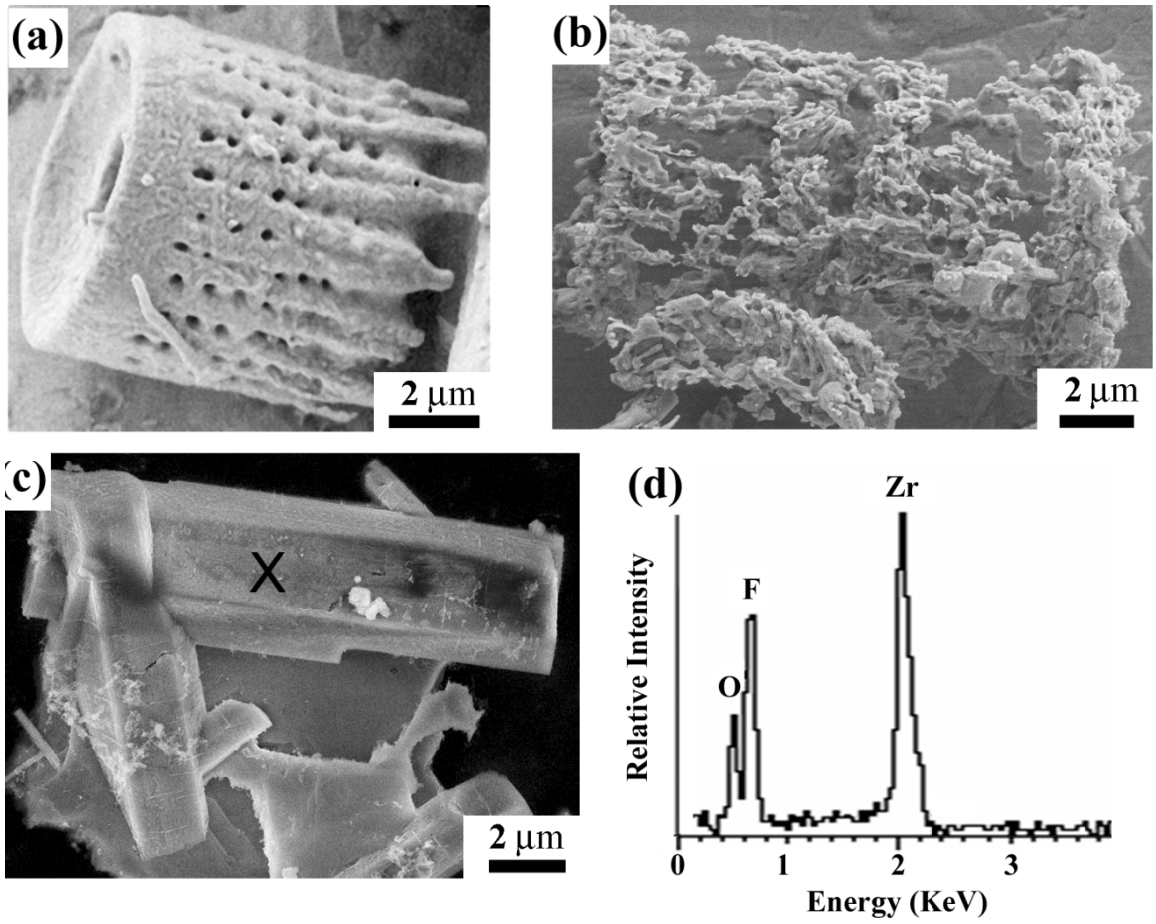

Figure 2.1: Secondary electron images of: (a) a starting, cylinder-shaped *Aulacoseira* diatom frustule; (b) a partially disintegrated frustule after exposure to ZrF_4(g) for 2 h at 600°C (molar ZrF_4:SiO_2 reactant ratio = 0.36:1); and (c) faceted Zr–O–F-bearing crystals formed near the partially disintegrated frustule shown in (b). (d) Energy-dispersive X-ray analysis of a crystal obtained at the position X in (c)

2.3.2 Two-step Displacement Reaction Method

A series of displacement reactions was used to convert the silica frustules first into magnesia-based replicas (via reaction with magnesium gas) and then into zirconia replicas (via reaction of the magnesia with zirconium tetrachloride gas). In the first step, diatom frustules were converted into magnesia-based replicas via the following net oxidation–reduction displacement reaction[11]:

$$SiO_2(s) + 2Mg(g) \Rightarrow 2MgO(s) + \{Si\} \quad (3)$$

where {Si} refers to silicon dissolved within a Mg–Si liquid, generated by the continued reaction of elemental silicon with excess magnesium vapor. During the reaction, this liquid species tended to migrate away from the MgO-based frustule replica[11], and upon cooling it could be further leached away by using sodium hydroxide solution. Magnesia replicas generated by reaction (3) may then be exposed to zirconium tetrachloride gas to form zirconia by the following metathetic displacement reaction:

$$2MgO(s) + ZrCl_4(g) \Rightarrow ZrO_2(s) + 2MgCl_2 \quad (4)$$

The standard Gibbs-free energy change per mole of the above reaction at 650°C is -75.0 kJ/mol[45,46], which is thermodynamically favored. The equilibrium partial pressure of $ZrCl_4$ vapor required for reaction (4) to proceed spontaneously at 650°C (assuming unit activities for pure condensed phase reactants and products) is only 4.3×10^2 torr, which is much smaller than the pressure of $ZrCl_4$ vapor generated from condensed $ZrCl_4$ at this temperature (the sublimation temperature of $ZrCl_4$ is only 336°C)[45,46]. Upon cooling to room temperature, the $MgCl_2$ product of this reaction may be selectively removed from the ZrO_2 product by dissolution in water.

Figure 2.2a shows a secondary electron image of an MgO replica of an *Aulacoseira* frustule. The shape of the starting SiO_2-based frustule (Figure 2.1a) was preserved after conversion into MgO. Secondary electron images obtained after reaction of the magnesia with zirconium chloride gas at 650°C for 2 h are shown in Figure 2.2b and Figure 2.2c. EDX analysis obtained at the position X in Figure 2.2b is shown in Figure 2.2d. The reacted frustules were embedded in a matrix phase that was Mg and Cl rich, which was consistent with a solidified $MgCl_2$-rich liquid (note: while the melting point of $MgCl_2$ is 714°C, a eutectic liquid can form in the $MgCl_2$–$ZrCl_4$ system at only 426°C[47]). The Mg–Cl-rich matrix phase could be selectively removed from the reacted frustules by dissolution in water. Secondary electron images of isolated frustules exposed after this dissolution treatment are shown in Figure 2.3a–c. EDX analysis of such an isolated frustule is shown in Figure 2.3d. The absence of a magnesium peak (at 1.25 keV) in the EDX pattern indicated that the frustules had been fully converted into zirconia within 2 h at 650°C. The cylindrical frustule shape, and the protruding rim and open hole at the end of the frustule, were preserved after conversion into zirconia.

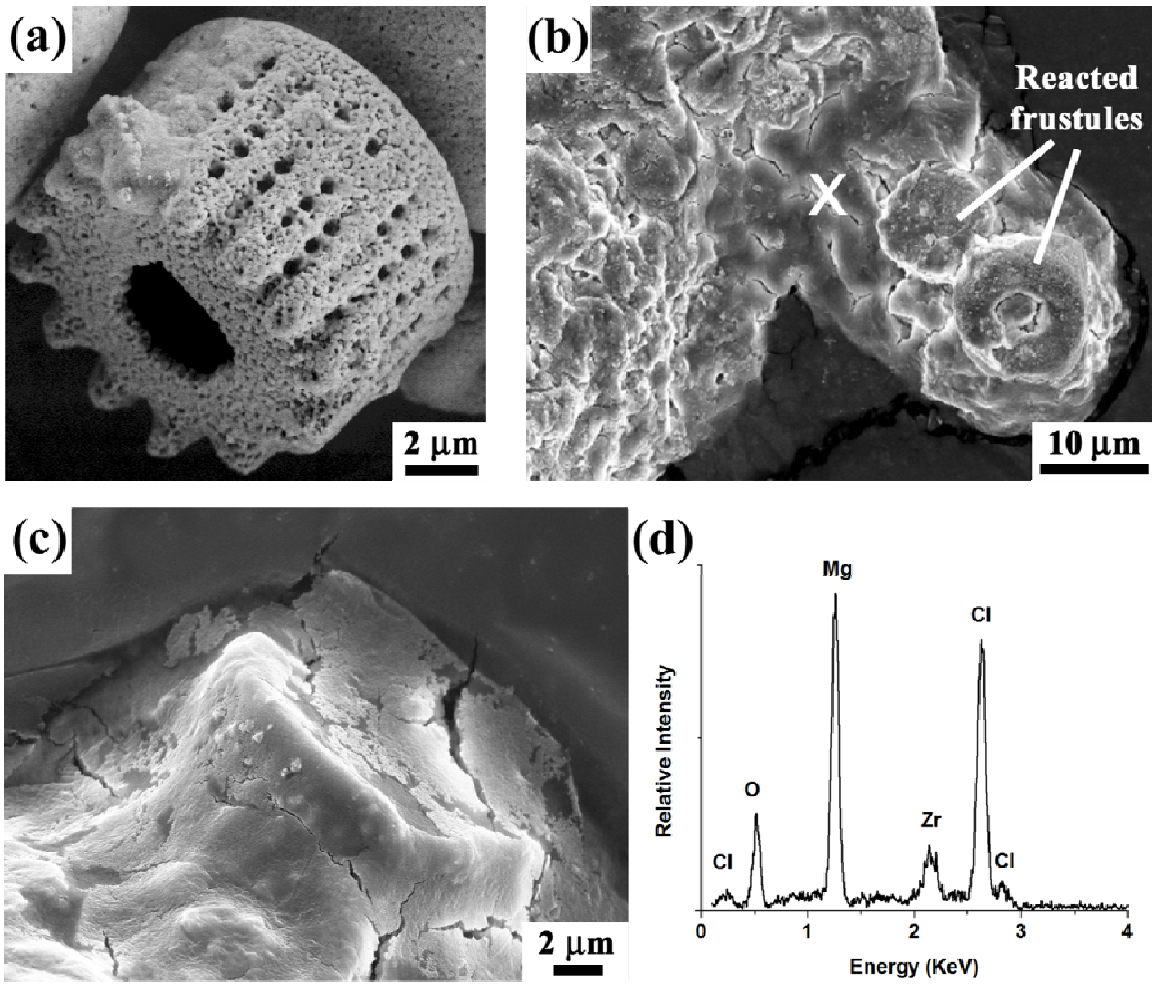

Figure 2.2: Secondary electron images of: (a) a MgO-based frustule replica after exposure to Mg(g) at 900°C for 1.5 h and then immersion in a 0.49M NaOH solution at 60°C for 3 h; (b), (c) the products of reaction between MgO diatom replicas and $ZrCl_4$(g) at 650°C for 2 h (molar $ZrCl_4$:MgO reactant ratio5 0.86:1); and (d) energy-dispersive X-ray analysis obtained at the position X in (b).

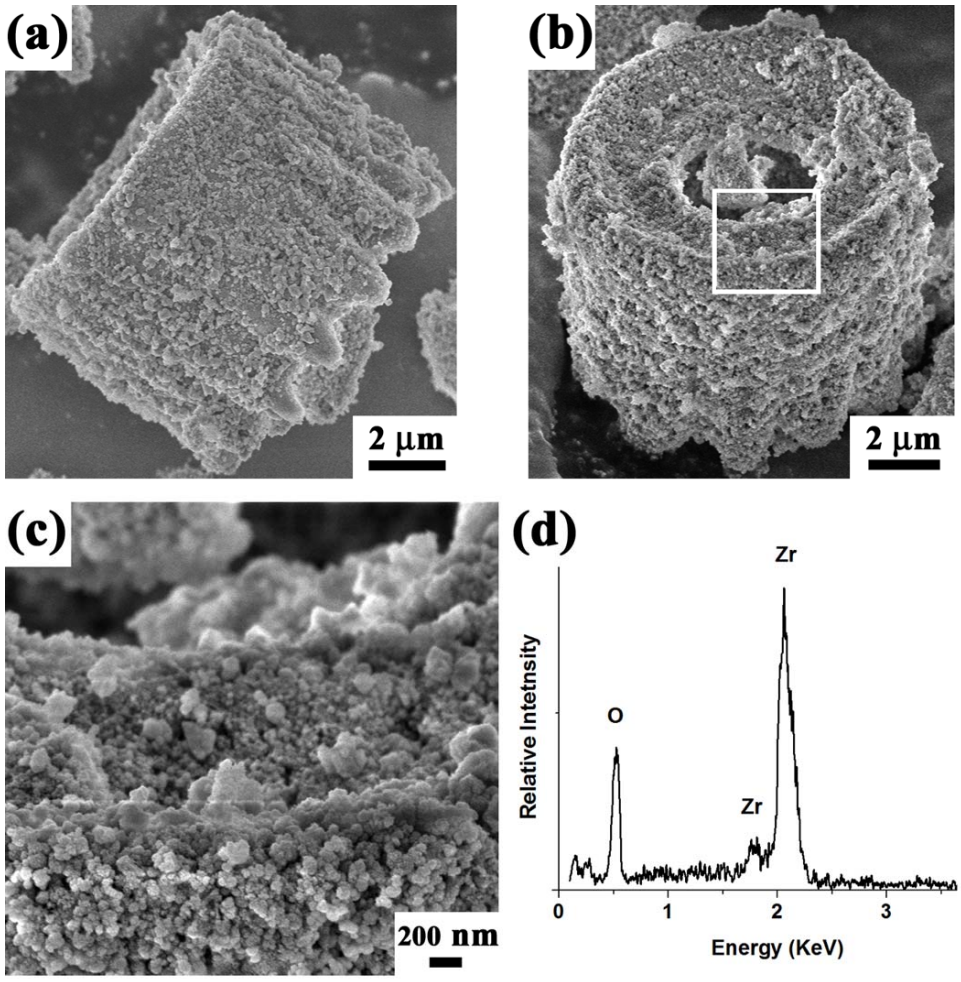

Figure 2.3: (a, b) Secondary electron (SE) images of nanocrystalline ZrO_2 replicas of *Aulacoseira* diatom frustules generated by the reaction of MgO frustule replicas with $ZrCl_4$(g) at 650°C for 2 h (molar $ZrCl_4$:MgO reactant ratio = 0.52:1) and then immersion in de-ionized water at 90°C for 1 h. (c) Higher magnification SE image of the region indicated by the rectangle shown in (b). (d) Energy-dispersive X-ray analysis of a nanocrystalline ZrO_2 replica.

Figure 2.4 shows the X-ray diffraction (XRD) analyses obtained from the zirconia-converted frustules. Diffraction peaks for the monoclinic and tetragonal zirconia polymorphs were detected, whereas diffraction peaks for magnesium oxide were absent (Powder Diffraction File, Card No. 45–946 for MgO, No. 37–1484 for ZrO_2 (monoclinic), No. 50–1089 for ZrO_2 (tetragonal), International Center on Diffraction Data, Newtown Square, PA). The relative amount of monoclinic zirconia generated upon reaction at 650°C for 2 h increased at the expense of tetragonal zirconia when the molar $ZrCl_4$:MgO reactant ratio was increased from 0.52:1 (near the stoichiometry of reaction (2)) to 1.2:1 (a significant excess of $ZrCl_4$).

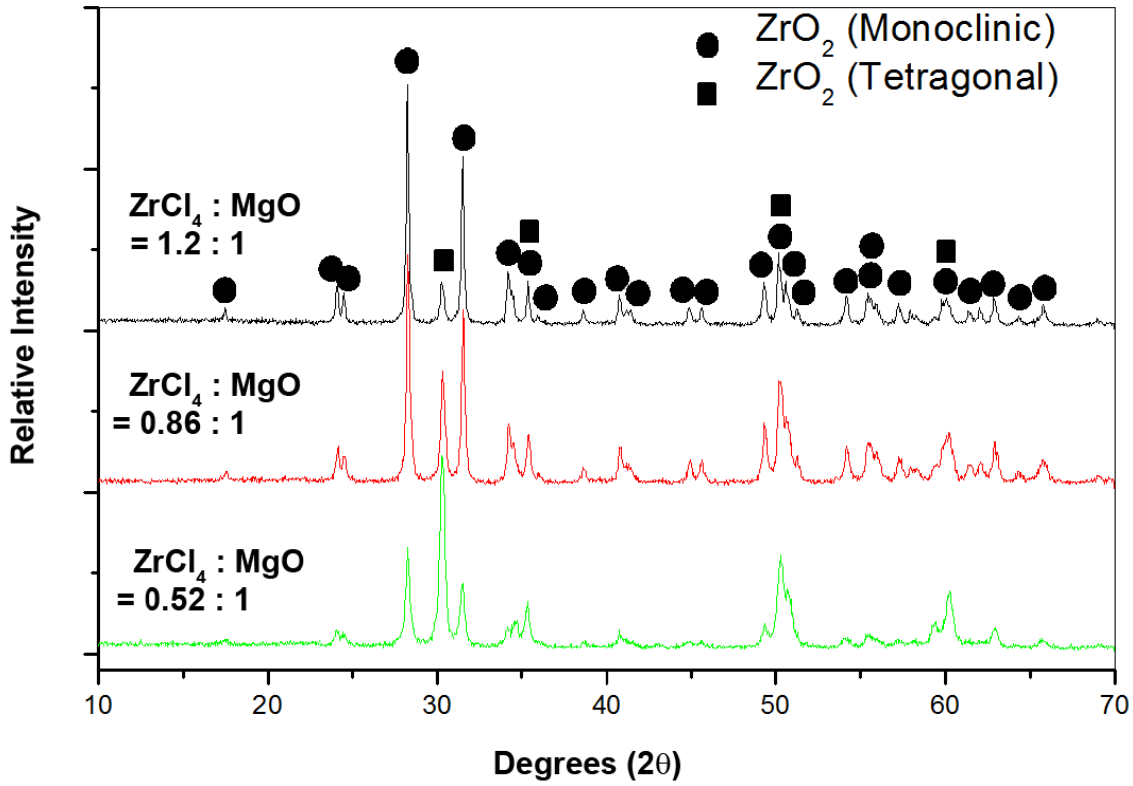

Figure 2.4: X-ray diffraction (XRD) analyses of the ZrO_2 frustule replicas generated by the reaction of MgO-based replicas with $ZrCl_4$(g) at 650°C for 2 h and then immersion in de-ionized water at 90°C for 1 h. The three XRD patterns are associated with different molar $ZrCl_4$:MgO reactant ratios.

Figure 2.5a-c show the transmission electron micrographs of cross-sections of zirconia-converted frustules generated with varied molar $ZrCl_4$:MgO reactant ratios. Figure 2.5d–f present the corresponding selected area electron diffraction (SAED) patterns obtained from these cross-sections. The SAED analyses indicated an increase in the amount of monoclinic zirconia relative to tetragonal zirconia with an increase in the starting molar $ZrCl_4$:MgO reactant ratio, which is consistent with XRD analyses. The crystallite size distribution was also observed to change with an increase in this reactant ratio. The zirconia crystallites formed with a $ZrCl_4$:MgO molar ratio of 0.52:1 (Figure 2.5a) were relatively small (~40 nm) and uniform in size. However, for a ZrCl4:MgO molar ratio of 0.86:1 (Figure 2.5b), the zirconia crystallites exhibited a bimodal size distribution; that is, a population of considerably larger crystallites (several hundreds of nanometer in size) was detected along with the finer crystals. This bimodal crystallite size distribution was consistent with XRD analyses of the average tetragonal and monoclinic zirconia grain sizes. The widths of major, non-overlapped diffraction peaks for monoclinic zirconia (the (-111) and (111) peaks near 28.2° and 31.5°, respectively, in Figure 2.4 and tetragonal zirconia (the (011) peak near 30.3° in Figure 2.4) were measured at half of the maximum intensity values and these values were inserted into the Scherrer equation[48] to calculate the average crystallite sizes for the tetragonal and monoclinic zirconia phases. For specimens with a $ZrCl_4$:MgO reactant ratio of 0.86:1, the average crystallite sizes for tetragonal and monoclinic zirconia were 48 and 380 nm, respectively. A similar bimodal crystallite size distribution was detected for a molar $ZrCl_4$:MgO reactant ratio of 1.2:1 (Figure 2.5c), although a higher concentration of the larger crystals was detected. The enhanced formation of relatively large zirconia crystallites, and of monoclinic zirconia, at 650°C with an increase in the amount of the $ZrCl_4$ reactant was consistent with prior reports on the effect of chlorine on the tetragonal-to-monoclinic zirconia transformation at temperatures below 1000°C[49,50].

Karapetrova, *et al*.[49] reported that zirconia specimens with relatively high initial chlorine contents (up to several percent, synthesized from oxychloride precursors) exhibited rapid grain growth between 600° and 800°C, and transformed more rapidly to monoclinic zirconia over this temperature range, than specimens containing little initial chlorine (on the order of 200 ppm, synthesized from nitrate precursors)[49]. Pasquevich, *et al*.[50] found that the growth rate of isolated crystallites, and the tetragonal-to-monoclinic transformation, occurred at faster rates in Ar–Cl_2 gas mixtures (with a chlorine partial pressure of 300 Torr) than in pure argon at 940°C[50].

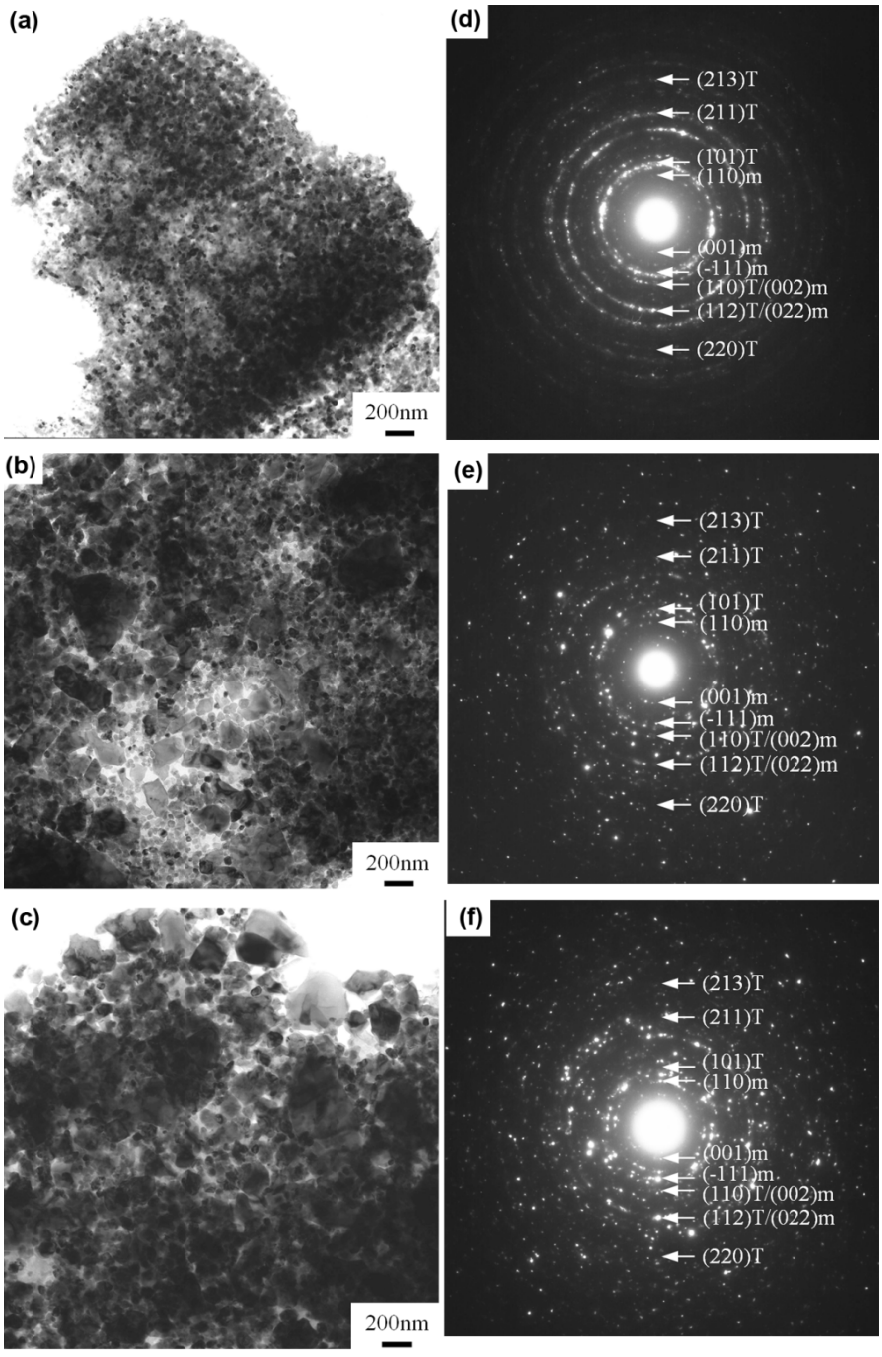

Figure 2.5: Transmission electron images of ion-milled cross-sections of ZrO_2 frustule replicas generated by the reaction of MgO replicas with $ZrCl_4$(g) at 650°C for 2 h, using molar $ZrCl_4$:MgO reactant ratios of: (a) 0.52:1, (b) 0.86:1, and (c) 1.2:1, and then immersion in de-ionized water at 90°C for 1 h. (d)–(f) Corresponding selected area electron diffraction patterns obtained from the specimens shown in (a)–(c), respectively (t and m refer to the tetragonal and monoclinic polymorphs, respectively, of zirconia).

2.4 Conclusions

The conversion of silica-based diatom frustules into nanocrystalline zirconia replicas, via the use of gas/solid displacement reactions, has been demonstrated for the first time. Initial experiments involving the reaction of the silica frustules with zirconium tetrafluoride gas resulted in disintegration of the frustules by a reactive evaporation process. Such reactive disintegration was avoided by converting the silica frustules into magnesia replicas prior to reaction with a zirconium halide gas (thereby avoiding the direct exposure of the silica frustules to a zirconium halide gas reactant). Magnesia-based replicas were generated via an oxidation–reduction displacement reaction between cylinder-shaped *Aulacoseira* diatom frustules and magnesium gas at 900°C. A metathetic displacement reaction between the magnesia replicas and zirconium tetrachloride gas at 650°C then yielded zirconia replicas embedded in a magnesium chloride- rich matrix. Selective dissolution of the magnesium chloride in water yielded freestanding, nanocrystalline assemblies of zirconia that retained the starting cylindrical *Aulacoseira* frustule shape. This serial displacement reaction process may be used to generate microscale zirconia assemblies with a wide variety of other controlled 3-D shapes available among the tens of thousands of species of extant diatoms and other silica-forming microorganisms. By utilizing self-replicating frustules as templates, large numbers of nano-crystalline zirconia micro-assemblies with similar, specific 3-D shapes may be produced for use as controlled-shape powders, reinforcement phases, or microdevice components for a host of applications.

CHAPTER 3: Shape-Preserving Chemical Conversion of Biological and Biomimetic Silica-Based Structures into TiO_2

3.1 Introduction

Titania is a material of significant interest to the scientific and technological communities. Controlled-feature titania, particularly in the micro- to nanometer scales can be attractive for many potential applications, including for photonic band gap materials, gas sensing, catalyst supports, photo-catalytic activity, and solar cells[51-53]. Most methods for producing titania are based on powders, film, and bulk components with simple two-dimensional shapes and morphologies.

A novel method to produce anatase in a complex 3-D geometry has been recently developed by applying shape-preserved conversion reactions to mineralized biological templates [11]. This method overcomes the limited range of compositions, mainly based on calcium carbonate or silica, of these bioclastic structures that are not well suited for many potential device applications. Unocic *et al.*[12] were able to demonstrate the feasibility of synthetic chemical conversion of *Aulacoseira* diatom frustule into titania while preserving the shape of the frustule. The shape-preserving metathetic gas/solid displacement reaction for converting silica into titania was established using a carefully chosen temperature (350ºC), reaction time (2 hours), and silica (diatom) to TiF_4 weight ratio. Under these conditions, the silica diatoms were converted to the anatase polymorph of titania, while silicon fluoride vapor was released.

In this chapter, the feasibility of applying this metathetic conversion reaction to different siliceous precursors was examined. The first silica structure was a cultured *Corethron criophilum* diatom frustule which has spines of high aspect ratio, and the second structure was a synthetic silicified scaffold fabricated by direct write assembly (DWA).

C. criophilum, one of the estimated 10^4 to 10^5 diatom species in existence, forms long silica spines that have a high aspect of length to diameter ratio. The spine shape is an attractive precursor for reactive conversion into titania as an alternative processing route to currently available methods for forming nanofibers of titania[54-58].

The DWA technique utilized a concentrated polyamine-rich ink[59] that is both specifically tailored for the direct-write assembly of 3-D micro-periodic structures and suitable for subsequent biomimetic silicification in a shape-preserving fashion[60]. The resulting synthetic scaffolds were hydrolyzed and condensed into inorganic silica-organic hybrids. Under appropriate conditions, silica condensation occurred uniformly throughout the polyamine-rich scaffolds leading to their increased thermal and mechanical stability. Xu *et al*, reported that the structure consisted of 52 wt% silica as determined by thermogravimetric analysis[60]. These silicified lattice-like structures can be structurally tailored to emulate the stunning shapes and fine features exhibited by some natural diatoms. An optical image of the DWA instrument and schematic illustration of this approach are shown in Figure 3.1a and b, respectively. Secondary electron images of several direct write assembled and silicified lattice structures, with different lateral dimensions and thicknesses (numbers of layers) are shown in Figure 3.1c and d below.

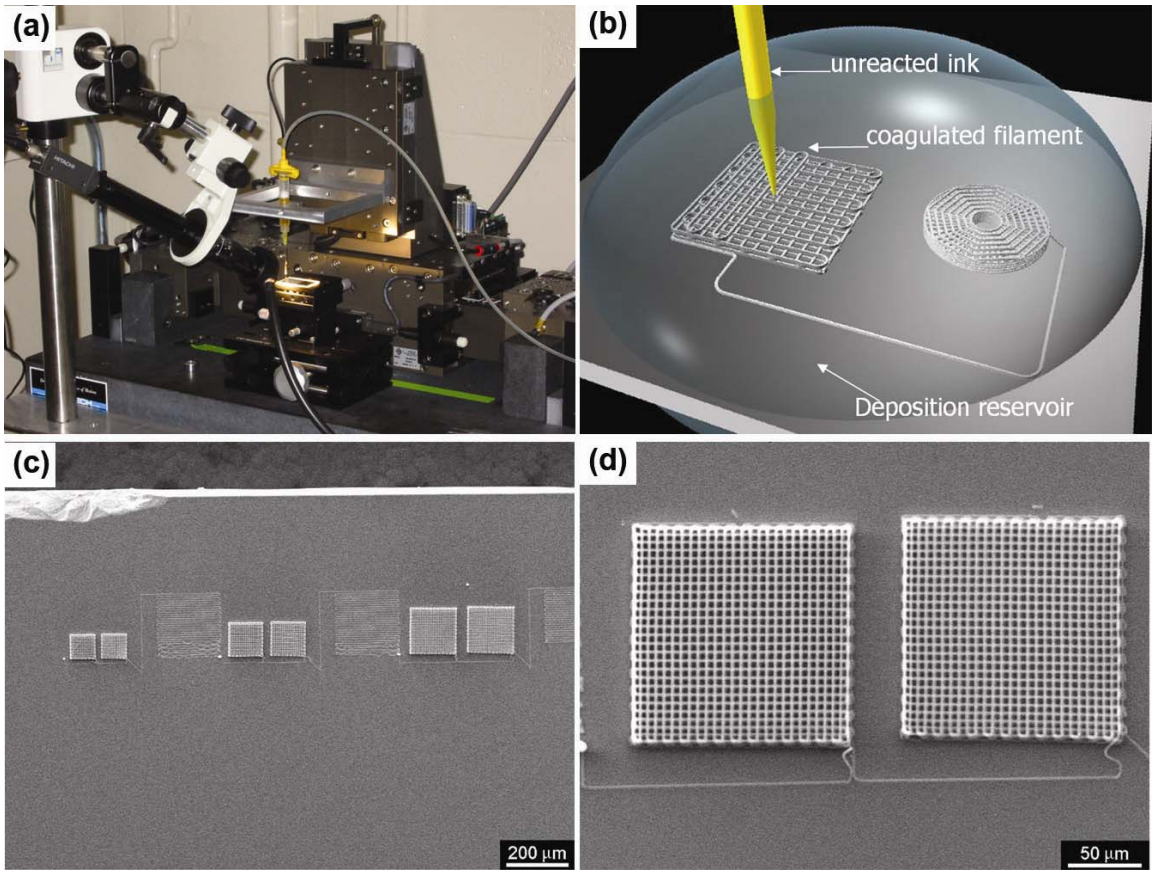

Figure 3.1: (a) Optical image of the robotic deposition machine used for DWA and (b) schematic illustration of the direct write process. (c) Secondary electron images of silicified 3-D structures: tetragonal structure with varying dimensions (80,120,160 μm) and number of layers (6 and 8 layers); (d) high magnification view of 8-layer (left) and 6-layer (right) structures (160 μm). (Images courtesy of Dr. Lewis group at UIUC).

3.2 Experimental Procedures

3.2.1 Preparation of C. criophilum Spines

C. criophilum cells were isolated and cultured by Dr. B. Palenik (Scripps Institution of Oceanography, UCSD) as follows. After isolation off of Scripps Pier (La Jolla, CA), the cells were treated with antibiotics according to Droop[61], and axenicity was confirmed by periodic inoculation into enrichment medium[62] and by visual inspection. Culturing media was prepared using local seawater filtered through a 0.22 μm polycarbonate filter (GE Osmonics, Minnetonka, MN) and autoclaved at 121°C. Nutrients were added at f/2 concentrations[63], and cells were kept at 20°C under continuous cool white fluorescent light (8.86 $\mu E\ s^{-1}m^{-2}$).

The *C. criophilum* cells were harvested from culture media by Dori Landry (Scripps Institution of Oceanography, UCSD) by filtration through a 5.0 μm polycarbonate filter (GE Osmonics, Minnetonka, MN), then were centrifugated (1550 x g) for 15 min. The cell pellet was resuspended in 4 mL sterile seawater and vortexed for 9 min to dislocate the spines from the cells. To separate the spine fraction from the cells and from organic materials, the sample was placed over a sucrose gradient consisting of 40% (w/v), 50% (w/v), and 60% (w/v) sucrose in water solutions and centrifuged (600 x *g*) for 20 min. After centrifugation, the gradient fractions were removed and placed in separate 2 mL tubes. The fractions were centrifuged (17000 x *g*) for 7 min, and the supernatant was discarded. The pellets were examined microscopically to determine fraction components. To better purify the spines, the pellet from the 50% (w/v) sucrose fraction was resuspended in 2 mL of sterile seawater and layered over another sucrose gradient consisting of 50% (w/v), 55% (w/v), and 60% (w/v) sucrose solutions. After centrifugation as above, the 55% (w/v) pellet was set aside and used as the spine enriched fraction.

3.2.2 Preparation of Silica Scaffolds via DWA

The silica scaffolds were prepared by Mingjie Xu (University of Illinois, Urbana Champaign), as follows. Concentrated polyelectrolyte complexes with a 2 : 1 ratio of $[NH_x]$: [COONa] ratio were produced by mixing appropriate amounts of poly-allylamine hydrochloride (PAH) (Polysciences, Warrington, PA), poly-acrylic acid (PAA) (Aldrich, Milwaukee, WI) and water, such that the total polymer concentration was 50% by weight. The mixture was magnetically stirred for 24 h until it became transparent and homogeneous. This mixture was the polyelectrolyte-based ink used in the subsequent direct writing process.

A robotic deposition apparatus (ABL9000, Aerotech Inc., Pittsburgh, PA) was used to assemble 3-D polymer scaffolds. The ink delivery system was mounted onto a moving xyz stage. The pattern of the intended structure was defined in a computer-aided, direct-write program (RoboCAD). This program controlled the 3-axis motion of the moving stage. A pressurized syringe equipped with a glass nozzle (μ-Tip, World Precision Instruments, Inc., Sarasota, FL) was used to deposit the ink at a steady flow rate onto a silicon wafer substrate.

Biomimetic silicification was conducted by immersing the as-fabricated scaffolds in 3.5 ml of an aqueous phosphate buffered (pH 8, 15 mM) silicic acid (50 mM) solution for 48 h followed by thorough rinsing with deionizied water.

3.2.3 Chemical Conversion into TiO_2

The chemical conversion of these biological and biomimetic silica-based structures into $TiOF_2$ was conducted in a sealed titanium ampoule (Figure 3.2). A nickel boat (McMaster-Carr, Atlanta, GA) containing the silica preforms was placed within a 2.3 cm internal diameter and 20 cm long titanium tube along with 500 mg solid TiF_4

powder (99% purity, Advanced Research Chemicals, Inc., Catoosa, OK). For *C. criophilum* spines conversion, the molar ratio of TiF_4:SiO_2 placed within the crucibles was 2.4:1. Since the amount of spines in a given reaction batch was less than 1 g, an extra silica source (*Aulacoseira* diatom frustule) were placed in a separate nickel crucible to make up to 100 mg of total silica content inside the reaction tube. For DWA conversion, no extra silica source was placed in the reaction tube. Both ends of the tube were crimped and welded shut. Because of the tendency of TiF_4 to react to oxygen and water vapor, the above procedures were conducted in an argon atmosphere glove box (Model Omni-Lab, Vacuum Atmosphere, Hawthorne, CA) maintained at an oxygen partial pressure below 0.1 ppm. The sealed metal ampoule was heated to the desired reaction temperature, in the range of 210 - 400°C, at a 5°C/min heating rate, held for 2 hours, and then allowed to cool to room temperature. The specimens were extracted after the tubes were cut open. For the conversion of $TiOF_2$ frustules into TiO_2, specimens were heated at 350°C for 2 to 8 h in moist flowing oxygen. Before entering the furnace, the oxygen was passed through a heated water bath (50°C) at a rate of 1 slpm. The measured humidity (using Model HMP234, Vaisala, Woburn, MA) at the gas outflow of the furnace was found to be at least 94% relative humidity.

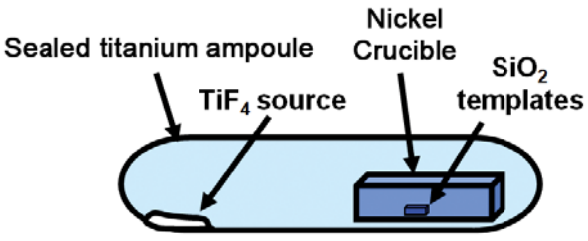

Figure 3.2: Schematic illustration of the sealed titanium ampoule in which the reaction of silica structures with TiF_4 was conducted.

3.2.4 Characterization

The morphology of the reacted samples was analyzed by scanning electron microscopy (SEM) (LEO-1530, Zeiss Germany). The elemental composition and crystalline phase of the frustules was studied with energy dispersive X-ray (EDX) detector (Oxford, England) attached to the SEM and X-ray diffractometer (Panalytical, Amelo, The Netherlands), respectively. Electron transparent cross-sections of the converted samples were examined by Dr. Y. Cai (Georgia Institute of Technology) with a transmission electron microscope (JEOL 4000FX, Tokyo, Japan) operated at 400 kV. The optical reflectance spectra were measured using an FTIR microscope (UMA-600 microscope and FTS-7000 FTIR, Digilab, Canton, MA) in the laboratories of Dr. J. Perry (Georgia Institute of Technology). At each FTIR measurement, the intensity of the reflected signal was normalized against the reflectance spectrum from a pure gold surface.

3.3 Result and Discussion

3.3.1 C. criophilum Spines

A series of secondary electron images of the initial *C. criophilum* diatoms are shown in Figure 3.3.The *C. criophilum* diatom contained organic matter within the siliceous skeletal structure. The holes where the spines had been attached at both ends of the frustule are visible in the low magnification image (Figure 3.3a, location A). The lateral dimension of the spines vary along the spine length (i.e., the farther from the diatom body, the smaller the lateral spine dimension). Figure 3.3c shows this variation: located at A is a spine area near the body while a spine area near the tip is located at B. The spines typically have lateral dimension ranging from 100 nm to 300 nm and lengths from 35 μm to 50 μm (i.e., a high aspect ratio). The cross-section of the spine, as shown

in the Figure 3.3d, resembles a three-pointed star shape. Along the three edges of the spines, periodic barbs as small as 50 nm in diameter protrude (see Figure 3.3b). In their natural aquatic environment, *C. criophilum* spines serve as a tool for movement. Also, the long spines provide protection for the main body from predators, such as zooplankton[64].

EDX analyses in Figure 3.4a shows the main elements comprising the spine are silicon and oxygen. The gold peak came from the coating applied to the specimen prior to SEM analysis. The sodium and magnesium peaks originated from the saline water-based growth medium. Selected area diffraction analyses (Figure 3.4b) revealed that the structure of the spine was amorphous, which is common for biological silica.

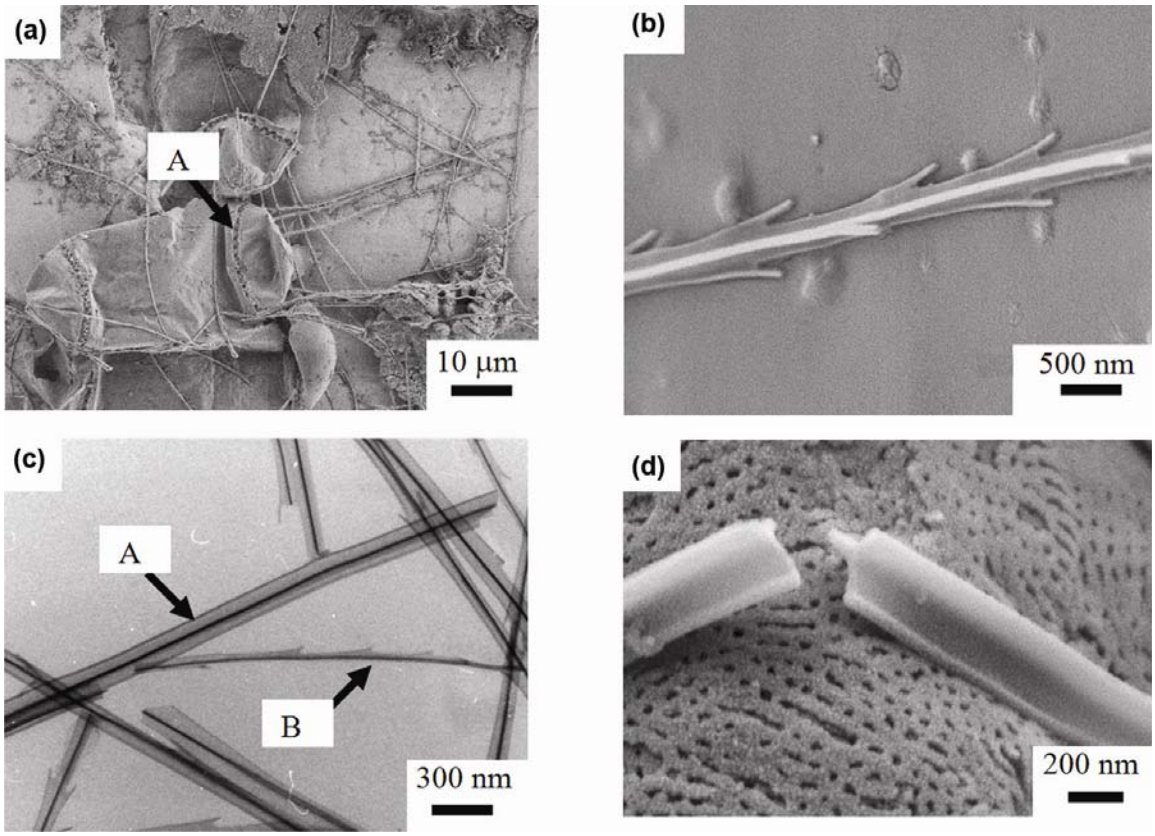

Figure 3.3: (a), (b), and (d) Secondary electron images of the *C. criophilum* diatom. (c) TEM image of the *C. criophilum* spines, indicating a degree of electron transparency of the spines.

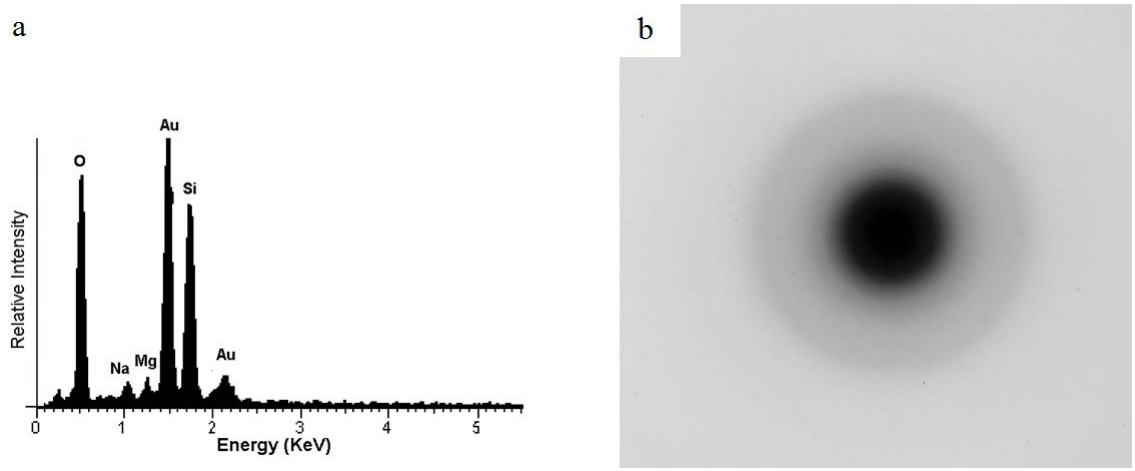

Figure 3.4: Characterization of *C. criophilum* diatom spines. (a) EDX analysis, and (b) selected area electron diffraction analysis. (Note: the gold peak in (a) resulted from a gold coating applied to prevent charging in the SEM. The Na and Mg peaks were associated with salts dissolved in the saline growth medium)

3.3.2 Reactive Conversion of C. criophilum Spines

A two-step reaction process was used to convert these silica-based *C. criophilum* diatom spines into titania replicas. The first step involved the metathetic reaction of SiO_2 with $TiF_4(g)$ to yield $TiOF_2$, which may have occurred by one or both of the following reactions:

$$TiF_4(g) + \tfrac{1}{2}SiO_2(s) \Rightarrow TiOF_2(s) + \tfrac{1}{2}SiF_4(g) \quad (1)$$

$$TiF_4(g) + \tfrac{2}{3}\ SiO_2(s) \Rightarrow TiOF_2(s) + \tfrac{1}{3}\ Si_2OF_6(g) \quad (2)$$

$$TiF_4(g) + SiO_2(s) \Rightarrow TiOF_2(s) + SiOF_2(g) \quad (3)$$

The equilibrium partial pressure of $TiF_4(g)$ over TiF_4 solid at 225°C is about 0.01 atm[45]. Although there is no thermodynamic data available in the literature for solid $TiOF_2$, the formation of the titanium oxyfluoride at ≥ 225°C from silica was apparently thermodynamically favored, as indicated by the following TEM and SEM analyses of the reacted samples.

An early attempt to conduct the conversion reaction at 350ºC as described by Unocic, *et al*.[12] resulted in vaporization of the siliceous structures. No solid product remained in the nickel boat. Such vaporization may be caused by the formation of intermediate Si-O bearing gas species which might be more predominant at 350°C. The vaporized Si-O may react with $TiF_4(g)$ according to the reactions described below and the solid product, $TiOF_2$, may formed at locations relatively far from the original SiO_2 source.

$$TiF_4(g) + Si_2OF_6(g) \Rightarrow TiOF_2(s) + 2SiF_4(g) \quad (4)$$

$$TiF_4(g) + SiOF_2(g) \Rightarrow TiOF_2(s) + SiF_4(g) \quad (5)$$

The reactive vaporization of the *C. criophilum* spines was minimized by lowering the reaction temperature to 300°C. As seen in Figure 3.5a, the overall shapes of the spines were preserved in the reacted samples. However, the finer features, such as the barbs and triangular cross-section, were lost during exposure to the TiF_4 gas at 300°C for 1 h. The smooth surfaces of the amorphous siliceous spines transformed into interconnected cubical crystals, with lateral size between 200 nm and 300 nm. Such cubical crystal formation is consistent with the cubic crystal structure of $TiOF_2$ at temperatures higher than 60°C (see Chapter 5). At reaction for 2 h at 250°C (Figure 3.5b), the sizes of cubic crystals were reduced, although the fine features of the spines were still missing. EDX analyses in Figure 3.5c and d show the presence of

titanium, oxygen, and fluorine peaks, and the absence of silicon peaks, which confirmed the transformation of silica into titanium oxyfluoride according to reaction (1) or (2).

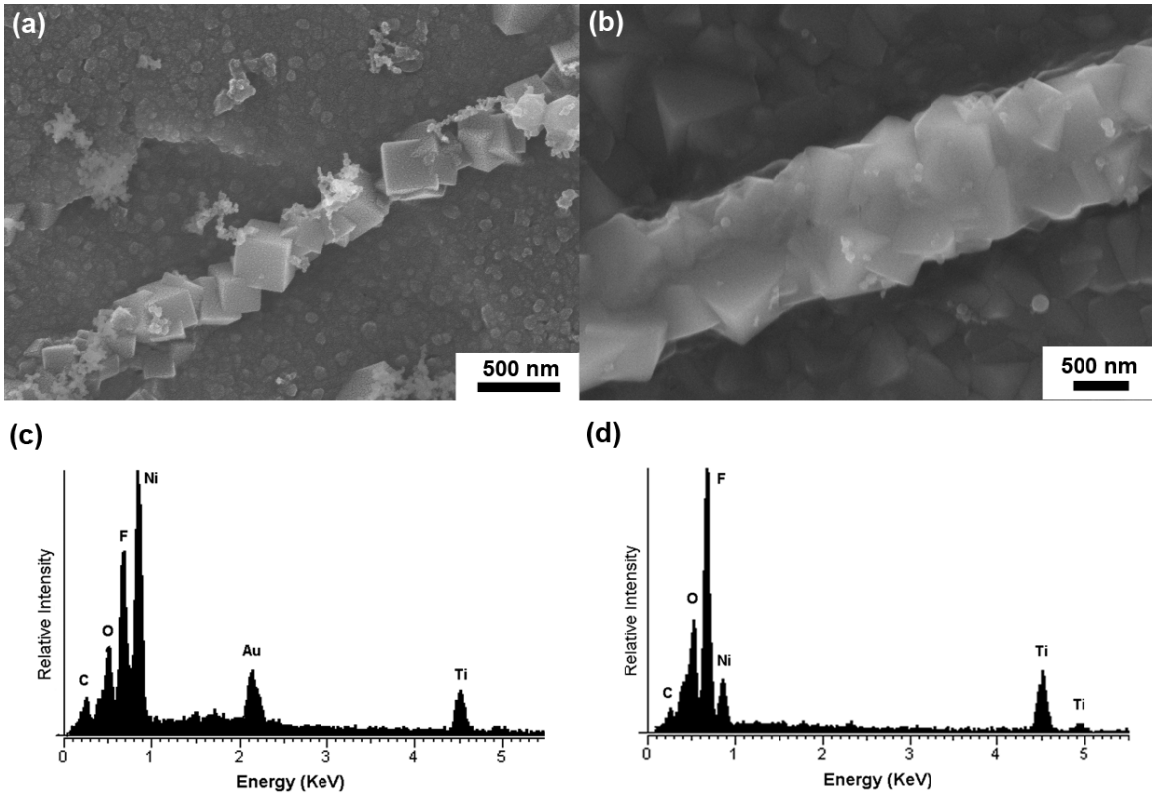

Figure 3.5: Secondary electron images and corresponding EDX analyses of *C. criophilum* spines that were exposed to TiF_4 at (a), (c) 300°C for 1 h and (b), (d) 250°C for 2 h. The nickel and gold peaks originated from the underlying substrate of the samples and the conductive coating applied to reduce charging, respectively.

Secondary electron images and associated EDX analyses are shown in Figure 3.6 after the reaction of *C. criophilum* spines with TiF_4 at 225°C for 2 h. As can be seen, some main features of the *C. criophilum* spines, such as the triangle shape of the cross section, were preserved after the conversion reaction. The presence of titanium, oxygen, and fluorine peaks, and the absence of silicon peaks, in the EDX analyses confirmed the transformation of silica into titanium oxyfluoride. Since a spot EDX analysis covers a relatively large area compared to the size of the spines, the elemental EDX maps helped distinguish the elements within the converted spines from the underlying nickel substrate (Figure 3.6d-f).

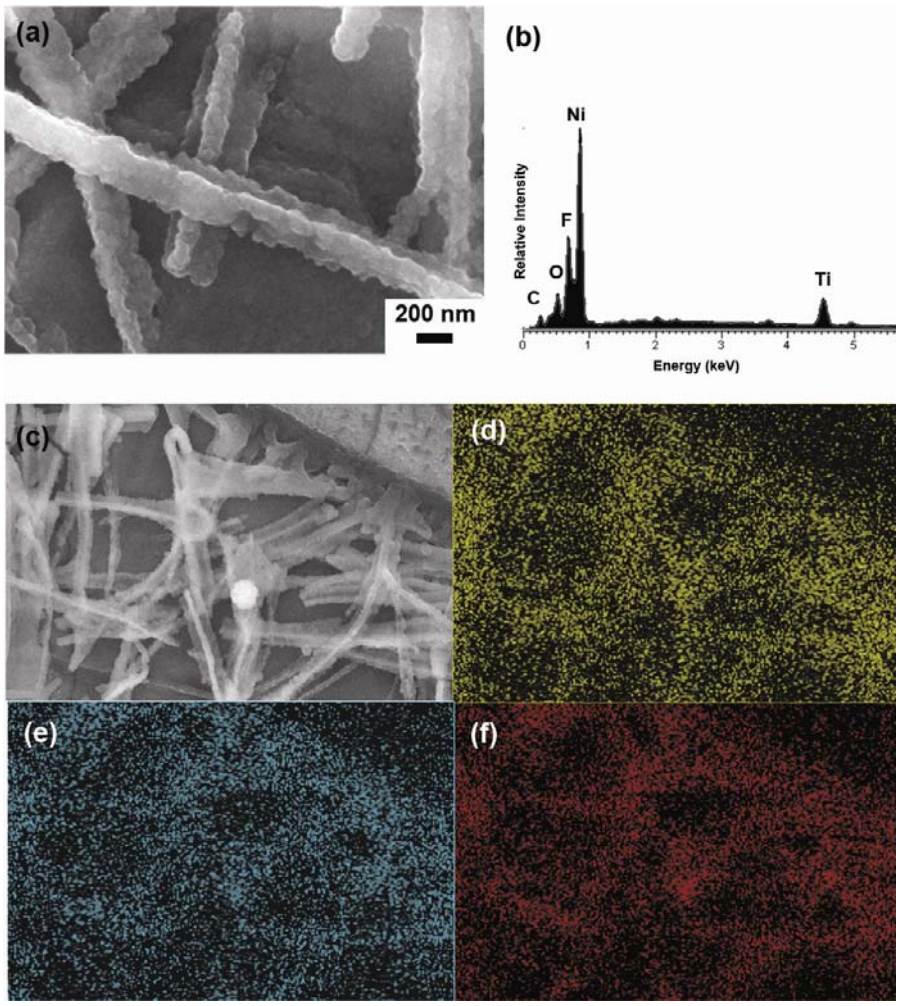

Figure 3.6: (a), (c) Secondary electron images of the *C. criophilum* spines after reaction with TiF_4(g) at 225ºC for 2 h. (b) EDX analysis of the spines in (a) revealing the absence of Si in the reacted sample. EDX elemental maps of (d) titanium, (e) oxygen, and (f) fluorine associated with the secondary electron image in (c). (Note: the nickel peak in (b) resulted from the underlying nickel substrate).

In the second step, the $TiOF_2$ reaction product was converted into TiO_2 through exposure to humid flowing oxygen. This conversion may have occurred via one or both of the following reactions[12]:

$$TiOF_2(s) + ½O_2(g) \Rightarrow TiO_2(s) + F_2(g) \quad (6)$$

$$TiOF_2(s) + H_2O(g) \Rightarrow TiO_2(s) + 2HF(g) \quad (7)$$

TEM analyses in Figure 3.7 indicated the formation of predominantly nanocrystalline anatase (5 to 10 nm crystals) in the fully converted *C. criophilum* spines. Secondary electron images in Figure 3.8 reveal the well-preserved morphology of the *C. criophilum* spines after reaction with $TiF_4(g)$ at 225°C for 2 h and then exposure to flowing humid oxygen at 350°C for 2 h. EDX analyses (i.e., EDX spectrum in Figure 3.8d and elemental maps in Figure 3.8e and f) indicated the absence of fluorine after the flowing humid oxygen treatment.

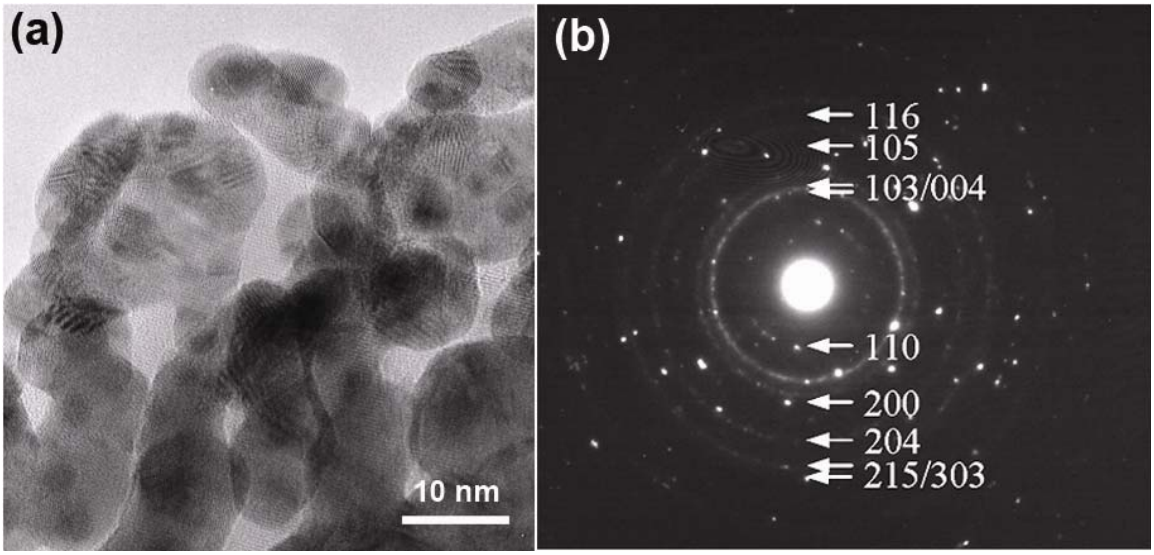

Figure 3.7: (a) TEM analyses of *C. criophilum* spines after reaction with TiF_4(g) at 225°C for 2 h, and exposure to flowing, humid oxygen gas at 350°C for 2 h. (b) Selected area electron diffraction analysis (the labels corresponded with anatase reflections) of converted *C. criophilum* spines shown in (a). The nano crystalline product was comprised of anatase TiO_2.

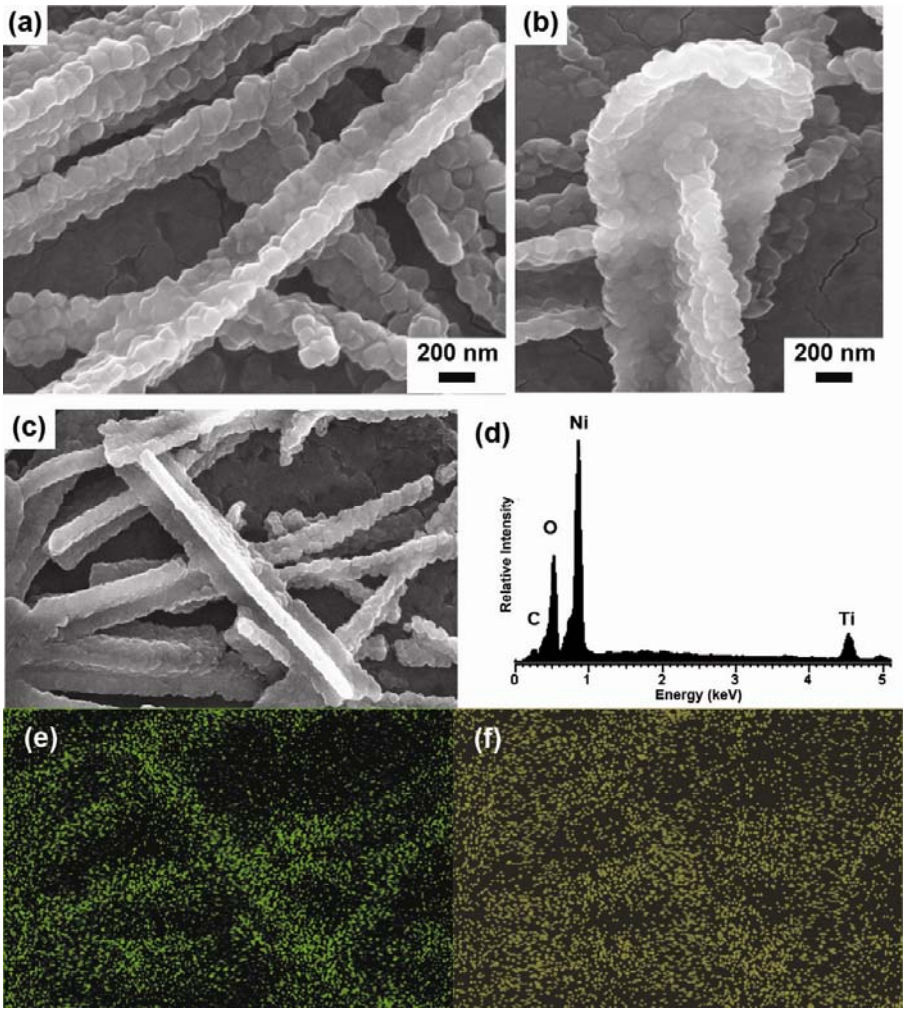

Figure 3.8: (a), (b), (c) Secondary electron images of the *C. criophilum* spines after reaction with TiF_4(g) at 225°C for 2 h and oxygenation at 350ºC for 2 h in flowing humid oxygen. (d) EDX analyses of these reacted *C. criophilum* spines revealed the absence of F peaks. EDX elemental maps of (e) titanium and (f) oxygen for the specimen shown in (c). (Note: the nickel peak in (d) resulted from the underlying nickel substrate).

3.3.3 Reactive Conversion of Silica Scaffold Synthesized via Silicification of DWA Templates

Figure 3.9a shows an 8-layered silicified DWA template for the reactive conversion process. EDX analyses in Figure 3.9b shows the main elements comprising the template are silicon and oxygen, which are uniformly distributed throughout the structure (see Figure 3.9c and d). Since the amount of inorganic matter in the structure was only 52%[60], a significant amount of carbon, which originated from the polymer precursors, was present and must also uniformly distributed throughout the structure.

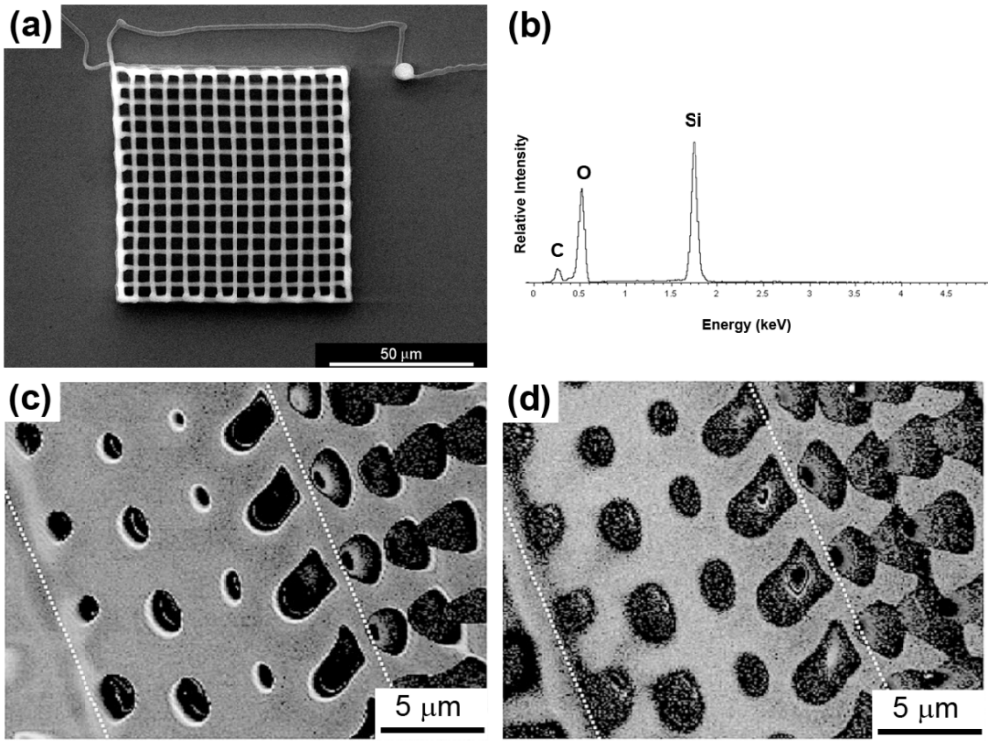

Figure 3.9: (a) Secondary electron image of an 8-layered silicified DWA template and (b) EDX spectrum obtained from this specimen. Elemental EDX maps of a focus ion beam (FIB) milled cross-section indicate the uniform distribution of (c) silicon and (d) oxygen throughout the cross-section. (Images (c) and (d) are courtesy of Dr. Lewis group at UIUC).

A heat treatment at 580°C for 1 h in air was sufficient to remove the carbon from the DWA structures beyond the minimum detectable limit of the EDX analyses (Figure 3.10c). The surface morphology (Figure 3.10b) appeared not affected by the heat treatment and the overall DWA structure was preserved (Figure 3.10a). An exposure to TiF_4(g) at 210°C for 12 h, however, resulted in significantly distorted structure. As seen in Figure 3.10d, the entire structure appeared folded and collapsed. EDX spectrum showed the presence of Ti and F after the reaction (Figure 3.10f), indicating a successful formation of titanium oxyfluoride (note: Si peak originated from the underlying silicon substrate). The structure distortion may be caused by the relatively porous nature of the filament (due to the prior 580°C heat treatment), which induced shrinkage and structure collapse during the reaction with TiF_4(g). The continuous polymer (carbon) matrix may be needed for a successful shape preservation reaction because it could provide a rigid framework for the DWA structure during the reaction with TiF_4(g). Thus, the next conversion reactions were conducted without heat treatment process.

A secondary electron image, corresponding elemental maps, and EDX spectral analyses in Figure 3.11 reveal the result of the reaction of an 8-layered silicified DWA template with TiF_4(g) at 210°C for 8 h, followed by fluorine removal via exposure to flowing humid oxygen at 300°C for 8 h. The specimen was enriched in Ti and O, and depleted in Si, relative to the underlying silicon substrate. The presence of titanium and oxygen, and the absence of fluorine, was consistent with conversion into titania. The large silicon peak in the EDX spectrum was generated by the substrate on which the structure was written (as is evident from the silicon x-ray map in Figure 3.11d). A transmission electron image of a cross-section of a filament obtained from a converted structure of the type shown in Figure 3.11 is presented in Figure 3.12a. The filament was dense and contained nanocrystalline anatase TiO_2, as indicated by the selected area electron diffraction pattern in Figure 3.12c.

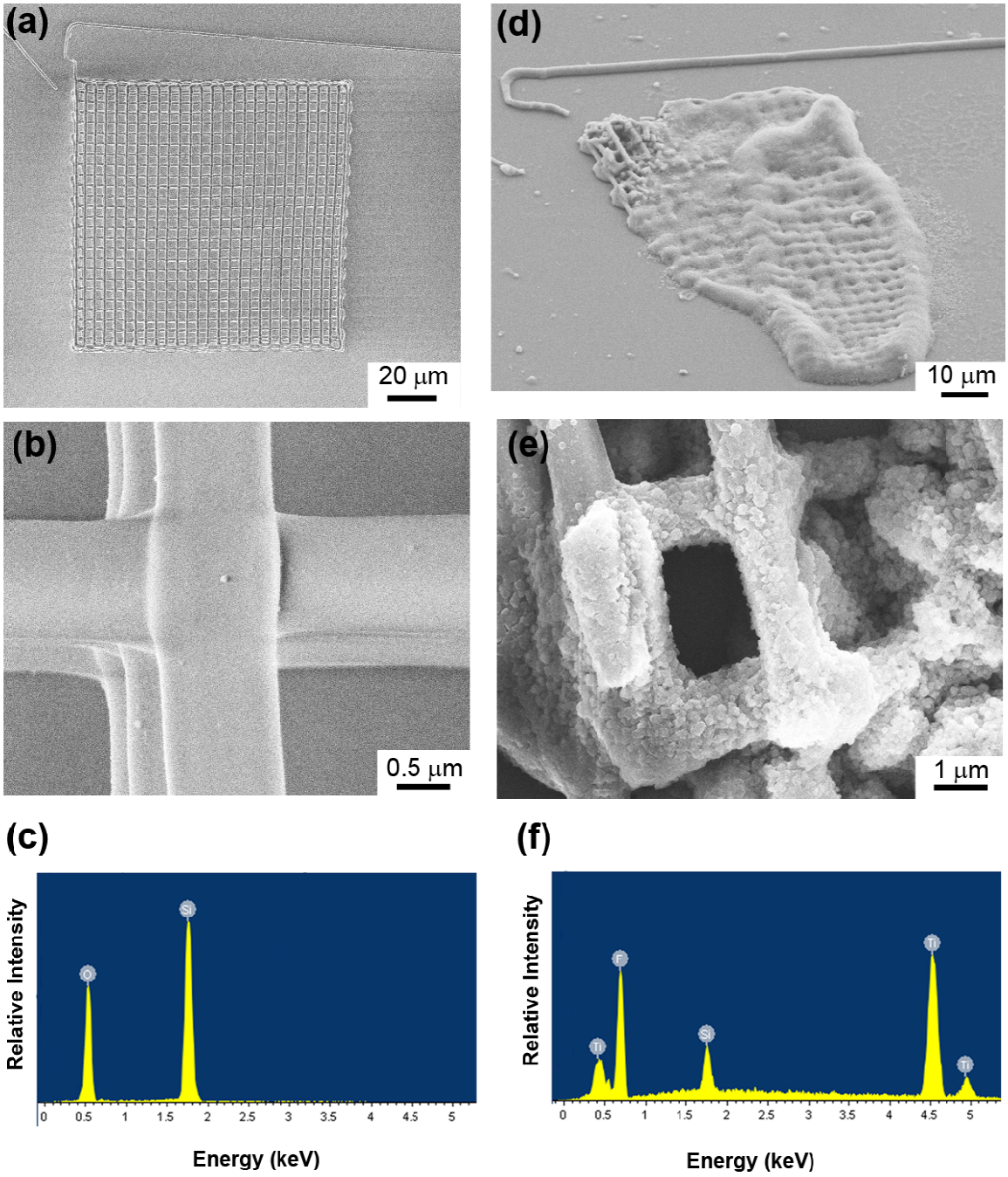

Figure 3.10: (a), (b) Secondary electron image and (c) EDX spectrum obtained from a 6 layer silicified DWA specimen after heat treatment at 580°C for 1 h in air. The lacks of carbon peak in the EDX spectrum indicates successful removal of polymer from the specimen. (c), (d) Secondary electron image and (f) EDX spectrum obtained from the same specimen after exposure to TiF_4(g) at 210°C for 12 h. The silicon peak in the (f) was most likely generated by the substrate on which the structure was located.

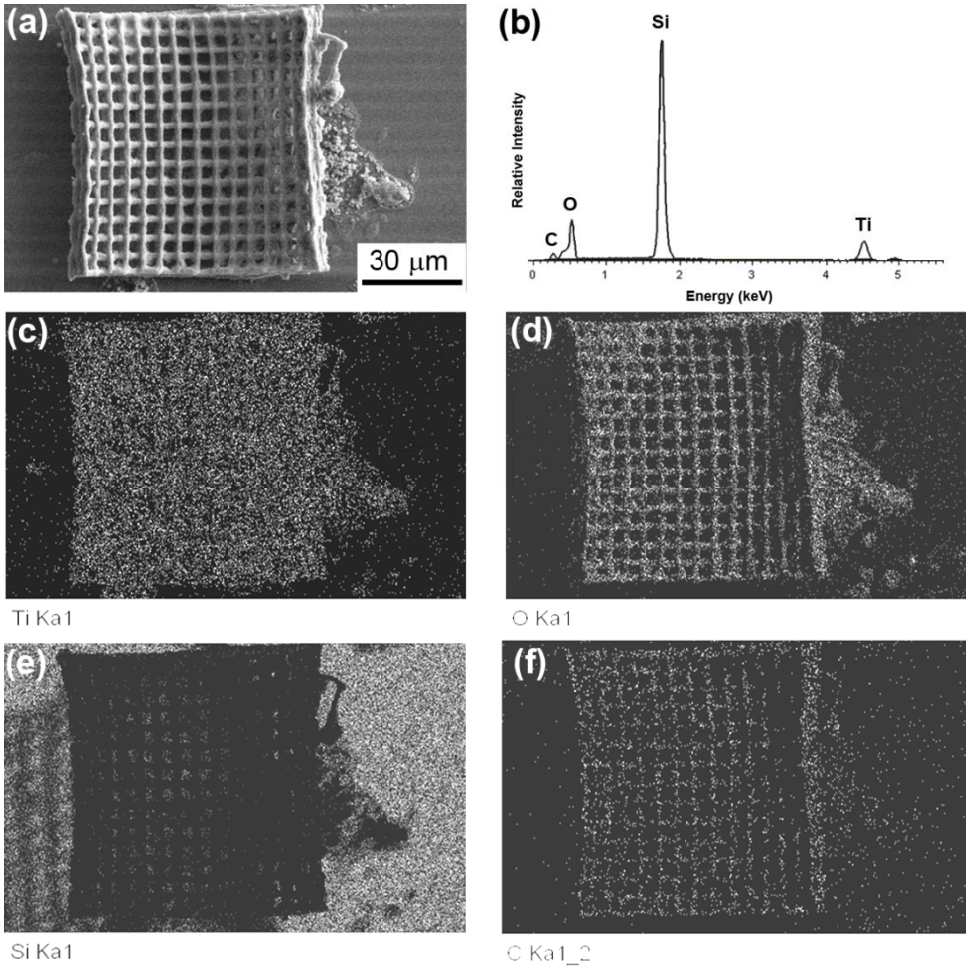

Figure 3.11: (a) Secondary electron image and (b) EDX spectrum obtained from a titania-converted 8 layer silicified DWA specimen (after exposure to TiF_4(g) at 210°C for 8 h and then to flowing H_2O(g)/O_2(g) at 300°C for 8 h). Elemental EDX maps for (b) titanium, (c) oxygen, (d) silicon, and (e) carbon obtained from this specimen. The large silicon peak in the EDX spectrum was generated by the substrate on which the structure was written.

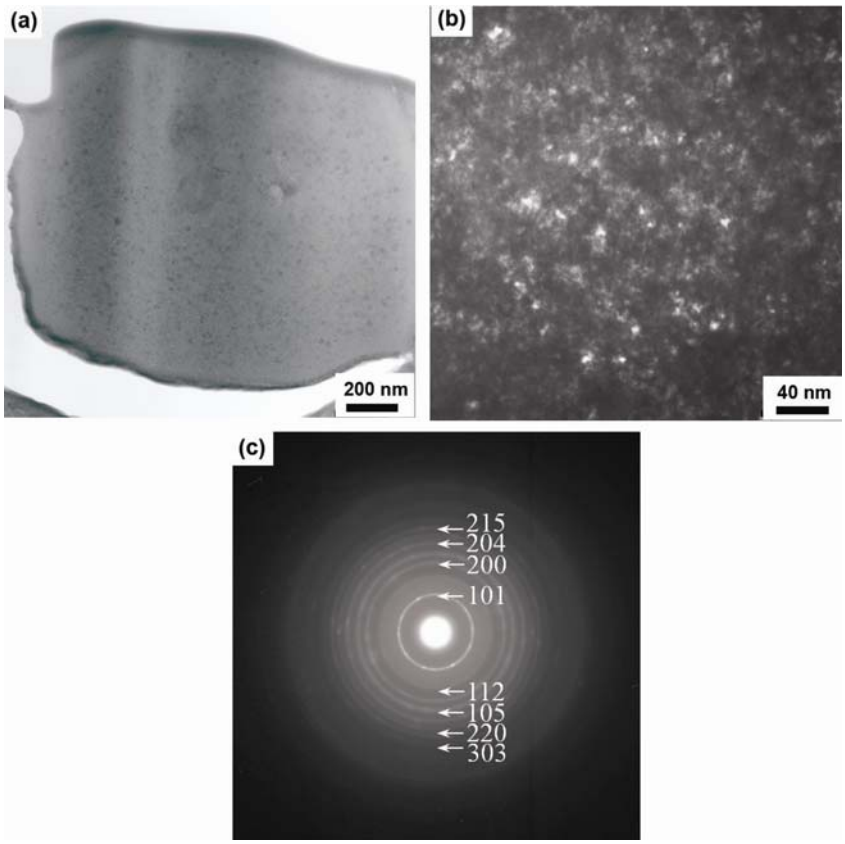

Figure 3.12: (a) TEM image of a cross-section of a filament obtained from a TiO_2-converted structure of the type shown in Figure 3.11. (b) Higher resolution TEM image revealing very fine titania crystallites (less than 10 nm) dispersed uniformly throughout the cross section, (c) selected area electron diffraction pattern, consistent with anatase TiO_2, obtained from the cross-section in (a) and (b).

While such conversion into titania yielded structures that retained the lattice morphology of the starting silicified specimens, appreciable warping (curling) of the specimens was observed (Figure 3.11). Such distortion was found to occur during exposure of the $TiOF_2$-converted specimens to flowing $H_2O(g)/O_2(g)$ at 300°C and was more pronounced on a larger size sample (Figure 3.13c). The warping that occurred during this treatment was accompanied by detectable shrinkage (on the order of 10% linear shrinkage). Since this second stage of heat treatment was conducted in an oxidizing atmosphere, and since residual organic material was likely to have been present within the specimens after the first stage of heat treatment (at 210°C in $TiF_4(g)/Ar(g)$), it was surmised that the shrinkage and warping was a result of the oxidation of the organic material. Indeed, the silicified DWA specimen typically contained 52 wt% silica[60] and there was no high temperature treatment (e.g., by heating to 500°C in air) performed on the sample prior to reactive conversion process (that could reduce the amount of organic material in the specimen). To avoid such distortion, the second heat treatment was modified by using argon as the carrier gas for the water vapor. Secondary electron images of the converted structures after the $H_2O(g)/Ar(g)$ treatment are shown in Figure 3.14. While some buckling was detected in the 8 layer structures (Figure 3.14d-f), the 6 layer structures (Figure 3.14a-c) were free of significant warping and exhibited less shrinkage (on the order of 4% linear shrinkage) than the specimens treated with $H_2O(g)/O_2(g)$.

A secondary electron image, and associated x-ray maps, of a 6-layer structure after reaction with $TiF_4(g)$ and then $H_2O(g)/Ar(g)$ are shown in Figure 3.15. The converted structure was enriched in titanium and oxygen, and depleted in silicon, relative to the underlying silicon substrate. As for the case of the $H_2O(g)/O_2(g)$ treatment (Figure 3.11e), residual carbon was also detected in this structure. Higher magnification secondary electron images of the converted titania structure are shown in Figure 3.16. The surfaces of the nanocrystalline filaments were relatively smooth, and the necked

regions between filaments in adjacent layers were preserved. The absence of apparent micro-cracking, particularly at the necked regions, indicated that the modest shrinkage during reaction processing occurred in an isotropic fashion.

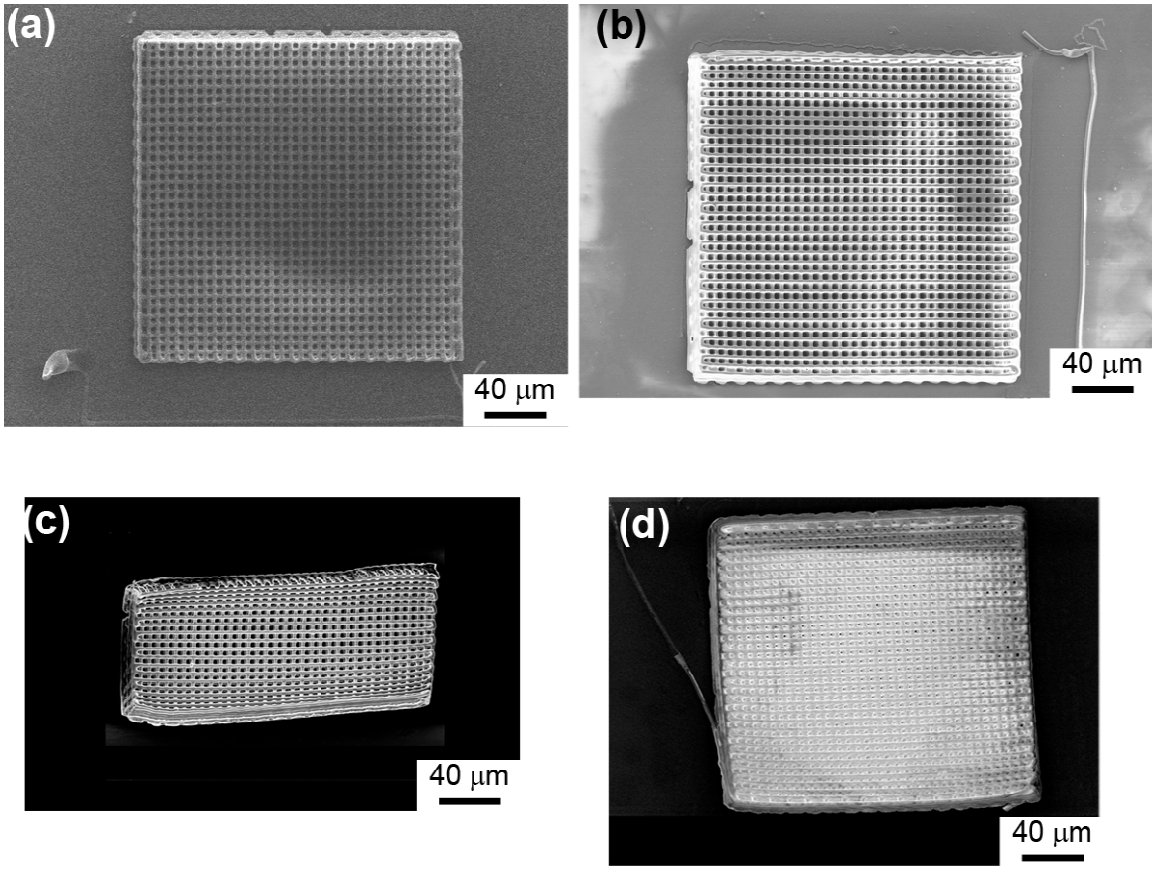

Figure 3.13: (a) Secondary electron image of an 8-layered silicified DWA specimen, (b) the same specimen after exposure to TiF_4(g) at 220°C for 12 h, and (c) after exposure to H_2O(g)/O_2(g) at 300°C for 5 h. (d) A similar specimen after exposure to TiF_4(g) at 220°C for 12 h, and then to H_2O(g)/Ar(g) at 300°C for 12 h. The specimen treated in oxygen-rich atmosphere (c), exhibits significantly more warping compared to the specimen treated in argon-rich atmosphere (d).

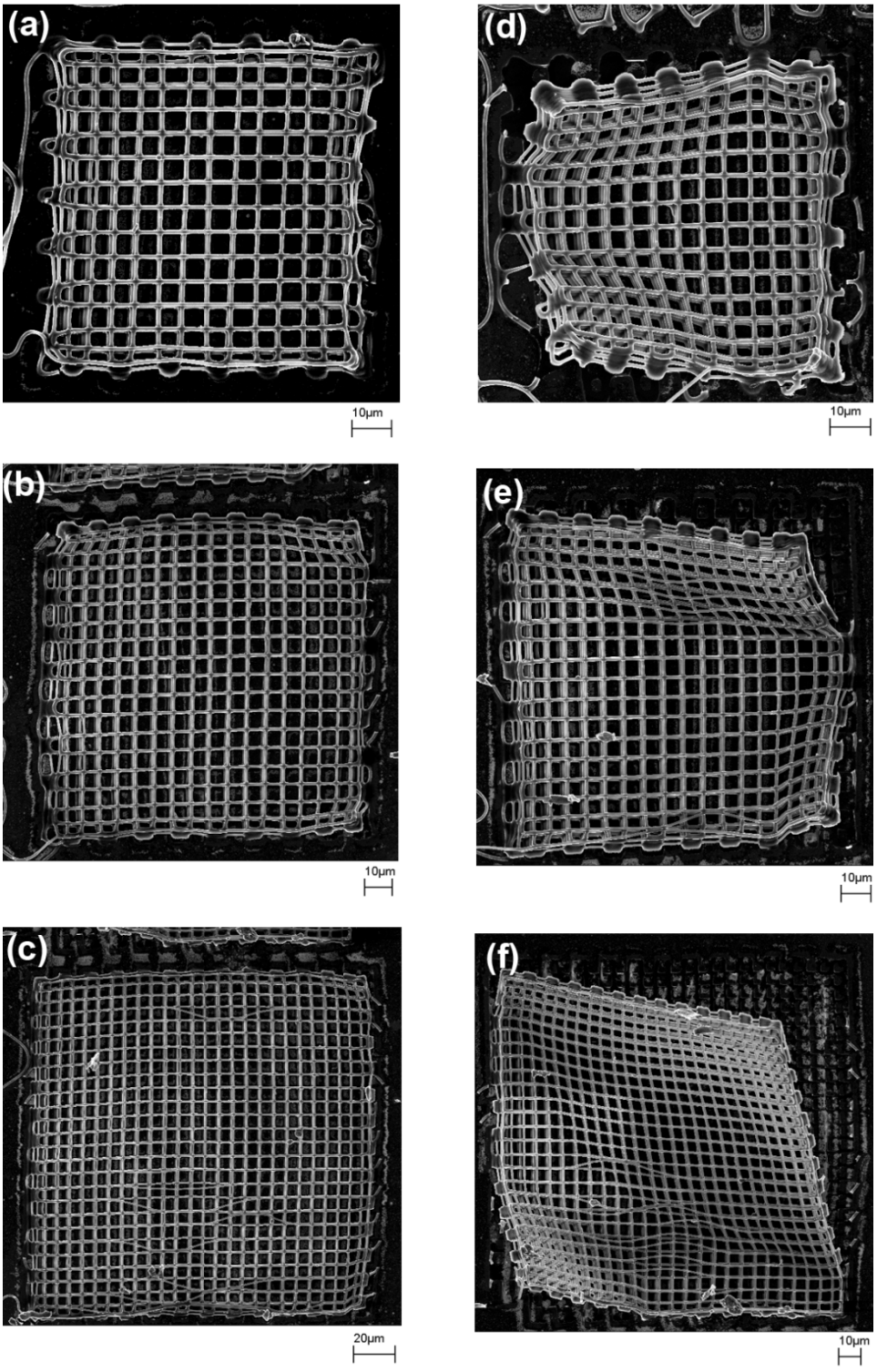

Figure 3.14: Secondary electron images of titania-converted silicified DWA specimens generated via reaction with TiF_4(g) at 210°C for 12 h, and then with H_2O(g)/Ar(g) at 300°C for 12 h. The structures in (a)-(c) contained 6 filament layers, whereas the structures in (d)-(f) contained 8 filament layers.

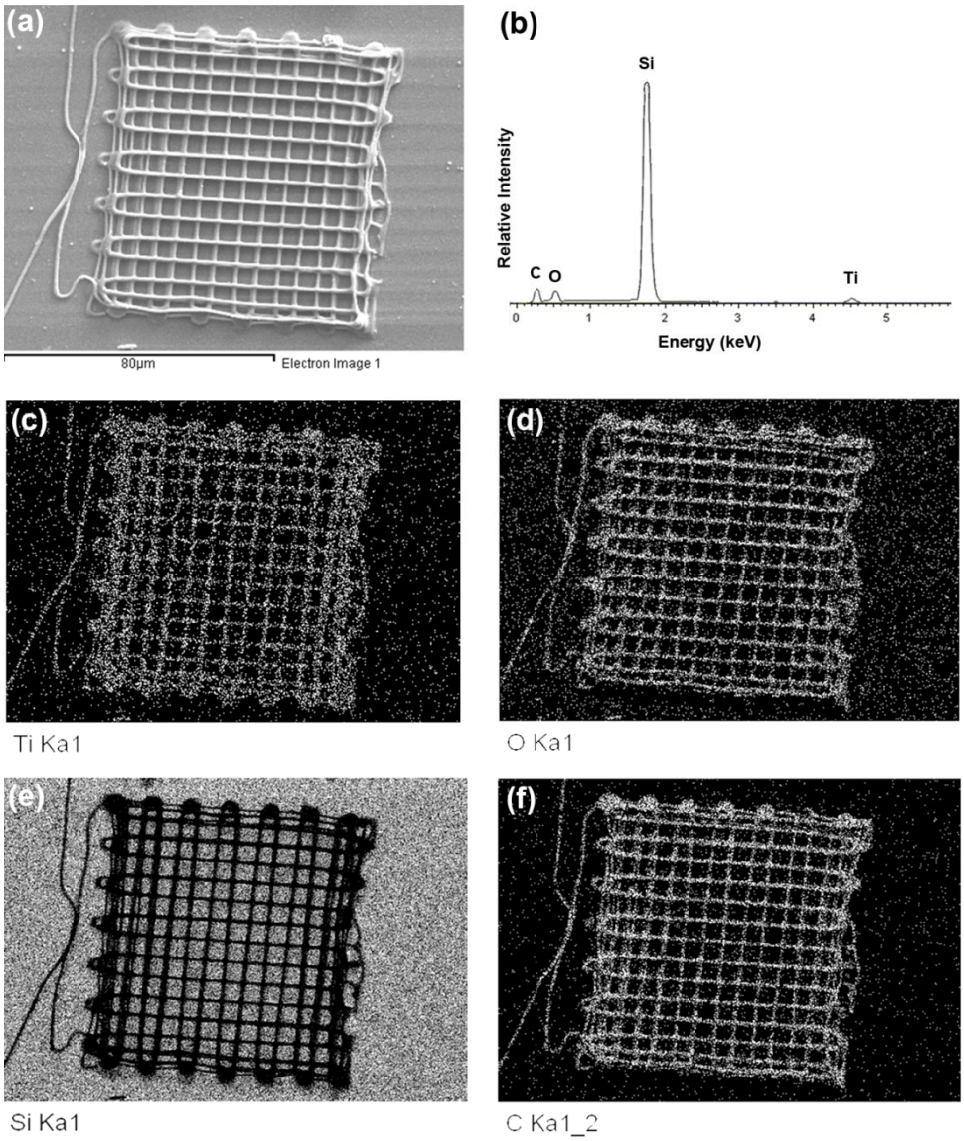

Figure 3.15: (a) Secondary electron image and (b) EDX spectrum obtained from a titania-converted 6 layer silicified DWA specimen (after exposure to TiF_4(g) at 210°C for 12 h and then to flowing H_2O(g)/Ar(g) at 300°C for 12 h). Elemental EDX maps for (b) titanium, (c) oxygen, (d) silicon, and (e) carbon obtained from this specimen. The large silicon peak in the EDX spectrum was generated by the substrate on which the structure was written

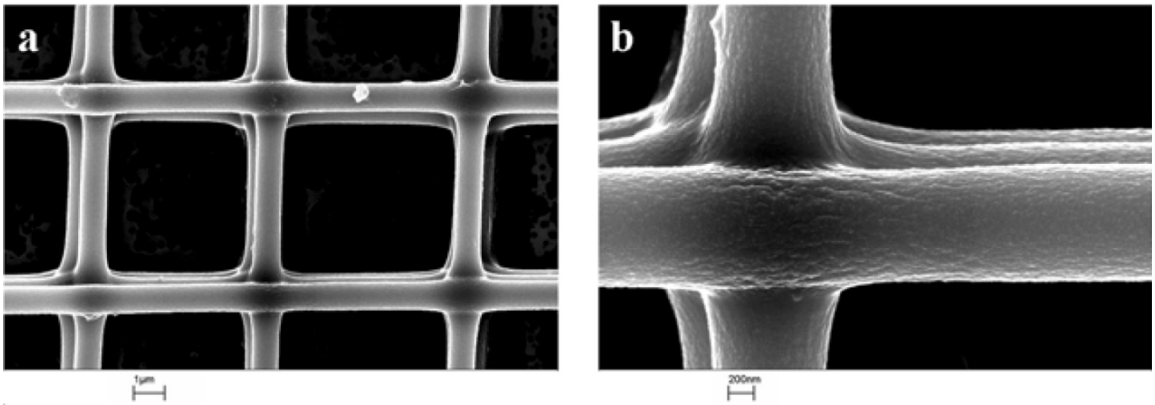

Figure 3.16: Secondary electron images obtained from a titania-converted 6 layer silicified DWA specimen (after exposure to TiF_4(g) at 210°C for 12 h and then to H_2O(g)/Ar(g) at 300°C for 12h).

3.3.4 Optical Properties of Titania-Converted DWA Woodpile Structures

A silicified DWA woodpile structure with 12 layers of filament stacking in face centered cubic configuration is attractive for photonic applications because of its capability to exhibit an optical band gap[65]. SEM images of such a titania-converted structure upon exposure to TiF_4(g) and H_2O(g)/Ar(g) are shown in Figure 3.17. A transmission electron image of a cross-section of a filament obtained from the converted structure is presented in Figure 3.18. The filament was dense and composed of clustered crystallites, which were distributed throughout the cross-section and near the surface of the filament. High resolution TEM image (Figure 3.18c) showed that the size of crystallites was in the order of 10 nm and the electron diffraction pattern of the cross section (Figure 3.18d) was consistent with anatase TiO_2.

Optical characterization was performed at each step of the fabrication process in order to characterize the optical response of the anatase woodpile photonic crystals, and relate it to the properties of the initial silica template. Figure 3.19a shows the reflectance spectrum from the silicified structures (a ~ 4 um). The peak near 7 μm has a maximum reflectance of 32%. Figure 3.19c and e present the reflectance spectra for the structure after exposure to TiF_4 at 210°C for 12 h and then after H_2O(g)/Ar(g) treatment at 250°C for 12 h, respectively. The intensity of largest peaks decreased after the first treatment However, the intensities of the largest reflectance peaks increased after the second treatment. The reflectance peak near 7 μm increased to 38% compared to 32% for the initial silicified structure. There is no significant shift on the main peak locations, although dimension measurements indicated that the lattice parameter was reduced by about 10% during the second treatment. The effect of the shrinkage to a peak shift may have been offset by the change in the effective refractive index of the structure[66], which was caused by the change in the structure's composition (i.e., from silica-organic into anatase-organic composite).

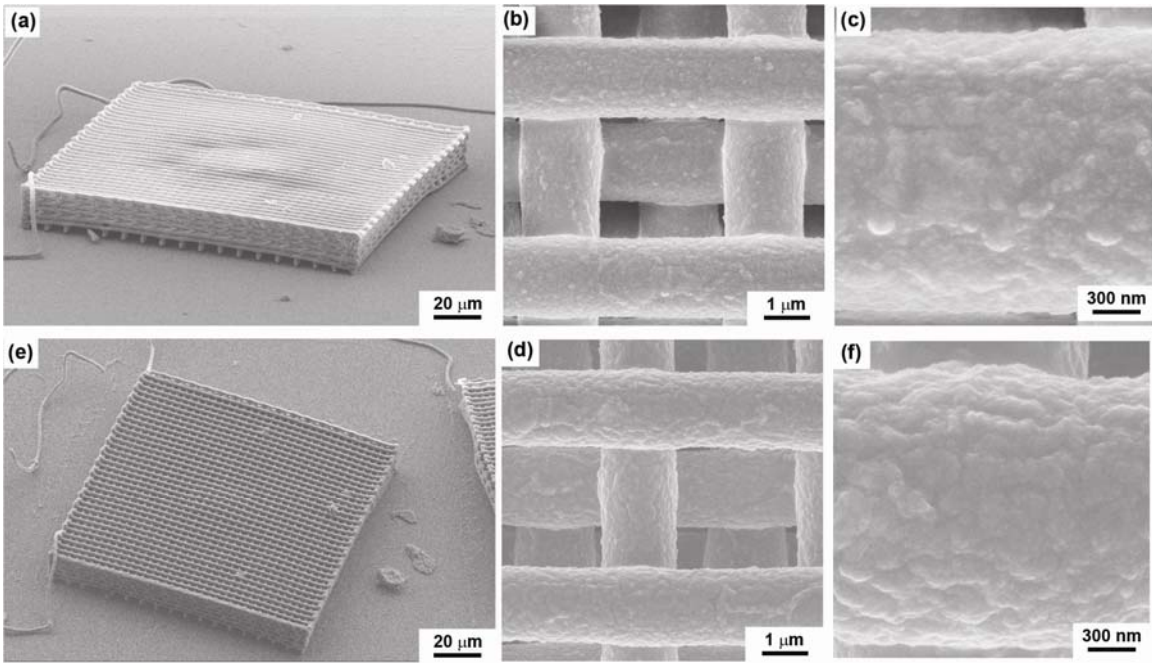

Figure 3.17: Secondary electron images at increasing magnification of a titania-converted 12 layer DWA structure for photonic optical reflectance measurements; (a) to (c) after exposure to TiF_4(g) at 210°C for 12 h and (d) to (f) after exposure to H_2O(g)/Ar(g) at 250°C for 12h.

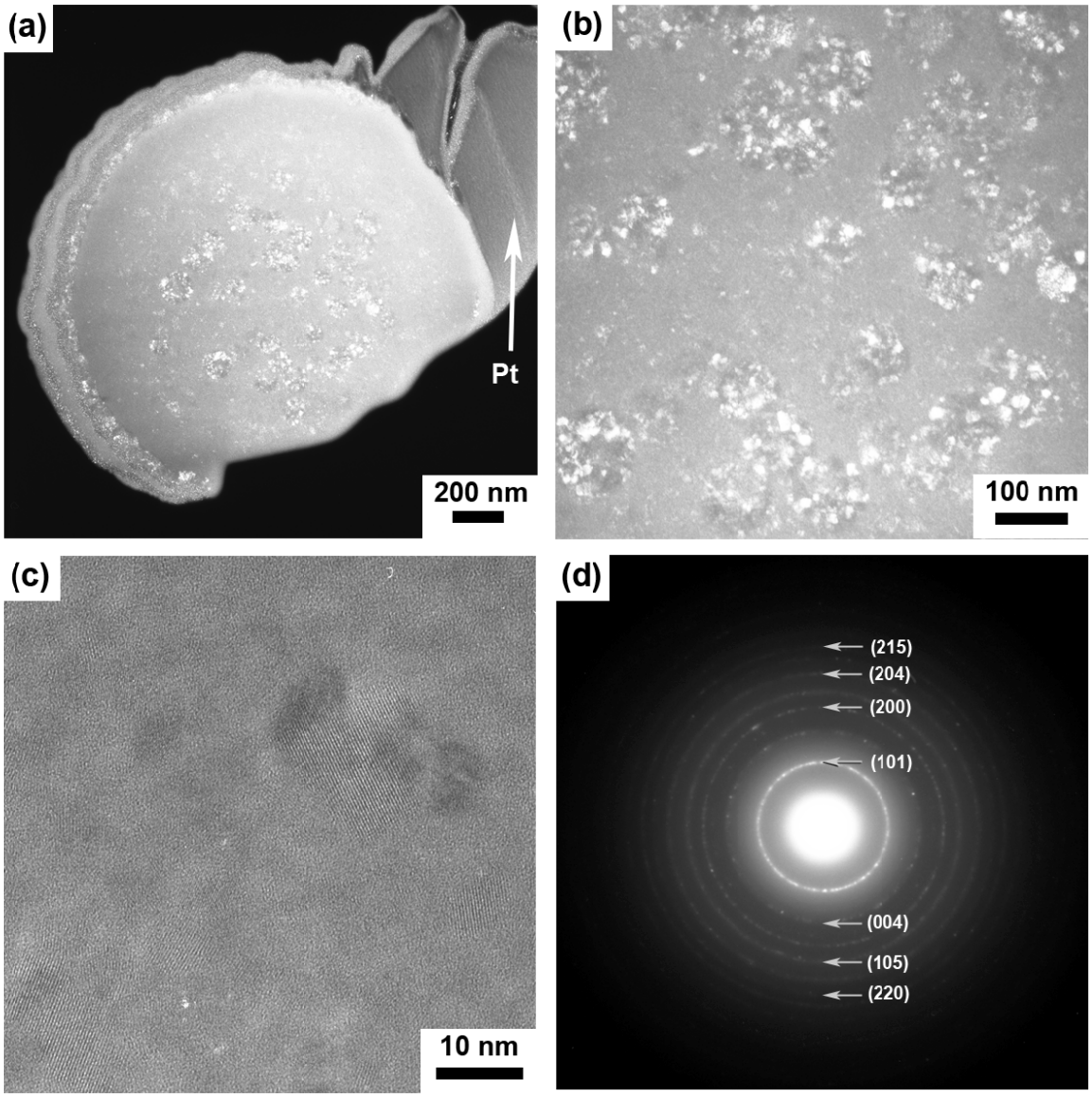

Figure 3.18: (a) and (b) TEM image of a cross-section of a filament obtained from a TiO_2-converted structure of the type shown in Figure 3.17e. (c) Higher resolution TEM image revealing very fine titania crystallites (≤10 nm) dispersed throughout the cross section. (d) selected area electron diffraction pattern is consistent with anatase TiO_2, indicating most of $TiOF_2$ were transformed into anatase during the oxygenation treatment with H_2O/Ar mixture at 250°C.

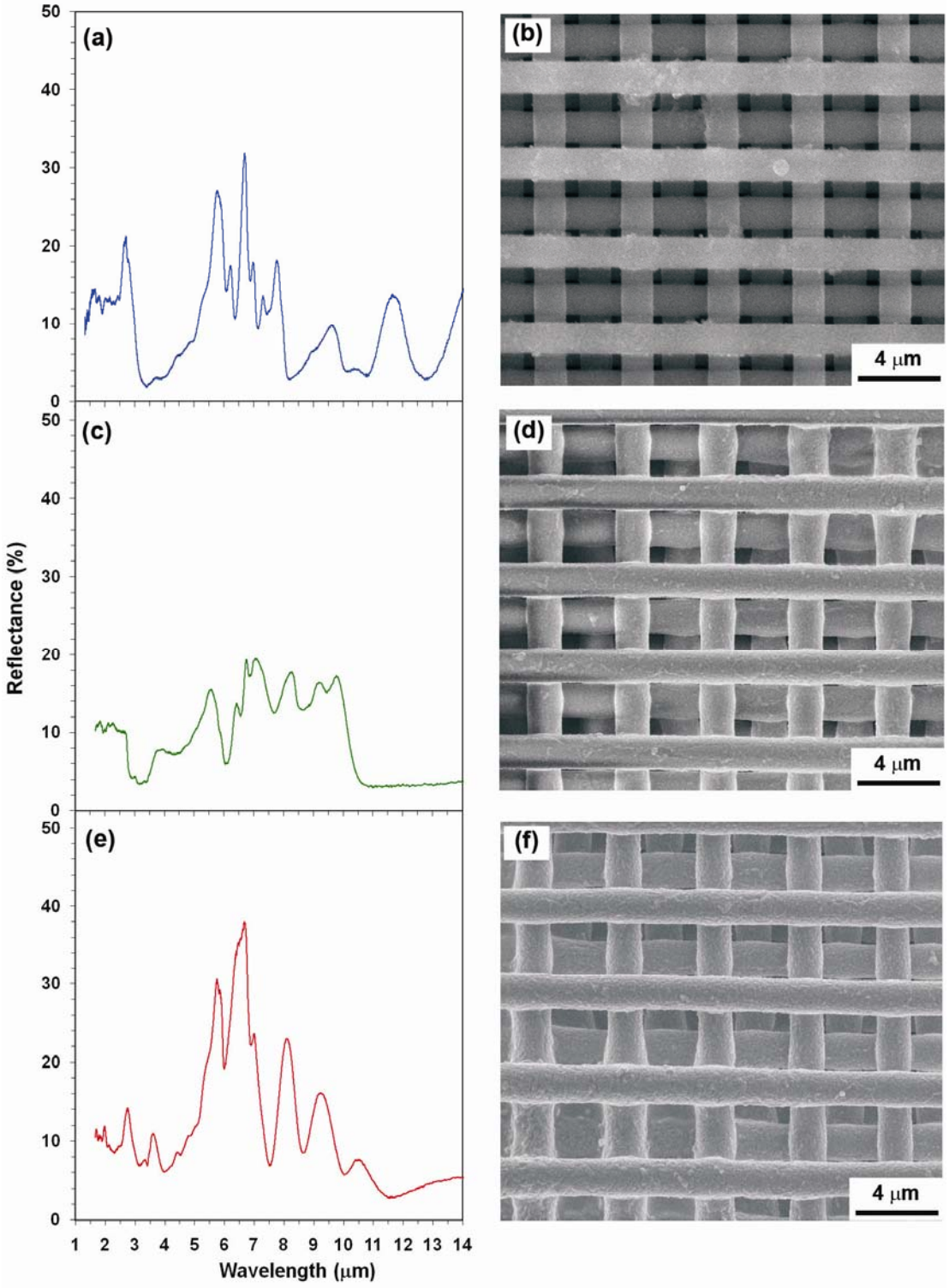

Figure 3.19: Reflectance spectrum and secondary electron images of the woodpile structure at different stage of processing: (a) and (b) Initial silicified woodpile structure (result: SiO_2); (c) and (d) after reactive conversion with TiF_4(g) at 210°C for 12 h (result: $TiOF_2$); (e) and (f) after H_2O(g)/Ar(g) treatment at 250°C for 12 h (result: TiO_2 anatase).

3.4 Conclusions

This work demonstrated the feasibility of a two-step (TiF_4 reaction; H_2O/O_2 or H_2O/Ar reaction) reactive conversion process for fabricating 3-D titania structures from both natural (*Corethron Criophilum* diatom spines) and synthetic templates (silicified direct write assembled logpile structures). By controlling the peak reaction temperature and time, the rapid coarsening of $TiOF_2$ could be minimized so as to yield $TiOF_2$ and then TiO_2 replicas that retained the shapes and fine features of the starting silica structures. . In the case of silicified structures derived from DWA process, the carbon (polymer) matrix was needed to provide a relatively rigid framework that minimized unwanted distortion and, thus, preserved the structure during the conversion processes. Certain atmospheric conditions may be required during the oxygenation ($TiOF_2$ to TiO_2) process to avoid structural distortion The loss of carbon during the $TiOF_2$ to TiO_2 conversion process of DWA structure could be minimized by heat treatment in a flowing mixture of H_2O(g)/Ar(g).

CHAPTER 4: Three-Dimensional Microscale TiO_2 Ethanol Gas Sensor Synthesized from a Diatom Frustule

Miniature ceramic-based sensors capable of responding rapidly to changes in gas composition are needed for a wide variety of advanced detection and control systems. Certain micro-organisms are adept at assembling open, nanoparticle-based bioclastic structures that are attractive for fast gas permeation and adsorption. The reactive conversion of the frustule of a single diatom cell into nanocrystalline anatase (TiO_2), with a preservation of shape and fine features is demonstrated in this chapter. The electrical conductivity of this single frustule sensor changed rapidly (relative to base electrical conductivity) and reproducibly with variations in ethanol vapor pressure. Such rate of response was significantly faster than has been previously reported.

4.1 Introduction

Ceramic-based gas sensors are widely used to monitor and provide vital feedback for the efficient control of processes that are central to modern transportation (automotive, aerospace), energy generation, manufacturing, food production and storage, and pollution control systems[67-69]. Such sensors can also provide critical detection capability in alarm systems for public safety (e.g., for the detection of carbon monoxide, ammonia, hydrogen; for alcohol analysis of breath)[70]. For current and new applications, the miniaturization of ceramic gas sensors is strongly desired in order to: (i) enable the detection of gradients in gas concentration over small distances or of gas concentrations within small, confined, or difficult-to-access volumes, (ii) minimize the effect of the gas sensor on the gas flow stream, (iii) allow for integration with microelectronic circuits,

and iv) reduce the power required to operate the sensor [71]. However, a high surface area is also desired of such ceramic gas sensors for enhanced sensitivity and rapid detection [72,73]. A ceramic sensor of high internal surface area and small external volume could be produced by assembling an interconnected 3-D network of gas-sensitive ceramic nanocrystals interspersed with a continuous 3-D network of pore channels. However, such assembly is complicated by the need for control over the 3-D nanostructure and chemistry (for desired performance), and the need for reproducible mass production (for low cost). These often-conflicting demands of fine-scale precision and large-scale fabrication may be resolved through self-assembly processes.

Diatoms are examples of microorganisms that self-assemble intricate 3-D nanoparticle assemblies. At the micro-scale, the silica-based diatom frustules are comprised of distinct pattern of fine features, such as pores, channels, ridges, protuberances, which are highly attractive for gas sensor applications[19,74,75]. Recent work has shown that silica-based diatom frustules can be converted into titania (TiO_2) via a metathetic displacement reaction route[12]. Titania-based compositions are widely used as gas sensors for the detection of ammonia, carbon monoxide, hydrogen, oxygen, nitrogen dioxide, methane, and alcohols[67]. The purpose of this chapter is to demonstrate that the attractive self-assembly and structural characteristics of diatom frustules can be coupled with synthetic chemical processing to generate miniature sensors that respond rapidly to a change in ethanol gas concentration.

4.2 Experimental Procedures

A nickel boat (20 × 15 × 4 mm) containing 100 mg of *Aulacoseira* diatom frustules (obtained as diatomaceous earth) and 500 mg of TiF_4 (99% purity, Advanced Research Chemicals, Inc., Catoosa, OK), for a molar TiF_4:SiO_2 reactant ratio of 2.4:1, were placed within a titanium tube (2.3 cm inner diameter × 20 cm long). Both ends of

the tube were crimped and welded shut inside a controlled atmosphere glove box filled with argon maintained at an oxygen partial pressure below 0.1 ppm. The sealed tube was heated to 350˚C at a ramp rate of 5˚C/min and held at this temperature for 2 hours inside a horizontal tube furnace. After cooling to room temperature, the tube was cut open, and the nickel boat containing the reacted frustules was removed. The reacted frustules were then heated in a flowing, humid air at 400˚C at a ramp rate of 5˚C/min for 4 hours. Before entering the furnace, the air was passed through a heated water bath (45°C) at a rate of 1 slpm. The measured humidity (using Model HMP234, Vaisala, Woburn, MA) at the gas outflow of the furnace was found to be at least 94% relative humidity. An SEM (LEO-1530, Zeiss, Germany) with EDX capability was used for imaging and localized elemental analysis. The elemental composition and crystalline phase of the frustules was studied with energy dispersive X-ray (EDX) detector (Oxford, England) attached to the SEM and X-ray diffractometer (Panalytical, Amelo, The Netherlands), respectively.

X-ray diffraction analyses were performed using an Alpha1 Panalytical Diffractometer (Almelo, The Netherlands) configured for Bragg-Brentano geometry. A Cu Kα X-ray radiation (1.5405980 Å) source was used. Information of the crystallite size was calculated from the peak broadening of the x-ray diffraction profile by using the Williamson Hall method in Jade software (MDI, Livermore, CA). The diffraction peaks was fitted using Pearson-VII profile function and the extracted integral breadth of the peaks was used in the Williamson-Hall plot to calculate crystallite size and strain. The isotherm curves of the samples were analyzed by using Autosorb-1 (Quantachrome Instrument, FL, USA), with nitrogen as an adsorbate at 77 K. Pore size distributions (PSD) and pore volumes were determined using Barrett-Joiner-Halenda (BJH) method on the desorption branch of the nitrogen isotherm data.

For gas sensing measurements, a single anatase-converted frustule was placed on a silicon wafer substrate coated with silicon nitride (Appendix E) and platinum electrodes were then applied to both ends of the replica with the aid of a focused ion beam instrument (Nova 200, FEI, Hillsboro, OR). A potentiostat (Reference 600, Gamry Instrument, Warminster, PA) was used to impose a constant bias voltage (100 mV to 2 V) across the frustule sensor, and to monitor the corresponding current passing through the sensor. The frustule sensor was positioned 2 mm under a nozzle through which an ethanol-bearing gas stream was passed at a constant flow rate (100 sccm) at a fixed operating temperature. Various ethanol concentrations were generated by mixing two streams of gases using mass flow controllers (Model FMA-2617A, Omega, Stamford, CT); one gas stream contained a known concentration of ethanol in synthetic air from a certified cylinder (Air Gas, Atlanta, GA) and the other gas stream contain high purity dry synthetic air from a cylinder (Air Gas, Atlanta, GA).

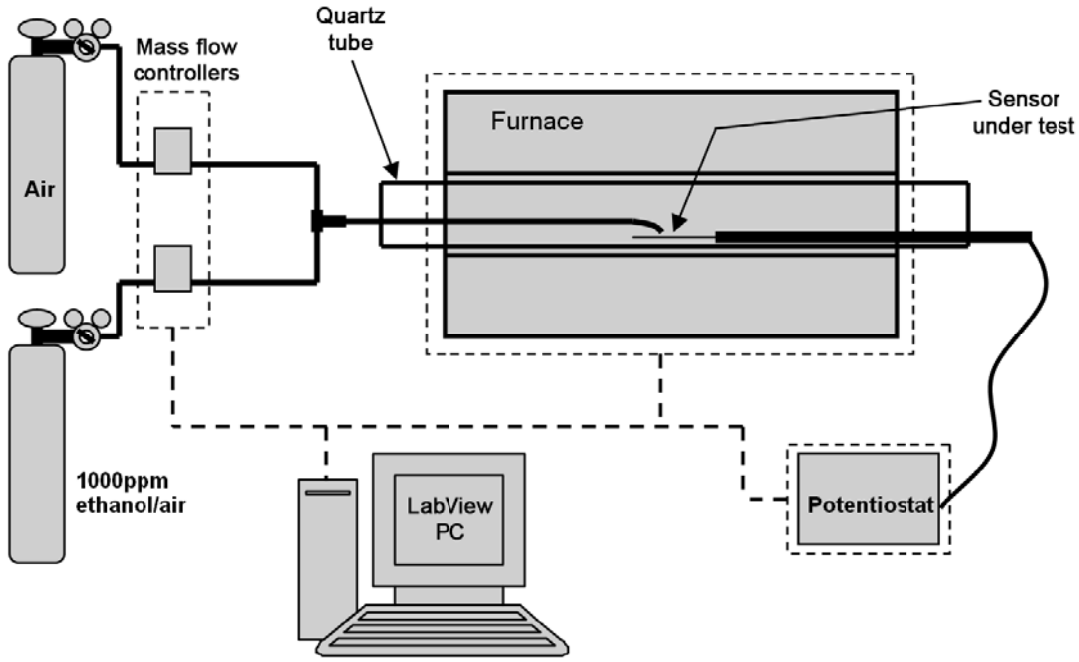

Figure 4.1: Schematic of the gas sensor measurement apparatus. A potentiostat was used to collect the electrical data from the sensor.

4.3 Results and Discussion

A secondary electron image of a starting *Aulacoseira* diatom frustule is shown in Figure 4.2a. The overall *Aulacoseira* frustule is cylindrical with end faces of the frustule possessing a circular hole with a protruding outer rim. The side walls of these cylindrical frustules contained rows of fine pores with diameters of a few hundred nanometers. EDX analyses shown in Figure 4.2c confirmed the silica-based composition of these frustules.

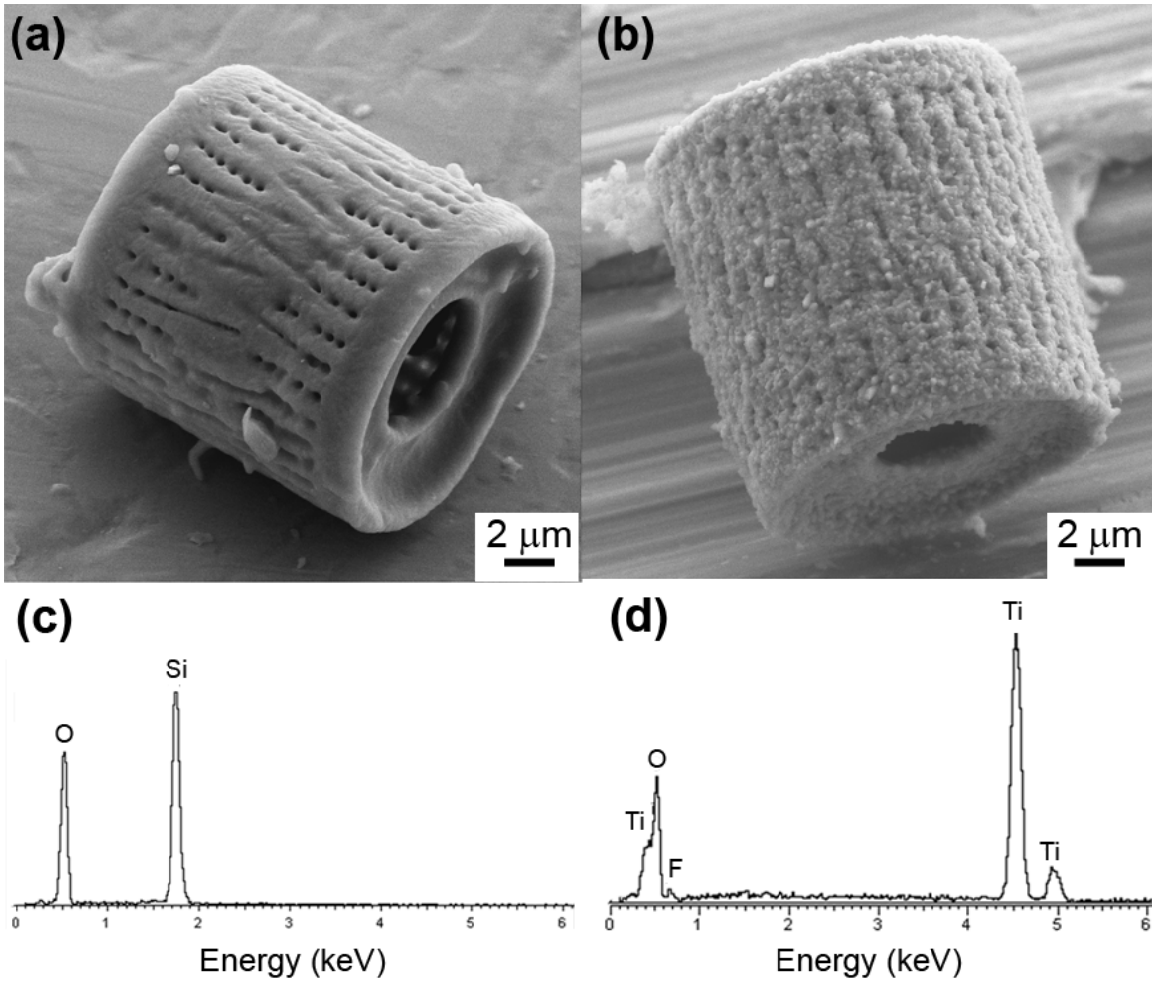

Figure 4.2: Secondary electron image of *Aulacoseira* diatom frustules (a) before treatment; (b) after treatment in a TiF_4–bearing atmosphere at 350°C for 2 h and subsequently oxygenated in a flowing H_2O/O_2 mixture at 400°C for 4 h. (c) and (d) are EDX analyses of the frustules in (a) and (b), respectively.

A two-step reaction process was used to convert *Aulacoseira* frustules into titania. In the first step, the silica-based frustules were exposed to titanium tetrafluoride gas at 350°C for 2 h to allow for conversion into titanium oxyfluoride according to one or more of the following reactions:

$$TiF_4(g) + ½\ SiO_2(s) \Rightarrow TiOF_2(s) + ½\ SiF_4(g) \quad (1)$$

$$TiF_4(g) + ⅔\ SiO_2(s) \Rightarrow TiOF_2(s) + ⅓\ Si_2OF_6(g) \quad (2)$$

$$TiF_4(g) + SiO_2(s) \Rightarrow TiOF_2(s) + SiOF_2(g) \quad (3)$$

In the second step, the titanium oxyfluoride was exposed to flowing, humid air at 400°C for 4 h to enable conversion into anatase, according to one or both of the following reactions:

$$TiOF_2(s) + ½\ O_2(g) \Rightarrow TiO_2(s) + F_2(g) \quad (4)$$

$$TiOF_2(s) + H_2O(g) \Rightarrow TiO_2(s) + 2HF(g) \quad (5)$$

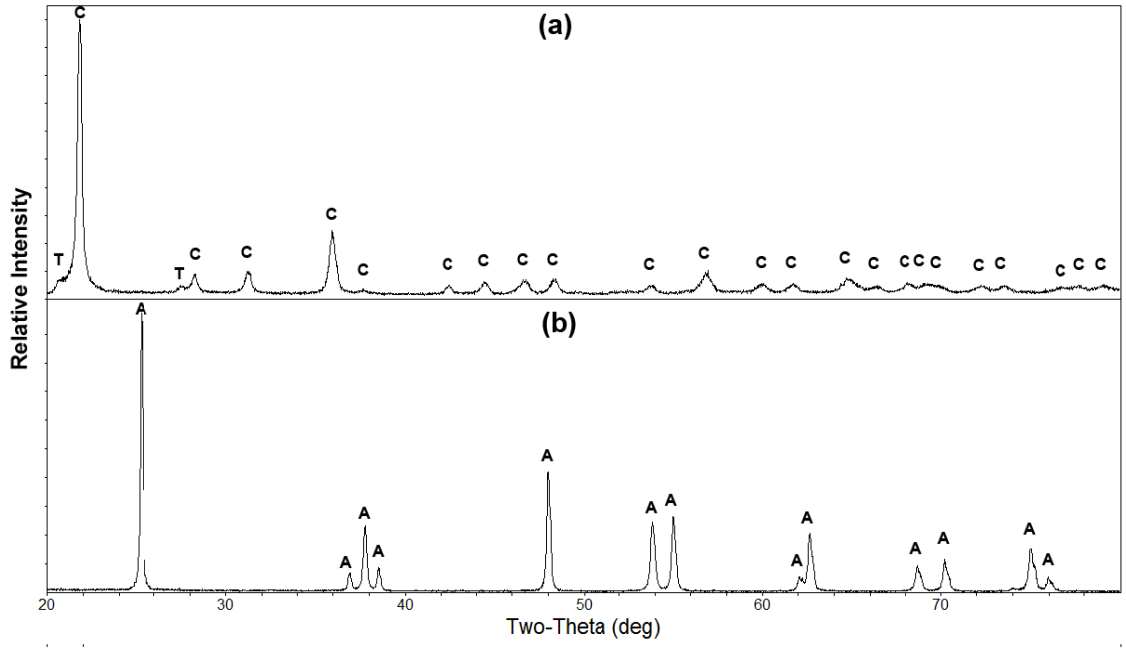

Figure 4.3: X-ray diffraction analyses of (a) the starting silica frustule and (b) after the metathetic conversion reaction into anatase. C = cristobalite (PDF# 00-039-1425), T = tridymite (PDF# 00-042-1401), A = anatase (PDF# 00-021-1272).

EDX analyses in Figure 4.2d revealed that the product was free of silicon (due to the formation of volatile silicon-bearing products in reactions (1), (2)) and enriched in titanium. A secondary electron image of the anatase product is shown in Figures 4.2b. This image reveals that the shape and fine features of the *Aulacoseira* frustules were retained during the silica-to-titania conversion process. X-ray diffraction analyses in Figure 4.3 show the predominantly cristobalite phase of the starting silica frustule was transformed into anatase phase after the conversion process. By applying Williamson-Hall method to the width of the peaks of anatase, the average crystallite size of the anatase frustule was found to be 56±1 nm, which is in good agreement with the 50 nm crystals size from TEM analyses previously reported by Unocic, et al[12]. Nitrogen physisorption analyses indicate an increase in the nitrogen uptake on the anatase frustule compared to the starting silica frustule (Figure 4.4). This increase reflected in the increase

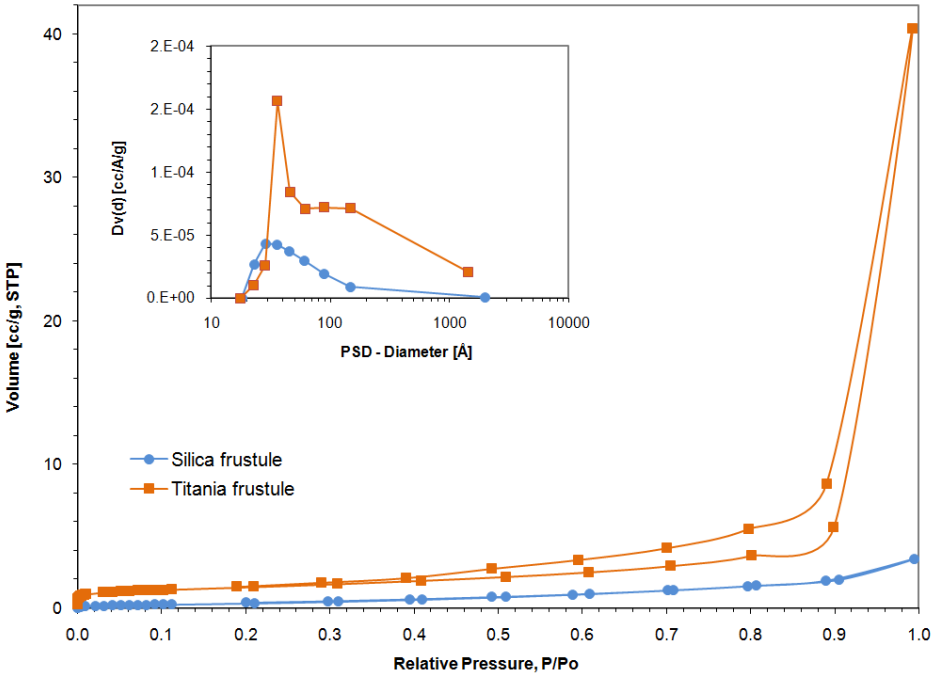

Figure 4.4: Nitrogen physisorption and BJH pore size distribution (inset) of the starting silica frustule and after the metathetic conversion reaction into titania.

of the BET specific surface area from 1.6 m^2/g for the silica frustules to 5.2 m^2/g for the anatase frustules. The BJH pore size distribution (inset in Figure 4.4), however, shows a relatively similar average pore size in the converted anatase frustules compared to the initial silica frustules.

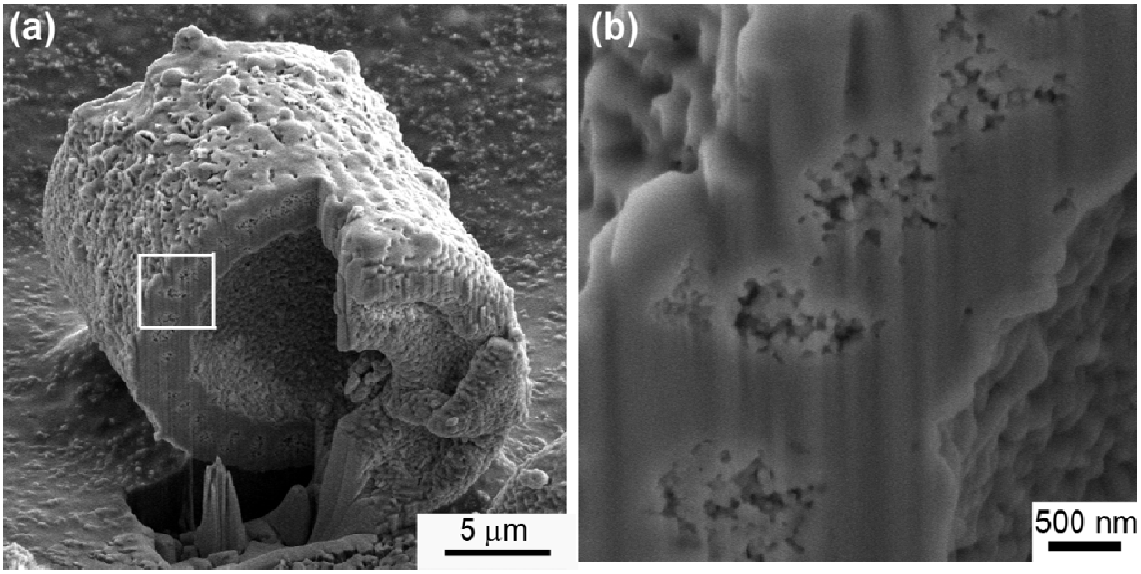

Figure 4.5: Secondary electron image of the anatase frustule that was cross-sectioned using focused ion beam. (a) This image shows the hollow cylindrical shape of the frustule. (b) Higher magnification image shows the porous nature of the frustule wall.

In the field of chemical sensors, the structural stability, porosity and surface to volume ratio are key properties for a sensing material[72,76]. As seen in Figure 4.5, the hollow, cylindrical (aspected) shape of the microscopic *Aulacoseira* frustule, and the porous, nanocrystalline structure after titania conversion are attractive characteristics for the sensing of alcohol (or other gases). Figure 4.6 shows the sensor device that was used to measure the performance of the anatase-converted frustule.

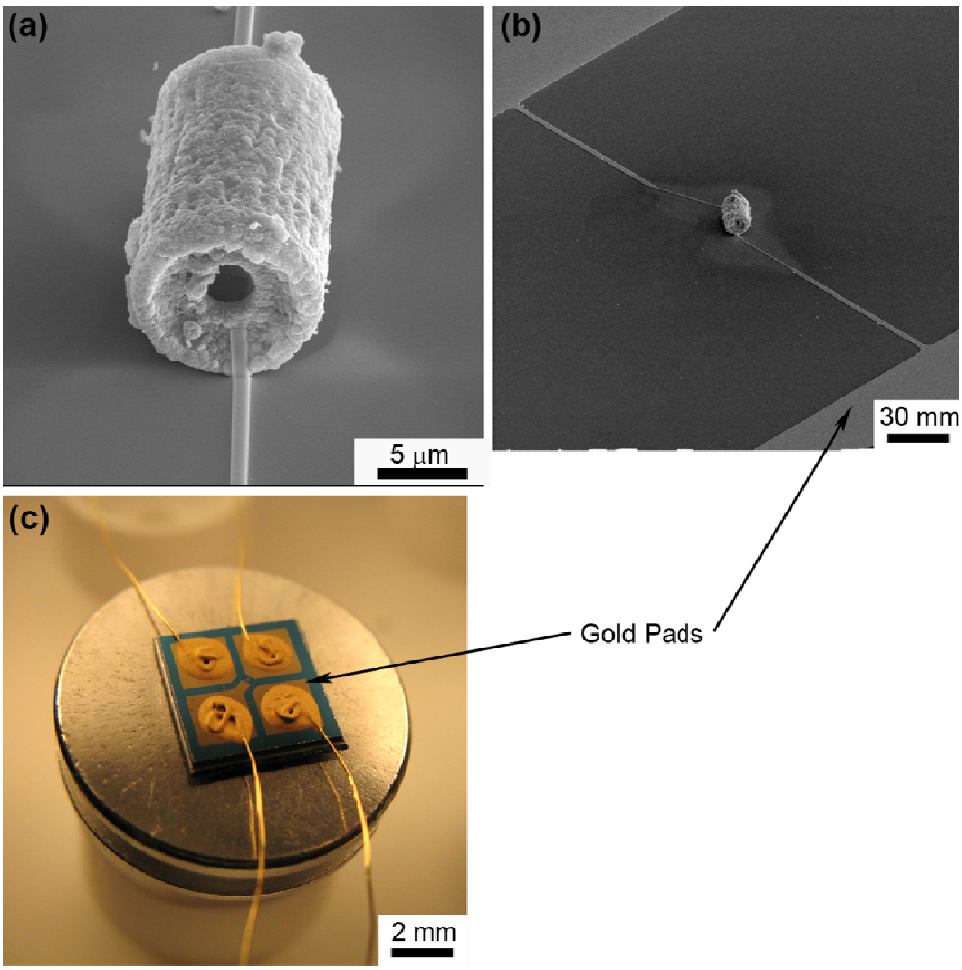

Figure 4.6: Secondary electron images of (a) a titania-converted frustule attached to two platinum electrodes and (b) the electroded diatom frustule between two gold pads on the substrate. (c) Optical image of the sensor substrate connected with gold wires.

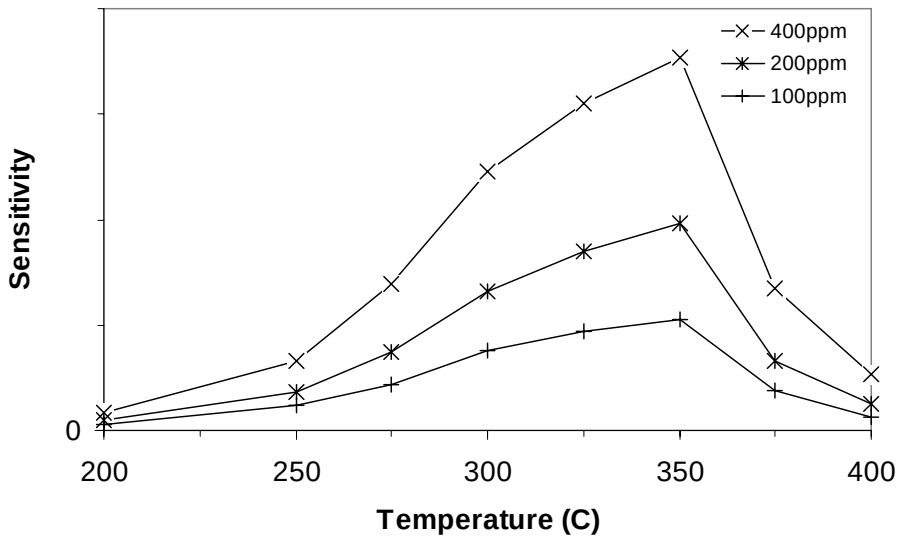

Figure 4.7: Sensitivity of the titania-converted frustule sensor at various temperatures. The sensor was exposed for 5 min at each concentration and temperature before the sensitivity was measured.

The frustule sensor was tested at several operating temperatures to determine the optimum condition for detecting ethanol vapor. The sensitivity is defined as:

$$S = \frac{G_g - G_0}{G_0} \cong \frac{I_g - I_0}{I_0} \tag{6}$$

where G_g and G_0 are sample conductance in the absence and presence of ethanol vapor, respectively, and I_g and I_0 are the amount of current flowing through the sample in the absence and presence of ethanol vapor, respectively[77]. At relatively low operating temperatures (200-300°C), the sensor was able to provide a detectable signal when the ethanol gas concentration was changed from zero to 100, 200, and 400 ppm. However, the response time was relatively slow and the sensitivity, as seen in Figure 4.7, was relatively low. In this temperature range, the sensor sensitivity increased when the

temperature increased, presumably because the rate of adsorption of the gas was enhanced due to an increase on the surface reaction rate between the oxide surface and the gas[78]. The optimum operating temperature was found to be 350°C, at which the sensitivity reached the highest value. At 400°C or higher, the desorption rate presumably exceed the surface reaction rate which, in turn, presumably decreased the sensor sensitivity[73]. It should be noted that the baseline current, I_0, increased as the temperature increased, -as has been reported for semiconducting anatase TiO_2 due to increasing charge carrier (i.e., electron) concentration and mobility with increasing temperature[73].

The dynamic electrical response at 350°C is plotted as a function of time in Figure 4.8. The sensor was exposed to ethanol gas at concentrations from 100 ppm to 1000 ppm at 100 ppm increments. As several authors have observed for conventional anatase sensors, the exposure to ethanol vapor resulted in an increase of current (a decrease in resistance) passing through the anatase frustule sensor[73,76,79].

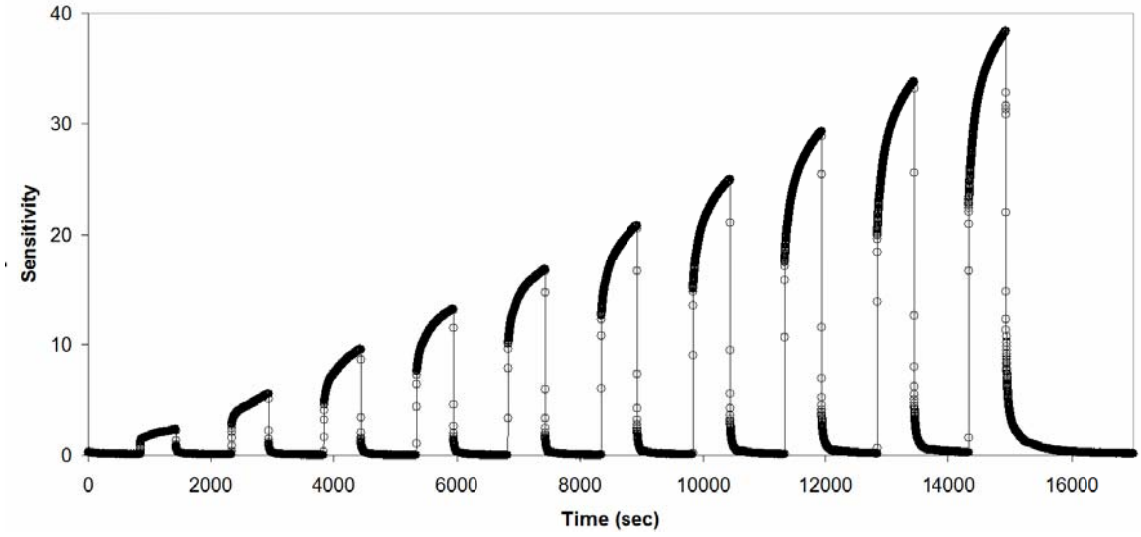

Figure 4.8: Dynamic of titania frustule sensor response toward ethanol pulses at increasing concentration, from 100 ppm to 1000 ppm, at 100 ppm intervals. The operating temperature was 350°C and the electrical data were collected once per second. The pulse width was 10 minutes and the time spacing between two consecutive pulses was 15 minutes.

Owing to the non-steady response of current at a given ethanol concentration (i.e., the sensitivity kept increase at prolonged exposure time), the typical methods of measuring the response time (i.e., 90% of $(S_g - S_0)$[79]) could not be directly applied for this single titania frustule sensor. Instead, the response times were obtained by measuring the widths of the peaks in the plots of the derivative value of sensitivity with time. The recovery times, however, can still be measured by using the 30% of $(S_g - S_0)$[79] method and also by the same derivative method as the response times calculation above. The examples of derivative method measurements are presented in Figure 4.9a and b for response times, and recovery times, respectively. The measured response and recovery times at various ethanol concentrations are tabulated in Table 4.1. The table shows that at ethanol concentrations of 300 ppm or less, the response time were 15 s or less, while at ethanol concentration of 400 ppm or larger, the response times were consistently at or below 6 s. The recovery times were typically 5-6 s by using the derivative method, which are longer than the typical 3 s recovery times calculated by using 30% of $(S_g - S_0)$ method. Typical reported recovery times for titania-based alcohol sensors have been on the order of 1 minute or more[73,79]. For alcohol sensors utilizing different oxides structures, such as vanadium oxide nanobelts or tin oxide nanoporous film, the reported recovery times were in order of 30 seconds or more[80,81]. Thus, the rate of recovery of this single anatase frustule sensor to the change in the ethanol vapor pressure was significantly faster than have been reported by other authors (i.e., faster by one order of magnitude or more by using 30% of $(S_g - S_0)$ method).

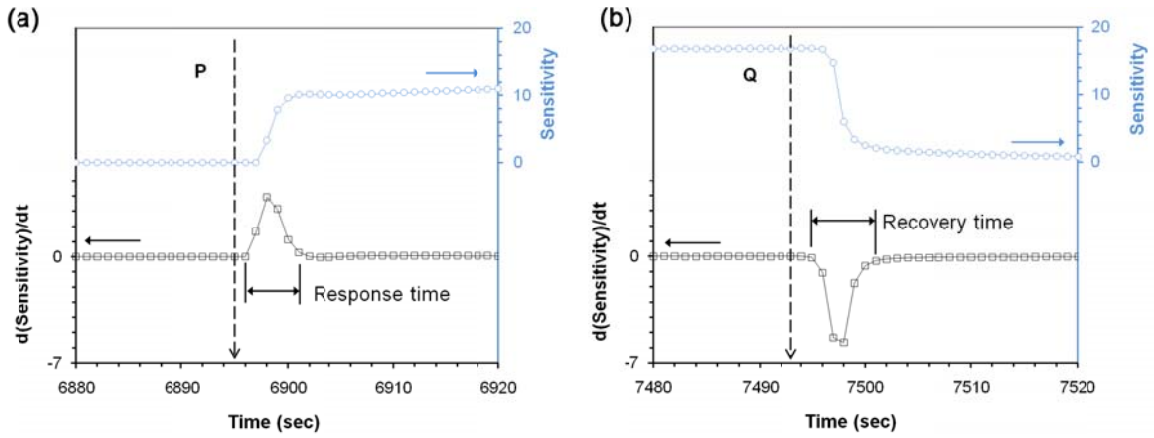

Figure 4.9: The titania-converted frustule sensor response (sensitivity) and the first derivative of sensitivity with respect to time when (a) 500 ppm ethanol vapor flow was started at time indicated by P and (b) when the gas flow was reverted back to 0 ppm ethanol at time indicated by Q. The lag between the time when the gas concentration started to change and the time when the sensor started to respond corresponded to the time required for the gas to flow along the length of the tube that connected the flow controllers to the tube nozzle where the sensor was located.

Table 4.1. Column two and three show the response and recovery times, respectively of the titania frustule sensor obtained from plots of the derivative of sensitivity with time method (Figure 4.9). †The last column shows the recovery times obtained using 30% of $(S_g - S_0)$ method.

Ethanol Concentration (ppm)	Response Time (second)	Recovery Time (second)	Recovery Time† (second)
100	15	7	3
200	9	6	3
300	8	5	3
400	6	5	3
500	5	6	3
600	5	6	3
700	5	6	3
800	5	6	3
900	4	6	3
1000	5	9	8

In a polycrystalline semiconductor, gas detection can result from a change of the depletion layer at titania surfaces and grain boundaries when a certain oxidizing or reducing gas is adsorbed. Since the depletion layer presents a significant barrier to the flow of charge carriers (or to total conductivity), the gas concentration can be directly related to the sample conductivity[72]. A model for a reducing gas such as CO or ethanol vapor involving the principle of a Schottky barrier is illustrated in Figure 4.10[82]. In this model, oxygen (O_2) from the ambient is adsorbed on the surface, extracting an electron from the near-surface-region to allow for O_2 ionization into O^-. This leads to the formation of a free electron-depletion region near surfaces and grain boundaries. At the boundary of two particles, electron depletion creates a back to back Schottky barrier against electron conduction. The conductivity is related to the barrier height (energy required to overcome the barrier), qV_s, by the equation:

$$\sigma_s = \sigma_0 e^{-\frac{qVs}{\kappa T}} \tag{7}$$

where V_s is Schottky barrier potential, and σ_s and σ_0 are the conductivity and the pre-exponential constant, respectively[82]. When the TiO_2 surface is exposed to detecting reducing gas (such as ethanol vapor) electrons are released to the oxide particle. This decrease in electron depletion reduces the Schottky barrier height (qV_s), and increases the conductivity (σ_s) as indicated in the equation above[82]. Since the conductivity change depends on the number electrons provided by the reducing gas, which depends on the concentration of the reducing gas, the concentration of the reducing gas may readily be determined by measuring the TiO_2 frustule conductivity.

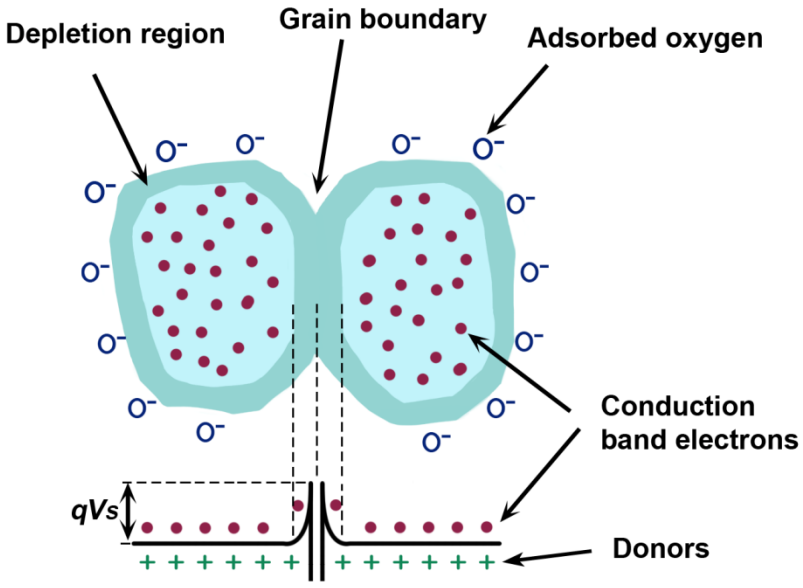

Figure 4.10: The Schottky barrier model which illustrates a sensing mechanism of polycrystalline TiO_2 upon contact with a reducing gas such as CO or ethanol[82].

The relative change in sensitivity with ethanol vapor pressure, $p_{ethanol}$, may be fitted to the following simple power law dependence[79,83]:

$$S = A[p_{ethanol}]^B \quad (8)$$

or

$$\log S = \log A + B \log (p_{ethanol})$$

Least-squares fitting of the log-log plot in Figure 4.11 yielded a slope (B value) of 1.24. (Please note that the sensor sensitivity value for a given ethanol concentration was determined when the derivative value of sensitivity reverted back to near zero as shown in Figure 4.9 and Table 4.1). This exponential B value is not far from values reported by Comini, *et al*. (0.84 to 1.2) and Garzella, *et al*. (0.66 to 1.14) for nanocrystalline anatase thin films exposed to ethanol/air mixtures at 400-500°C [73,79].

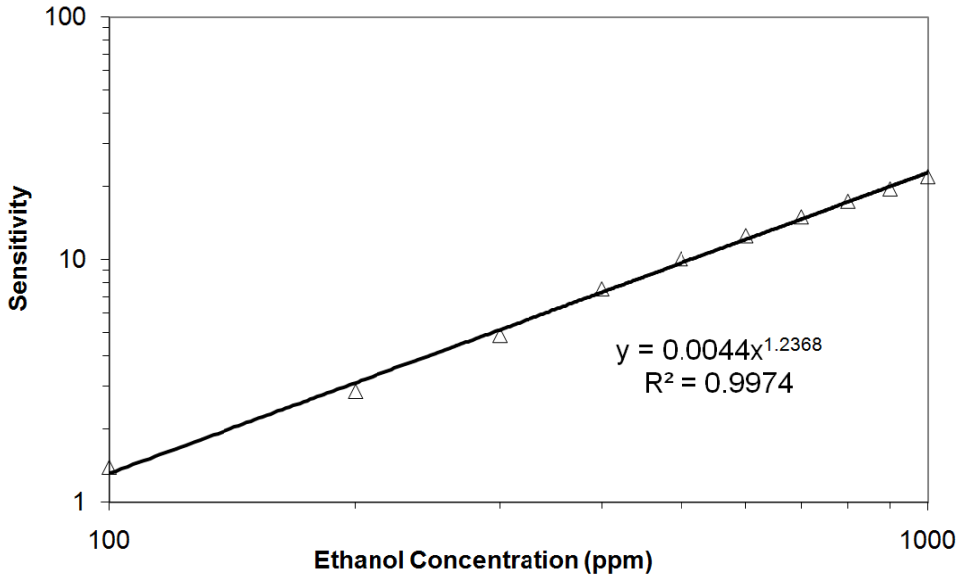

Figure 4.11: Sensitivity of the titania-converted frustule sensor as a function of ethanol vapor pressure. The sensitivity values for this plot were obtained at the seconds indicated in Table 1 after the start of a given ethanol pulse.

One potential application of this sensor is for use as a breadth analyzer. The legal limit of blood alcohol content in many states in USA is typically 0.08 g/dL[84], which is a value corresponding to about 200 ppm alcohol in breath. The TiO_2 frustule sensor was able to detect well below this limit. Some possible improvements to anatase-based alcohol gas sensors have been reported in the literature. Doping of the titania, such as with platinum or tungsten, has have been reported to increase both sensitivity and selectivity toward different gases[73,79,85]. Such doping may also be used to enhance the sensitivity and selectivity of the titania frustule sensors of the present work. Moreover, the use multi-frustule in a sensor device may exhibit enhanced sensitivity to alcohol vapor, given the increase in available surface area.

4.4 Conclusions

Novel, sensitive, and fast response ethanol sensors based on single TiO_2-converted diatom frustules has been successfully fabricated. The TiO_2 frustules were synthesized using a relatively simple process, based on a low-temperature gas-solid displacement reaction, which may be adapted for large-scale production. The sensing results indicate that the frustule sensor may potentially be used for fast and accurate breath alcohol analyses.

CHAPTER 5: Accelerated Hydrolysis of Organophosphorous Esters Induced by Titania-Based Replicas of Diatom Frustules

The research presented in this chapter has been reported in the following publication:

Lee, S.-J.; Huang, C.-H.; Shian, S.; Sandhage, K. H; *J. Am. Cer. Soc.* 2007, 90, 1632

5.1 Introduction

Owing to exceptionally high surface areas, modified surface structures, and other nanoscale phenomena, nanostructured metal oxides, such as titanium dioxide (TiO_2) nanoparticles, have been shown previously to have excellent catalytic properties for the degradation of environmental pollutants[86-95]. Unocic et al., reported a successful conversion of silica diatom frustule into titania replicas, which comprised of a nanoporous network of anatase crystals with sizes on the order of 50 nm[12]. The cylindrical shape of the converted *Aulacoseira* frustules possessed the fine features (nanoscale pores, channels) of the starting silica diatom frustules. The open, nanocrystalline nature of such 3-D anatase frustule replicas is attractive for the use in catalytic-like applications. In this chapter, the anatase frustules derived from silica-based diatom frustules were used to enhance the rate of hydrolysis of the organophosphorous esters, methyl paraoxon (MOX) and methyl parathion (MTH). Such rate enhancement was achieved in the absence of light and at near neutral pH conditions. MOX and MTH are widely used insecticides in crop and fruit production and home gardening, and are structural mimics of nerve agents[96].

5.2 Experimental Procedures

5.2.1 Materials

Titania-based replicas were prepared by converting the silica-based diatom assemblies through the use of the two steps gas/solid reactions. In the first step, a nickel boat (20 × 15 × 4 mm) containing 100 mg of *Aulacoseira* diatom frustules (obtained as diatomaceous earth) and 500 mg of TiF_4 (99% purity, Advanced Research Chemicals, Inc., Catoosa, OK), for a molar TiF_4:SiO_2 reactant ratio of 2.4:1, were placed within a titanium tube (2.3 cm inner diameter × 20 cm long). Both ends of the tube were crimped and welded shut inside a controlled atmosphere glove box filled with argon maintained at an oxygen partial pressure below 0.1 ppm. The sealed tube was heated to 350˚C at a ramp rate of 5˚C/min and held at this temperature for 2 hours inside a horizontal tube furnace. After cooling to room temperature, the tube was cut open, and the nickel boat containing the reacted frustules was removed. In the second step, the reacted frustules were then heated in a flowing, humid air at temperature between 400 to 600°C at a ramp rate of 5˚C/min for 2 or 5 hours. Before entering the furnace, the air was passed through a heated water bath (45°C) at a rate of 1 slpm. The measured humidity (using Model HMP234, Vaisala, Woburn, MA) at the gas outflow of the furnace was found to be at least 94% relative humidity. Three types of frustule replicas (I-III) were prepared by varying the second processing step above. FI replicas were not processed in the second step. FII through FIII replicas were exposed to the second processing step by varying the heat treatment temperature. Heat treatment temperatures of 400°C for 2 h and 450°C for 5 h were applied to FII and FIII, respectively.

Two commercially available TiO_2 nanoparticles were also examined for comparison: 20 nm anatase/rutile particles (~75% anatase, 25% rutile[97], P25, Degussa, USA) and 10 nm anatase particles (99% anatase, Nanostructured and Amorphous

Materials, Houston, USA) that are referred to herein as P25 and NAM nanoparticles, respectively.

Stock solutions of MOX and MTH (98% purity, Chem Service, West Chester, PA, USA) were prepared by dissolving them in a HPLC grade methanol and then stored in a freezer maintained at -10°C. Other chemicals employed in this study including 4-nitrophenol (4-NP), salicylic acid (SA), benzoic acid (BA), methyl salicylate (MS), methyl benzoate (MB), methyl 4-(aminomethyl)benzoate (MAMB) hydrochloride, phosphoric acid, acetic acid, 2-(N-morpholino)ethanesulfonic acid (MES), 4-morpholinepropanesulfonic acid (MOPS), sodium borate, and sodium fluoride, were obtained from Aldrich (St. Louis, MO, USA) or Fisher Scientific (Fairlawn, NJ, USA) at a greater than 97% or of HPLC grade, and were used without further purification. All stock solutions (e.g., buffers, stock solutions) of these compounds were prepared using Milli-Q purified water (Millipore, MA, USA).

5.2.2 Characterization

The BET surface area, BJH pore volume, and average pore volume of the oxides were determined using the Autosorb-1 (Quantachrome Instrument, FL, USA), with nitrogen as an adsorbate at 77 K. A scanning electron microscope (SEM) (LEO 1530, Germany) with energy dispersive X-ray spectroscopy (EDX) capability was used for imaging, sizing and localized elemental analysis. Zeta potentials of various titania suspensions were measured by Seung-Jin Lee using a zeta potentiometer (ZetaPlus, Brookhaven Instrument, NY, USA). The concentration of titania in the aqueous suspension was 0.1 g/L and the pH of the solution was varied by adding small amount of strong acid or base. The pH of isoelectric point (i.e., the point of zero zeta potential; pH_{IEP}) of titania was obtained from the zeta potential versus pH plots.

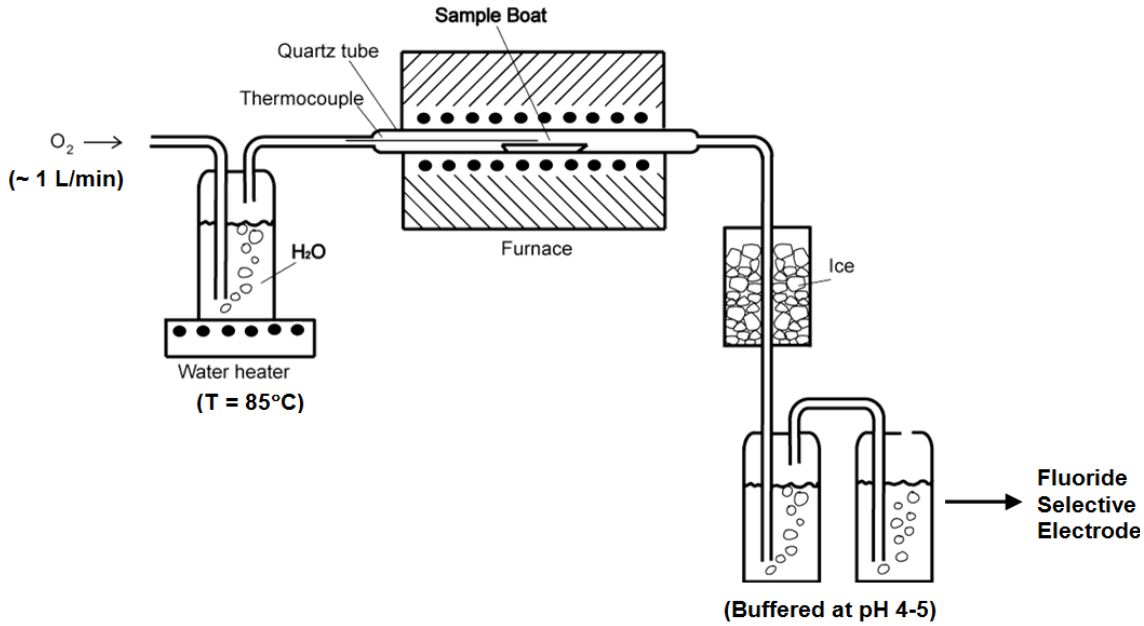

Figure 5.1. Schematic of the pyrohydrolysis setup to measure the fluorine content in the titania-based frustule replicas.

The amount of residual fluorine in the titania frustules was determined by using a pyrohydrolysis setup[98] as shown in Figure 5.1. An alumina crucible with about 100 mg of the powder sample was placed inside a furnace. The furnace was heated to 950°C at a 10°C/min heating rate and held for one hour while a stream of moist oxygen gas (1 liter per minute, water heater temperature: 85°C) was passed through the sample tube. During this treatment, fluorine reacted with water and formed hydrofluoric acid gas. Water premixed with buffer solution (a mix of 10 g potassium acetate and 5 mL acetic acid and diluted with water to 1 L) was utilized at the end of vapor stream to trap the acid gas. A fluoride ion-selective electrode (Denver Instrument, USA) was used to determine the fluoride potential in the trap solution and the overall fluorine content in the frustule sample was calculated by comparing the potential to a prepared standard curve.

5.2.3 Hydrolysis Experiments

The MOX and MTH hydrolysis experiments were conducted by Seung-Jin Lee at the laboratory of Prof. Ching-Hua Huang (School of Civil and Environmental Engineering, Gatech). The procedures are as follows. Batch kinetic experiments were conducted in 25-60 mL amber borosilicate bottles that were protected from light. Dry TiO_2 particles, buffered reagent water (10 mM acetic acid, 2-(N-morpholino)ethanesulfonic acid [MES], 4-morpholinepropanesulfonic acid [MOPS], and their corresponding sodium salt for pH ranges of 4-5, 5.5-7, and 7-8, respectively), 10 mM NaCl, and a stir bar were added to each bottle. The reactors were maintained at 22°C with constant stirring. After 1-2 h, an appropriate amount of pesticide stock solution (MOX or MTH in a methanol/water mixture) was added to initiate reaction. The starting pesticide concentration was 100 μM and the initial titania loading was 1.0 g/L. The initial reaction solution contained 2.5 vol% methanol. Sample aliquots were periodically collected and centrifuged prior to analysis. The MOX, MTH, and their hydrolysis product, 4-nitrophenol (4-NP), were analyzed by a high performance liquid chromatography (HPLC) system (Model 1100MSD, Agilent, Santa Clara, CA) with a Zorbax RX-C18 column (4.6 × 250 mm, 5μm) and a diode-array UV/Vis detector operating at 275 nm. The mobile phase consisted of solution of 1 mM phosphoric acid or trifluoroacetic acid and pure acetonitrile at 65:35 and 40:60 (v/v) ratios for methyl paraoxon and methyl parathion, respectively. A 5 min isocratic elution of 95:5 (v/v) acid solution:acetonitrile was applied prior to the above conditions.

5.3 Result and Discussion

5.3.1 Properties of frustule replicas

In the first conversion step, the silica-based diatom frustules were reacted with gaseous TiF_4 according to one or more of the following reactions:

$$2TiF_4(g) + SiO_2(s) \Rightarrow 2TiOF_2(s) + SiF_4(g) \quad (1)$$

$$3TiF_4(g) + 2SiO_2(s) \Rightarrow 3TiOF_2(s) + Si_2OF_6(g) \quad (2)$$

$$TiF_4(g) + SiO_2(s) \Rightarrow TiOF_2(s) + SiOF_2(g) \quad (3)$$

Energy dispersive x-ray (EDX) and X-ray diffraction (XRD) analyses[12] indicated that this reaction resulted in complete conversion of the SiO2 frustules into TiOF2 replicas (FI). In the second step, the titanium oxyfluoride frustules was exposed to flowing, humid air at 400^{o}C for 4 h to enable conversion into anatase, according to the following reactions:

$$TiOF_2(s) + (1\text{-}a)O_2(g) \Rightarrow TiO_{2\text{-}a}F_b(s) + (2\text{-}b)F_2(g) \quad (4)$$

where $TiO_{2\text{-}a}F_b(s)$ refers to F-doped titania. As seen in Figure 5.2, the resulting anatase products retained the starting frustule shape and fine features (nanoscale pores, channels). There were no appreciable differences in the morphologies among the different titania frustule specimens that were prepared at different temperature for the reaction (4).

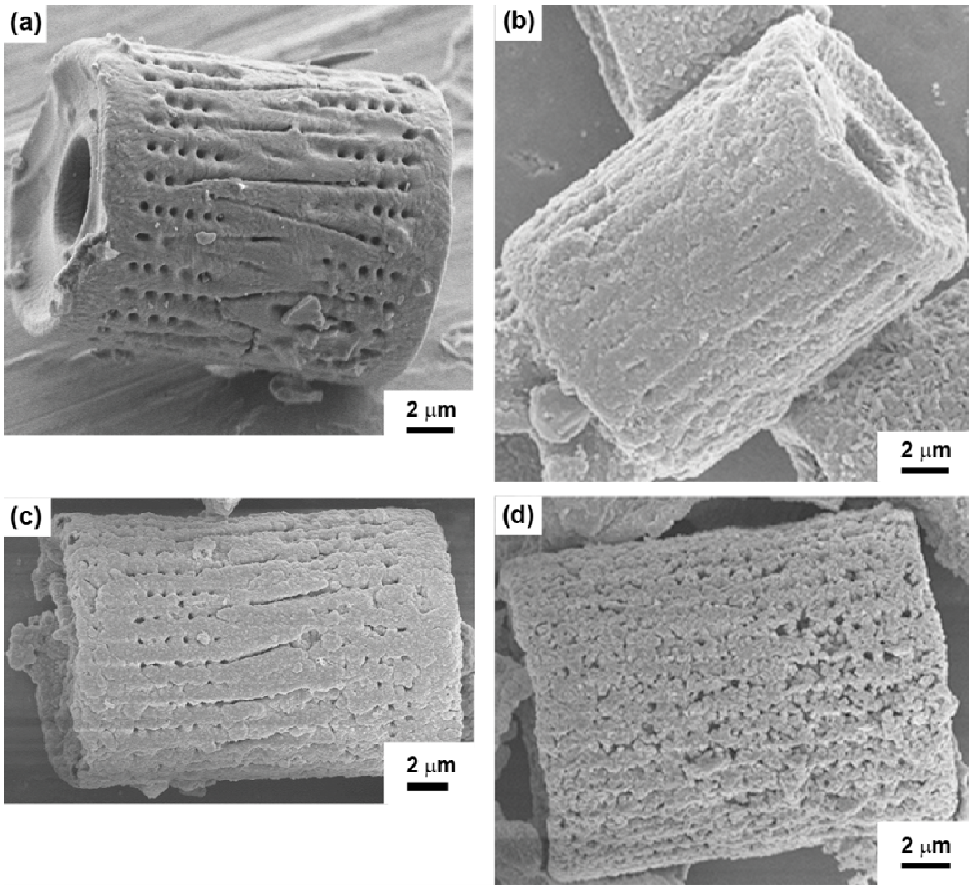

Figure 5.2. Scanning electron images of (a) the starting silica frustules and the frustule replicas: (b) FI ($TiOF_2$-based), (c) FII (TiO_2-based, with 5.5 wt% F) and (d) FIII (TiO_2-based, with 1.4 wt% F).

Table 5.1 summarizes a range of properties of the TiO_2 frustule replicas and commercially obtained TiO_2 particles that were used in this study. According to the manufacturer, the commercial titania particles P25 consist of approximately 75% of anatase and 25% of rutile[97] and the NAM particles consist of nearly 99% of anatase phase. TiO_2 frustules have a diameter of approximately 12 μm and a height of about 16 μm based on SEM images (Figure 5.2). In contrast, P25 and NAM have much smaller reported particle diameters (30 nm and 10 nm, respectively) by the manufacturers' data. The BET analysis indicates that the TiO_2 frustules have much lower specific surface areas (2.1 - 4.2 m^2/g) than P25 and NAM titania particles (i.e., 54.4 m^2/g and 312 m^2/g,

Table 5.1. Characteristics of frustule replicas (FI-FIII) and commercial titania nanoparticles (P25, NAM).

Particles	Oxygenation Temp. (°C)	Crystalline Structure[a]	Particle Size	BET Surface Area (A_s, m^2/g)	BJH Pore Vol. (cm^3/g)	pH of Isoelectric Point	wt% of Fluorine
P25	-	75%A+25%R[b]	30 nm[b]	54.4 ± 2.7	0.132	5.2	-
NAM	-	A[b]	10 nm[b]	312 ± 15	0.324	6.0	-
FI	-	$TiOF_2$	12 μm	2.1 ± 0.1	0.076	2.5	27.3 ± 4.5
FII	400	A	(dia.) ×	4.2 ± 0.1	0.011	3.3	5.5 ± 0.2
FIII	450	A	16 μm	3.5 ± 0.1	0.010	4.0	4.9 ± 0.6
FIII	600	A	(length)[c]	2.6 ± 0.2	0.009	4.3	1.4 ± 0.2

[a]As determined from XRD, A = anatase, R = rutile; [b]from manufacturer; [c]from SEM images;

respectively). The TiO_2 frustules also appeared to have smaller pore volumes than the commercial titania particles (Table 5.1).

According to the zeta potential measurement (Figure 5.3), titania frustules exhibited considerably lower isoelectric points (pH_{IEP} = 2.5 - 4.3) than are typically observed for anatase[99,100] (i.e., pH_{IEP} values of 5.2 - 6.0 were obtained for P25 and NAM, respectively), The low pH_{IEP} values indicate that the titania frustules possessed a stronger surface acidity than the commercial particles. The titania frustules also possessed significantly higher fluorine contents, i.e., up to 5.5% for the frustule heat treated at 400°C. This fluorine content decreased as the second heat treatment temperature increased. Notably, the decline in residual F-content coincided with the increase in pH_{IEP} (i.e., decreasing surface acidity) of the frustule replicas (Table 5.1).

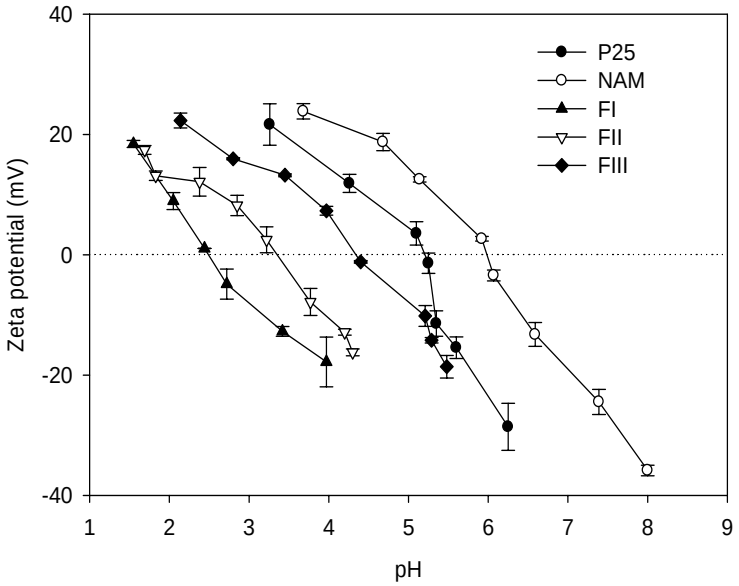

Figure 5.3: Zeta potentials of titania nanoparticles and titania-based frustule replicas in aqueous suspensions ([TiO_2] = 0.1 g/L) as a function of pH.

5.3.2 Hydrolysis of Organophosphorous Esters in the Presence of TiO_2

The rates of hydrolysis of MOX and MTH in the presence or absence of titania were found to follow pseudo-first-order kinetics. Least-square linear regression analyses of plots of the log parent compound concentration versus time yielded lines with R^2 values greater than 0.96. The pseudo-first-order rate constants (obtained from the slopes of these lines) are shown in Figure 5.5. In all of the experiments, the loss of MOX and MTH coincided with the generation of 4-NP, reaching >95% of overall mass balance throughout the reaction (an example is shown in Figure 5.4).

As shown in Figure 5.6, the hydrolysis rates of MOX and MTH were enhanced in the presence of all types of particles examined. However, the frustule replicas (particularly the FII specimens) were substantially more effective at increasing the hydrolysis rates than were the P25 and NAM nanoparticles. The relative rates of

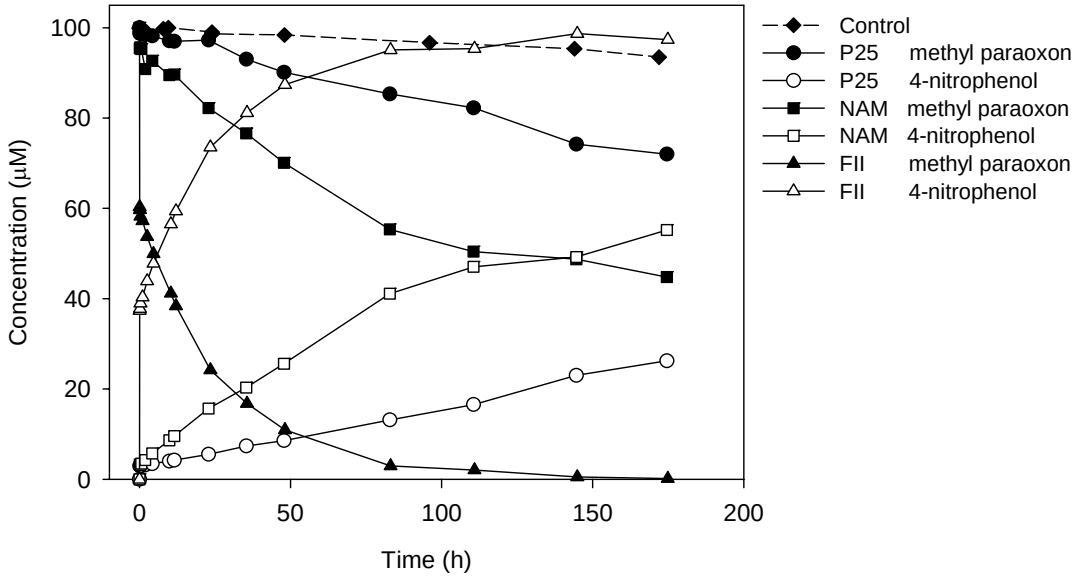

Figure 5.4. Reaction time course of methyl paraoxon (MOX) hydrolysis and 4-nitrophenol product generation in the presence and absence (control) of titania nanoparticles and titania-based frustule replicas.

hydrolysis (k/k_0 values) of MOX over the pH range of 4.5-7.9 increased by factors of 102-129 in the presence of the FII replicas, whereas the P25 and NAM nanoparticles enhanced the rates by factors of 3.8-5.8 and 10.7-15.2, respectively. A similar, although less pronounced, trend was observed for the hydrolysis of MTH. The enhancements in the hydrolysis rates resulting from the titania frustule replicas decreased as the temperature used for conversion into anatase increased from 400^{o}C to 600^{o}C.

Although more effective at enhancing the hydrolysis rates of MOX and MTH, the titania frustule replicas possessed substantially lower specific surfaces areas (2.6-4.2 m^2/g) than the P25 (54.4 m^2/g) and NAM (311.6 m^2/g) nanoparticles. In other words, the influence of the anatase frustule replicas on hydrolysis became even more pronounced when the particle surface areas were taken into account. For example, the values of the specific relative rate constants ($k/[k_0A_s]$) for MOX hydrolysis in the presence of the FII particles were 290-400 and 590-820 times higher than in the presence of the P25 and NAM nanoparticles, respectively!

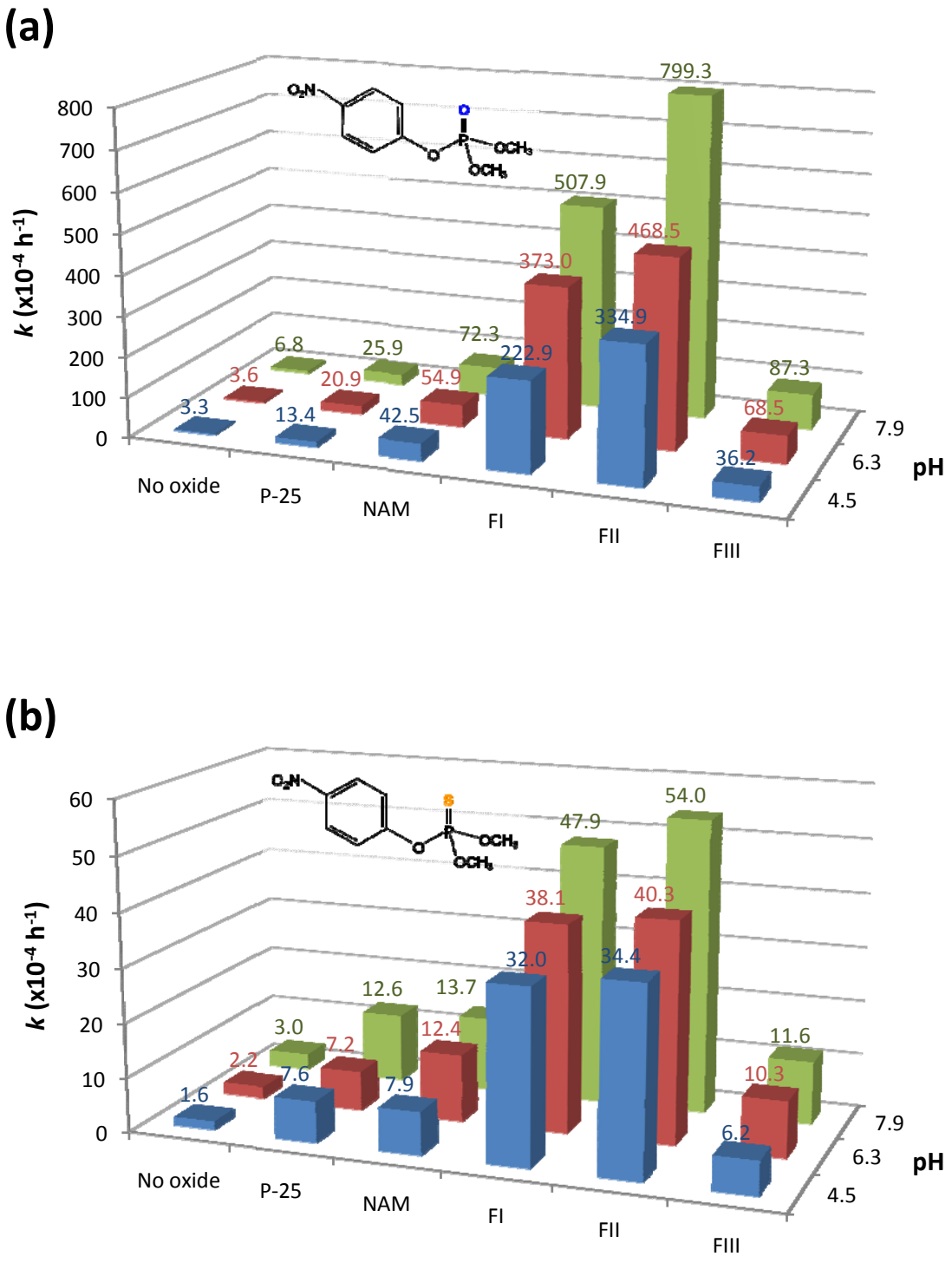

Figure 5.5. Pseudo-first-order rate constants (*k*) for the hydrolysis of (a) methyl paraoxon (MOX) and (b) methyl parathion (MTH) in the presence and absence of commercial titania particles or frustule replicas.

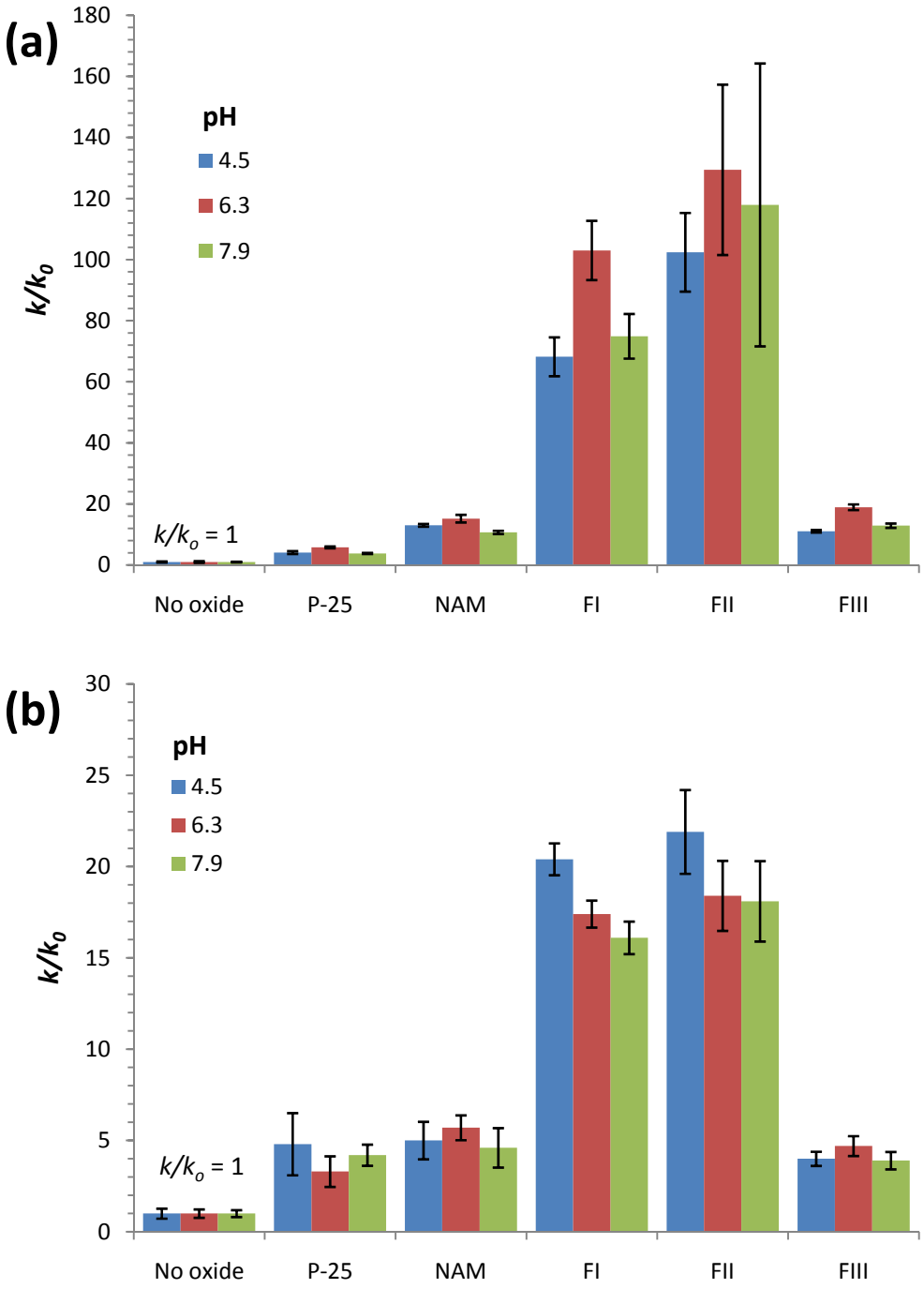

k_o : was the rate constant in the absence of titania particles for a given pH condition.

Figure 5.6. The comparison (k/k_0) of pseudo-first-order rate constants (k) for the hydrolysis of (a) methyl paraoxon (MOX) and (b) methyl parathion (MTH) in the presence of commercial titania particles or frustule replicas relative to the condition in the absence of oxide (k_0). The error bars indicate the standard deviation of the measurement.

It is well known that metal ions can catalyze the hydrolysis of carboxylic esters, amides, and phosphorous esters by (i) coordinating such compounds in a manner that raises their susceptibility towards nucleophilic attack, (ii) coordinating the nucleophile in a manner that raises its reactivity toward electrophilic sites, or (iii) a combination of these mechanisms[101,102]. Mechanism (i) is strongly related to the ability of metal ions to coordinate the compound (e.g., the O atom of the P=O bond) and polarize electrons away from the nucleophilic site (e.g., the P center of the P=O bond). Mechanism (ii) is strongly tied to the ability of metal ions to induce the deprotonation of coordinated water through reactions such as: $Me^{2+} + H_2O = MeOH^+ + H^+$, $*K_1 = [MeOH^+][H^+]/[Me^{2+}]$. Thus, metal ions of stronger Lewis acidity and greater affinity to the compound ligand donor atoms would be stronger catalysts. The catalysis of metal oxide surfaces on hydrolysis reactions is essentially similar to that of dissolved metal ions[100,103-106]. In addition, other factors such as surface area, charge, morphology and active site density may also play a role.

Based on the above discussion, the stronger surface acidity of the titania frustule replicas due to F-doping likely led to the enhanced hydrolysis of MOX and MTH relative to the P25 and NAM titania particles. Earlier studies have documented that fluorine incorporation in alumina and silica-alumina catalysts (with F replacing surface or lattice O and OH groups) increased the acidity of both protonic (Bronsted) and nonprotonic (Lewis) sites on the surfaces, owing to the stronger electronegativity and polarizing effect of fluorine[107,108]. F-modified alumina has exhibited enhanced catalytic activity for reactions such as cracking, isomerization, alkylation, disproportionation, and polymerization[107,108]. By analogy, the presence of fluorine in the anatase titania of this study likely resulted in increased Lewis acidity and excess positive charge on the surface-bound Ti(+IV), as indicated by the lower pH_{IEP} values of the titania frustule replicas. The enhanced susceptibility of MOX to hydrolysis, relative to MTH, in the presence of the

titania frustule replicas can also be explained. MOX possesses a “hard” O donor that is likely to coordinate more strongly to the “hard” Ti(+IV) metal center than MTH’s “soft” S donor[109], thus rendering a greater susceptibility for hydrolysis via the mechanism (i) discussed above. Sulfur is also less electro-negative than oxygen, resulting in a less electrophilic (and thus less reactive) phosphorous center in the thionates than in the oxonates.

5.4 Conclusion

Significant enhancement of hydrolysis of pesticide-like compounds were observed in the presence of porous 3-D assemblies of nanocrystalline F-doped anatase TiO_2 under near neutral conditions and in the absence of light (non-photocatalytic conditions). The enhanced activity of such nanostructured titania assemblies without the need for a strong UV light source is quite attractive for the hydrolytic destruction of environmental pollutants in remote locations. Furthermore, SiO_2-based diatomaceous earth, which has long been used in water purification applications[110], is readily available in large quantities at low cost, and the chemical conversion technique employed in this study is a scalable means of converting diatomaceous earth into fluorine-doped titania nanoparticle structures.

CHAPTER 6: Crystal Structure and Phase Transformation of $TiOF_2$

6.1 Introduction

A recently developed process referred to as BaSIC (Bioclastic and Shape-preserving Inorganic Conversion), enables the microfabrication of three dimensional structures of various chemistries through a the chemical conversion of biomineralized templates, such as the silica-based microshells (frustules) of diatom (single-celled algae)[10]. One of the conversion methods in the BaSIC process is the metathetic reaction of bio-silica template with gaseous titanium tetrafluoride. This method has been successfully used to convert the relatively complex 3-D structure of a silica diatom frustule into a titania replica that retained the overall frustule shape and nano scale features[12]. In another subsequent report, a three dimensionally ordered macroporous titania structure (inverse opal) was produced from silica preforms using this reaction process[111]. The process involves one or both of the following metathetic reactions of SiO_2 with $TiF_4(g)$ to yield the oxyfluoride, $TiOF_2$:

$$2TiF_4(g) + SiO_2(s) \Rightarrow 2TiOF_2(s) + SiF_4(g) \quad (1)$$

$$3TiF_4(g) + 2SiO_2(s) \Rightarrow 3TiOF_2(s) + Si_2OF_6(g) \quad (2)$$

$$TiF_4(g) + SiO_2(s) \Rightarrow TiOF_2(s) + SiOF_2(g) \quad (3)$$

Vorres and Donohue reported the syntheses of $TiOF_2$ with cubic crystal structure by stoichiometric reaction of TiO_2 with HF[112]. The reported diffraction peaks of $TiOF_2$ (Powder Diffraction File, Card No. 04-007-8589, International Center on Diffraction Data, Newtown Square, PA), however, do not match with those of $TiOF_2$ synthesized from reaction (1) or (2) above. The purpose of this paper is two-fold; i) to report the crystal structure of $TiOF_2$ that was prepared by using SiO_2(s) and TiF_4(g) reactants, and ii) to present the temperature-induced reversible transformation of the crystalline $TiOF_2$ from hexagonal to cubic at around 61°C.

The cubic ReO_3-type structure consists of a three dimensional network of corner-sharing MO_6 octahedra[113]. During the cubic to hexagonal phase transformation of ReO_3-type structures, the metal octahedra rotate around one of the triad axes of the cubic phase. According to Glazer[114], this tilt process is classified as $a^-a^-a^-$. Besides rotation, these octahedra also become distorted (becoming elongated or squashed) along the rotation axis when breaking the cubic symmetry. Such transformation is usually accompanied by changes in physical properties such as dielectric relaxation, specific heat, and birefringence[113].

6.2 Experimental Procedures

The conversion of silica to $TiOF_2$ was conducted in a sealed chamber. The as-received silica was processed with no pre-heat treatment. A nickel boat containing 100 mg of 1 μm diameter Stöber silica spheres (Angstrom Spheres, New Bedford, MA) was placed within a 2.3 cm inner diameter and 20 cm long titanium tube, along with solid TiF_4 powder (99% purity, Advanced Research Chemicals, Inc., Catoosa, OK), for a molar TiF_4:SiO_2 reactant ratio of 2.4:1. Both ends of the tube were crimped and welded shut. Because of the tendency of TiF_4 to react with oxygen and water vapor, the above procedures were carried out in an argon atmosphere glove box (Model Omni-Lab,

Vacuum Atmosphere, Hawthorne, CA), maintained at an oxygen partial pressure below 0.1 ppm. The sealed tube was heated to 350°C at a 5°C/min heating rate, held for 2 hours, and then allowed to cool along with the furnace to room temperature (approximately 15°C/min). The specimens were extracted after the tubes were cut open. The morphologies of the specimens were evaluated with a field emission scanning electron microscope (LEO-1530, Zeiss Germany) equipped with energy-dispersive X-ray analysis capability (Oxford Instrument, Bucks, UK). Differential scanning calorimetry (DSC) was performed on the sample (crimped in an aluminum pan) by using a Shimadzu DSC-60 (Japan). Thermogravimetric analyses (TGA) was performed on the sample using a Netzsch STA Jupiter 449c (Germany).

For high resolution room temperature measurement, the X-ray diffraction pattern was obtained in ambient atmosphere using an Alpha-1 Panalytical Diffractometer (Almelo, The Netherlands) configured for Bragg-Brentano geometry. A symmetrical incident beam Johansson monochromator ensured that only the $K\alpha 1$ component of Cu radiation (1.5405980 Å) was used. The peak profile data acquisition was conducted using a solid-state position sensitive ultrafast detector (X'Celerator, Panalytical, Almelo, The Netherlands). A divergence slit of 1/4° and Soller slits of 0.02 rad. were used in the incident beam path. On the diffracted beam path, a 0.02 rad. Soller slit and a 5.0 mm antiscattering slit were used. A mask of 10 mm was inserted in the incident beam path to adjust the size of the probing X-ray spot.

For the phase transformation investigation, the X-ray diffraction patterns were collected inside an Anton-Paar HTK 1200 (Graz, Austria) high-temperature furnace. The converted $TiOF_2$ powder was spread on an alumina pedestal and was heated to the desired temperatures (25-250°C) at rate of 60°C/min in air atmosphere. After 15 min of holding time, the diffraction pattern was collected and then the temperature was increased

to the next value. As shown by the reversibility of the transformation (Figure 6.4), the 15 min of waiting time was sufficient to ensure equilibrium temperature inside the furnace.

Diffraction patterns were measured using an MPD Panalytical Diffractometer (Almelo, The Netherlands), configured for Bragg-Brentano geometry. Cu Kα radiation (1.5405980 Å, 40 keV) was used as the x-ray source. A Cu W/Si multilayered focusing mirror (Goebel mirror) was attached to the incident beam path to create a high intensity parallel beam and to minimize the effect of sample displacement to the diffracted peak locations. A divergence slit of 1/2° was used in the incident beam path. The peak profile data acquisition was conducted using a solid-state position-sensitive ultrafast detector (X'Celerator, Panalytical, Almelo, The Netherlands). A 5 mm antiscattering slit and 0.02 rad Soller slit were used on the diffracted beam path.

Rietveld refinements of the XRD data were performed using X'Pert Highscore Plus software (Version 2.2b, Amelo, The Netherlands). The x-ray data were fit using the pseudo-Voigt profile function. The specimen displacement, polynomial coefficients for the background function, lattice parameters, profile parameters, Gaussian and Lorentzian profile coefficients were refined. The atomic coordinate of titanium was fixed (because of symmetry constraint) while the coordinate of both anions, F and O, were allowed to converge. The refined structures were visualized using the Jade software (MDI, Livermore, CA).

6.3 Results and Discussion

6.3.1 $TiOF_2$ Crystal Structure

The synthesized $TiOF_2$ powder formed at 350°C had a light gray color. Energy dispersive x-ray (EDX) analyses revealed the presence of appreciable levels of titanium, fluorine, and oxygen in the powder (Figure 6.1b). Powder X-ray diffraction analyses of the sample at room temperature (Figure 6.2) indicated that all the peaks could be indexed with the allowed reflections from a hexagonal unit cell with $a \approx 5.33$ Å and $c \approx 13.23$ Å. The crystallographic data resulting from Rietveld refinement is presented in Table 6.1.

The structure consists of titanium atoms octahedrally coordinated by a random distribution of oxygen and fluorine atoms (Figure 6.3). The TiO_2F_4 octahedra share all six corners with neighboring octahedra. Each unit cell has six $TiOF_2$ molecules. The

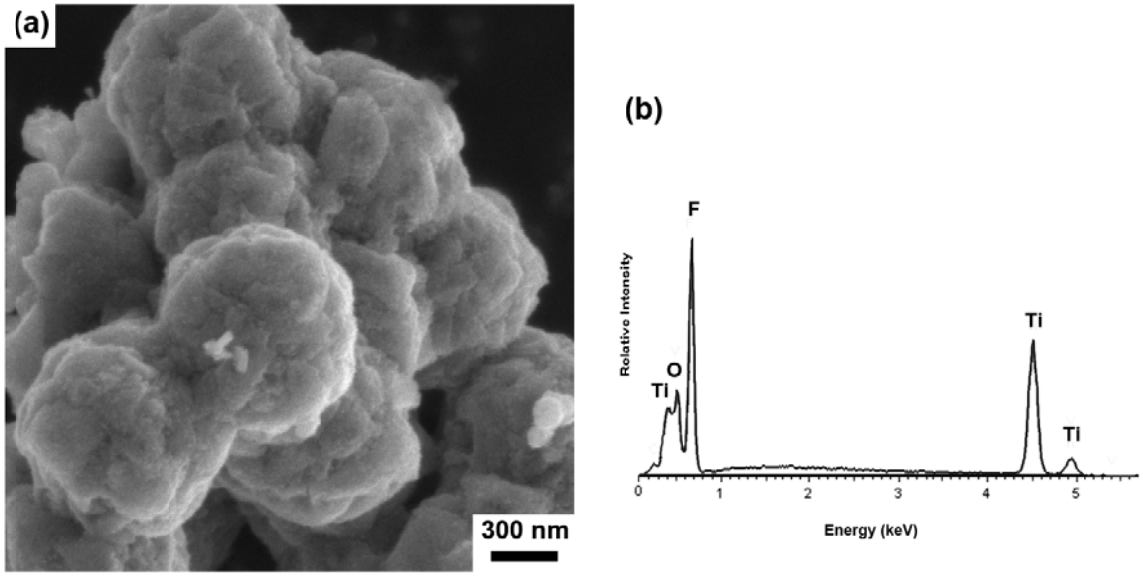

Figure 6.1: (a) Secondary electron image of $TiOF_2$ sample generated by reacting 1 μm diameter Stöber silica with TiF_4(g) at 350°C for 4 h. (b) EDX analyses shows appreciable amount of Ti, O, and F, and the lack of Si peak (located at 1.8 keV).

calculated theoretical density and Ti-*X* distances are 3.12 g/cm^3 and 1.911 Å, respectively. These values are similar to 3.09 g/cm^3 and 1.90 Å reported by Vorres and Donohue for room temperature cubic $TiOF_2$[112].

The six most intense peaks for $R\bar{3}c$ $TiOF_2$ reflections are at similar locations as the four most intense peaks from $Pm3m$ $TiOF_2$ reflections currently registered in the ICDD database (Powder Diffraction File, Card No. 04-007-8589). This similarity might lead to inaccurate identification of hexagonal $TiOF_2$ for cubic $TiOF_2$. In several reports, such inaccuracy has caused confusion for assigning the $TiOF_2$ $R\bar{3}c$ reflection at around 39.5° for a different phase [12,115]. The 39.5° peak is absent in the $Pm3m$ pattern. The first distinguishing reflection that belongs to $Pm3m$ is located at around 41°, which is rather weak. If the diffractometer was not optimized for resolution and/or if the crystallite size was relatively small, the closely located pair of reflections of $R\bar{3}c$ $TiOF_2$ at around 33.5° and 54° may be indistinguishable and may be incorrectly assumed to be single reflections.

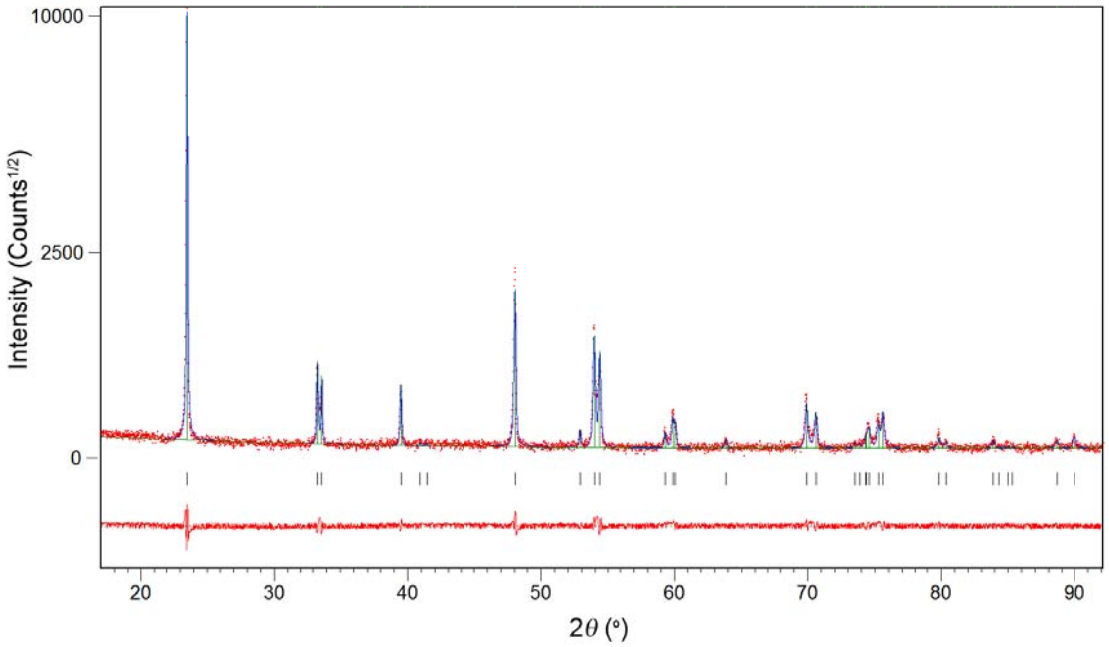

Figure 6.2: Rietveld refinement (showed by continuous line) of room temperature XRD data of $TiOF_2$ (shown as dots). The allowed reflections of $R\bar{3}c$ are indicated with tick marks. The difference plot (between experimental data and refined pattern) is shown below the tick marks.

Table 6.1. Crystallographic data of room temperature $TiOF_2$ synthesized from the reaction of SiO_2 with TiF_4(g) at 350°C.

Space group	$R\bar{3}c$ (No. 167)
Unit cell	a = 5.3325(1) Å
	c = 13.2321(4) Å
Atom coordinate	Ti (0, 0, 0); Occupancy = 1
	F (0.5486(5), 0, ¼); Occupancy = ⅔
	O (0.5486(5), 0, ¼); Occupancy = ⅓
Rietveld statistic:	R_{exp} = 9.86, $R_{weighted\ profile}$ = 12.62, χ^2 = 1.64

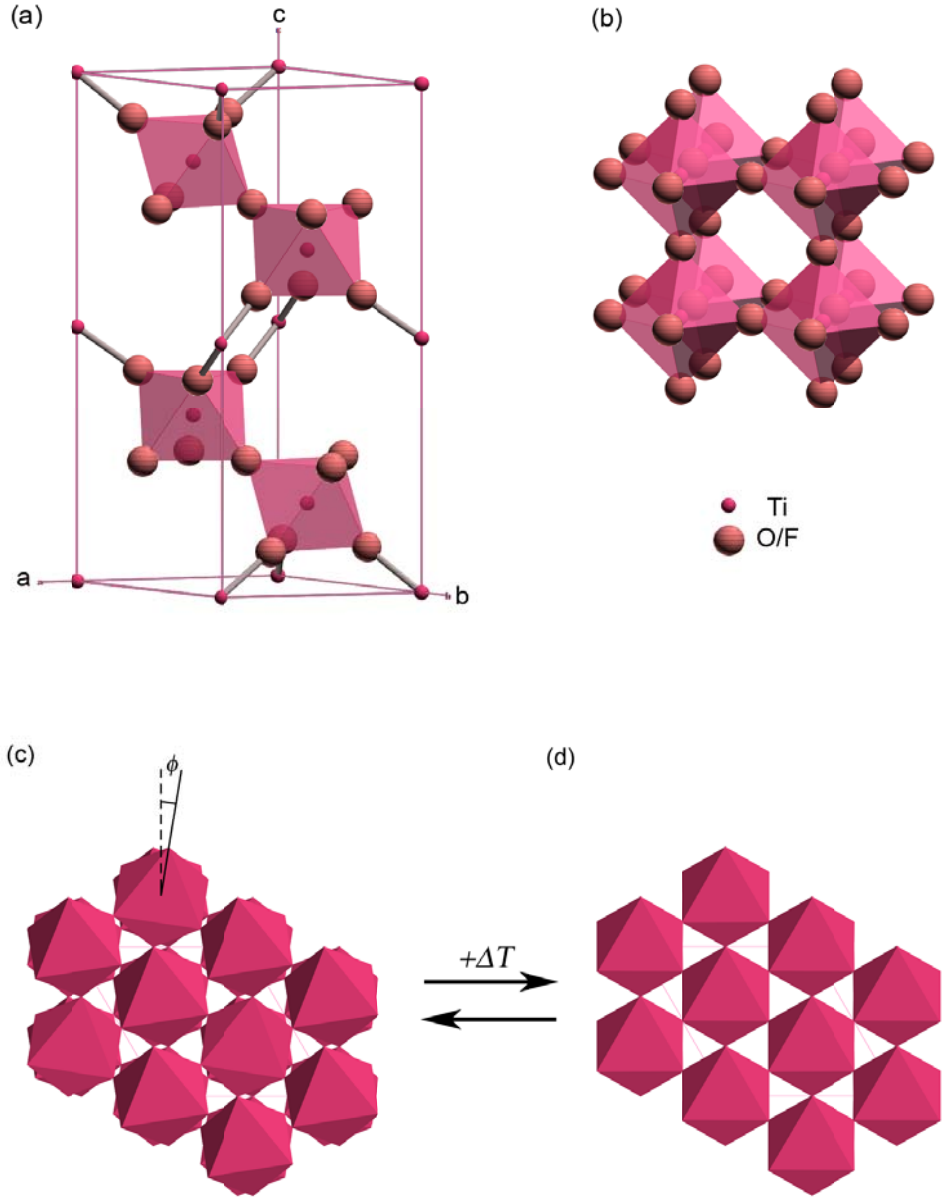

Figure 6.3: (a) The unit cell of hexagonal $TiOF_2$ ($R\bar{3}c$) at room temperature. (b) The unit cell of cubic $TiOF_2$ (*Pm3m*) is not readily apparent in this schematic but can be easily imagined since all Ti atoms is located in corner of the cubic cell. The orientation of TiO_2F_4 octahedra in (c) hexagonal and (d) cubic $TiOF_2$ viewed down the $[001]_{hexagonal}$ direction which is equivalent to the $<111>_{cubic}$ direction. The tilt angle of octahedra in the hexagonal polymorph is ϕ, which becomes zero when the transition to the cubic polymorph is completed[113].

6.3.2 Thermally Induced Phase Transformation of $TiOF_2$

Heating the synthesized $TiOF_2$ powder (prepared by reaction at 350°C) to 60°C resulted in a gradual decrease of the intensities of several hexagonal reflections, such as the (113) reflection near $2\theta = 39°$ and the (211) reflection near $2\theta = 53°$. In addition, several nearby hexagonal reflections, such as (104) and (110) near $2\theta = 33°$ and (116) and (122) near $2\theta = 59°$, converged into single reflections as the sample was heated

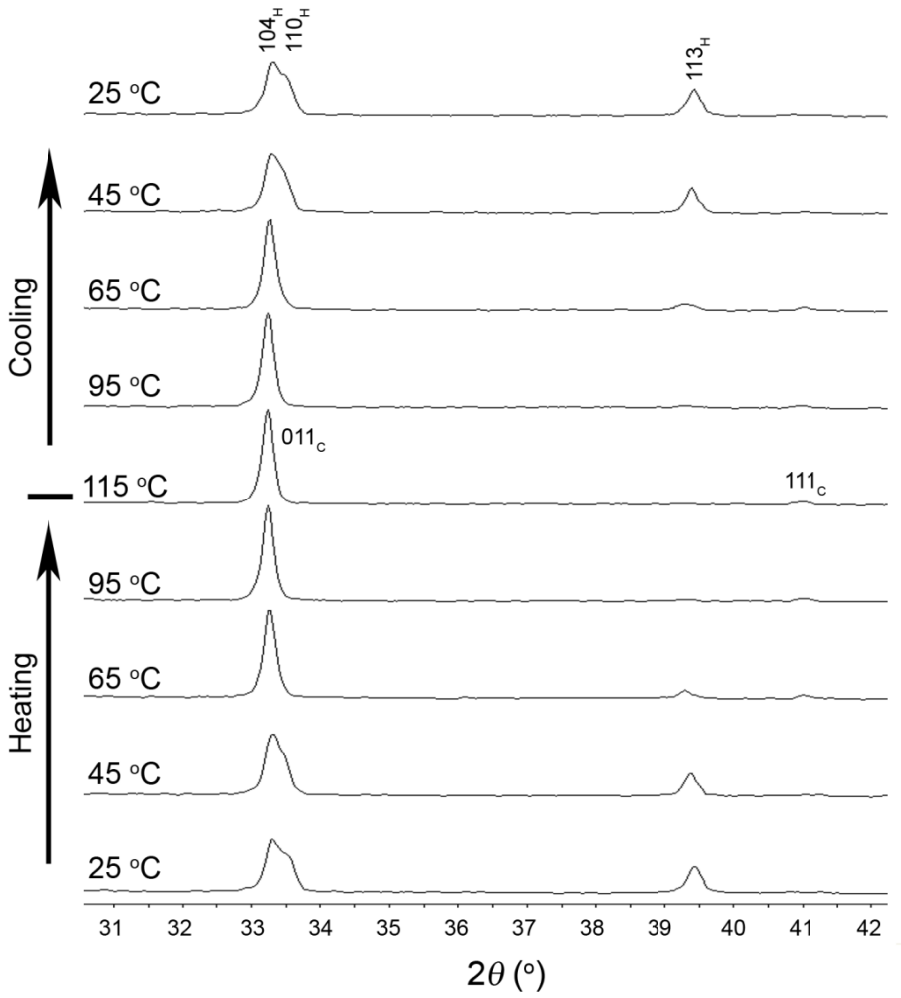

Figure 6.4: Diffraction patterns of $TiOF_2$ in a selected 2θ range upon heating (25 to 115°C) and cooling (115 to 25°C) show the reversible progressive transition from hexagonal (subscript H) to the cubic (subscript C) structure. Each pattern was taken after 15 min of equilibrium time at the corresponding temperature.

(Figure 6.4). As seen in Figure 6.4, the phase transformation of $TiOF_2$ was reversible upon heating and cooling through the transition temperature. TGA analyses on the sample by cycling the temperature from 30 to 100°C (Figure 6.5) did not show any appreciable loss of mass that could be associated with fluorine volatilization.

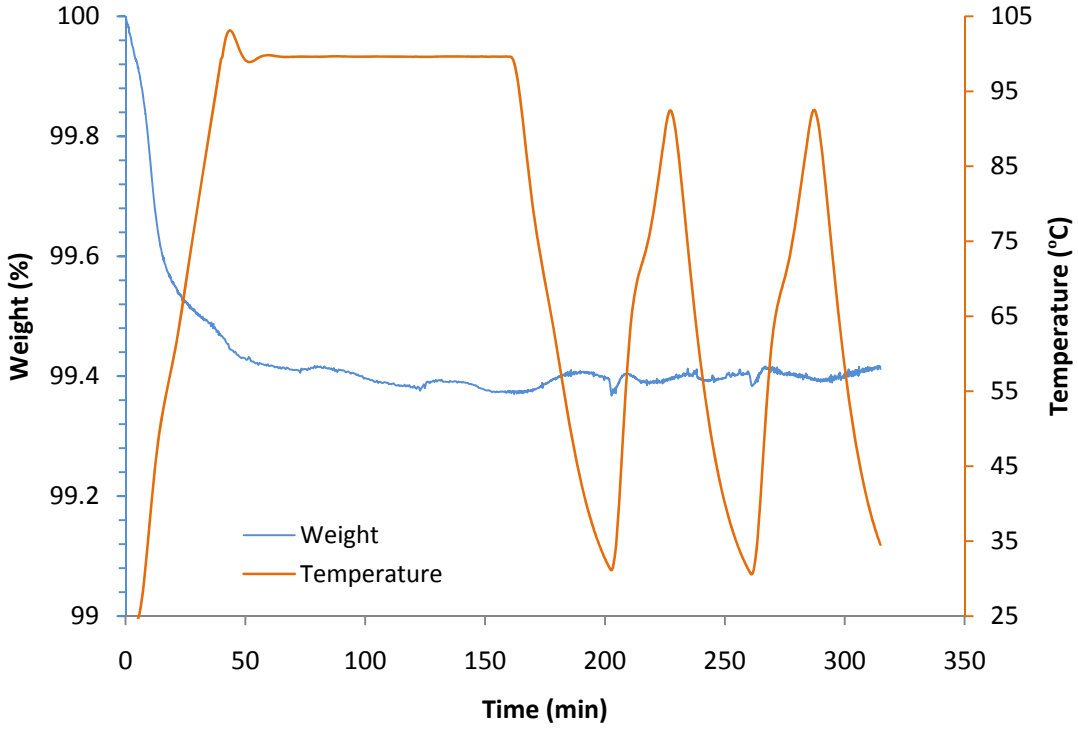

Figure 6.5: Thermogravimetric analysis (TGA) of $TiOF_2$ by cycling the temperature from 30 to 100°C (between 200 to 325 min) shows no appreciable loss of mass that could be associated with fluorine volatilization. The initial loss of weight (at < 150 min) was attributed to the physisorbed water.

Diffraction patterns collected at 95°C or higher exhibited only reflections associated with cubic (*Pm3m*) $TiOF_2$. These gradual changes are an indication of the TiO_2F_4 octahedra rotating from lower symmetry $R\bar{3}c$ (hexagonal) toward higher symmetry *Pm3m* (cubic) upon heating. The cell parameter of $TiOF_2$ reported by Vorres and Donohoe (a = 3.798 Å at room temperature) is indeed quite similar to the cell parameter of *Pm3m* $TiOF_2$ obtained at 95°C (a = 3.806 Å, R_{exp} = 2.48, $R_{weighted\ profile}$ = 6.30, χ^2 = 6.4) in the present work.

Based on the diffraction data alone, it was not possible to assign the most appropriate crystal symmetry at temperature between 65°C to 85°C. Although the peaks near 2θ = 33° and 2θ = 59°C appeared to be converged at temperature above 60°C, the (113) reflection near 2θ=39°C, which is belong to hexagonal symmetry, did not fully disappeared until ≥95°C. Rietveld analyses did not give preference on using either symmetry at this temperature range, i.e., either using hexagonal or cubic symmetry resulted on similar good of fit values. To determine the accurate transformation temperature, DSC analyses of was performed on the $TiOF_2$ powder. As shown in Figure 6.6, the estimated transformation temperature was 61°C, which is the average of onset temperature during heating and cooling[116]. Thus, based on DSC analyses, cubic symmetry was assigned for diffraction patterns at temperature ≥65°C. The calculated molar enthalpy of transformation, $\Delta H^{H\rightarrow C}$, is 109±8 J/mol.

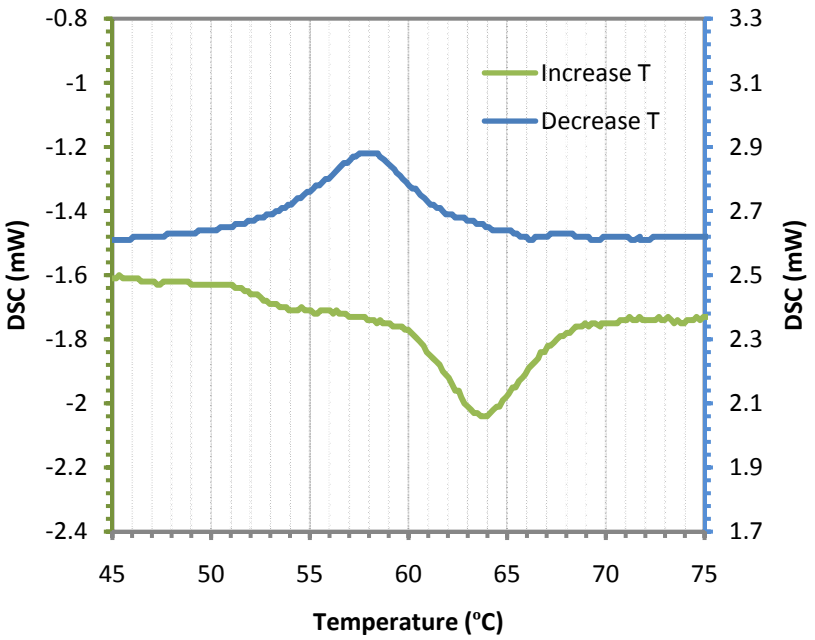

Figure 6.6: Differential scanning calorimetry (DSC) of $TiOF_2$ powder shows minima and maxima. The average onset temperatures during heating and cooling are 60°C and 62°C, respectively.

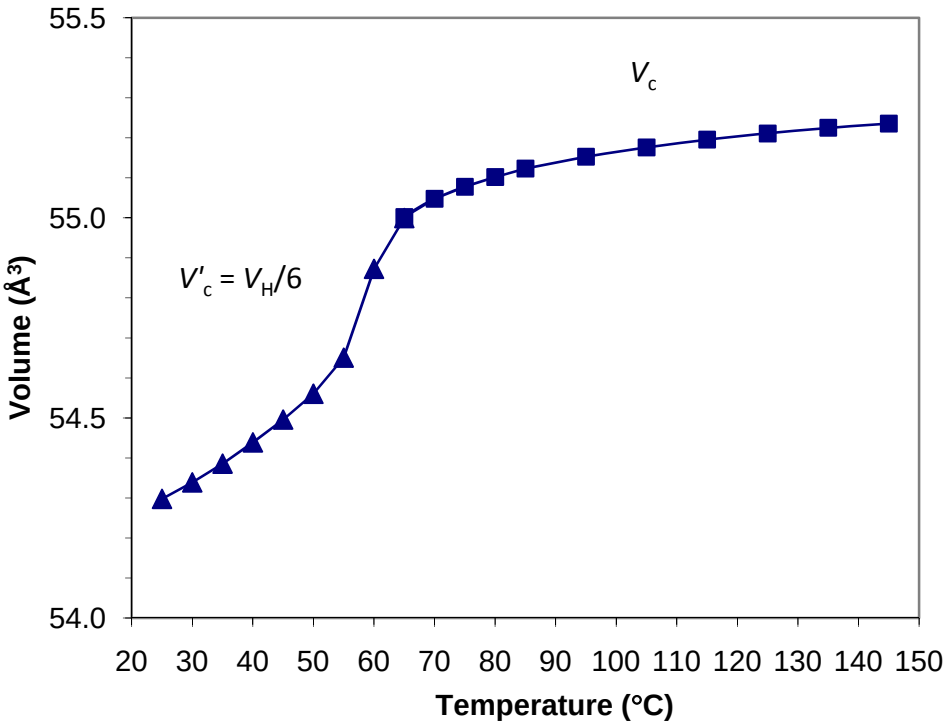

Figure 6.7: Volume of the $TiOF_2$ unit cell as a function of temperature. V'_c is the cubic equivalent volume of a hexagonal unit cell ($T \leq 60°C$).

Examination of the temperature dependence of the unit cell volumes, shown in Figure 6.7, suggests that there is a significant change in thermal expansion coefficient during the transformation. At temperatures below the transition point of 61°C, the cell volume increased more rapidly with heating than at temperatures above than the transition point. This behavior is similar to the TiF_3 transformation from hexagonal to cubic at 102°C reported by Kennedy and Vogt[117]. O^{-2} and F^{-1} ions have similar effective ionic radii ($r_{O^{-2}}$ = 1.4 Å and $r_{F^{-1}}$ = 1.33 Å for atomic coordination number of 6[118]) and both effectively have the same number of total electrons. Thus, the replacement of one of the fluorine anion with a single oxygen anion is not likely to have dramatic impact on the overall cell structure and thermal behavior, which led to the similar behavior between TiF_3 and $TiOF_2$.

The lattice parameters *a* and *c* of the hexagonal setting of $R\bar{3}c$ $TiOF_2$ behave differently during heating; that is, the a-axis was elongated while the c-axis was slowly shortened. Calculated for cubic equivalence, the values of the *a* and *c* lattice parameters eventually merged upon completion of the cubic transformation (Figure 6.8). Both lattice parameter and volume change analyses suggest that this transition is continuous upon heating.

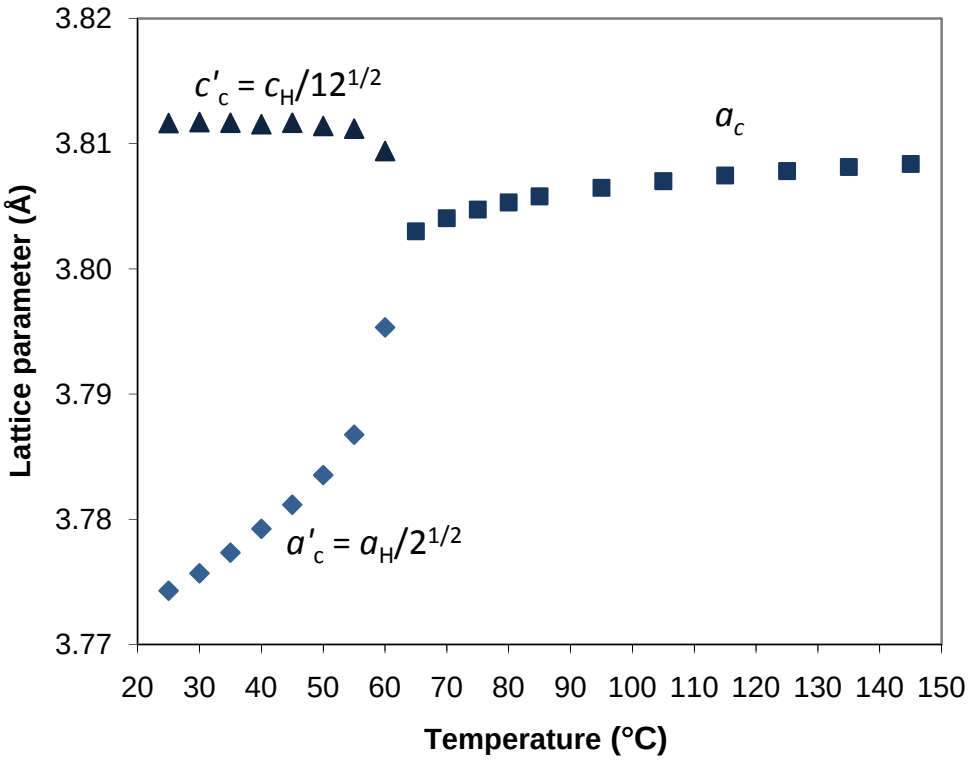

Figure 6.8: The cubic-equivalent lattice parameters of hexagonal (a'_c and c'_c) and cubic (a_c) $TiOF_2$ as a function of temperature.

The TiO_2F_4 octahedral tilt angle (ϕ) in the $R\bar{3}c$ can be calculated using the following formula:

$$\tan \phi = 2(x - ½)\sqrt{3} \quad (4)$$

where x is the location of anion (x, 0, ¼) at the hexagonal unit cell[119]. At room temperature, the octahedral tilt angle is about 9° and as shown in Figure 6.9, the octahedral tilt angle progressively decreased as temperature increased and become zero when the transition was completed. The schematic in Figure 6.3c and d illustrates the octahedral before and after the phase transformation. All octahedra tilt through the same angle ϕ, with half of the octahedra rotating clockwise around the triad axis, and the other half rotating counterclockwise[113].

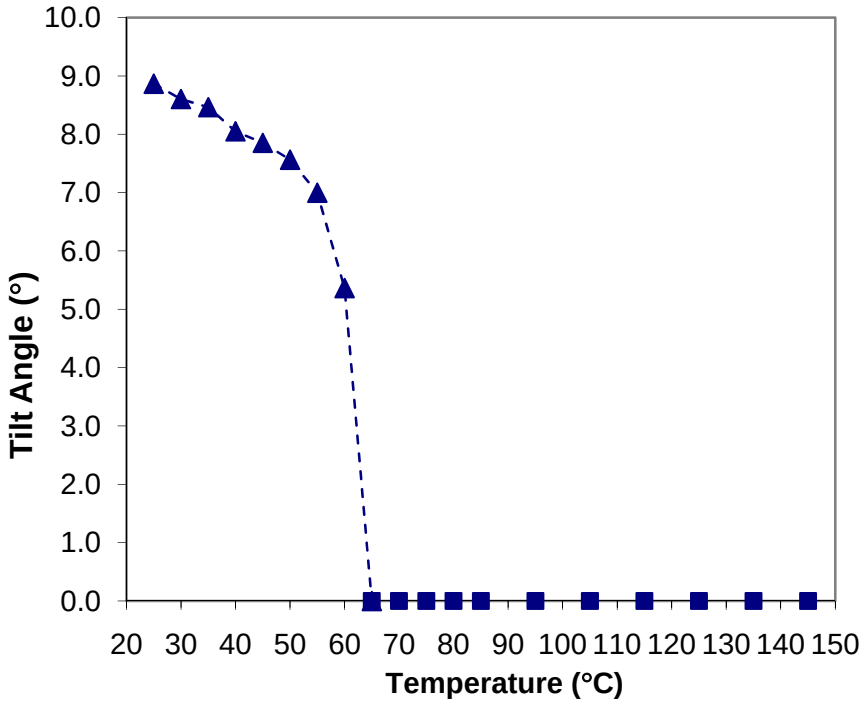

Figure 6.9: TiO_2F_4 octahedra tilt angle as a function of temperature. The tilt angle ϕ is given by $\tan \phi = 2(x - ½)\sqrt{3}$ where anions, F and O, are located at (x, 0, ¼).

6.4 Conclusion

Using X-ray powder diffraction data and Rietveld analyses, the room temperature crystal structure of polycrystalline $TiOF_2$ (that was synthesized through the metathetic reaction of silica with TiF_4(g)) was found to have $R\bar{3}c$ symmetry with a = 5.33252(11) Å and c = 13.2321(4) Å. Upon heating to 61°C, the $TiOF_2$ crystal underwent a transformation from the hexagonal $R\bar{3}c$ structure to the cubic *Pm3m* structure.

CHAPTER 7: Design and Development of a Gas-Tight Reaction Chamber for Containment of Gas/Solid Reactions for High Temperature XRD Analyses

7.1 Introduction

A recently developed process, referred to as BaSIC (Bioclastic and Shape-preserving Inorganic Conversion), enables the microfabrication of three dimensional structures of various chemistries through the chemical conversion of biomineralized templates, such as the silica-based microshells (frustules) of diatoms (microscopic algae)[10]. One of the demonstrated methods of the BaSIC process is the metathetic reaction of such biosilica templates with gaseous titanium tetrafluoride. This method has been successfully used to transform the relatively complex 3-D structure of silica diatom frustule into a titania replica that retained the overall frustule shape and nano-scale structural features[12]. In a subsequent report, a three dimensionally ordered macroporous structure (inverse opal) of titania was produced by applying this method to silica preforms[111]. The metathetic reaction of SiO_2 with $TiF_4(g)$ to yield the oxyfluoride, $TiOF_2$, may occur by the following reactions:

$$2TiF_4(g) + SiO_2(s) \Rightarrow 2TiOF_2(s) + SiF_4(g) \quad (1)$$

$$3TiF_4(g) + 2SiO_2(s) \Rightarrow 3TiOF_2(s) + Si_2OF_6(g) \quad (2)$$

$$TiF_4(g) + SiO_2(s) \Rightarrow TiOF_2(s) + SiOF_2(g) \quad (3)$$

High-temperature x-ray diffraction (HTXRD) analysis is an attractive analytical method for the dynamic evaluation of phase evolution and of reaction kinetics for solid/solid and fluid/solid reactions[120-124]. HTXRD has frequently been used to analyze gas/solid reactions involving reactant gas species that exist as gases at room temperature (e.g., O_2,N_2,H_2, and CO_2)[125-127]. However, a number of reactions of scientific and technological interest involve reactant species that can only be generated as gases with appreciable vapor pressures at elevated temperatures (i.e., such species are stable as solids or liquids at room temperature). In the above reaction, TiF_4 exists as a solid at room temperature, and sublimes at 285°C[45]. HTXRD analyses of the above reaction is complicated by the need to generate TiF_4 vapor, and to confine the hot reactive gas in the vicinity of the SiO_2 solid reactant, for a sufficient time as to enable evaluation of the progress of reaction. Temperature differences at various locations may also cause vapor deposition of solid TiF_4 in the cooler areas and, thus, should be avoided. New experimental designs are needed to allow for HTXRD analyses of such reactions.

The purpose of this chapter is to describe the design and use of a sealed, heated, x-ray transparent chamber capable of containing a moderate pressure reactive gas generated from a solid source within the chamber, to allow for the dynamic HTXRD analysis of a gas/solid displacement reaction. This design is an improvement of a similar chamber made from monolithic graphite reported by Haluska, *et al.*[128] for evaluation of a magnesiothermic reaction. This new chamber design has been successfully implemented to investigate the reaction between TiF_4(g) and SiO_2(s).

7.2 Chamber design

Materials selection for the reaction chamber should satisfy the following criteria: (1) relatively transparency to X-rays, (2) inertness with respect to the gas reactant (TiF_4) and gas reaction product (SiF_4) , (3) ability to maintain a seal (gas tight) and to exhibit

sufficient mechanical strength as to withstand the gas pressure generated at the operating temperature (up to 350°C), and (4) be relatively easy to machine or to form[128]. Among several metals that were considered, aluminum or aluminum-rich alloys are particularly attractive, owing to thermal stability (at 350°C) and relatively inertness to TiF_4. Moreover, aluminum has a relatively high thermal conductivity (2.37 W/cm K at 27°C and 2.31W/cm K at 327°C[129]) and is relatively easy to machine. The high thermal conductivity is particularly important for ensuring a uniform temperature distribution inside the chamber and for minimizing the temperature difference between the inside of the chamber and the thermocouple location outside of the chamber.

Kapton has been widely used as an X-ray transparent (window) material, especially for cases where mechanical stability at modest temperature is required[130,131]. However, Kapton was observed to react with TiF_4(g) at elevated temperatures, rendering it more opaque both optically and towards X-rays. One solution was to line the Kapton with thin aluminum foil on the inner side of the windows, so that the aluminum foil would act as a chemical barrier. Cu Kα x-rays can penetrate two layers of 130 μm Kapton film and 13 μm of aluminum foil while retaining more than 57% of the incident beam intensity[132]. Other possible commercially available materials for X-ray windows are listed in Table 7.1.

Table 7.1. Calculated transmission of possible materials for use in X-ray windows for a sealed reaction chamber[132].

Material	Thickness (μm)	Transmission (Cu Kα radiation)
Aluminum	13	0.84
	25	0.71
Kapton	25	0.98
	130	0.90
Nickel	25	0.33
	10	0.64
Teflon	130	0.69
	50	0.86

Figure 7.1a shows a schematic drawing of a side view of the reaction chamber. The chamber consisted of a main body, a layer of windows, window frames, and a sample holder with a lid. The main body (outer dimensions: 25 mm tall x 25 mm wide x 16 mm deep) was machined from an aluminum 6061 alloy (McMaster-Carr, Atlanta, GA). The side surfaces of the main body where the window was to be attached were polished flat using 1200 grit SiC impregnated paper (Buehler, Ltd., Lake Bluff, IL). Eight holes were drilled and threaded on each side of the face of the main body (see Figure 7.1e and d) to allow for the window frame to be attached securely, using type 18-8 stainless steel screws (McMaster-Carr, Atlanta, GA). The window frames were machined from 2 mm thick, type 316 stainless steel plates (McMaster-Carr, Atlanta, GA), and eight holes were drilled on the frames in alignment with the threaded holes in the main body. The sample holder (15 mm long x 15 mm wide x 3 mm tall, Figure 7.1b) was cut and formed from 0.25 mm thick nickel foil (McMaster-Carr, Atlanta, GA). The lid of the sample holder was slightly larger than the top of the sample holder and was loosely placed on the sample holder so that it would allow for the gas reactant from the sample holder to flow

throughout the chamber. The lid was used to hold the solid silica sample reactant in position for exposure to the X-ray beam. In the middle of the lid, a groove (1 mm deep x 2 mm wide) was formed to attach a standard material, which for the present work was an alumina plate (99% purity, Coorstek Golden, CO). The use of such a standard material was required to correct for changes in X-ray intensity due to the dynamic change of gas density/composition inside the reaction chamber throughout the reaction.

130 μm thick Kapton film and 13 μm thick aluminum foil (McMaster-Carr, Atlanta, GA) were cut to the size of 18 mm x 18 mm to fully cover the window opening.

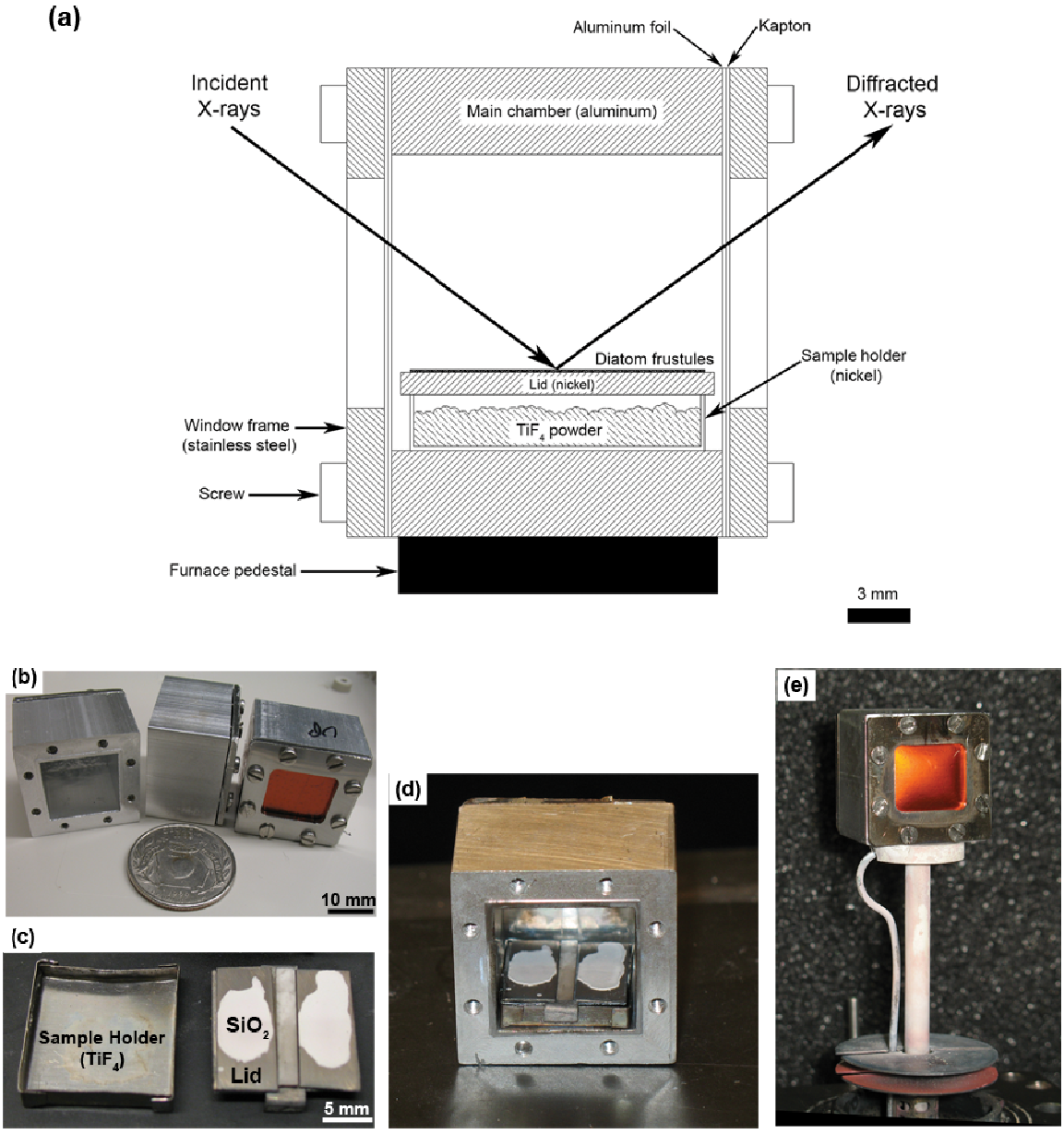

Figure 7.1: (a) Schematic (side view of cross section) of the reaction chamber. (b) Optical image of partially assembled chamber viewed from different sides, (c) the sample holder (left) and the lid (right) with the solid silica sample and alumina strip on top, (d) the position of sample holder inside the main chamber body, and (e) the position of the chamber on the Anton Paar furnace pedestal.

7.3 Experimental Procedures

In a typical experiment, 150 mg of solid TiF_4 powder (99% purity, Advanced Research Chemicals, Catoosa, OK) was loaded into the sample holder. A few drops of a silica diatom (*Aulacoseira*) frustule suspension (with about 15 mg of solid silica) in water was spread on the sample holder lid and then dried on a hot plate. The molar TiF_4:SiO_2 ratio placed in the sealed chamber was in excess of 7:1.

Optical images revealing the location of the diatom frustules on the lid of the sample holder and TiF_4 powder in the sample holder are shown Figure 7.1c and d. After placing the silica and TiF_4 reactants in the reaction chamber (Figure 7.1d), the window frames were secured to the main body. The reactant loading and chamber sealing were performed inside an argon-filled glove box (Model Omni-Lab, Vacuum Atmosphere, Hawthorne, CA) maintained at an oxygen partial pressure below 0.1 ppm. Next, the sealed reaction chamber was placed within a high-temperature x-ray-diffraction (HTXRD) system, which was heated with an Anton-Paar HTK 1200 high-temperature furnace (Graz, Austria). The reaction chamber was placed on furnace pedestal and was heated at a rate of 60 °C/min to the desired reaction temperature (160-350°C) and held at this temperature for a sufficient amount of time to allow for complete reaction (typically between 3 and 24 hours). The temperature inside the reaction chamber was calibrated against a thermocouple reading by using the differential thermal expansion method according to Drews[133] (See Appendix B).

Diffraction profiles were measured using an MPD Panalytical Diffractometer (Almelo, The Netherlands) configured for Bragg-Brentano geometry. A Cu Kα X-ray radiation (1.5405980 Å) source was used. A Cu W/Si multilayered focusing mirror (Goebel mirror) was attached to the incident beam path to create a high intensity parallel beam so as to ensure that a high signal to noise ratio would be achieved during a relatively short measuring time. The peak profile data acquisition was conducted using a

solid-state position-sensitive ultrafast detector (X'Celerator, Panalytical, Almelo, The Netherlands). A divergence slit of 1/2° and a 6.6 mm antiscattering slit were used in the incident beam path and on the diffracted beam path, respectively.

7.4 Results and Discussion

Initial attempts to use the graphite reaction chamber described by Haluska, *et al.*[128], were not fully successful (See Appendix C). It was found that that the gas reactant leaked through machined graphite chamber, presumably through micro-cracks in the thinnest walls where the x-rays passed. The leaking gas depleted the solid reactant source, causing the reaction to stop prematurely. The micro-cracks were thought to have developed during the machining of the brittle graphite. Increasing the graphite wall thickness may help minimize the micro-cracks however such additional barrier compromised the signal to noise ratio, especially for a relatively low energy Cu Kα incident beam. This obstacle prevented proper analysis on the data gathered during high temperature X-ray scans.

A room-temperature x-ray-diffraction pattern of the fully assembled reaction chamber containing the solid reactants (silica based diatom frustules) and standard (alumina strip) is shown in Figure 7.2a. The XRD pattern reveals predominant peaks for the cristobalite polymorph of silica (Powder Diffraction File, Card No. 00-039-1425), the alumina standard strip (Powder Diffraction File, Card No. 04-007-5143), the nickel lid (Powder Diffraction File, Card No. 00-004-0850), and the aluminum window (Powder Diffraction File, Card No. 00-004-0787). The diffraction peak for nickel resulted from the diffraction of Cu Kα X-rays with the horizontal surface of the nickel lid/pedestal located under the SiO_2 frustules. The aluminum diffraction peak came from the front vertical aluminum foil of the reaction chamber window that was facing the incident X-ray

beam. This aluminum peak was slightly shifted to a higher 2θ value than indicated by the powder diffraction file, because the incoming beam hit the window at a higher position than the centered position for the Bragg-Brentano geometry. The higher angle peaks of aluminum were missing because the diffracted beam was absorbed by the top side of the chamber main body. Although thermodynamics calculation shows that the formation of AlF_3 and NiF_2 from the reaction of TiF_4 with Ni and Al, respectively, are possible, no observable visual change to the surface finish of either metal in the range of temperature of interest (< 350°C). Indeed, the diffraction pattern did not indicate any peak from AlF_3 or NiF_2 throughout the course of reaction.

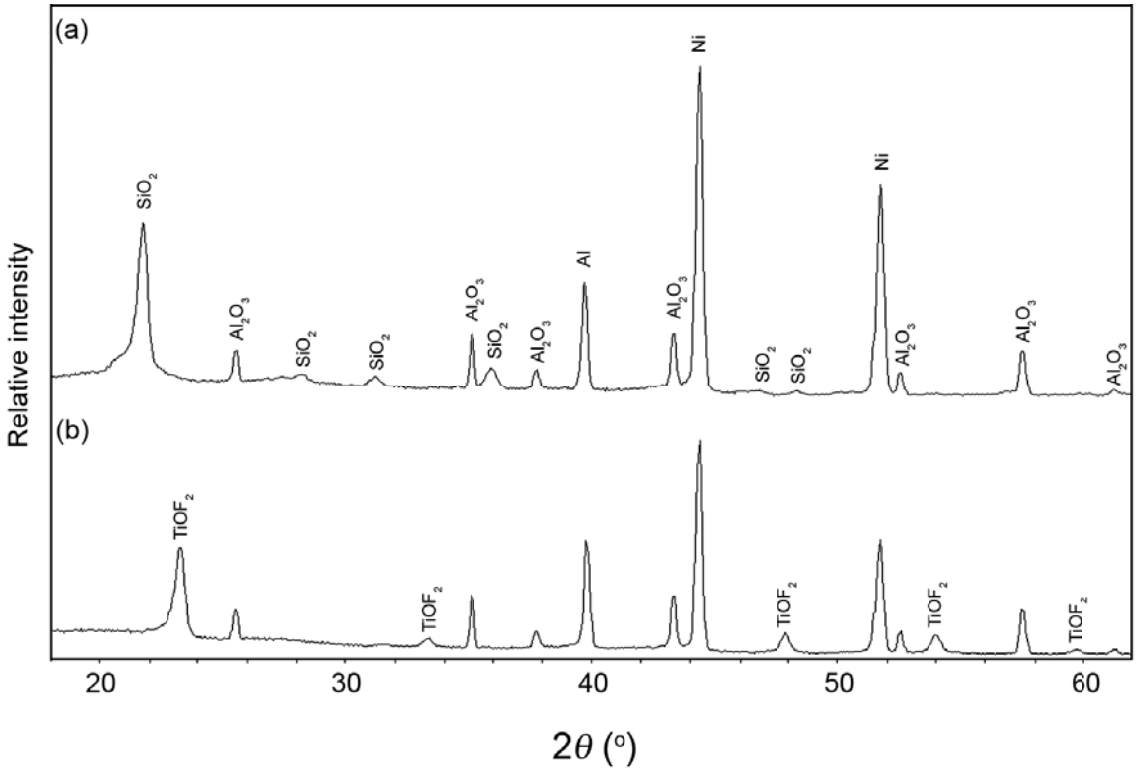

Figure 7.2: Room temperature X-ray diffraction pattern of the loaded chamber: (a) before the reaction began and (b) after the reaction at 180°C ended (i.e., after 6 h).

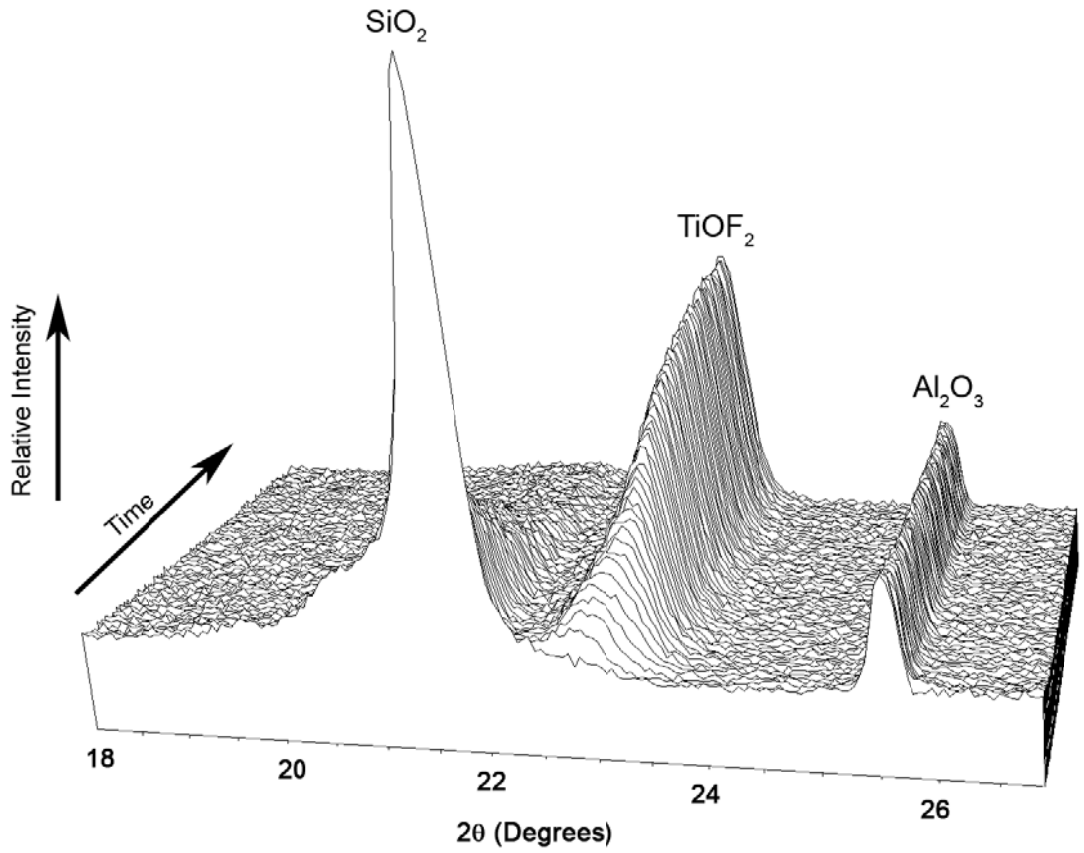

Figure 7.3: Portions of the X-ray diffraction patterns obtained with time during isothermal reaction of SiO_2 diatom frustules with TiF_4 gas at 180°C (4 min interval between successive scans).

Because these frustules were physically separated from the TiF_4 solid within the reaction chamber, the frustules could only react with the gaseous form of TiF_4 generated upon heating to 180°C. The standard equilibrium vapor pressure of TiF_4 vapor over solid TiF_4 at 180°C is 1.1×10^{-2} atm[45], which was apparently enough to drive the reaction forward. The HTXRD patterns obtained at 180°C are shown in Figure 7.3, where diffraction peaks for SiO_2, $TiOF_2$, and Al_2O_3 were clearly detected. The relative intensity of the SiO_2 diffraction peak decreased, and the relative intensity of the $TiOF_2$ peak increased, with increasing reaction time. The gradual, monotonic changes in the relative intensities of the SiO_2 and $TiOF_2$ diffraction peaks in Figure 7.3 indicated that the reaction of silica frustules with TiF_4 gas inside the closed, heated reaction chamber could be carefully tracked with time at 180°C by HTXRD analyses.

The X-ray diffraction pattern in Figure 7.2b shows that the silica peaks were missing and completely replaced by $TiOF_2$ peaks, which indicates the completion of the reaction within 6 h at 180°C. The intensities of the alumina standard peaks and the aluminum peak were relatively constant, while the intensity of nickel peaks were slightly reduced. The decrease on nickel peak intensity was likely to have been caused by a change in the coefficient of absorption of the solid reactant upon conversion from SiO_2 to $TiOF_2$.

7.5 Conclusions

This is the first time that HTXRD analysis has been used to dynamically monitor the extent of a metathetic displacement reaction between SiO_2 solid and TiF_4 gas reactants that were confined within a closed, heated chamber. This approach may also be used on a variety of reactions involving gaseous reactants that possess appreciable vapor pressures only at elevated temperatures (i.e., gaseous reactants that are generated by

heating condensed sources). Owing to the flexibility of the choice of materials for the main chamber body and window, reactions that require special materials (such as the need for an inert material relative to a reaction system or the need for higher temperatures) can be easily accommodated in this HTXRD chamber design.

CHAPTER 8: Fundamental Kinetic Studies of the Gas-Solid Metathetic Conversion Reaction of SiO_2 into $TiOF_2$

8.1 Introduction

Previous chapters have demonstrated the feasibility of using the BaSIC process to produce faithful titania replicas of diatom frustules through a $TiF_4(g)/SiO_2(s)$ reaction. Despite successful demonstrations of the BaSIC concept, the underlying mechanism(s) for the shape-preserving chemical conversion into $TiOF_2$ and TiO_2 is lacking. This chapter will focus on the kinetic mechanism(s) of the following possible metathetic conversion reactions:

$$2TiF_4(g) + SiO_2(s) \Rightarrow 2TiOF_2(s) + SiF_4(g) \quad (1)$$

$$3TiF_4(g) + 2SiO_2(s) \Rightarrow 3TiOF_2(s) + Si_2OF_6(g) \quad (2)$$

$$TiF_4(g) + SiO_2(s) \Rightarrow TiOF_2(s) + SiOF_2(g) \quad (3)$$

The conversion of complex 3-D shaped bio-silica reactants (e.g., diatom frustules and silica structures from plants) are difficult to model for quantitative kinetic analyses. To simplify such analyses, specimens with simple shapes, such as a flat plate or a sphere, should be used. Owing to its relatively high total surface area compared to a flat plate geometry, a spherical geometry could allow for significantly enhanced reaction rates and, thus, may allow for significantly reduced total reaction time required for kinetics experiments. For this study, amorphous Stöber silica spheres were chosen as reactants

because of the availability of analytical solutions for various rate-limiting steps for this specimen geometry.

There is little literature available on the $TiOF_2/SiO_2$ gas-solid reaction. Other than a short communication written by Unocic, *et al.*[12], the closest recent work on the $TiOF_2(g)/SiO_2(s)$ reaction is a subsequent paper published by Lytle, *et al*[111].. In that paper, they described the transformation of 3-D ordered macroporous silica into titania using the same method (gas-solid metathetic reaction in a sealed reaction tube followed by an oxygenation reaction). However, to our knowledge, there has been no prior study of the fundamental kinetic mechanism of the shape preserving conversion reaction of SiO_2 into $TiOF_2$.

8.2 Kinetic Models

Better understanding of the metathetic conversion reaction, and quantitative assessment of the effect of varying the reaction conditions, can be achieved by kinetic modeling. Kinetic modeling could provide insight into the rate-limiting mechanisms of TiF_4-SiO_2 chemical reactions. Since the mechanisms and dynamics of the reaction system are interconnected, it is then possible to optimize the reaction conditions based on understanding of the rate-limiting mechanism.

There are several possible kinetic models available in the literature to describe non-catalytic solid-gas reaction mechanisms[134-138]. These include the sharp interface (shrinking core) model, the particle-pellet model, the single pore model, the distributed pore size model, and the random pore model. Literature reports[138-140] have shown that microstructural observations play an important role in evaluating the validity of a particular model. SEM and TEM analyses of the evolution of the solid reactant and product microstructures during reaction can provide insights as to the possible reaction mechanism(s). While a given model might be suitable for a specific reaction system and

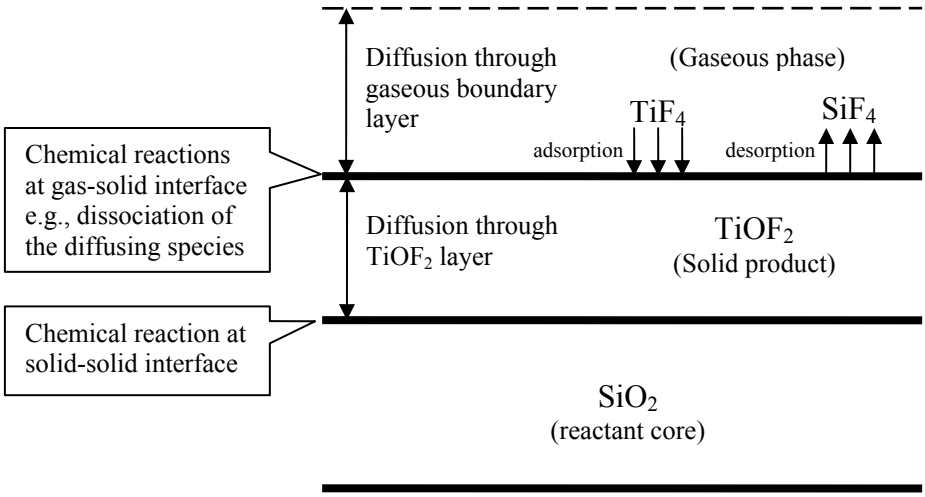

Figure 8.1: Schematic of possible rate-limiting steps.

condition, various authors[137,139,141-143] have utilized the sharp interface model, which is also known as shrinking core model (SCM), for evaluating reacting gas-solid systems for which a distinct interface exists between a solid reactant and a solid product.

The SCM describes a diminishing solid reactant covered by a growing continuous, coherent layer of product during reaction with a gas. According to the SCM, the overall rate at which a solid reacts with a gas may be limited by:

1) Gas phase mass transfer of the reactant (e.g., prior to TiF_4 adsorption) or the product (e.g., after SiF_4 desorption);
2) Diffusion through a dense or porous product layer;
3) Chemical reaction control (e.g., at the $SiO_2/TiOF_2$ interface or at the gas/$TiOF_2$ interface).

The basic steps (as illustrated in Figure 8.1) are assumed to occur in series. Thus, the slowest of these steps in the sequence will be the rate-limiting step of the overall reaction. The derivation of the governing equations of the SCM has been presented for

three different simple geometries, i.e., for plate, tube, and spherical geometries[137]. In the following section, the governing equations for each rate-limiting step will be discussed for a spherical geometry.

Consider the following reaction on the surface of a sphere,

$$A(g) + bB(s) \rightarrow cC(s) + dD(g) \tag{4}$$

where *b*, *c*, and *d* are the stoichiometric coefficients of the solid reactant B, the solid product C and the gas product D, respectively. If the rate-limiting step is diffusion through a gas boundary layer or a film of constant thickness, then the extent of the reaction, X, can be modeled by the following equation [137]:

$$\frac{t}{\tau_{film}} = X \tag{5}$$

$$\tau_{film} = \frac{\rho_B R}{3bk_g C_{A(g)}} \tag{6}$$

where τ_{film} is the time for complete conversion of the sphere, $C_{A(g)}$ is the concentration of the reactant gas species in the bulk gas, ρ_B is the density of the reactant oxide B, R is initial radius of the sphere, and k_g is the mass transfer coefficient of gas species. The extent of reaction of the sphere specimen is determined by measuring the ratio of unreacted zone radius, r_c, to the starting sample radius, R, and then calculated using the definition $X = 1 - (r_c/R)^3$. According to this equation, X should increase linearly with time, t.

If diffusion through the solid product layer is rate-limiting, then the following equation will be used to describe the solid B consumption rate[137]:

$$\frac{t}{\tau_{Diffusion}} = 1 - 3(1 - X)^{2/3} + 2(1 - X) \tag{7}$$

$$\tau_{Diffusion} = \frac{\rho_B R^2}{6bD_e C_{A(g)}} \tag{8}$$

where D_e is the solid-state diffusion coefficient of a particular species across the solid product. From this equation, the plot of the right side of equation, $1 - 3(1 - X)^{2/3} + 2(1 - X)$, against time ($t$) should exhibit a linear dependence.

If a chemical reaction at the solid/solid (e.g., $TiOF_2/SiO_2$) interface is the rate-limiting step, then for a first-order rate constant, *k"* with respect to the reactant gas species, the following relation can apply [137]:

$$\frac{t}{\tau_{reaction}} = 1 - (1 - X)^{1/3} \tag{9}$$

$$\tau_{reaction} = \frac{\rho_B R}{bk"C_{A(g)}} \tag{10}$$

From this equation, the plot of the right side of equation, $1 - (1 - X)^{1/3}$, should exhibit a linear dependence with the time (t).

In the above models, the size of the sphere was assumed constant throughout the reaction progress. In most cases, however, the total volume of the solid product C differs from the total volume of the solid reactant B. Such a volume difference introduces a variation in the radius of the sphere throughout the reaction progress. For example, if the total volume of C is larger than the total volume of B, the overall radius of the sphere will increase with reaction time, causing an increase in the diffusion path (for the solid-state diffusion rate control model) or an increase in the overall reaction area (for chemical rate

control on the surface of the sphere). Thus, the above rate control equations may not be the true representation of the actual kinetics rate. To compensate for the physical volume difference, Carter[141] introduced a term *z* to represent the volume of solid product C formed per unit volume of solid reactant B consumed, or:

$$z = \frac{cV_{M(C)}}{bV_{M(B)}} \tag{11}$$

where $V_{M(B)}$ and $V_{M(C)}$ are the molar volumes of solid B and C, respectively. For solid state diffusion control, equation (7) becomes[141]:

$$z + \frac{2(1-z)kt}{r_o^{\,2}} = [1 + (z-1)X]^{2/3} + (z-1)(1-X)^{2/3} \tag{12}$$

where r_o is the starting radius of the reactant sphere, and k is the temperature-dependent reaction rate constant. This equation is known as the Carter model for the solid-state diffusion-controlled reaction, in which, if obeyed, the plots of the right side of equation (12) against time should yield a straight line at a given reaction temperature.

For chemical reaction control at the solid-solid surface (i.e., the interface between solid product C and solid reactant B), equation (9) above still holds valid because the surface area of the reacting solid B is the same as in the case of constant volume. However, if the chemical reaction control on the surface of the sphere (i.e., the interface between gas reactant A and solid product C) is the rate limiting step, equation (9) becomes[144] (See Appendix G for derivation):

$$\frac{t}{\tau_{reaction}} = \frac{[1 + (z-1)X]^{1/3} - 1}{z^{1/3} - 1} \tag{13}$$

where $\tau_{reaction}$ is the same as indicated in equation (10)[144]. From this equation, the plot of the right side of equation, $\{[1+(z-1)X]^{1/3}-1\}/(z^{1/3}-1)$, should exhibit a linear dependence with the time (*t*).

The plot of *X* versus *t* might deviate from any of the equations above. The deviations might be attributed to several possible causes including, but not limited to, a mixed mode of solid state diffusion and chemical reaction, or a change in the rate of diffusion, such as may result from porosity formation. In the mixed mode of kinetics (e.g., when the rate of solid state diffusion and the rate of chemical reaction are of the same order), the *X* versus *t* plot may have an intermediate behavior between the two competing rate-limiting steps. Typically, the total time to complete the reaction is the arithmetic sum of the individual rate-limiting steps if the steps occur in series[137].

8.3 Experimental Procedures

8.3.1 High Temperature XRD

In a typical experiment, about 150 mg of solid TiF_4 powder (99% purity, Advanced Research Chemicals, Catoosa, OK) was loaded into the sample holder, as mentioned in Chapter 6. A few drops of Stöber silica particle (0.6, 1.54, and 3.16 μm diameters, Bangs Laboratories, Fisher, IN) suspension (about 15 mg dry solid silica weight) in water were spread on the sample holder lid and then dried on a hot plate. The molar TiF_4:SiO_2 ratio placed on the chamber was in excess of 7:1. To minimize the effect of adsorbed water, the Stöber silica spheres were heat treated at 700°C for 20 minutes in a furnace located inside an argon-filled glove box (Vacuum Atmospheres, Hawthorne, CA) maintained at an oxygen partial pressure less than 0.1 ppm

After placing the reactants in the chamber and securing the chamber window, the reaction chamber was placed within a high-temperature x-ray-diffraction (HTXRD)

system, which was heated by an Anton-Paar HTK 1200 high-temperature furnace (Graz, Austria). The reaction chamber was placed on a furnace pedestal (see Figure 7.1e in Chapter 6) and was heated at a rate of 60 °C/min to the desired reaction temperature and held at this temperature for a sufficient amount of time to allow for complete reaction (between 3 and 24 hours). The $TiOF_2$ conversion reaction was studied in the temperature range of 180°C to 260°C. The temperature inside the reaction chamber was calibrated against the external thermocouple reading by using the differential thermal expansion method of Drews[133] (see Appendix B).

Diffraction profiles were measured using an MPD Panalytical Diffractometer (Almelo, The Netherlands) configured for Bragg-Brentano geometry. A Cu Kα X-ray radiation (1.5405980 Å) source was used. A Cu W/Si multilayered focusing mirror (Goebel mirror) was attached to the incident beam path to create a high intensity parallel beam so as to ensure that a high signal to noise ratio would be achieved during a relatively short measuring time. The peak profile data acquisition was conducted using a solid-state position-sensitive ultrafast detector (X'Celerator, Panalytical, Almelo, The Netherlands). In order to reduce unwanted effects, such as instrumental peak broadening, a divergence slit of 1/2° was used in the incident beam path. On the diffracted beam path, a 6.6 mm antiscattering slit was used.

8.3.2 Modeling Procedure

The extent of reaction was evaluated with the aid of the Jade program (version 8, MDI, Livermore, CA) by measuring the area under the primary $TiOF_2$ diffraction peak (the cubic $TiOF_2$ (100) peak). The peak height, 2θ, FWHM, shape, and skew variables were refined during profile fitting using the Pseudo-Voigt model[145]. The peak area of $TiOF_2$ was normalized with the peak area of the inert Al_2O_3 standard for a given reaction temperature and time. During the HTXRD experiment, the reaction was continued until

the (001) peak of $TiOF_2$ (located near $2\theta = 23.5°$) reached a plateau; i.e., until no observable change in the height, and the maximum area of this peak was observed. Thus, the fraction of reaction product, $TiOF_2$ at a given time was simply the ratio of the instantaneous peak area to the maximum peak area observed for $TiOF_2$ (note: the Stöber silica spheres were amorphous, so crystalline silica peaks were not available for direct measurement of silica consumption)

8.3.3 Characterization

The morphologies of the samples were evaluated with a field emission scanning electron microscope (LEO-1530, Zeiss Germany) equipped with energy-dispersive X-ray analysis capability (Oxford Instrument, Bucks, UK). Transmission electron microscopy (TEM) and selected area electron diffraction (SAED) analyses were performed by Dr. Ye Cai (Georgia Institute of Technology), using a JEOL 4000 EX instrument (Japan Electron Optics Laboratory, Tachikawa, Tokyo). Quantitative analyses of the SEM or TEM images (i.e., dimension measurement of the spheres) were performed using Image-Pro Plus software (v4.5, Media Cybernetics Inc., Bethesda, MD). One SEM/TEM image was used for a particular size and treatment of the sphere. Prior to feature measurements, an internal spatial calibration was performed against the micron bar in a given image. For the SEM image that contained spheres, a uniform-spacing rectangular grid was constructed so that 20 of the spheres were located in the intersection of the lines. The diameter of these randomly selected spheres was then measured using four-point best fit circle method. Since the number of the measurable sphere cross-sections was limited for a given TEM image, the unreacted silica diameters were measured using eight-point best fit circle method for a better average value. At the sphere with maximum measured diameter, the thickness of the outer product layer was measured at random positions by overlaying a concentric 15-lines mask that originated from the center of the sphere and intersected the layer at an equal distance.

The adsorption/desorption isotherm curves of the samples were analyzed, to determine the specific surface area (BET analyses[146]) of the initial, partially-reacted, and fully-reacted spheres, by using Autosorb-1 (Quantachrome Instrument, FL, USA), with nitrogen as an adsorbate at 77 K. Pore size distributions (PSD) and pore volumes were determined using the Barrett-Joiner-Halenda (BJH) method and the non-local density functional theory (NLDFT) method provided in Autosorb-1 data reduction software[147] (v1.55). The BJH method was applied to the desorption branch of the nitrogen isotherm data. For NLDFT fitting, a cylindrical pore geometry in a silica matrix was assumed, and both adsorption and desorption isotherms were used.

8.4 Results and Discussion

The physical characteristics of the Stöber sphere samples are shown in Table 8.1. The particle size measurements from SEM image analyses are in good agreement with the manufacturer's specification. The BET surface areas derived from nitrogen adsorption analyses were higher than the geometrical surface area, which may be attributed to a rough surface or slightly porous spheres[148,149]. Lecloux et al., reported an up to three times difference of the BET surface area compared to the geometrical surface area for 8 - 206 nm diameter Stöber silica spheres[149]. A secondary electron image of the spheres is shown in Figure 8.2a. The spheres shown in this image possessed radii of 1.44 ± 0.07 μm. A secondary electron image of such spheres after complete reaction with TiF_4(g) (at 200°C for 12 h) is shown in Figure 8.2b. Although the reacted specimens were more granular in appearance, these specimens retained a roughly spherical shape. As a result, reaction models based on a spherical specimen geometry could be used in these HTXRD experiments.

Table 8.1. Characteristics of Stöber silica spheres and *Aulacoseira* diatom frustules.

Particle size† (μm)	Density† (g/cm^3)	Geometrical surface area (A_s, m^2/g)	SEM (image analyses) size (μm)	Measured BET surface area (A_s, m^2/g)
0.6	1.96	5.0	0.59±0.02	9.5±0.1
1.54±0.16	1.96	2.0	1.44±0.07	4.8±0.2
3.16±0.25	2.0	0.95	3.05±0.09	3.1±0.2
Aulacoseira frustule		-		1.62 ± 0.03

†Data provided by the manufacturer (Bangs Laboratories Inc.)

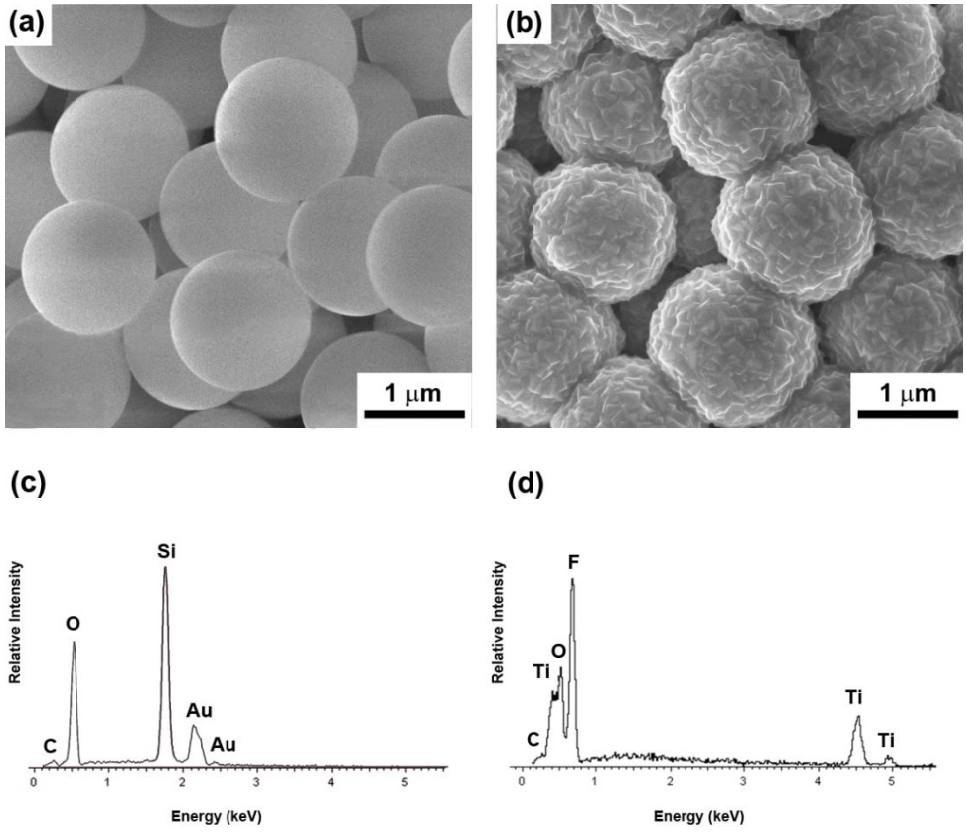

Figure 8.2: Secondary electron images and EDX analyses of (a), (c) amorphous silica spheres (1.44 μm diameter) prior to reaction with TiF_4(g) and (b), (d) after complete reaction with TiF_4(g) at 200°C for 8 h. The gold peaks in (c) originated from the coating applied to the sample in order to minimize charging.

8.4.1 HTXRD Results

A representative HTXRD analysis, obtained during the reaction of 0.6 μm diameter amorphous silica sphere specimens with TiF_4 gas generated from a solid TiF_4 source, is shown in Figure 8.3. Distinct diffraction peaks for $TiOF_2$ started to appear in the first scan and increased in intensity with further reaction time. In a typical experiment, the first few scans were conducted in a limited 2θ range ($21° \leq 2\theta \leq 27°$) so that a shorter scan time (about 20 s) could be achieved while maintaining a high signal-to-noise ratio. The initial short scan time could capture fast reaction dynamics at the beginning of reaction that might otherwise be missed if longer scan times were initially used. The relatively constant intensity alumina diffraction peaks, which were used as standards, are also visible in Figure 8.3. An aluminum peak, due to diffraction from the chamber windows, was also detected.

A typical $TiOF_2$ peak area evolution plot (the extent of reaction of the silica spheres) is shown in Figure 8.4. The extent of reaction was characterized by a relatively fast initial rate of reaction and then, as time went by, the rate of reaction gradually decreased and became relatively constant until the reaction reached completion. For example, at 180°C, (Figure 8.4), the initial high rate of reaction continued until the reaction time reached about 4000 seconds, after which the slope then gradually decreased and eventually became constant. Most of the reaction occurred during the initial kinetic regime, especially for the higher reaction temperatures. At 230°C and 260°C, more than 70% of the silica was consumed in less than 1500 seconds.

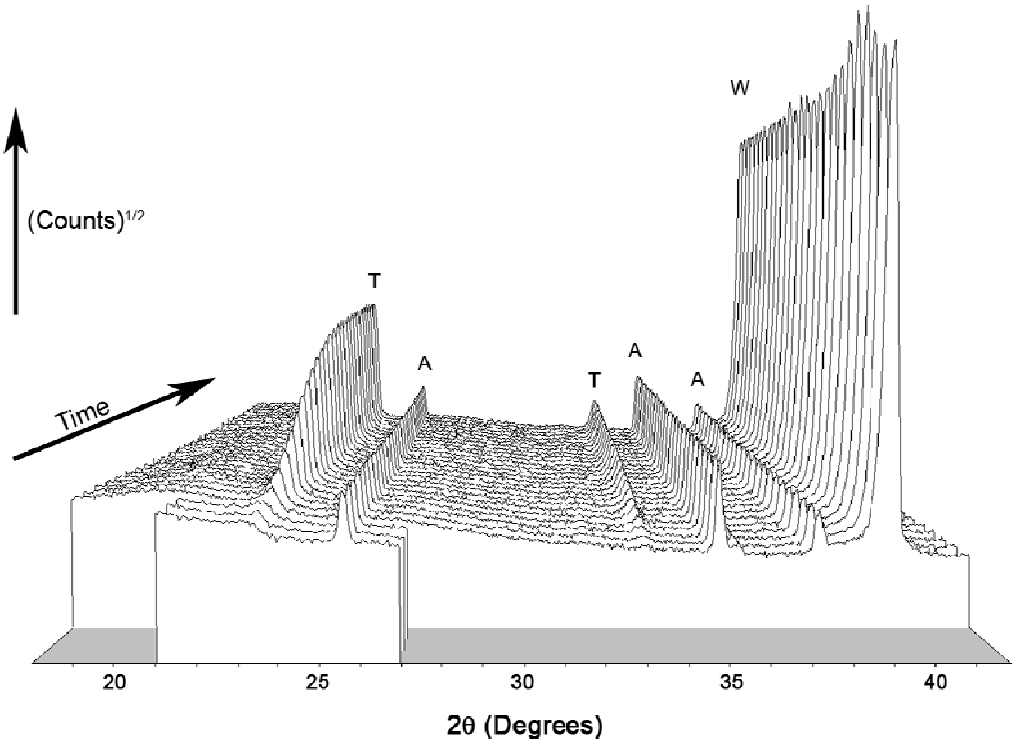

Figure 8.3: Selected isothermal plots of HTXRD scans of 0.59 μm SiO_2(s) spheres reacted with TiF_4(g) at 180°C. In this plot, the time interval between selected scans is 7 minutes. In a typical run, the first 30 scans were performed at a shorter 2θ range to minimize the time required between two consecutive scans. (T = $TiOF_2$, A = Al_2O_3, W = aluminum window)

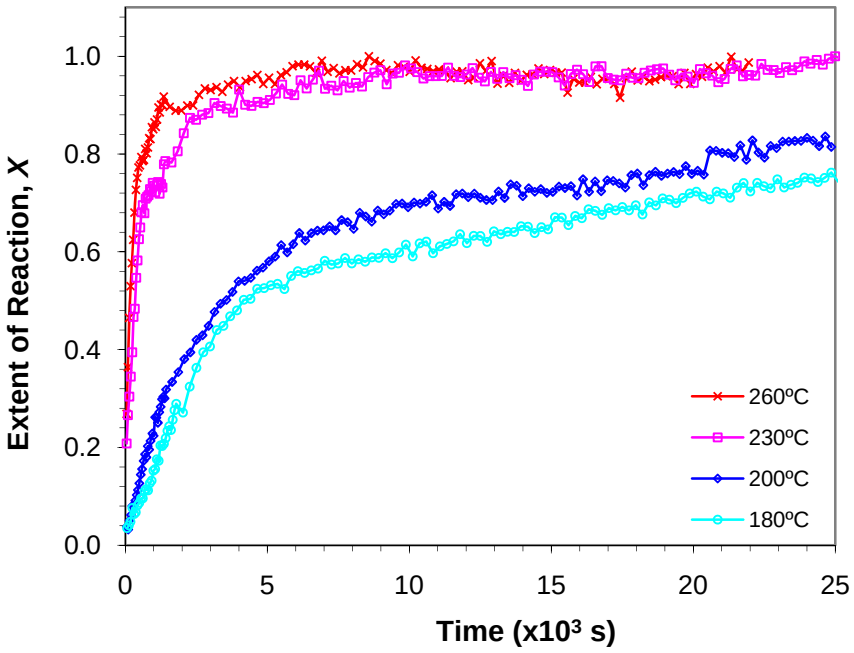

Figure 8.4: Reaction progress of 1.44 μm SiO_2(s) spheres with TiF_4(g) at different temperatures ranging from 180 to 260°C.

8.4.2 Microstructure Evolution

The TEM analyses of microstructural evolution of the 1.44 μm spheres before and after reaction with TiF_4(g) at 230°C for various reaction times are shown in Figure 8.5 and Figure 8.6 at lower and higher magnification, respectively. The starting silica spheres appeared dense and the sphere surfaces appeared to be relatively smooth (Figure 8.6a). The SAED analyses of the starting silica (Figure 8.7a) yielded typical patterns for amorphous materials (i.e., distinct diffraction spots or rings were absent). After 10 min of reaction, crystals on the order of 50 to 100 nm appeared on the sphere surfaces (Figure 8.5b). The SAED analysis on the crystals (Figure 8.7b) shows single crystal patterns with d-spacing that corresponds to the most intense (012) reflection of hexagonal $TiOF_2$. With increasing reaction time, the size and number of $TiOF_2$ crystallites increased so that the neighboring particles eventually coalesced and covered the surface of the spheres. Such surface covering on the spheres can be seen in the TEM image in Figure 8.5c for the 40 min, 230°C sample. The SAED analyses in Figure 8.7c, which was obtained from the outer product layer of the sphere, matched with the allowed reflections for the $TiOF_2$ hexagonal structure. In the other hand, SAED analyses obtained from the core of this sphere (not shown) were similar to SAED analyses obtained from the starting amorphous sphere which indicated that $TiOF_2$ crystals formed only on the surface of the sphere at this stage of reaction. Such complete surface coverage by $TiOF_2$ crystallites was coincidental with the reduction of the overall reaction rate (see Figure 8.4). The compact layer of $TiOF_2$ crystallites apparently obstructed both the access of the gas reactant to SiO_2 and the escape of any gas product.

In contrast to the amorphous SAED pattern obtained from the unreacted core of the 40 min, 230°C sample, the SAED pattern obtained from the 80 min, 230°C sample of the same location (in the core of the sphere) reveals a definitive ring pattern of $TiOF_2$ (Figure 8.7d). These rings appeared to have a relatively uniform intensity along the ring

circumference, suggesting that the diffraction originated from a polycrystalline source. Indeed, the TEM image shown in Figure 8.5d reveals dark dots throughout the core of the sphere, which are fine crystals of $TiOF_2$. These fine $TiOF_2$ crystals (shown by arrow 2 in Figure 8.6d) were less than 10 nm in size. On the other hand, the SAED analyses of coarse crystals of $TiOF_2$ located in the outer layer of the sphere after 80 min reaction time at 230°C was similar to Figure 8.7c.

After 160 min of reaction time at 230°C, the number of $TiOF_2$ crystals inside the core of the spheres increased, while the thickness of the outer $TiOF_2$ layer remained approximately constant (Figure 8.5e). As shown by arrow 2 in Figure 8.6e, crystallites size up to 20 nm in size were found, which were larger than the crystallites detected in the core after 80 min at 230°C. SAED analysis of the core of the sphere (Figure 8.7e) yielded similar $TiOF_2$ diffraction rings as for the 80 min sample. After prolonged reaction time (24 h), the size of the $TiOF_2$ crystals inside the sphere increased, indicating grain coarsening. The higher magnification TEM image in Figure 8.7f shows that the $TiOF_2$ crystals located inside the sphere can be up to 40 nm in size after 24 h of reaction at 230°C. These crystals, however, were significantly smaller than the crystals formed on the surface of the spheres (> 100 nm).

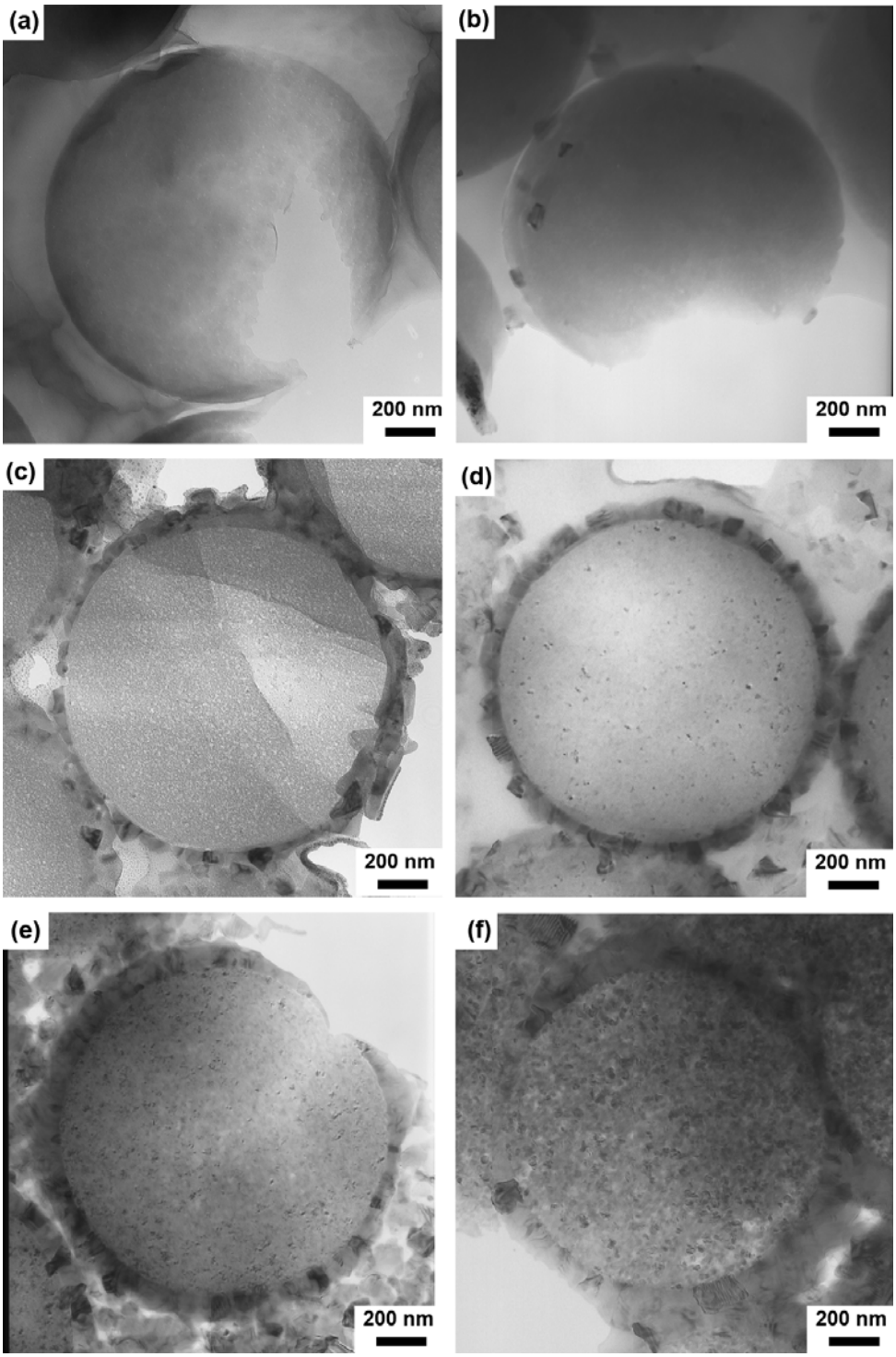

Figure 8.5: TEM images of cross-sections of: (a) an initial 1.44 μm diameter silica sphere and spheres exposed to TiF_4(g) at 230°C for (b) 10 m, (c) 40 m, (d) 80 m, (e) 160 m, and (f) 24 h.

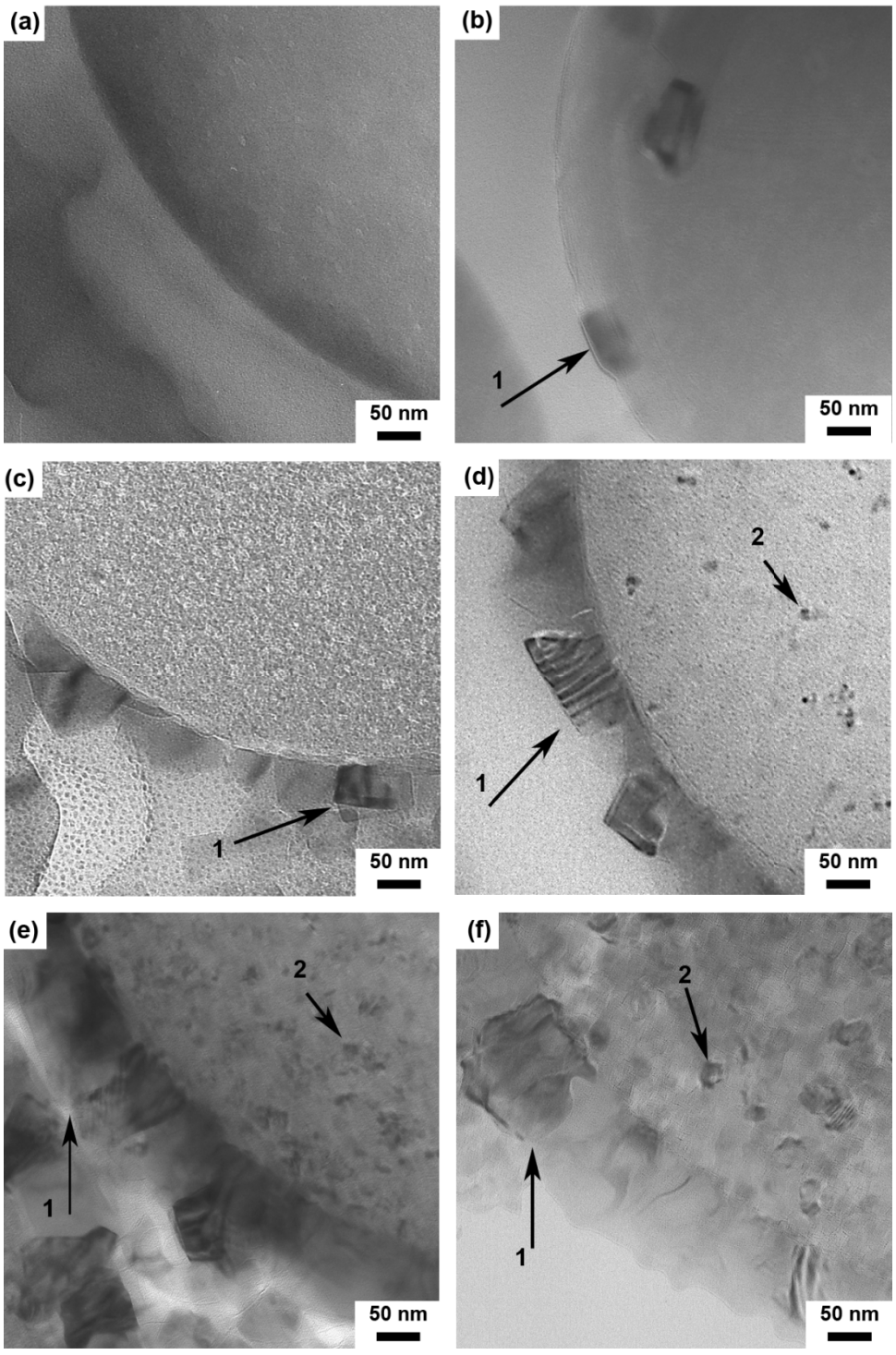

Figure 8.6: Corresponding higher magnification TEM images of the specimens shown in Figure 8.5. Locations 1 indicate $TiOF_2$ crystals formed on the surface of the sphere while locations 2 indicate the crystals formed inside the sphere. (a) The starting 1.44 μm diameter silica sphere, and spheres exposed to TiF_4(g) at 230°C for (b) 10 m, (c) 40 m, (d) 80 m, (e) 160 m, and (f) 24 h.

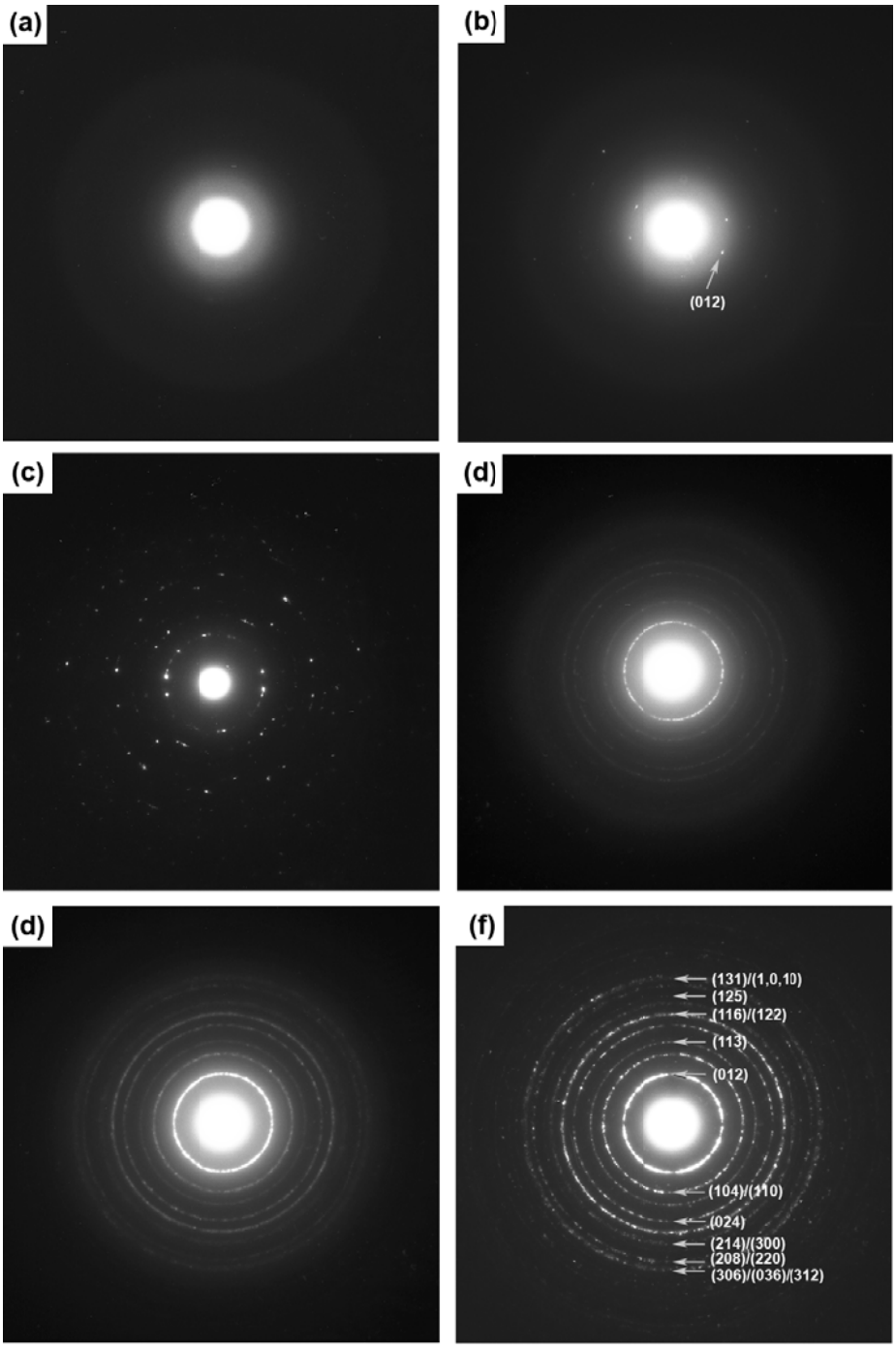

Figure 8.7: Selected area electron diffraction patterns obtained from the specimens shown in Figure 8.5. Pattern (a) shows the amorphous nature of the starting 1.44 μm diameter silica sphere, and the rest of the patterns were obtained from spheres exposed to TiF_4(g) at 230°C for (b) 10 m, (c) 40 m, (d) 80 m, (e) 160 m, and (f) 24 h. Patterns (b) and (c) were obtained from the $TiOF_2$ crystals located on the surface of the spheres, while patterns (d), (e), and (f) were obtained from center of spheres.

8.4.3 *Nitrogen Physisorption Analyses*

Nitrogen adsorption analyses indicated that the BET surface area of partially-reacted samples (shown in Figure 8.8) increased dramatically during the initial rapid kinetic regime. An increase in specific surface area of more than an order of magnitude was observed for 1.44 μm spheres at a temperature of 230°C after 10 minutes of reaction time (i.e., from 4.8 m^2/g to 146 m^2/g). After this initial period of increase at 230°C, the surface area plateaued and then decreased, and at the completion of reaction (within 24 h), it reached a value close to the initial surface area (4.7 m^2/g). The increase of surface area may be due to the contributions of (i) the formation of $TiOF_2$ crystals on the surface of spheres, (ii) an increase on SiO_2 sphere surface roughness, and (iii) the formation of pores inside SiO_2 sphere. The following discussion will assess the possibility of each contribution.

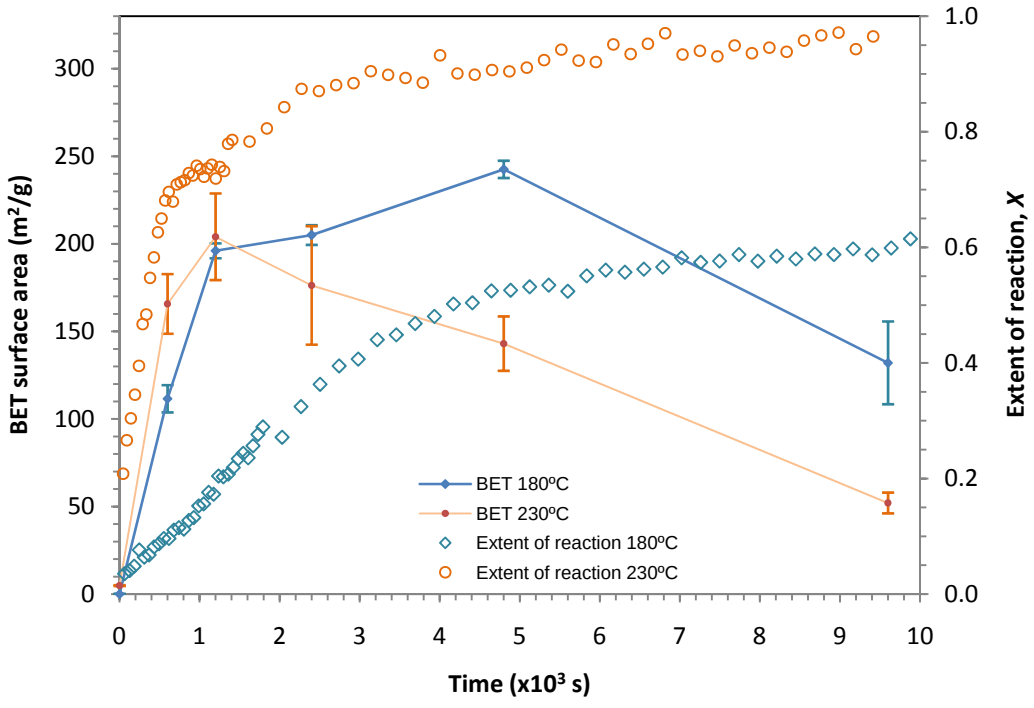

Figure 8.8: The evolution of specific surface area compared with the extent of reaction. (1.44 μm diameter spheres reacted at 180°C and at 230°C). The error bars on the BET surface area indicate the standard deviation of the measurements.

A similar surface area increase (from 13.1 m^2/g to 293 m^2/g) was reported by Khalil, et al., when fine titania particles were hydrolyzed and deposited onto Stöber silica surfaces[150]. However, the contribution of surface $TiOF_2$ crystals to the surface area increase may be insignificant. BET analyses indicate that the specific surface area had already increased by more than an order of magnitude (i.e., from 4.8 m^2/g to 166 m^2/g) only after 10 min of reaction at 230°C, when the number of surface $TiOF_2$ crystals was still relatively small (see Figure 8.5b). Indeed, if such a surface area increase was a result of surface $TiOF_2$ formation, then a large number of much smaller $TiOF_2$ crystals (i.e., in the order of 10 nm, as reported by Khalil et al.[150]) would have been required.

Examination of the sphere morphology evolution by electron microscopy may support the second explanation. The secondary electron images in Figure 8.9 show that the surface of a partially reacted sphere was not smooth. Beside $TiOF_2$ crystallites, the surface also featured crevices (or pores). Yet, such mechanism may have provided a trivial contribution to the observed surface area increase since, even after 40 min reaction time at 230°C, in which $TiOF_2$ crystals already covered the whole surface of the sphere (Figure 8.5c), the specific surface area was still relatively high (i.e., 176 m^2/g).

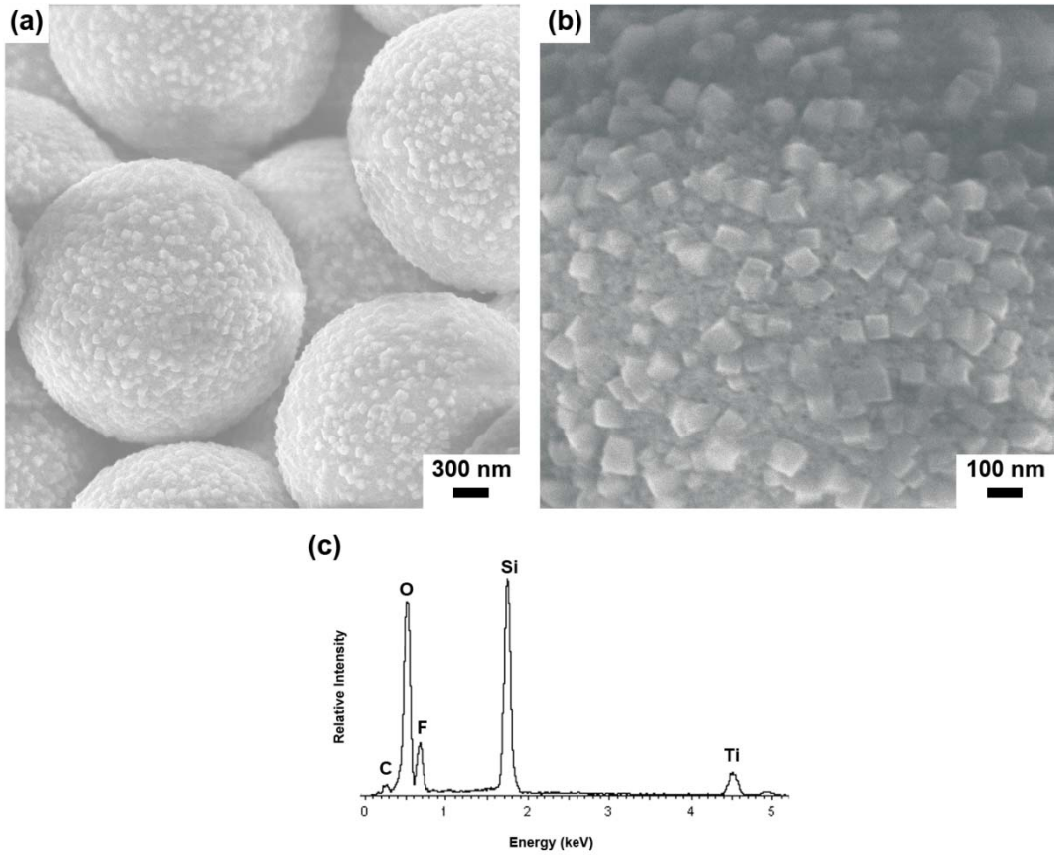

Figure 8.9: (a) Secondary electron image of partially reacted spheres, which reveals the formation of cubic $TiOF_2$ crystals on the sphere surfaces. Surface porosity indicated by black spots is also visible in the higher magnification image (b). An EDX analysis in (c) indicates that these spheres were still mainly composed of silica. (3.05 μm diameter spheres reacted at 180°C for 20 min).

The shape of the physisorption isotherm of the partially-reacted samples exhibited a mixture of type I (microporosity) and type IV (mesoporosity)[146]. An example of such an isotherm is shown in Figure 8.10, which exhibits an initial filling of micropores (pore size < 2 nm) at relative pressure < 0.1 and a multilayer filling of mesopores (pore size between 2 to 50 nm)[146] at relative pressure > 0.1. The steady rise of N_2 adsorption during the filling of mesopores took the larger part of the overall N_2 volume (>70%). The percent of porosity can be estimated by dividing the total amount of porosity (calculated from nitrogen physisorption analyses) by the total geometrical volume of the spheres (calculated from the number of spheres for a given batch and the diameter of the spheres from quantitative TEM image analyses). Such a calculation is presented in Table 8.2. The table shows that a significant amount of porosity developed (up to 31% - 1.7% = 29.3% using NLDFT method) during the reaction of 1.44 μm diameter spheres with TiF_4(g) at 230°C. Since the volume of the solid $TiOF_2$ layer was about 32% of the total volume of the sphere (assuming a layer thickness of 100 nm on the surface of a 1.44 μm diameter sphere), it is concluded that such a large percentage of porosity must have been located on the inside of the spheres (i.e., inside of the external $TiOF_2$ layer). Therefore, mechanism (iii) (i.e., porosity formation inside the spheres) was likely to be the major contributor to the observed surface area increase.

The later decrease of surface area could be attributed to the filling up of pores with solid $TiOF_2$ crystals. With increasing reaction time, the number of $TiOF_2$ crystallites formed in the core of the sphere increased, which could have resulted in pores filling and a decrease in the surface area. TEM images in Figure 8.6d-f reveal such $TiOF_2$ crystallite formation inside the sphere. As mentioned in the previous subchapter, the sizes of these crystals were less than 10 nm at 80 m reaction time, and less than 20 nm at 160 m reaction time, for 1.44 μm diameter spheres reacted at 230°C. Indeed, the sizes of these

$TiOF_2$ crystallites are within the same order of magnitude as the dimensions of pores indicated by the pore size distribution analyses in Figure 8.11.

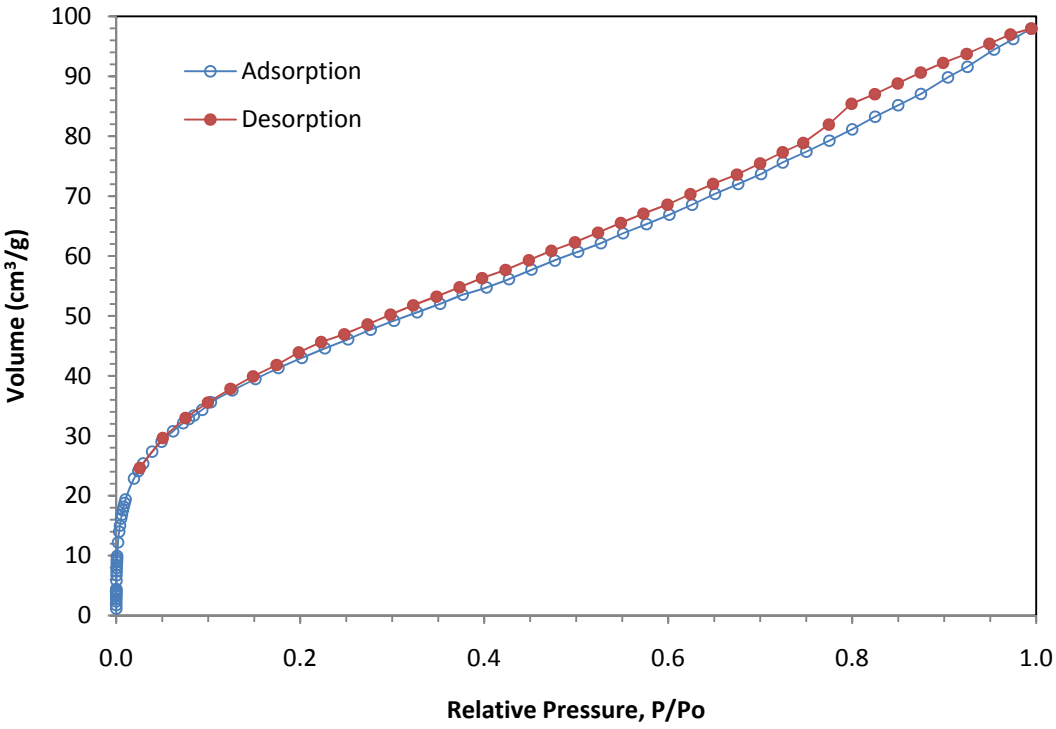

Figure 8.10: The physisorption isotherm curve obtained from a 1.44 μm diameter silica sphere reacted at 230°C for 80 min, which exhibited a mixture of type I (microporosity) and type IV (mesoporosity)[146]. The steady rise of N_2 adsorption at relative pressures > 0.1 indicated the multilayer filling of mesopores[146].

Table 8.2. Estimated percent of porosity for 1.44 μm diameter silica spheres reacted at 230°C. The BJH method was applied to the desorption branch of the nitrogen isotherm data, while the NLDFT method used both adsorption and desorption isotherms for fitting.

Time (min)	Number of 1.44 μm dia. spheres ($x10^9$)	Geometrical Volume† ($x10^{-3}$ cm^3)	NLDFT Method		BJH Method	
			Pore Volume ($x10^{-3}$ cm^3)	Porosity (%)	Pore Volume ($x10^{-3}$ cm^3)	Porosity (%)
0	62	97	1.7	1.7	4.2	4.4
10	7.8	12	2.4	19	2.8	23
40	8.7	16	4.9	31	6.0	37
80	8.5	17	4.4	25	5.1	30
160	8.6	21	2.6	12	2.9	14

†The total solid volume of the spheres were calculated based on the average outer diameter of the cross-section of the sphere at a given reaction time from quantitative TEM image analyses.

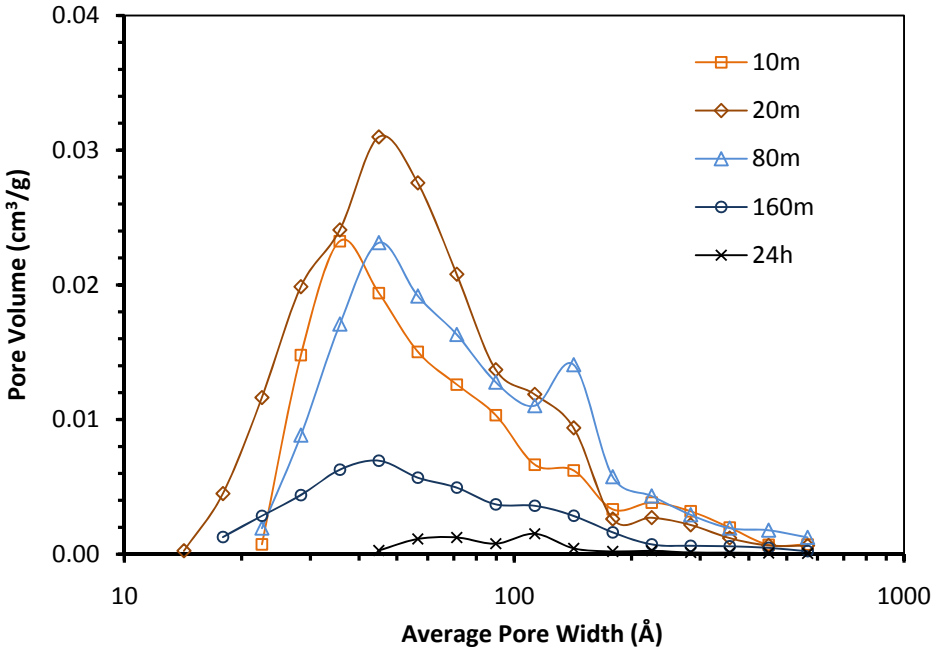

Figure 8.11: The evolution of pore size distribution (PSD) of 1.44 μm diameter spheres reacted at 230°C. The PSD was calculated from the nitrogen isotherm using NLDFT data reduction program in Autosorb-1 software by assuming cylindrical pore shape.

8.4.4 Reaction Mechanism

EDX analyses of fully converted ($TiOF_2$) spheres (Figure 8.2d) indicated the absence of silicon from these specimens. Vapor phase transport and loss of silica may have proceeded through the formation of volatile Si-O bearing species. $SiOF_2(g)$ and $Si_2OF_6(g)$ are two possible volatile Si-O-F bearing gas species[45,151]. Thermodynamic analyses indicate that that the following equilibrium reaction should strongly favor the formation of $Si_2OF_6(g)$ over $SiOF_2(g)$ at temperature below 827°C. According to Shinmei, *et al*. the equilibrium $p(SiOF_2)/p(Si_2OF_6)$ associated with the following reaction ranges from 1.3×10^{-48} at 25°C to 1.3×10^{-7} at 827°C[151].

$$Si_2OF_6(g) = SiOF_2(g) + SiF_4(g) \quad (14)$$

For the silica spheres reacted with $TiF_4(g)$ at 350°C for 4 h, the mass of the $TiOF_2$ product was 127±12% larger than the starting mass of the silica. This mass increase is closest to the mass increase indicated by reaction equation (2), supporting the above analyses that $Si_2OF_6(g)$ may be the predominant byproduct during $TiOF_2$ formation (The theoretical mass increases of reactions (1), (2), and (3) are 240%, 105%, and 70%, respectively).

If $Si_2OF_6(g)$ was the predominant volatile Si-O-bearing gas species formed from the SiO_2 spheres within the sealed reaction chamber, then the formation of an external $TiOF_2$ layer and the formation of porosity (and the increase in surface area) may be explained by one or a combination of the following mechanisms: (a) through direct vaporization of SiO_2, and (b) through the formation of intermediate $Si_2OF_6(g)$. These mechanisms will be elaborated in the following paragraphs.

In the first mechanism, the formation of an intermediate $Si_2OF_6(g)$ within the sphere may proceed according to the following reaction (the same equation as equation (2)):

$$3/2TiF_4(g) + SiO_2(s) \Rightarrow 3/2TiOF_2(s) + ½\ Si_2OF_6(g) \quad (15)$$

The volume of 1.5 moles of $TiOF_2$ is 71% larger than the volume of 1 mole of amorphous silica (49.5 cm^3/mole versus 29 cm^3/mole[152]). At the start of the reaction, when the $TiOF_2$ crystals were still relatively small (< 100 nm) and did not continuously cover the sphere surface, $Si_2OF_6(g)$ may have diffused away from the outer surface of the spheres and reacted with $TiF_4(g)$ according to the following reaction:

$$Si_2OF_6(g) + TiF_4(g) \Rightarrow TiOF_2(s) + 2SiF_4(g) \quad (16)$$

Under certain conditions, such as perhaps at a relatively high temperature, the $Si_2OF_6(g)$ species may have had a significantly longer mean free path before it collided and reacted with $TiF_4(g)$ to form $TiOF_2(s)$, so that the formation of some $TiOF_2(s)$ may have occurred at locations far away from the original sphere surface. This condition is analogous to the formation of $ZrOF_2$ away from the location of the diatom frustule surface discussed in Chapter 2.

The second mechanism may have proceeded through the following reaction:

$$3/2SiF_4(g) + 1/2SiO_2(s) \Rightarrow Si_2OF_6(g) \quad (17)$$

The equilibrium reaction constant, $p°(Si_2OF_6)/\ p°(SiF_4)^{3/2}$, for the above reaction (assuming unit activities for pure condensed phase reactants) is 0.19 and 0.097 at 150 and

250°C, respectively[45]. In this reaction, the source of $SiF_4(g)$ was from the aforementioned reaction 1. This volatile $Si_2OF_6(g)$ may diffuse away from the location it formed within the sphere, leaving porosity behind. $Si_2OF_6(g)$ could then react with $TiF_4(g)$ according to reaction (16) to form $TiOF_2(s)$ on the surface of the spheres.

In the proposed mechanisms above, the formation of one solid product, namely $TiOF_2$, was assumed. This assumption was supported by the lack of evidence for other solid reaction products beside $TiOF_2$ during the course of reaction, from both the real-time XRD analyses (i.e., bulk analyses) and the SAED analyses inside the partially reacted spheres (i.e., local analyses). Background noise, especially in XRD analyses, however, may obscure the existence of an intermediate solid phase, especially if it was amorphous and/or only present in a small quantity (e.g., less than 1%) at any given time.

The first reaction mechanism involves the formation of $TiOF_2(s)$ (as indicated by equation 15), inside the silica sphere. Since SAED analyses of the spheres reacted at 230°C for 10 min and for 40 min revealed no indication of any crystalline phase present inside the spheres, the second reaction mechanism (i.e., direct vaporization of silica via reaction with $SiF_4(g)$ formed by reaction (1)) was more likely operative than the first.

8.4.5 *Modeling of HTXRD Kinetic Data*

Based on the microstructural evolution discussed in the previous section, a change in the mechanism controlling the reaction with time is surmised; i.e., the rate was controlled by a faster kinetics at short times during $TiOF_2$ formation on the surface of the spheres and then a slower controlling mechanism took place during $TiOF_2$ formation inside the spheres. Such a change in mechanism was substantiated by the fact that none of the SCM equations was not able to fit the data over the entire reaction time. Thus, the conversion data could be divided into two kinetic regimes as illustrated in Figure 8.12.

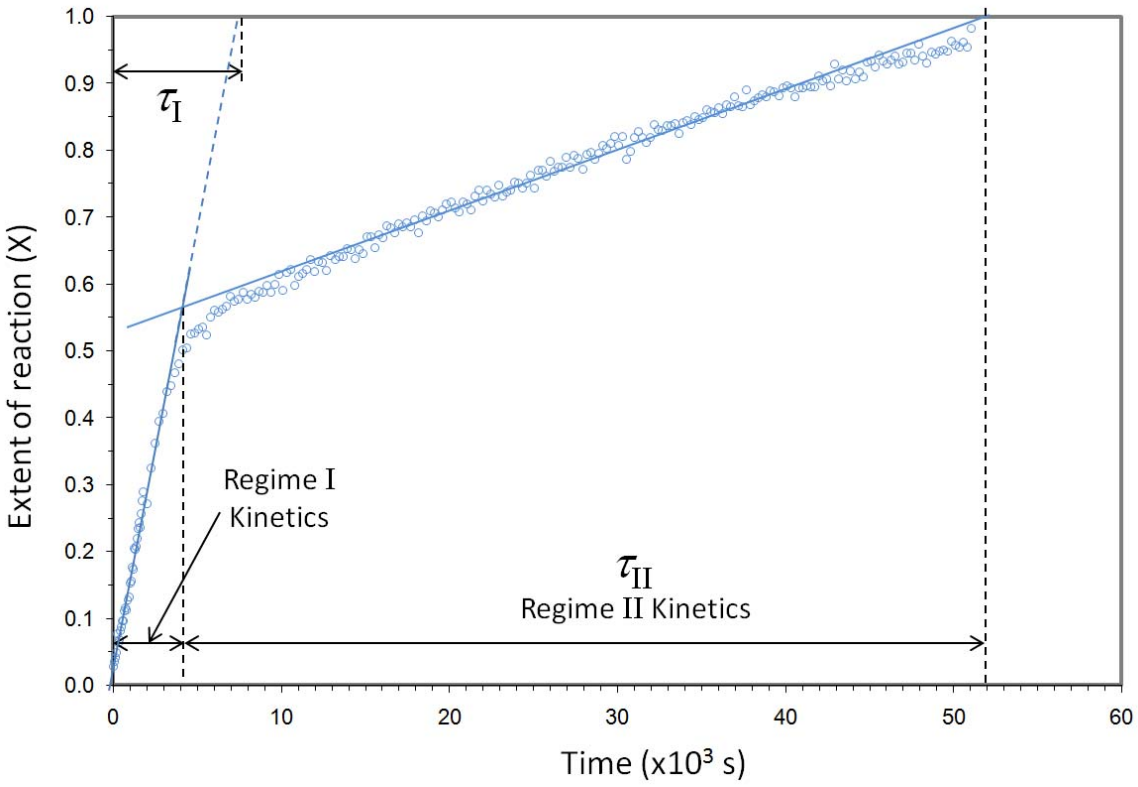

Figure 8.12: Illustration of the two kinetic regimes for the HTXRD conversion data of the spheres. The circles indicate the reaction progress at a given time for the reaction of 1.44 μm silica spheres with TiF_4(g) at 180°C.

8.4.5.1 Kinetic Regime I

Figure 8.13 reveals fits of the extent of reaction data of 0.6 μm silica spheres at 230°C to three possible models for different rate controlling mechanisms according to the shrinking core model for a spherical sample. As seen in this figure, the correlation factor for chemical reaction control ($R^2 = 0.997$) model was the best among the three, although only by a small margin compared to the correlation factor for gas phase diffusion control ($R^2 = 0.967$) or solid state diffusion control ($R^2 = 0.965$). To confirm that chemical reaction control was the rate limiting step, the possibility of other rate limiting steps will be discussed below.

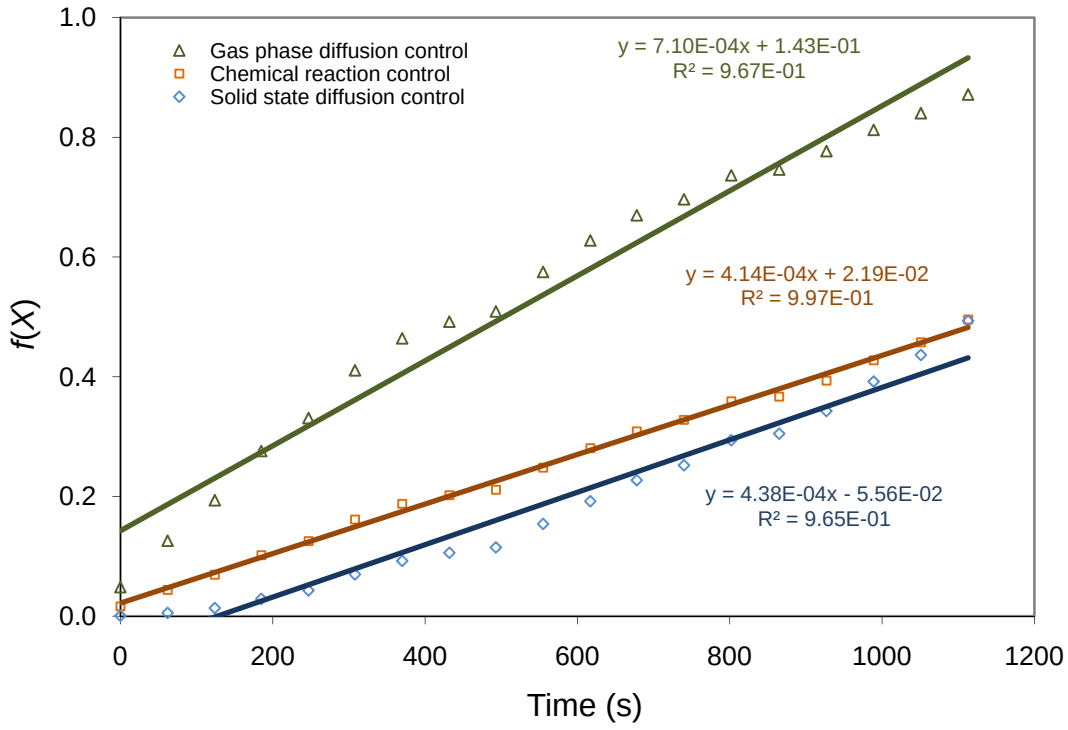

Figure 8.13: Plots of the extent of reaction with time for three possible rate limiting steps in the shrinking core model for the reaction of 0.59 μm SiO_2(s) spheres with TiF_4(g) at 230°C. Note: $f(X) = X$ for gas diffusion control, $f(X) = 1 - (1-X)^{1/3}$ for chemical reaction control; and $f(X) = 1 - 3(1-X)^{2/3} + 2(1-X)$ for solid state diffusion control; where X is the extent of reaction.

Solid state diffusion may have been the rate limiting step if a continuous and dense product layer was developed on the surface of the reacting solid. This solid product layer acted as a mass transport barrier for the reacting gas (TiF_4) to reach the reacting solid SiO_2 and also for the gaseous byproduct (e.g., SiF_4) to escape from the reaction site. A relatively slow solid state diffusion path may be bypassed by much faster gas diffusion path when the product layer was sparse. As shown by the microstructural evolution discussion in the previous section, there was no indication of the formation of continuous and dense $TiOF_2$ product layer on the surface of the sphere during the initial kinetic regime, suggesting that solid state diffusion control was least likely to be the rate controlling step.

In gas phase diffusion control, the consumption of gaseous reactant during the reaction was assumed to be sufficiently fast, that a concentration boundary layer developed in the gas phase. This boundary layer is characterized by a concentration gradient of the reacting gas species, whose value is assumed become constant with time. During HTXRD analyses, the thickness of the silica sphere bed was significantly smaller than the distance between the sphere bed and the solid TiF_4 source (0.1 mm vs. 5 mm), that all silica spheres may be assumed to react at the same rate. If the bed of silica spheres reacted at a faster rate than the rate of mass transfer of TiF_4, then a concentration gradient may have developed between the surface of the spheres and the source of TiF_4(g). In such a condition, mass transfer of TiF_4(g) through the concentration gradient of constant thickness could be the rate limiting step of the overall observed reaction rate. The possibility of gas phase diffusion control can be examined by comparing the value of the mass transfer coefficient, k_g, derived from the gas phase diffusion control (equation 6) in the SCM, and the value of k_g derived from the diffusion coefficient of TiF_4 in argon. If the k_g values from both calculations are similar, the gas phase diffusion rate control may be considered as a rate limiting step.

Assuming that the diffusion in gas phase is the rate limiting step, the slope of the conversion curve in Figure 8.13 is related to the mass transfer coefficient of gaseous phase (k_g) according to the following equation (recalling equation (6)):

$$\frac{1}{Slope} = \tau_{film} = \frac{\rho_{SiO_2} R_{sphere}}{3bk_g C_{TiF_4(g)}}$$

For the TiF_4 – SiO_2 system at 230°C (503 K):

$$C_{TiF_4(g)} = \left(\frac{n}{V}\right)_{TiF_4(g)} \approx \frac{P_{TiF_4(g)}}{RT} = \frac{1.27\times10^4}{8.314\times503} = 3.04 \text{ mole/m}^3$$

$$\rho_{SiO_2} = 1.96\times10^3 \text{ kg/m}^3 = 3.27\times10^4 \text{ mole/m}^3$$

$$R_{sphere} = 295 \text{ nm} \approx 3\times10^{-7} \text{ m}$$

$$\text{Slope} = 7.10\times10^{-4} \text{ s}^{-1}$$

Thus,

$$k_g = \frac{3.27\cdot10^4 \times 3\cdot10^{-7} \times 7.10\cdot10^{-4}}{3\times3.04} = 7.6\times10^{-7} \text{ m/s}$$

The diffusion coefficient of TiF_4(g) in argon, assuming both nonpolar and nonreacting molecules, can be calculated by using the following equation[153]:

$$D_{AB} = \frac{0.001858T^{3/2}\left[\frac{1}{M_A} + \frac{1}{M_B}\right]^{1/2}}{P\sigma_{AB}^2\Omega_D} \qquad (18)$$

where D_{AB} is the diffusion coefficient of A in B, in cm^2/s; T is the absolute temperature, in K; M_A, M_B are the molecular weights of A and B, respectively; P is the absolute pressure, in atmospheres; σ_{AB} is the "collision diameter," a Lennard-Jones parameter, in Å; and Ω_D is the "collision integral" for molecular diffusion, dimensionless number as a function of $\kappa T/\varepsilon_{AB}$; κ is the Boltzmann constant, which is 1.38×10^{-16} ergs/K; and ε_{AB} is the energy of molecular interaction for the binary system A and B, a Lennard-Jones parameter, in ergs.

For argon, the values of σ and ε_A/κ, are 3.418 Å and 124 K, respectively[153]. As of the time of writing, there is no published data for the Lennard-Jones parameters of TiF_4(g), however, the parameters may be estimated from similar molecules (i.e., same coordination number and comparable atomic radii), such as SiH_4 and $SiCl_4$. Since for SiH_4, σ and ε_A/κ, are 4.08 Å and 207.6 K, respectively, and for $SiCl_4$, σ and ε_A/κ, are 5.08 Å and 358 K, respectively, the σ and ε_A/κ values of TiF_4, by taking the average of that of SiH_4 and $SiCl_4$, are estimated to be ~4.5 Å and ~280 K, respectively. Thus,

$$\sigma_{AB} = \frac{\sigma_A + \sigma_B}{2} = \frac{3.418 + 4.5}{2} = 3.9 \text{ Å}$$

$$\varepsilon_{AB}/\kappa = \sqrt{(\varepsilon_A/\kappa)(\varepsilon_B/\kappa)} = \sqrt{124\times280} = 186 \text{ K}$$

At condition, T = 230°C = 503 K and P = 1 atm:

$$\frac{\varepsilon_{AB}}{\kappa T} = \frac{186}{503} = 0.37 \Rightarrow \frac{\kappa T}{\varepsilon_{AB}} = 2.7$$

By using the function table of Ω_D from Welty[153]:

$$\Omega_D = f\left(\frac{\kappa T}{\varepsilon_{AB}}\right) = f(2.7) = 0.98$$

Since $M_{TiF4} = 124$ and $M_{Ar} = 40$, then:

$$D_{AB} = \frac{0.001858 \times 503^{3/2} \times \left[\frac{1}{40} + \frac{1}{124}\right]^{1/2}}{1 \times 3.9^2 \times 0.98} = 0.26 \text{ cm}^2/\text{s} = 2.6 \times 10^{-5} \text{ m}^2/\text{s}$$

In the case of a sphere, the mass transfer coefficient, k_g, is related to the gas diffusion coefficient, D_g, by the following expression[137]:

$$Sh = \frac{d_p k_g}{D_g} \tag{19}$$

where d_p is the sphere diameter and Sh is the Sherwood number. The Sherwood number is typically written in the sum of molecular diffusion and forced convection contributions as[153]:

$$Sh = Sh_o + C\,\mathrm{Re}^m\, Sc^{1/3} \tag{20}$$

where C and m are correlating constants, Re, and Sc are the Reynolds number and the Schmidt number, respectively. If there is no forced convection, then the Sherwood number is 2 (i.e., $Sh = Sh_o = 2$)[153]. Thus, the mass transfer coefficient of TiF_4(g) for the case of 0.59 μm sphere is:

$$k_g = \frac{Sh \cdot D_g}{d_p} = \frac{2 \times 2.6 \cdot 10^{-5}}{0.59 \cdot 10^{-6}} = 88 \text{ m/s}$$

As can be seen, the mass transfer coefficient from the theoretical calculation is significantly larger than the mass transfer coefficient from the assumed kinetic calculation (i.e., 88 m/s >> 7.6×10^{-7} m/s). Such a large k_g difference led to a conclusion that the gas phase diffusion between the sphere bed and TiF_4 gas source was not the rate limiting step for the condition of the experiment performed in this work.

The above analyses may not be an accurate description of the actual dynamics during the HTXRD kinetics measurement because equation (19) only considers the case of a single sphere. For a packed bed of sphere, the tortuosity of the gas path for the spheres located below the top layer may significantly affect the mass transfer of the gaseous reactant/byproduct. In this condition, the concentration gradient may have been developed *within* the bed (i.e., from the top to the bottom of the bed), instead being developed on the transport path between the bed and the gas source. A more precise description of the bed may require a calculation of the second Damköhler number, which compares the time scale of the chemical reaction rate with the time scale of the mass transfer rate in the absence of convection[154]:

$$Da_{II} = \frac{kC^{n-1}}{k_g a} \tag{21}$$

where k is the chemical reaction rate, n is the reaction order, and a is the interfacial area. If the second Damköhler number is greater than 1 (i.e., the time scale for mass transport rate is smaller than the time scale for chemical reaction rate), the gas phase diffusion within the bed may be the rate limiting step. For TiF_4(g)-SiO_2(s) reaction system, the value of k, which is measured in the absence of mass transfer limit, however, is not available in literature at this moment. Nonetheless, since the effective penetration depth of x-ray was less than 53 μm (see Appendix D), the above conclusion may still valid because HTXRD analyses mostly probed the spheres located on the top layers where the gas diffusion path was minimally affected by the bed tortuosity.

After both solid state diffusion control and gas phase diffusion control were ruled out, thus, the equation for chemical reaction control (Equation 9) was applied to the conversion data for short reaction times (kinetic regime I). The result of such fitting is shown in Figure 8.16a, Figure 8.17a, and Figure 8.18a for the conversion data of 0.59 μm, 1.44 μm, and 3.05 μm spheres, respectively from 180 to 260°C. As seen in those figures, the correlation factors for the fitting to the conversion data are quite high, i.e., R^2 values ranged from 0.966 to 0.997 for all samples under these conditions.

8.4.5.2 Kinetic Regime II

Based on the microstructural evolution discussed in the previous sections, the kinetic regime II was marked by the existence of continuous and dense solid $TiOF_2$ product layer. Such a continuous and dense $TiOF_2$ layer played a role as a diffusion barrier for both gaseous reactant and gaseous product, indicating that mass transport may be the rate limiting control. This rate-limiting mass transport may have been attained through several possible mechanisms such as solid-state diffusion through the $TiOF_2$ lattice, solid-state diffusion along grain boundaries or dislocations in $TiOF_2$, gas phase diffusion through pore channels in the $TiOF_2$, and diffusion along the $TiOF_2$/gas surfaces of the pore channels. The exact mass transport mechanism may be assessed if the effective diffusion coefficient could be derived from the kinetics data and then compare this values to the typical diffusion coefficient values for a similar system. The analytical equation of mass transport control in regime II will be derived in the next page.

Beside mass transport control, the rate controlling mechanism in the kinetic regime II may be caused by a relatively slower chemical reaction at the $TiOF_2/SiO_2$ interface (as opposed to the chemical reaction control at gas/SiO_2 interface in the kinetic regime I). This slow chemical reaction was hinted by the formation of relatively smaller size of $TiOF_2$ crystals within the silica spheres. The equation for chemical reaction control (equation 9), however, cannot be used to model the conversion data in regime II because $TiOF_2$ crystals were formed in homogenous manner within the spheres.

The equation for solid-state diffusion control (Equation 7), however, is not suitable to model the conversion data in regime II because the solid product layer thickness was approximately constant in this kinetic regime. Figure 8.14 presents a quantitative analyses of the TEM images of 1.44 μm silica spheres reacted with TiF_4(g) at 230°C. As can be seen from the figure, the $TiOF_2$ layer thickness was relatively constant in the kinetic regime II (within the measurement error). In the shrinking core model, the thickness of the solid product layer increases with increasing reaction time, until it reached the initial radius of the initial sphere. Thus, a different model is needed to accommodate the constant product layer thickness.

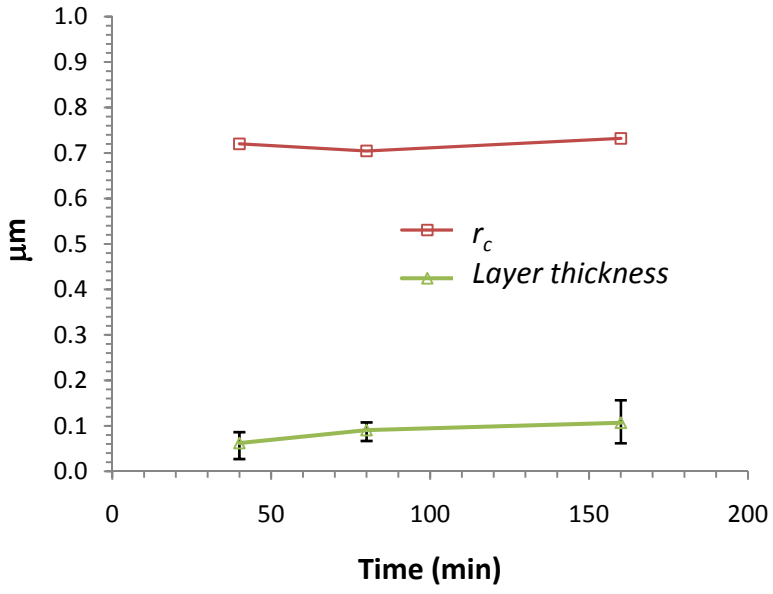

Figure 8.14: Plots of the outer solid $TiOF_2$ layer thickness and the inner core radius, r_c, with time for 1.44 μm diameter silica spheres exposed to TiF_4(g) at 230°C. Error bars indicate the maximum and the minimum measured dimension from quantitative TEM images analyses.

Figure 8.15 illustrates the condition of a sphere in the kinetic regime II. The lower part of the image shows the TiF_4(g) concentration profile outside and throughout the reacting sphere. The reactant gas concentration, C_{Ac}, at the interface between SiO_2 and the $TiOF_2$ layer may have not been zero. A zero concentration for the gas reactant on the reacting interface (or at the interface between the product layer and unreacted core) implies a sufficiently fast reaction process that all of the reactant gas was essentially consumed at the reacting interface at any given time and that the resulting product will form at nearest distance to the gas source (i.e., at the interface). However, TEM images (Figure 8.5) show a uniform formation of $TiOF_2$ throughout the silica core. This uniform internal $TiOF_2$ formation suggests that once TiF_4 reaches SiO_2/$TiOF_2$ interface, the TiF_4 can then rapidly diffuse through the interconnected pores and react at SiO_2/pore surfaces

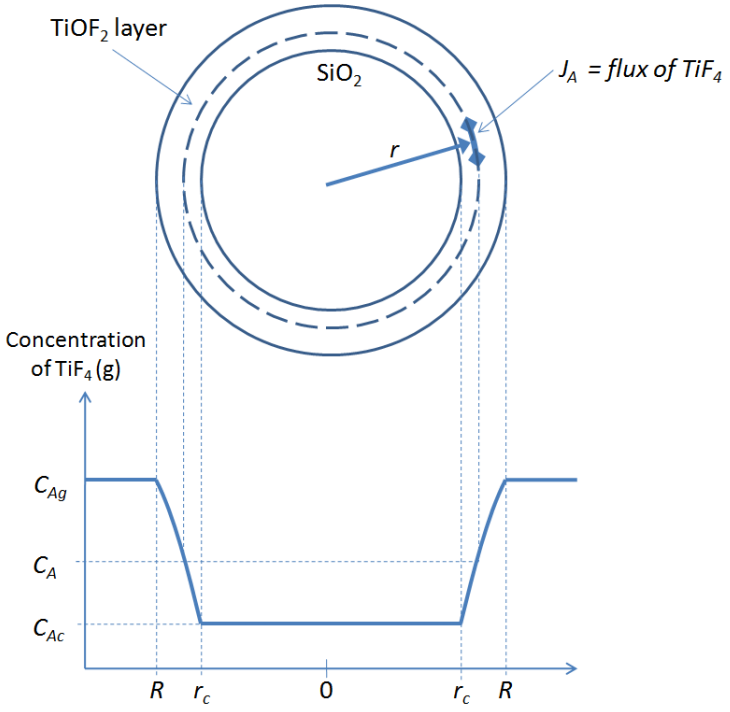

Figure 8.15: Illustration of a reacting sphere in the regime II when diffusion through solid $TiOF_2$ is the controlling rate.

throughout the core of the sphere. The availability of interconnected pores as a means for internal TiF_4 gas diffusion is supported by the nitrogen physisorption data (i.e., the amount of porosity was in the excess of 19% from 10 - 160 min of reaction at 230°C as shown in Table 8.2). This condition is contrast with a dense unreacted core assumed in the SCM, where the gas concentration at the reaction front and inside the unreacted core is assumed to be zero[137].

Assuming a steady-state condition, the rate of reaction of TiF_4 at any instant in kinetic regime II is proportional to its flux through the solid $TiOF_2$ layer[137]:

$$-\frac{dN_A}{dt} = 4\pi r^2 J_A \tag{22}$$

where N_A is the number of moles of TiF_4 molecules at the reaction front, r is radius of the analyzed surface in the $TiOF_2$ layer, and J_A is the molar flux of TiF_4 within the solid $TiOF_2$ layer. The right side of the equation indicates a molar flux of species A diffusing through the surface ($4\pi r^2$) of the sphere. Assuming equimolar counterdiffusion (as in the reaction equation (1)), J_A can be expressed by Fick's law:

$$J_A = D_e \frac{dC_A}{dr} \tag{23}$$

where D_e is the effective diffusion coefficient of TiF_4 in solid $TiOF_2$. The exact mechanism on how TiF_4 species move through solid $TiOF_2$ layer, however, is not known. Combining equations (22) and (23):

$$-\frac{dN_A}{dt} = 4\pi r^2 D_e \frac{dC_A}{dr} \tag{24}$$

By rearranging and integrating across the layer of solid $TiOF_2$ (i.e., from R to r_c and $C_A = C_{Ag}$ at R and $C_A = C_{Ac}$ at r_c):

$$-\frac{dN_A}{dt}\int_R^{r_c}\frac{dr}{r^2} = 4\pi D_e \int_{C_{Ag}}^{C_{Ac}} dC_A \tag{25}$$

$$-\frac{dN_A}{dt}\left(\frac{1}{r_c}-\frac{1}{R}\right) = 4\pi D_e\left(C_{Ag}-C_{Ac}\right) \tag{26}$$

By using the relation $-dN_B = -bdN_A$ (according to Equation (4)), and since $\overline{R}$ and $\overline{r_c}$ were constant in regime II (Figure 8.14), the above equation can be rearranged and integrated to get the time dependence:

$$-\left(\frac{1}{r_c}-\frac{1}{R}\right)\int_{N_{Bo}}^{N_{Bt}} dN_B = 4b\pi D_e\left(C_{Ag}-C_{Ac}\right)\int_0^t dt \tag{27}$$

$$-\left(\frac{1}{r_c}-\frac{1}{R}\right)\left(N_{Bt}-N_{Bo}\right) = 4b\pi D_e\left(C_{Ag}-C_{Ac}\right)t \tag{28}$$

where N_{Bt} and N_{Bo} are the moles of SiO_2 at time t and at t=0 (started regime II), respectively. By writing the extent of reaction as

$$X = 1-\frac{N_{Bt}}{N_{Bo}} \tag{29}$$

$$\Rightarrow N_{Bt}-N_{Bo} = -N_{Bo}X = -\rho_B V_{Bo}X = -\frac{4}{3}\pi r_c^3 \rho_B X \tag{30}$$

and substituting this equation into the equation above, the following equation is obtained:

$$\frac{t}{\tau_D} = X \tag{31}$$

$$\tau_D = \frac{\rho_B r_c^3}{3bD_e\left(C_{Ag} - C_{Ac}\right)}\left(\frac{1}{r_c} - \frac{1}{R}\right) = \frac{\rho_B r_c^2 \left(R - r_c\right)}{3bD_e R\left(C_{Ag} - C_{Ac}\right)} \tag{32}$$

where τ_D is the time for complete conversion of the sphere in regime II (see Figure 8.12). According to this equation, X should increase linearly with time, t. The results of such fitting are shown in Figure 8.16b, Figure 8.17b, and Figure 8.18b for the conversion data of 0.59 μm, 1.44 μm, and 3.05 μm spheres, respectively, at 180 - 260°C. As seen in those figures, the correlation factor, R^2, for the fitting of the model to the conversion data are fairly good, ranging from 0.799 to 0.997 for all sample conditions.

In order to calculate intrinsic reaction parameters, such as D_e, several reaction variables need to be known. While r_c and R have been directly measured by TEM analyses of cross sections of the partially-reacted spheres, other variables in equation (32), such as C_{Ac} may not be directly available or be precisely estimated. Such a lack of complete information prevents accurate calculation of D_e. However, the estimated minimum value of De can be calculated if the chemical driving force, ($C_{Ag} - C_{Ac}$), is set to maximum, i.e., $C_{Ac} = 0$. For 1.44 μm diameter spheres reacted at 230°C shown in Figure 8.5: $r_c \approx 0.7$ μm, $R \approx 0.8$ μm, $\rho_{SiO_2} = 3.27\times10^4$ mole/m^3, $C_{Ag} = C^{\circ}_{TiF_4,\ 230°C} = 3.04$ mole/m^3, and $\tau_D = 12600$ s, then:

$$D_e \approx \frac{3.27\cdot10^4 \times \left(7\cdot10^{-7}\right)^2 \left(8\cdot10^{-7} - 7\cdot10^{-7}\right)}{3\times8\cdot10^{-7}\times\left(3.04 - 0\right)\times12600} = 1.7\times10^{-14}\ \mathrm{m^2/s}$$

The effective diffusion coefficient above is significantly smaller than estimated Knudsen diffusion in micropores (For example, the estimated Knudsen diffusion coefficient for TiF_4(g) in pore of 10 and 0.1 nm diameter at 230°C are 2×10^{-6} and 2×10^{-8} m^2/s, respectively)[155]. The reported solid-state diffusion coefficient of oxygen in single-crystal rutile at 710°C is 4.7×10^{-21} m^2/s[156], which mean that a faster diffusion mechanisms than the solid-state diffusion through $TiOF_2$ lattice but slower than Knudsen diffusion may play role during the transport process in kinetic regime II.

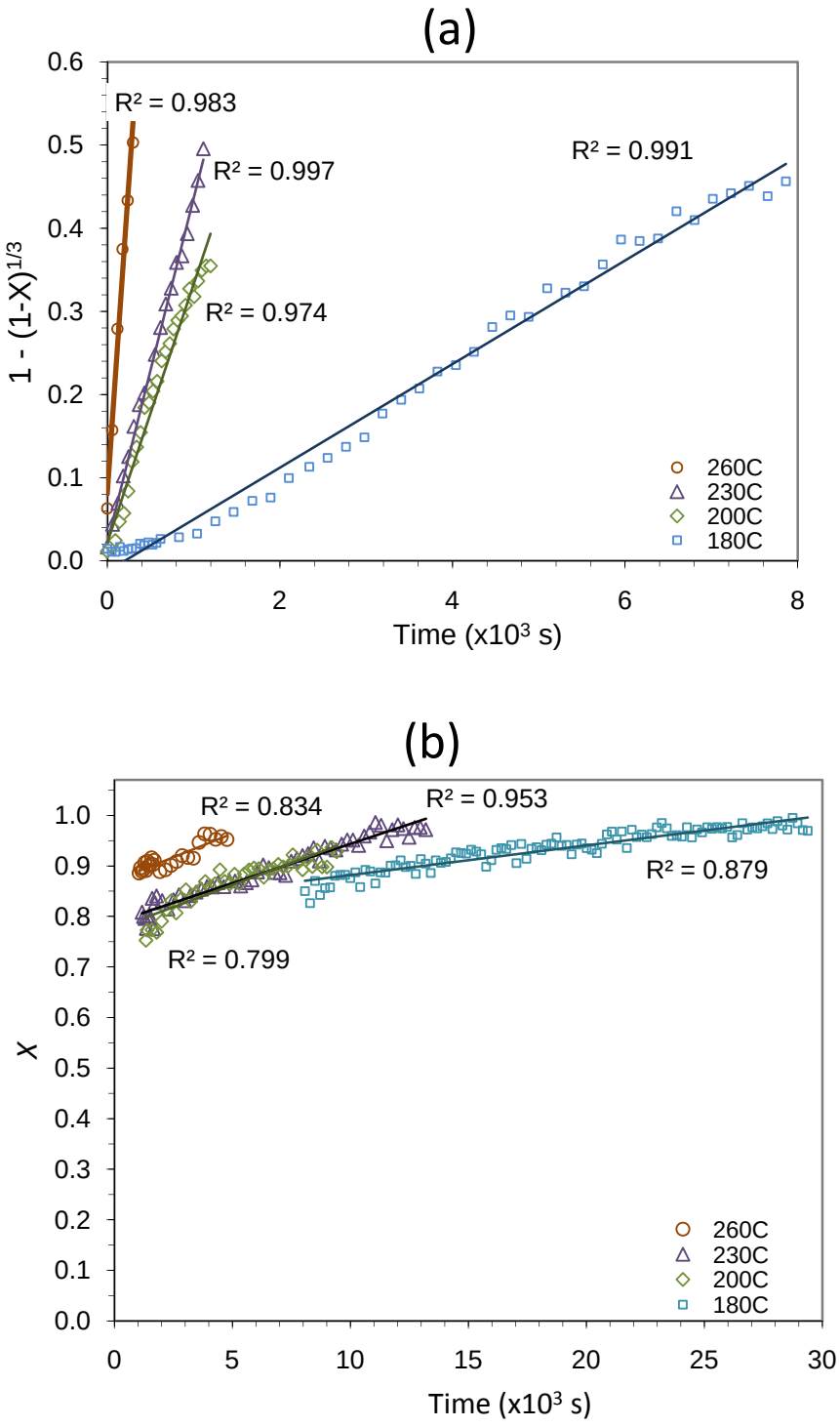

Figure 8.16: Plots of the extent of reaction with time for (a) chemical reaction control and (b) modified mass transport (solid state diffusion) control for the reaction of 0.59 μm diameter silica spheres with TiF_4(g).

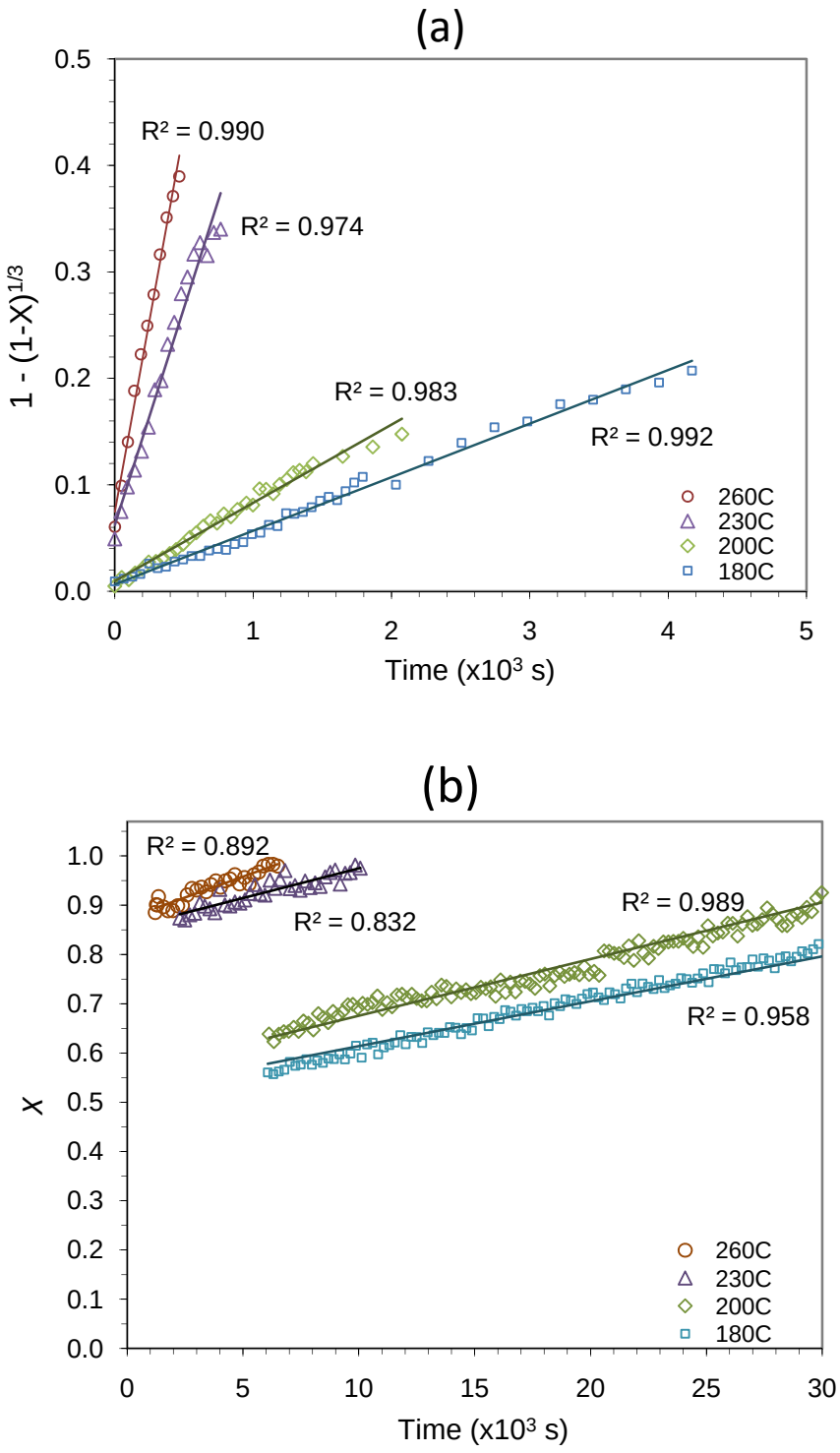

Figure 8.17: Plots of the extent of reaction with time for (a) chemical reaction control and (b) modified mass transport (solid state diffusion) control for the reaction of 1.44 μm diameter silica spheres with TiF_4(g).

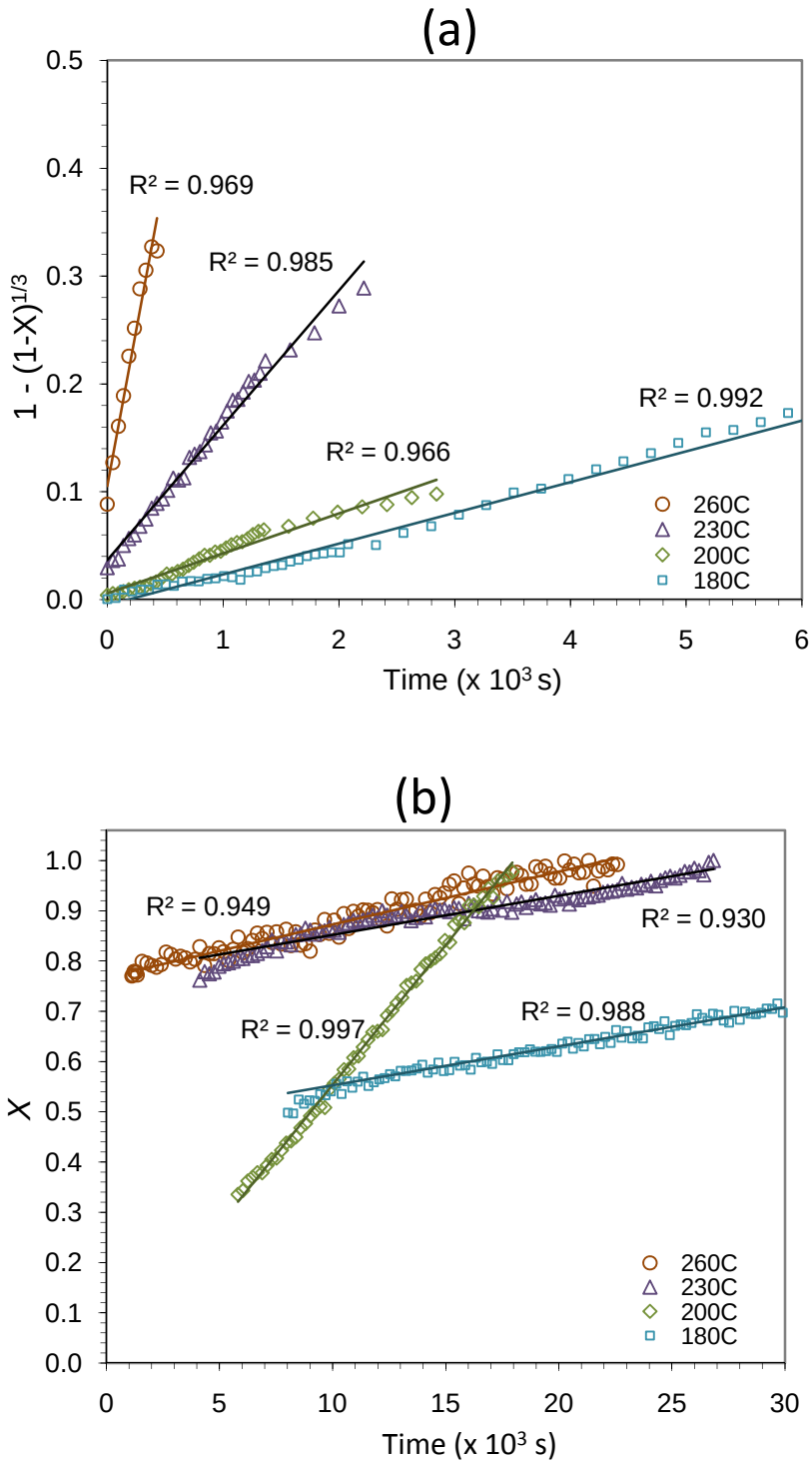

Figure 8.18: Plots of the extent of reaction with time for (a) chemical reaction control and (b) modified mass transport (solid state diffusion) control for the reaction of 3.05 μm diameter silica spheres with TiF_4(g).

8.4.6 Effect of the Reaction Temperature

The plot of the time constant, τ_C, obtained from the fitting of the chemical reaction control shrinking core model with temperature and with initial sphere diameter is shown in Figure 8.19. As can be seen from this figure, an increase in the reaction temperature resulted in a decrease in the time required to finish the reaction in regime I (i.e., the value of τ_C). This temperature trend was consistent across different sphere sizes.

There are at least three different temperature dependent parameters in the chemical reaction rate controlling SCM for the current SiO_2(s) – TiF_4(g) reaction system, i.e., the chemical reaction rate constant, the TiF_4(g) partial pressure, and the SiO_2 density (equation (10)). Since the equilibrium partial pressure of TiF_4(g) over solid TiF_4 is available from thermodynamic data, the chemical reaction rate constant can be readily calculated by using equation (10). The calculated rate constant, *k''*, is plotted in Figure 8.20, which shows that the reaction rate constant was roughly of same order of magnitude for all reaction conditions examined. The *k''* values were not strongly correlate with reaction temperature or initial sphere size. This suggested that for the range of reaction temperatures analyzed in this work, the effect of temperature on the overall reaction rate was primarily the result of the change in the partial pressure of TiF_4(g). Indeed, thermodynamic calculations indicate large increases in the equilibrium partial pressure of TiF_4(g) with temperature; i.e., p^o increases from 0.011 to 0.42 atm when temperature increases from 180 to 260ºC. Such large increases in $p(TiF_4)$ with temperature may have obscured the effect of temperature on the reaction rate constant, especially if the activation energy of the reaction was relatively small.

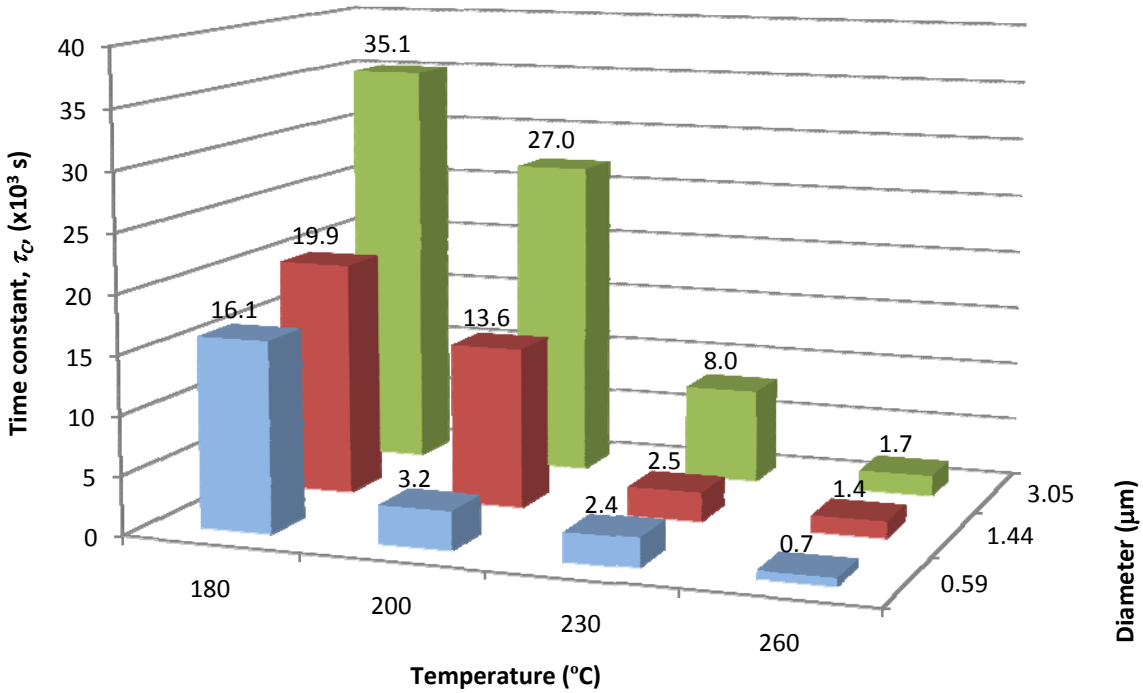

Figure 8.19: 3-D chart showing the effects of reaction temperature and initial sphere size on the time constant for chemical reaction control in kinetic regime I.

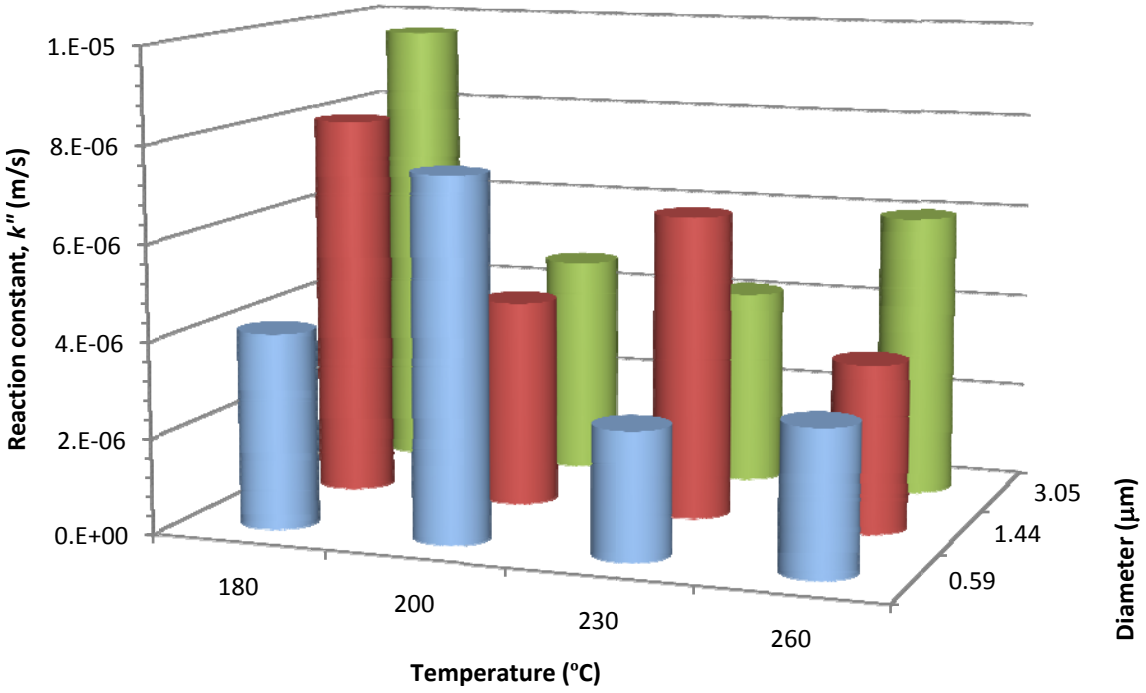

Figure 8.20: Calculated chemical reaction constant, *k''*, in kinetic regime I plotted against temperature and initial sphere size.

As seen in Figure 8.21, the trends of the time constant, τ_D, with temperature and sphere size in kinetic regime II, however, is not as distinct as the trends for the time constant in kinetic regime I. Although the effect of temperature on the time constant for 1.44 μm diameter spheres was as expected (i.e., τ_D decreased as temperature increased), the temperature effect on the time constant for the other sphere sizes did not follow a clear pattern. These non-monotonic trends of time constant with temperature and sphere sizes may be caused by the relatively small slope on the kinetic regime II compared to the slope on the kinetic regime I. Such a small slope may have prevented accurate measurement of the total reaction time (i.e., a slight change in the slope caused a large change in the intersection of the slope with $X = 1$ lines, which is the total time required for the completion of reaction – see Figure 8.12).

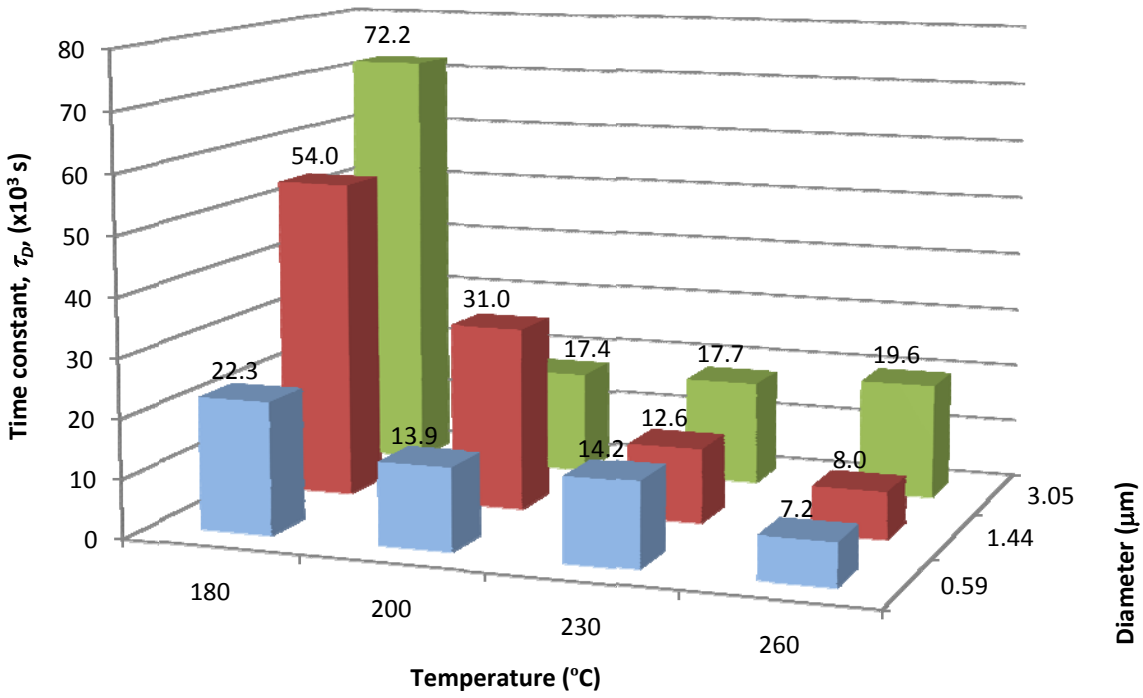

Figure 8.21: 3-D chart showing the effects of reaction temperature and initial sphere size on the time constant for mass transport (solid state diffusion) control in kinetic regime II.

8.4.7 Effect of the Initial Sphere Size

According to the shrinking core model, the correlation between the time constant, τ, and the initial size of the sphere could be used to assess the rate controlling step[137]. For chemical reaction control, equation (10) suggests that the time constant should be proportional to the initial sphere size. Such a relation is plotted in Figure 8.22, which shows that as the initial sphere size increased, the time required for reaction also increased. The correlation coefficients were reasonably good, (i.e., 0.86 to 0.99). Another characteristic of the shrinking core model is that the linear fit should be back-extrapolated to the origin, because for infinitely small particles, the reaction should theoretically proceed instantenously[137]. In other models, such as the crackling core model, similar plots will be back-extrapolate to a certain positive, non-zero, time constant[139]. The fitting lines shown Figure 8.22, however, do not indicate complete agreement with the requirement of the hypothetical zero-size particle reaction time constant, i.e., the fit for 180C reaction temperature does not back-extrapolated to zero. A better assessment of such plots may be achieved if the number of samples, which include a larger variation in sphere sizes, was increased, for enhanced statistics.

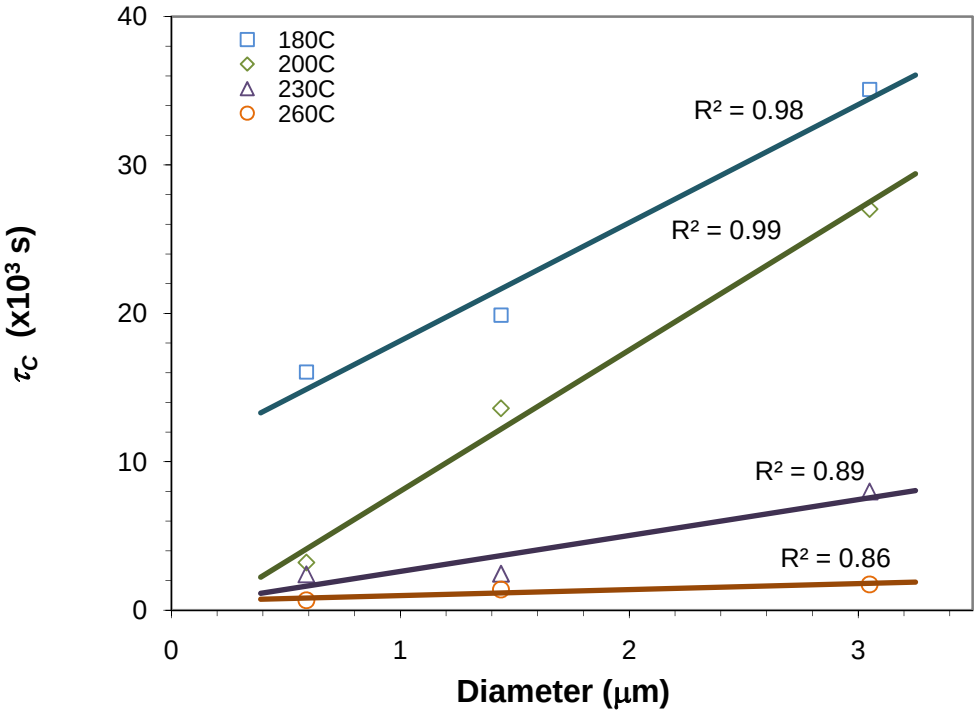

Figure 8.22: Plots of initial size of the spheres vs. chemical reaction control time constant, in kinetic regime I.

For kinetic regime II, the effect of initial sphere size on τ_D can be evaluated by equation (32). If $R = \delta + r_c$, where δ is the thickness of the external $TiOF_2$ layer, and for a relatively small value of δ compared to the value of r_c, then the time constant, τ_D, can be expressed as:

$$\tau_D = \frac{\rho_B r_c^2}{3bD_e\left(C_{Ag} - C_{Ac}\right)}\left(\frac{R - r_c}{R}\right) = \frac{\rho_B r_c^2}{3bD_e\left(C_{Ag} - C_{Ac}\right)}\left(\frac{\delta}{\delta + r_c}\right)$$

$$\tau_D \approx \frac{\rho_B r_c\, \delta}{3bD_e\left(C_{Ag} - C_{Ac}\right)} \qquad (33)$$

This equation indicates that the correlation of the time constant, τ_D, with the initial sphere size is also dependent on the thickness of the diffusion layer, δ. Additional research is needed to evaluate δ as a function of the initial sphere size. Furthermore, this constant product layer thickness may vary for different initial sphere sizes.

8.5 Conclusions

HTXRD was used to evaluate the rate of conversion of SiO_2 spheres into $TiOF_2$ via reaction with TiF_4(g). The combination of HTXRD analyses, with analyses of microstructural evolution and of nitrogen physisorption data, suggested that the kinetics of the reaction could be modeled by assuming the existence of 2 kinetic regimes with time. The initial kinetic regime followed a chemical reaction control model, while the second regime followed a mass transport control model involving a $TiOF_2$ layer of constant thickness. The total reaction time was influenced by the initial size of the silica spheres and the TiF_4 partial pressure.

CHAPTER 9: Summary and Outlook

The research presented in this doctoral work was sparked by the invention of BaSIC process where one of nature's tiniest 3-D bio-ceramic micron-size structures, namely silica diatom frustules, transformed into an entirely different composition, namely magnesia, and, most importantly, maintained an intact morphology[11]. Such a fascinating finding has initiated a significant effort to examine various reaction routes in order to produce diatom frustules, or generally speaking any promising 3-D silica microstructures, into numerous different compositions[12-14,16,157-161]. Here, a fraction of such efforts has been presented; the reaction of halide gases, i.e., TiF_4, ZrF_4, and $ZrCl_4$, with a number of 3-D silica structures; i.e., diatom frustules, silicified direct-write assembly scaffolds, and Stöber silica spheres. Additionally, two promising applications of the converted structures were also presented.

When gaseous zirconium fluoride was found to vaporize the silica structure, a new method of using a serial of displacement reaction process was developed. The serial-reaction process took an advantage of the prior technique of converting silica frustules into its magnesia replicas, which later reacted with gaseous zirconium chloride to produce zirconia replicas. The resulting solid reaction products were easily separated by using water to dissolute magnesium chloride byproduct. This two step gas-solid displacement process has been successfully demonstrated to generate microscale zirconia assemblies without a loss of the original microtemplate shape (i.e., the cylinder shape of *Aulacoseira* diatom frustules). Such process may be applied to a wide variety of other controlled 3-D shapes available among the tens of thousands of species of extant diatoms and other silica-forming microorganisms.

The majority of the works presented here have been devoted on the investigation of metathetic reactions that produces titania replicas. The successful conversion of silica structures into anatase replicas with features preservation in the size of down to 100 nm has been demonstrated through the work on the *Corethron criophilum* diatom spines. Reaction temperature played a critical role for the shape preservation. A relatively small increase in the reaction temperature (i.e., from 225°C to 250°C) was found to cause significant coarsening of $TiOF_2$ crystallites and, in effect, eliminated the fine features of the *C. criophilum* spines. An optimum reaction condition, i.e., at 225°C for 2 h, was needed to achieve a significant fidelity of the shape and fine features of the starting spines in the titania replicas. Certain atmospheric conditions were also required during the oxygenation process (i.e., conversion from $TiOF_2$ into TiO_2) to avoid structural distortion. In the case of silicified structures derived from DWA, the loss of carbon within the structure needs to be minimized to reduce unwanted deformation which can be accomplished by heat treatment in a flowing mixture of $H_2O(g)/Ar(g)$.

On the efforts of investigating potential applications of the anatase diatom frustules, ethanol sensors based on a single TiO_2-converted diatom frustules has been successfully fabricated. This sensor exhibited very fast response to the ethanol concentration change compared to similar sensors reported in the literature at the time of this publication. Since the sensor also sufficiently sensitive to detect at least 100 ppm of ethanol in air, commercial use of such sensor is foreseeable if an inexpensive method to mass produce the sensor device and associated electronic peripheral would have been developed. Currently, the placement of electrodes that could provide reliable electronic contacts on the micron-scale converted diatom frustules has been a great technical challenge.

Significant enhancement of hydrolysis of pesticide-like compounds were observed in the presence of F-doped anatase TiO_2 diatom frustules under near neutral

conditions and in the absence of light (non-photocatalytic conditions). The enhanced activity of such nanostructured titania assemblies without the need for a strong UV light source is quite attractive for the hydrolytic destruction of environmental pollutants in remote locations. Furthermore, SiO_2-based diatomaceous earth, which has long been used in water purification applications[110], is readily available in large quantities at low cost, and the chemical conversion technique employed in this study is a scalable means of converting diatomaceous earth into fluorine-doped titania nanoparticle structures. Fluorine doping has been found to improve the *photocatalytic* activity of anatase towards the decomposition of acetaldehyde, trichloro-ethylene, acetone, and phenol[162-164]. Further research aimed at probing the photocatalytic effects of these nanostructured assemblies on pesticide hydrolysis and other types of reactions could be quite fruitful.

X-ray powder diffraction data and Rietveld analyses has been successfully characterized the crystal structure of polycrystalline $TiOF_2$ that was synthesized through the metathetic reaction of silica with TiF_4(g). The room temperature crystal structure of polycrystalline $TiOF_2$ was found to have $R\bar{3}c$ symmetry with a = 5.33252(11) Å and c = 13.2321(4) Å. Upon heating to 61°C, $TiOF_2$ crystals underwent a transformation from the hexagonal $R\bar{3}c$ structure into the cubic *Pm3m* structure. A higher temperature study in which $TiOF_2$ transformed into anatase titania, could provide a better understanding of the exhibited fast sensor ethanol response or the fluorine doping effects.

To better understand the kinetics reaction of TiF_4(g) with SiO_2, a novel HTXRD reaction chamber was developed. A layer of window materials placed within the chamber (namely Kapton and aluminum foil) was capable of providing the mechanical and chemical integrity of confining the gaseous reactant at the temperature of interest and, at the same time, was sufficiently transparent toward X-rays. This approach may also be used on a variety of reactions involving gaseous reactants that possess appreciable vapor pressures only at elevated temperatures (i.e., gaseous reactants that are generated by

heating condensed sources). Owing to the flexibility of the choice of materials for the main chamber body and window, reactions that require special materials (such as the need for an inert material relative to a reaction system or the need for higher temperatures) can be easily accommodated in this HTXRD chamber design. The utilization of the HTXRD chamber in evaluating the rate of reactive conversion associated with the reaction between SiO_2(s) and TiF_4(g) was a major success for such chamber design. HTXRD analyses were capable of providing an important and unique complementary data to the other analytical techniques so as to properly evaluate the kinetics reaction mechanism during the conversion reaction.

The combination of HTXRD conversion data, with analyses of microstructural evolution and with analyses of nitrogen physisorption data suggested that the kinetics of the reaction could be modeled by assuming the existence of 2 kinetics regimes with time. The initial kinetic regime followed chemical reaction control, while the second regime followed mass transport control through a $TiOF_2$ layer of constant thickness. The total reaction time was influenced by the initial size of the silica spheres and the TiF_4 partial pressure.

Naturally occurring biosilica microstructures with a wide variety of 3-D shapes are generated by diatoms, radiolaria, sponges, plants, mollusks, echinoderms, arthropods, and other silica-forming organisms[19,20,41,42,75,165-172]. Even for the phylum of diatom only, the biodiversity of the diatom frustule morphologies is immense (See Figure 9.1 for a few handpicked examples). Future advances in genetic engineering may yield an even greater variety of biosilica morphologies. Indeed, recent advances in the sequencing of a diatom genome, and in the development of transformation-based approaches for introducing and expressing genes in diatoms, are the first steps toward the genetic engineering of shape-tailored diatom frustules[9,173]. Large-scale culturing (of the type currently used in aquaculture operations) of naturally occurring or genetically modified diatoms (or other

organisms) could be used to produce enormous numbers of biosilica microtemplates with targeted, similar 3-D shapes[42]. Shape-preserving metathetic displacement reactions of the type discussed in this work could be used to convert such biologically self-assembled silica microtemplates into functional microparticles, comprised of either nanocrystalline zirconia or titania, with well-controlled 3-D morphologies for a variety of catalytic/chemical, biological, electrical, thermal, mechanical, or other applications.

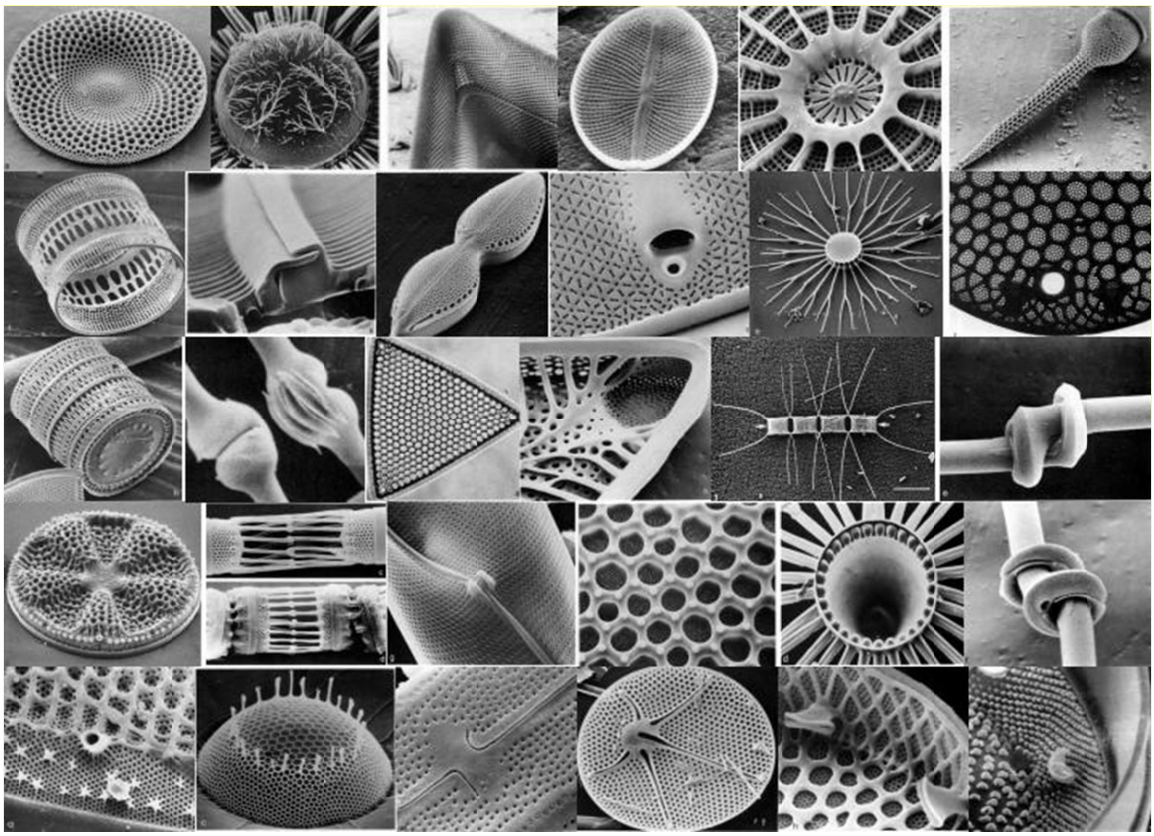

Figure 9.1: Secondary electron image collection of silica frustules of various diatom species. (F. E. Round *et. al.*, *The Diatoms : Biology & Morphology of the Genera,* Cambridge University Press, 1990).

APPENDIX A : X-ray Diffraction Analysis of TiF_4 Powder

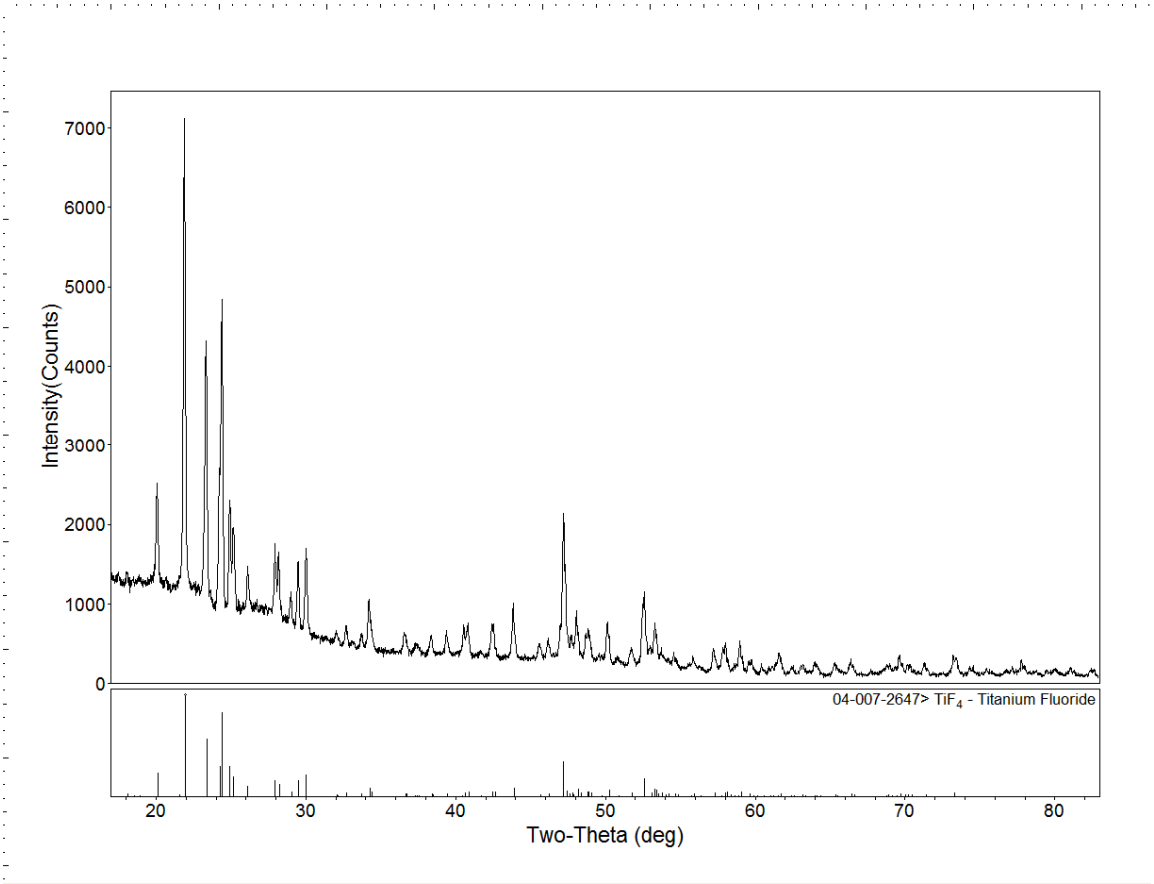

Figure A.1: X-ray diffraction analysis of TiF_4 powder used to generate TiF_4 during the reaction with SiO_2 (99% purity, Advanced Research Chemicals, Inc., Catoosa, OK). The measured diffraction pattern matches the reported diffraction pattern of TiF_4 in literature (PDF# 04-007-2647, ICDD). To prevent contamination with moisture during x-ray analysis, the powder was placed inside an Argon-filled sealed aluminum enclosure with Kapton windows.

APPENDIX B : Temperature Calibration Inside HTXRD Chamber

Temperature calibration inside the gas-tight aluminum reaction chamber was performed by differential thermal expansion method as described by Drews[133]. This method utilizes the *relative thermal expansion* of two separate diffraction peaks, either for peaks from a mixture of phases, or from a single phase that has anisotropic thermal expansion. Owing to the use of the relative separations of closely spaced peaks, this method is relatively fast and insensitive to geometric aberrations.

Alpha alumina (99.9% purity, Alfa Aesar, Ward Hill, MA) and silver (99.9% purity, Alfa Aesar, Ward Hill, MA) powder was mixed in a mortar and pestle. The ratio of two powders was chosen such that the height of the alpha alumina (111) peak is relatively the same as the height of the silver (200) peak. The mixture was spread onto the nickel lid, which then placed in the aluminum reaction chamber and sealed with Kapton windows. The sealed reaction chamber was placed in the Anton Paar furnace and heated to the desired calibration temperatures (65 to 375ºC). An equilibrium time of 15 min is required before measuring the diffraction profile.

Figure B.1 shows the diffraction profile of the alumina and silver mixture at various holding temperature. As can be seen in the figure, the relative peak position of the alumina (111) and silver (200) peaks decreased with increasing temperature. The peak positions were then determined by peak profile fitting in Jade software. By using Pearson-VII profile shape function, the peak's height, 2-theta, full width half maximum, shape, skew, and background were refined in the fitting. The measured d-spacing of both materials, and the measured difference are presented in Figure B.2.

The thermal expansion of alumina and silver as a function of temperature are given by the following empirical equations[133]:

$$\frac{\Delta L_{Al_2O_3}}{L_0}(T) = -0.176 + 5.431\times10^{-4}T + 2.150\times10^{-7}T^2 - 2.810\times10^{-11}T^3$$

$$\frac{\Delta L_{Ag}}{L_0}(T) = -0.515 + 1.647\times10^{-3}T + 3.739\times10^{-7}T^2 - 6.283\times10^{-11}T^3$$

where $\frac{\Delta L}{L_0}$ is percent expansion relative to 293K and T is temperature measured in Kelvin. The furnace thermocouple in HTXRD is assumed accurate at room temperature (25ºC), because there was no heat source in the system that causing temperature difference. Thus the d-spacing of both alumina and silver at room temperature were used to calculate their respective d-spacing at higher temperature using the above thermal expansion equations. The calculated d-spacing difference as a function of temperature is showed by green line in Figure B.2. The resulting calibration curve is shown in Figure B.3, which reveals the temperature difference between the calculated temperature (i.e., calibrated temperature) and the temperature shown by the furnace controller.

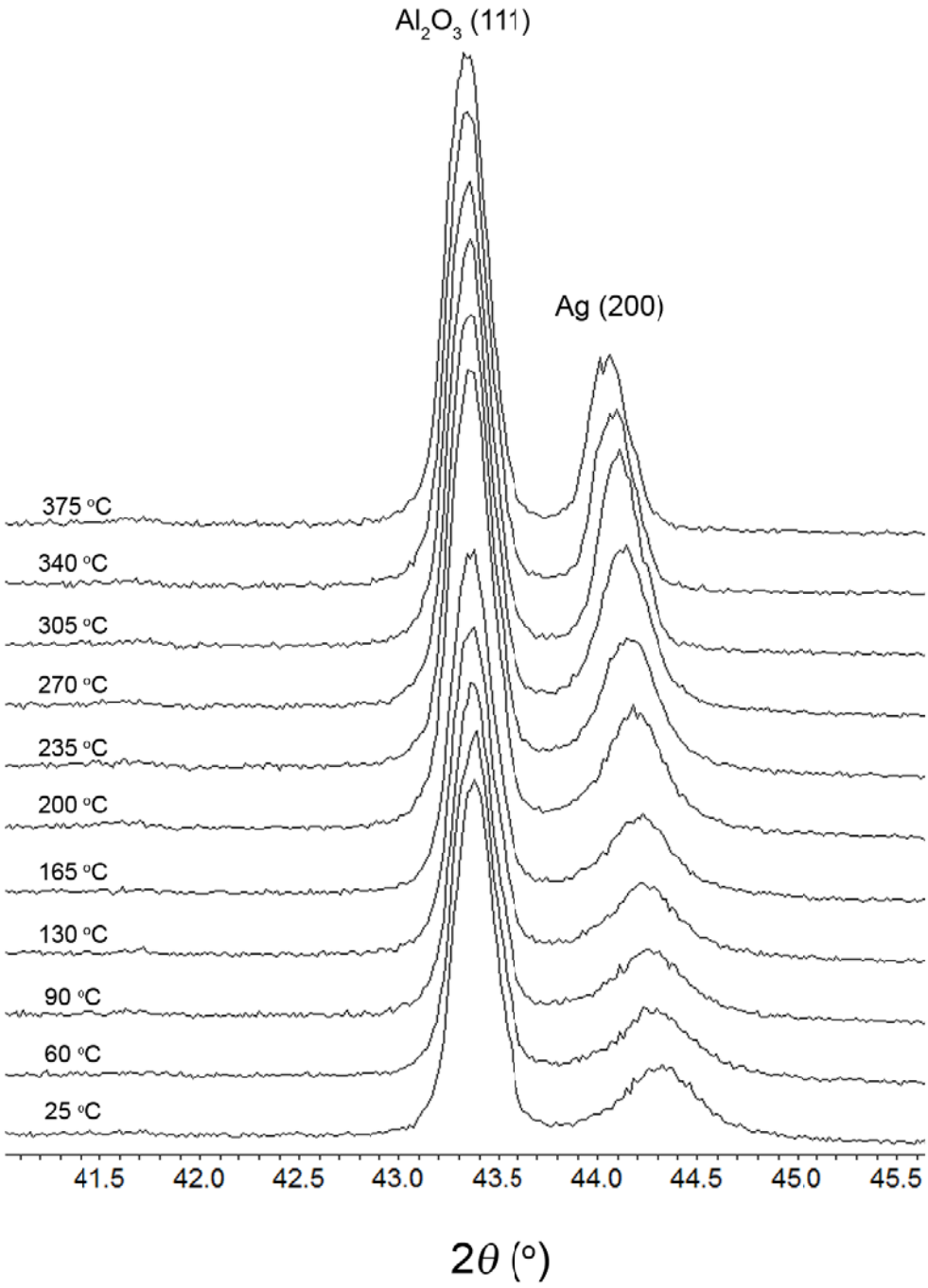

Figure B.1: Diffraction patterns of the Al_2O_3 and Ag mixture powder in a selected 2θ range upon heating from room to 375°C.

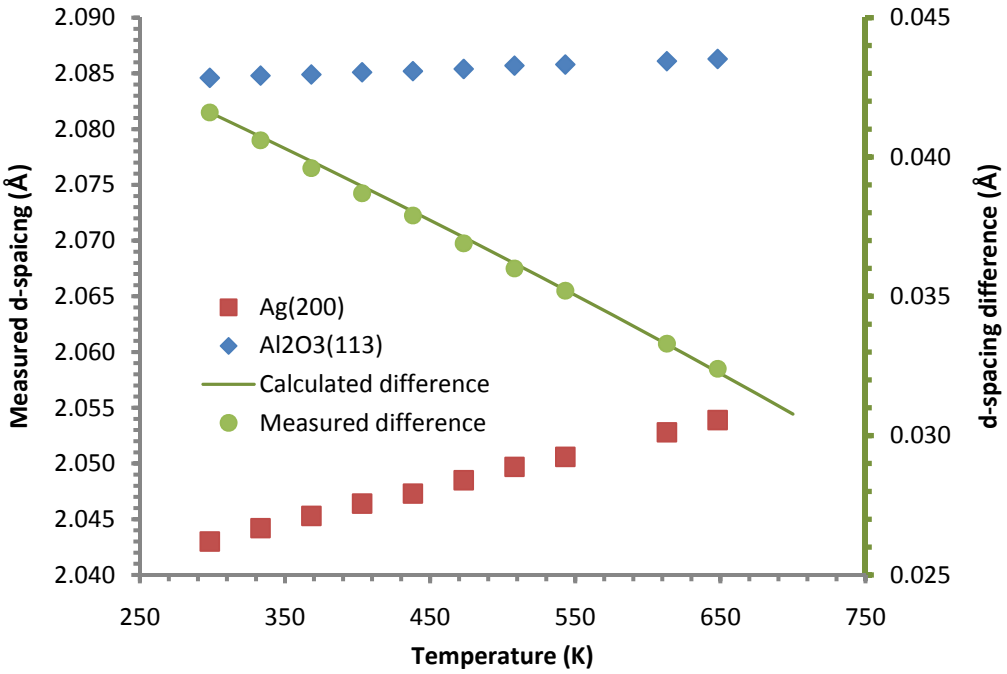

Figure B.2: Measured d-spacing of Ag(200) and Al_2O_3(113) between 25 to 375°C is showed on left vertical axis. The measured d-spacing difference and calculated d-spacing difference are showed on right vertical axis.

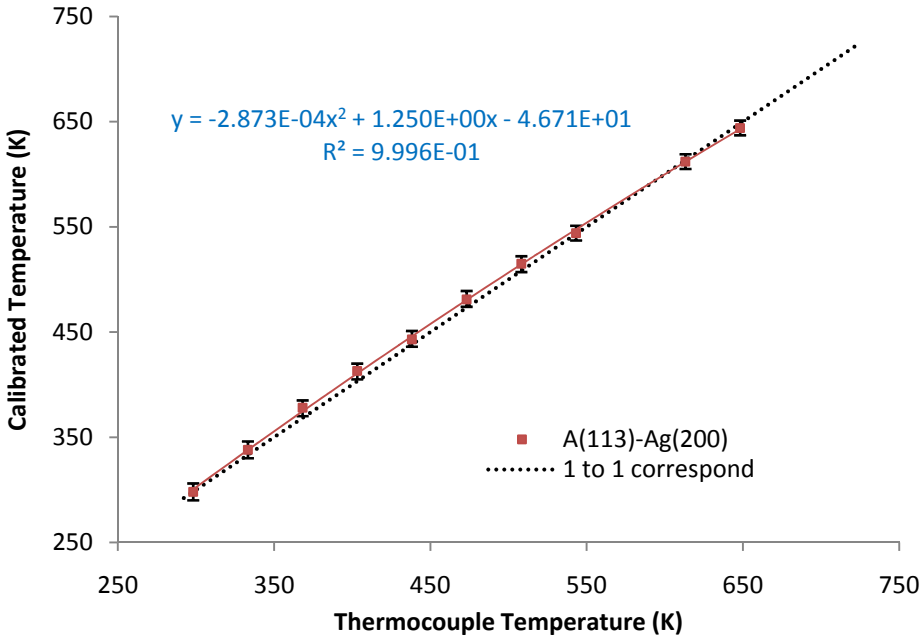

Figure B.3: The plot of the actual (calibrated) temperature of the sample inside the reaction chamber with the thermocouple temperature of the furnace.

APPENDIX C : HTXRD Reaction Chamber Using Graphite

Initial HTXRD experiments were conducted using graphite chambers designed in SolidWorks software and milled using CNC machine. The chamber design was an improvement over the initial graphite chamber design by Dr. Michael Haluska[128]. The sample holder was separated from the main body so that a relatively easier sample loading could be achieved, especially if the chamber sealing was performed inside a glovebox. Other main improvement feature was the use of nickel for the bottom lid, where the threaded holes were located. The use of metal nickel allowed a tighter closure between the chamber and the lid, minimizing the escape of gas reactant. In the original graphite chamber design, threads were located in the main graphite body, limiting the maximum torque for screws. Excessive torque on the screws would cause thread wear on the graphite chamber, rendering it useless.

Figure C.1 shows 3-D renderings and a schematic drawing of a side view of the graphite reaction chamber. The chamber consisted of 4 main parts: the graphite enclosure, the graphite sample holder, the reactant source holder (graphite), and the nickel bottom lid. The dimensions of the main parts are shown in Figure C.2 and Figure C.3. During an experiment of the reaction of TiF_4 and SiO_2, a layer of Teflon tape was placed between the nickel bottom lid and the graphite enclosure to ensure proper seals. Also, nickel foils were placed on both side of the gas-reactant source holder and on the top of the graphite enclosure to block unwanted X-ray strays and to ease sample height adjustment in the HTXRD Anton-Paar furnace (See Figure C.4a and b).

Typical HTXRD patterns are shown in Figure C.5, where diffraction peaks for SiO_2, $TiOF_2$, and graphite were clearly detected. At the initial of the reaction the relative

intensity of the $TiOF_2$ peak increased with increasing reaction time before the peak height became stagnant. The relative intensity of the cristobalite SiO_2 diffraction, however, was relatively constant, if not changed by a minor amount, throughout the reaction course. It was found that that the gas reactant leaked through machined graphite chamber, presumably through invisible micro-cracks in the thinnest walls where the x-rays passed. The leaking gas depleted the solid reactant source, causing the reaction to stop prematurely.

Further investigation found that the weight of the holder assembly decreased in order of half the weight of the loaded TiF_4 reactant. (i.e., a weight loss of 10 mg was typically found after a run ended). Also the color of the TiF_4 changed from white to dark gray, probably from the result of the reaction with diffused oxygen or water vapor into the chamber. Using methanol as an agent for leak test, the main enclosure was found to have leak on the thinnest part where incoming and diffracted X-rays passed through (See Figure C.4c). The pressure of the gas system, which contains argon, TiF_4(g), and SiF_4 (or Si_2OF_6) was thought to be high enough to cause significant leak during the run.

The micro-cracks were thought to have developed during the machining of the brittle graphite. Increasing the graphite wall thickness may help minimize the micro-cracks however such additional barrier thickness compromised the signal to noise ratio, especially for a relatively low energy Cu Kα incident beam. This obstacle prevented proper analysis on the data gathered during high temperature X-ray scans. Thus another reaction chamber was conceived as discussed in Chapter 7.

This graphite chamber design, however, may still be useable for the study of other gas-solid reaction system, such as Mg-SiO_2 system where a relatively low pressure of gas was developed during the reaction course.

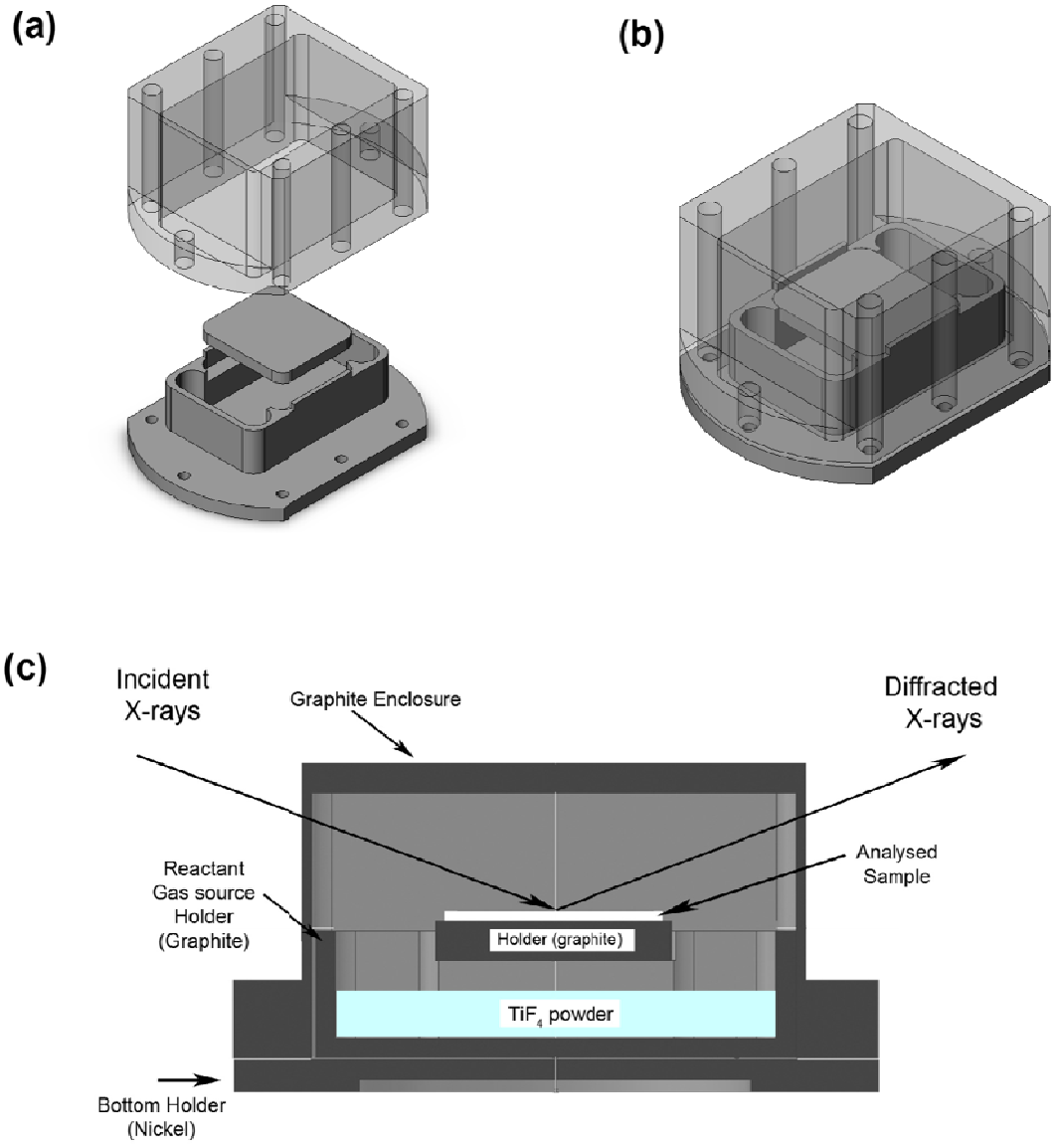

Figure C.1: (a), (b) 3-D rendering of the graphite chamber. The chamber consisted of 4 main parts: the graphite enclosure, the graphite sample holder, the reactant source holder (graphite), and the nickel bottom lid. (c) Schematic (side view of cross section) of the reaction chamber.

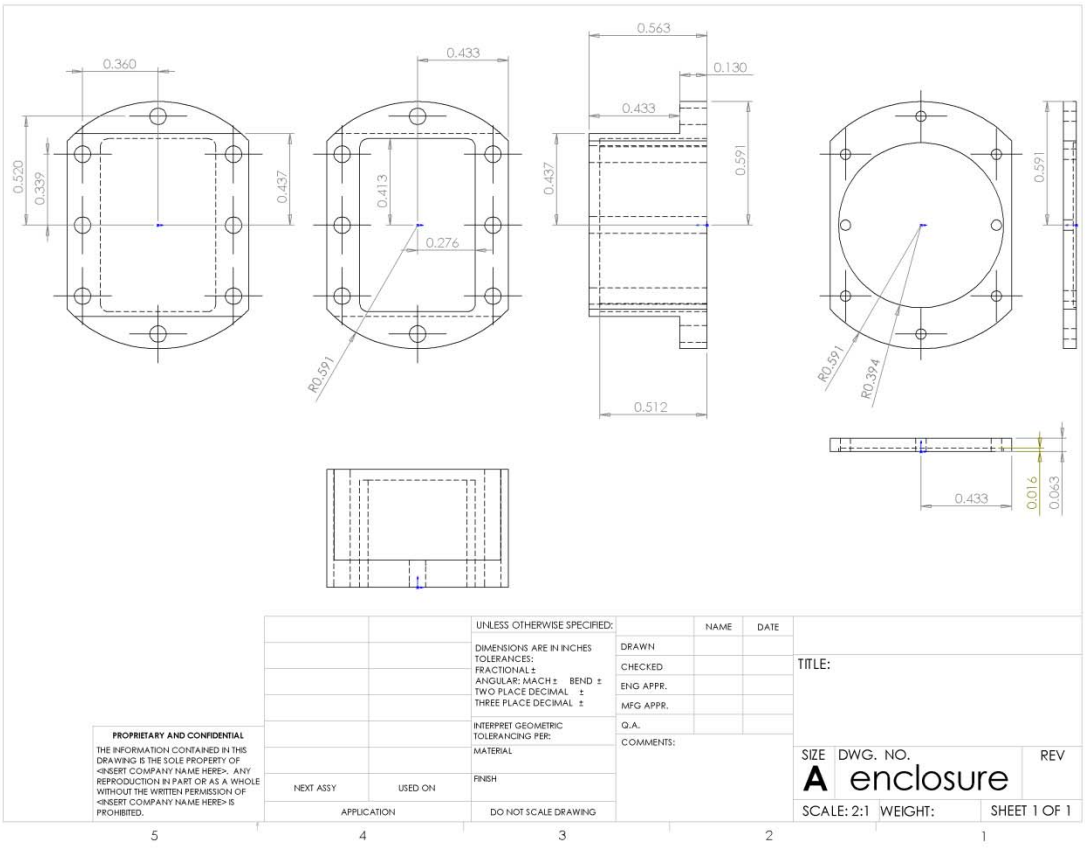

Figure C.2: Schematic drawings showing the dimensions of the graphite enclosure (left) and the nickel bottom lid (right).

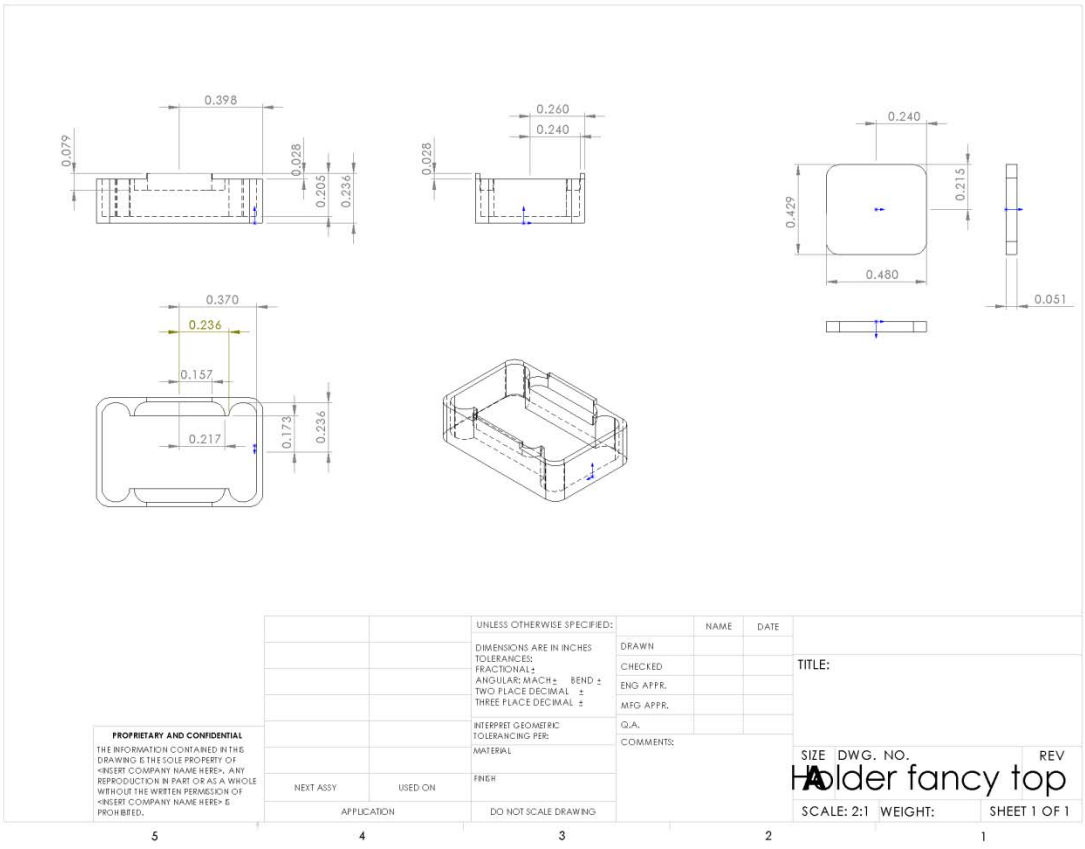

Figure C.3: Schematic drawings showing the dimensions of the graphite gas-reactant source holder (left) and the graphite sample holder (right).

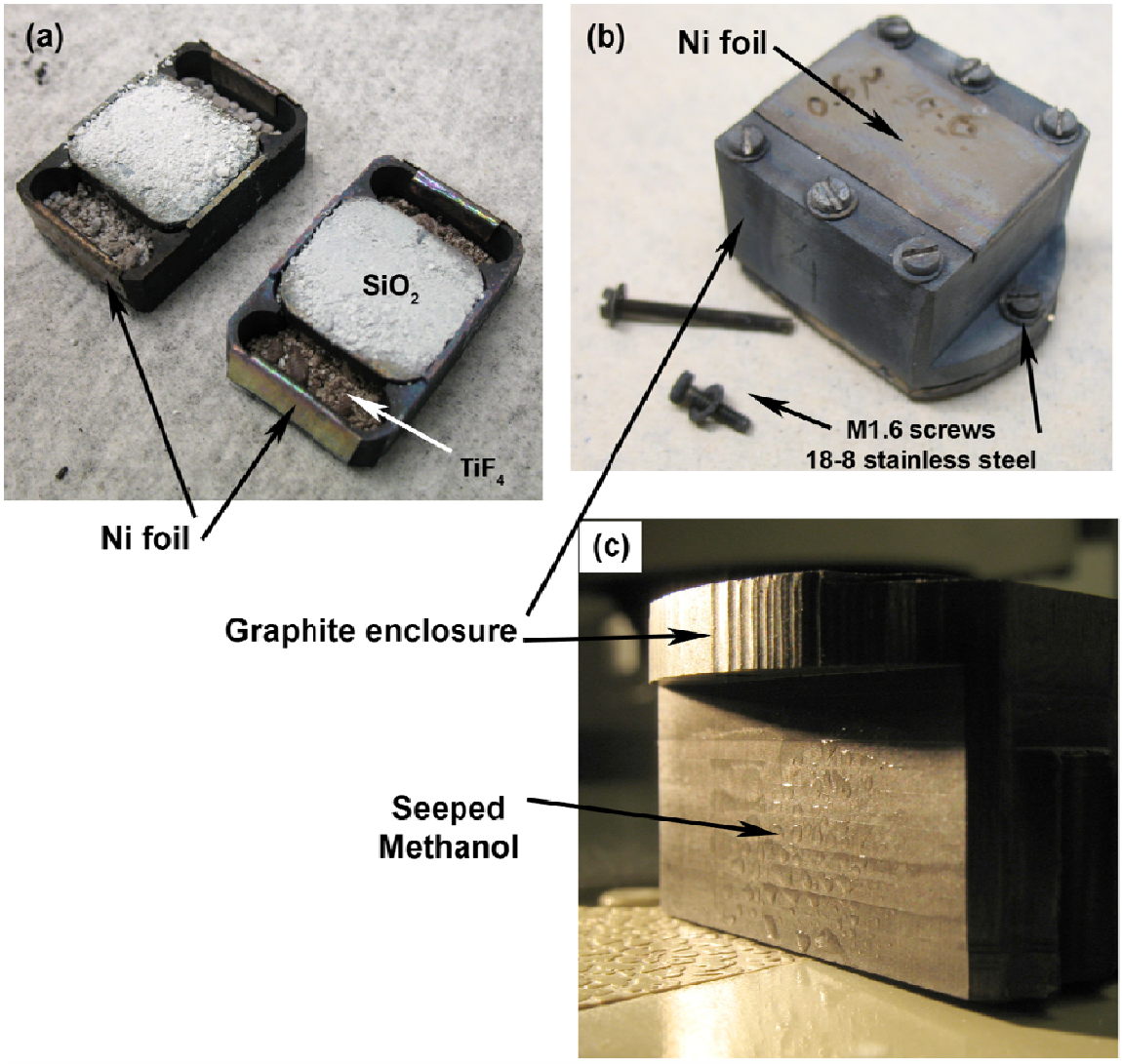

Figure C.4: Optical pictures of (a) the sample holder with silica on top and the gas reactant source (TiF_4) holder, (b) the assembled sample holder with stainless screws, and (c) the leakage of methanol through the main graphite enclosure.

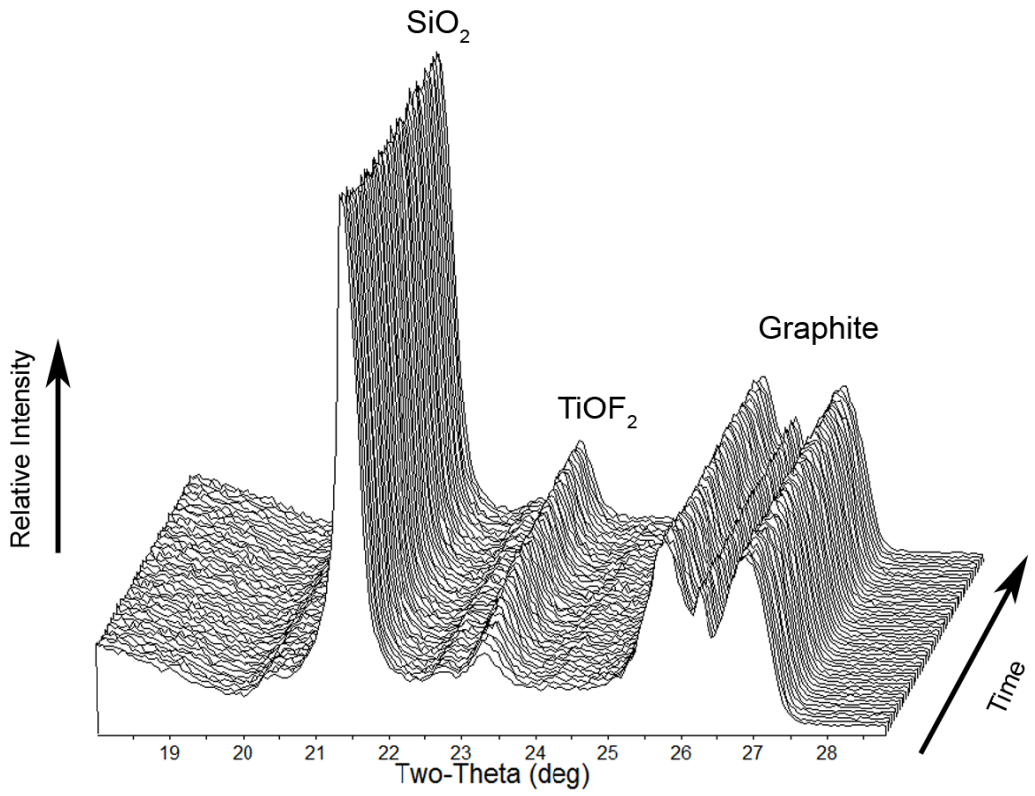

Figure C.5: Portions of the X-ray diffraction patterns obtained with time during isothermal reaction of SiO_2 diatom frustules with TiF_4 gas at 280°C (4 min interval between successive scans).

APPENDIX D : Calculation of the Effective Penetration Depth of X-rays

The effective penetration depth of X-rays, *x*, during diffraction analyses can be calculated by the following equation[48]:

$$x = \frac{\sin\theta}{2\mu} \cdot \ln\left(\frac{1}{1-G_x}\right)$$

where θ and μ are the 2θ diffraction angle and the linear absorption coefficient of x-rays, respectively. G_x is the ratio of intensity diffracted from up to depth of *x* to the total measured intensity. For example, if G_x is equal to 0.95, then 95% of the total measured intensity comes from the diffraction from surface to the depth of *x*.

The mass absorption coefficient of a substance, μ/ρ, can be calculated from the weight fraction, *w*, of its elements[48]:

$$\frac{\mu}{\rho} = w_1\left(\frac{\mu}{\rho}\right)_1 + w_2\left(\frac{\mu}{\rho}\right)_2 + ...$$

where ρ is the density of the substance. For Cu Kα (8.04 MeV), the mass absorption coefficient of elementals O, F, Si, and Ti, are 11.6, 16, 64.7, and 202.3 cm^2/g, respectively[132]. Using the above equation, the mass absorption coefficients of SiO_2 and $TiOF_2$ were calculated to be 36.5 and 103 cm^2/g, respectively. By using density of 2.0 g/cm^3 for Stöber silica and 3.12 g/cm^3 for $TiOF_2$, the effective depth of penetration of Cu Kα at 2θ = 22º are:

$$x_{SiO_2} = \frac{\sin 11^o}{2\times(36.5\times 2.0)} \cdot \ln\left(\frac{1}{1-0.95}\right) = 3.9\times10^{-3}\,\text{cm}$$

$$x_{TiOF_2} = \frac{\sin 11^o}{2 \times (103 \times 3.12)} \cdot \ln\left(\frac{1}{1-0.95}\right) = 8.9 \times 10^{-4}\ \text{cm}$$

The above calculations assumed a solid bed of materials. If the bed consisted of packed spheres with voids between the spheres, and assuming a closed packed arrangement of spheres (packing factor = 0.74), then the corrected depth of penetration become:

$$x'_{SiO_2} = \frac{3.9 \times 10^{-3}}{0.74} = 5.3 \times 10^{-3}\ \text{cm} = 53\ \mu\text{m}$$

$$x'_{TiOF_2} = \frac{8.9 \times 10^{-4}}{0.74} = 1.2 \times 10^{-3}\ \text{cm} = 12\ \mu\text{m}$$

In a typical HTXRD, the sphere bed thickness is about 100 μm. These calculations indicate that 95% of the measured diffraction intensities were coming from the one half of the bed at the initial of the reaction and gradually decreased (as the SiO_2 transformed into $TiOF_2$) to roughly one-tenth of the initial bed thickness at the completion of reaction. For the largest silica sphere (3.05 μm diameter) used in the kinetic experiments in Chapter 8, it can be concluded that 95% of the total measured diffraction intensity at near the completion of reaction was roughly coming from at least 4 layers of the spheres.

APPENDIX E : Sensor Substrate Preparation

During sensing performance measurement, the frustule was placed on a non-conductive substrate with gold pattern (and pad) for easy electrical connection to the potentiostat instrument. The substrate layer was designed by Dr. Sehoon Yoo (Gatech). Since silicon can be relatively conductive at the measurement temperatures (200-400°C), a dielectric nitride layer was applied on the top of silicon substrate (Figure E.1). Titanium layer was applied between nitride and gold layers to enhance the adhesion of gold to the substrate. Before titanium deposition, RF bias sputtering was applied on the nitride layer for at least 5 minutes for thorough cleaning. The mask pattern for the titanium and gold layers was drawn using AutoCAD software (Figure E.2a). The substrate preparations (photoresist, coatings, and cutting) were performed with the help of Dr. Jason Nadler in the Georgia Tech Research Institute (GTRI).

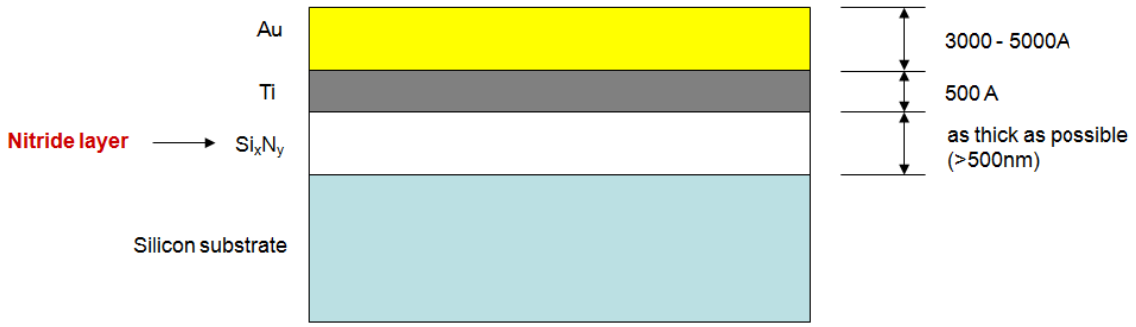

Figure E.1: Schematic of the sensor substrate cross section designed by Dr. Sehoon Yoo.

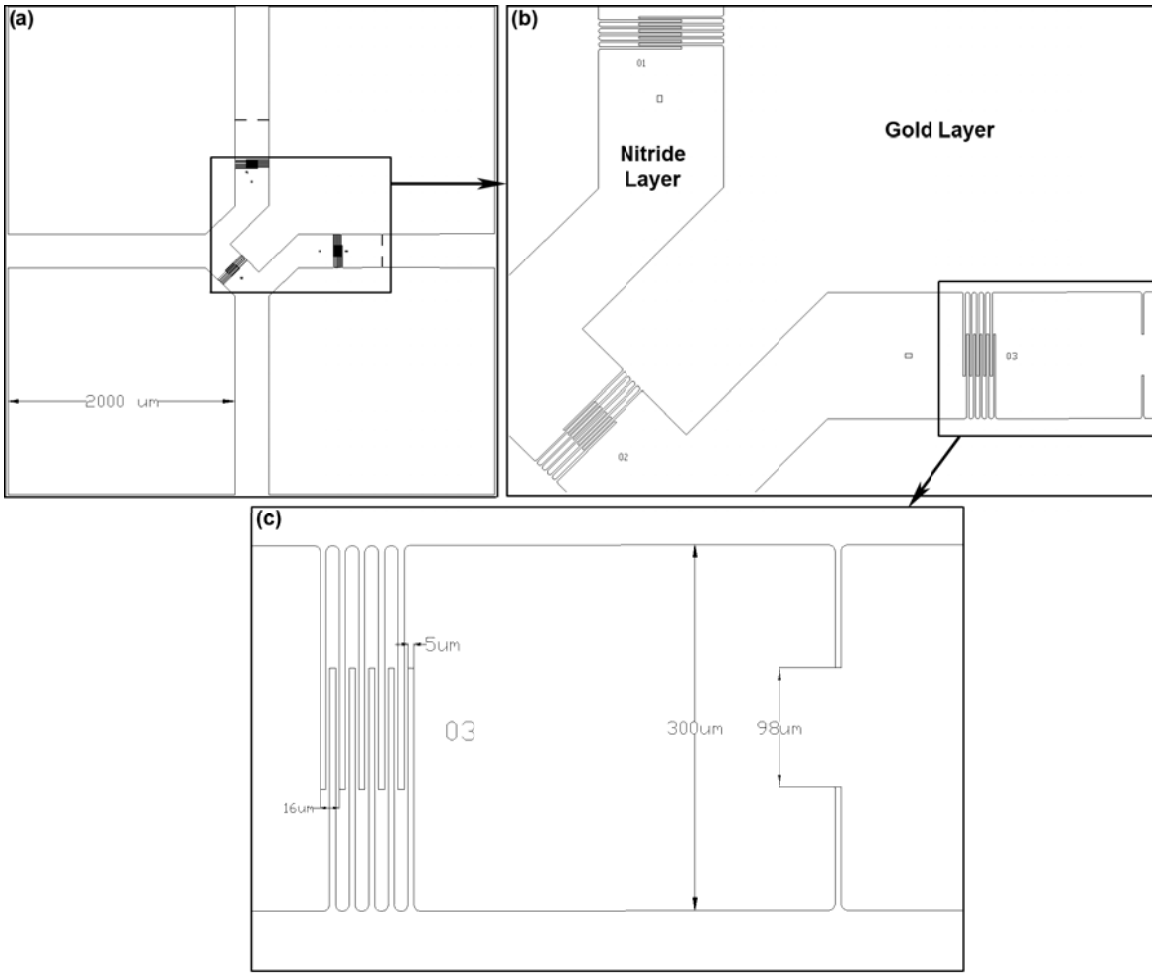

Figure E.2: Schematic of the gold pattern on the sensor substrate at increasing magnifications from (a) to (c).

APPENDIX F : LabVIEW Interface for Sensor Measurements

During a gas sensor measurement, the concentration of gas being analyzed (e.g., ethanol or No_x), was automatically controlled through a preprogrammed 'scheduler'. The scheduler was custom written in Labview software (v7.1). The front interface of the scheduler is shown in Figure F.1. The Labview diagrams of the scheduler are shown in Figure F.3, Figure F.4, and Figure F.2. A compact FieldPoint backbone (cFP-2000, National Instruments) with several analog input/outputs (cFP- AI-100, cFP-AO-210, cFP-TC-120) was used for hardware data acquisitions and controls.

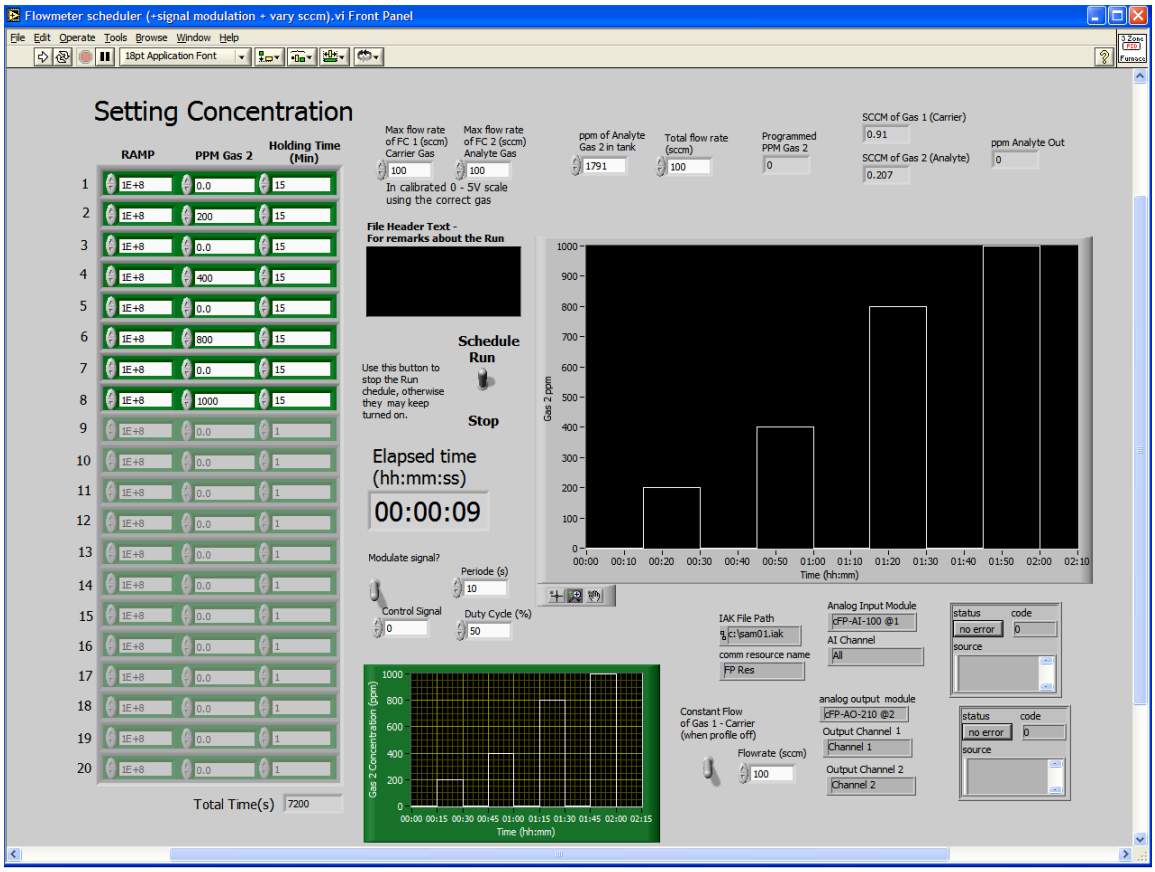

Figure F.1: Labview front interface for automatic gas concentration change during a measurement of gas sensor performance.

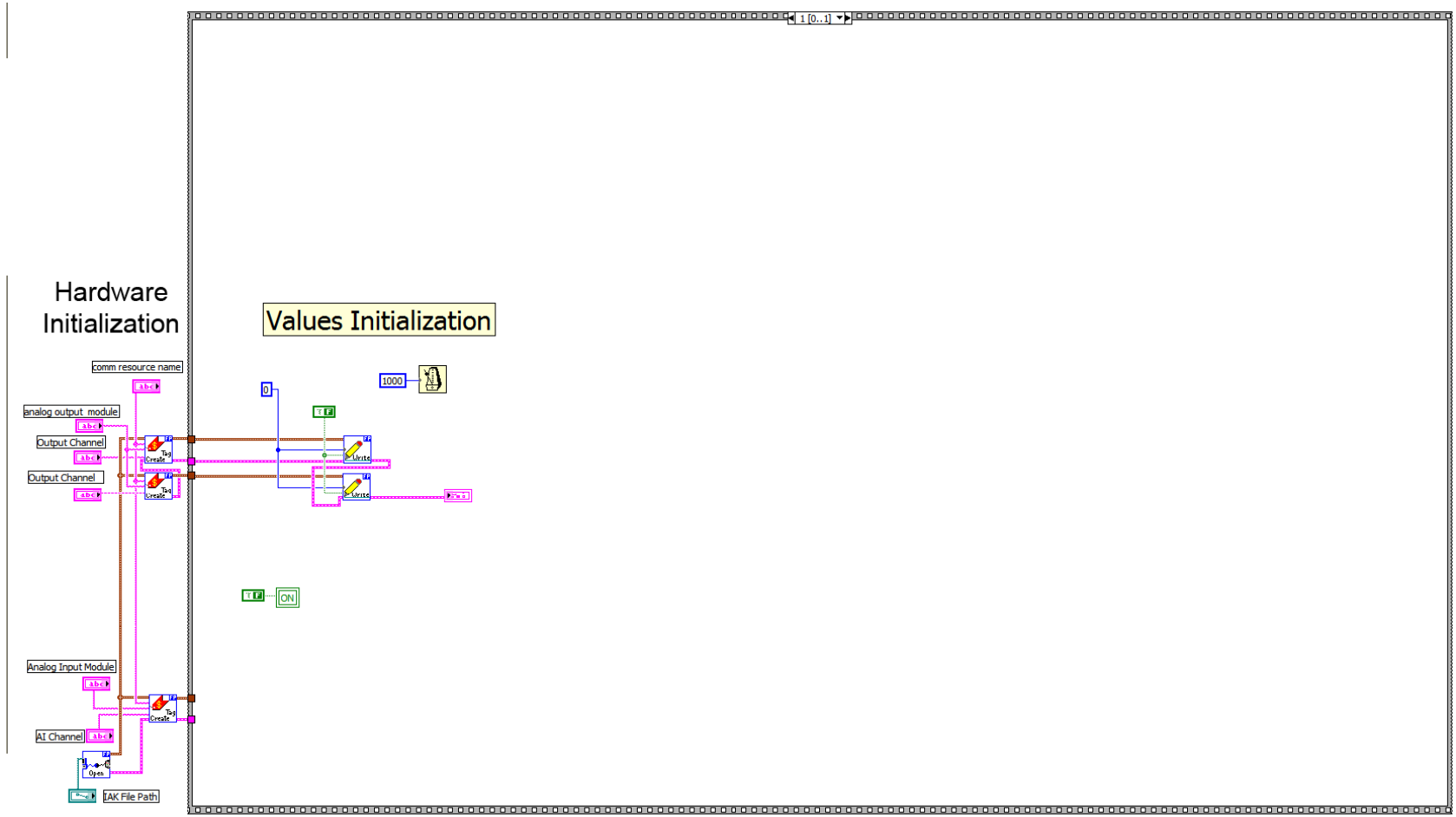

Figure F.2: Labview diagram A

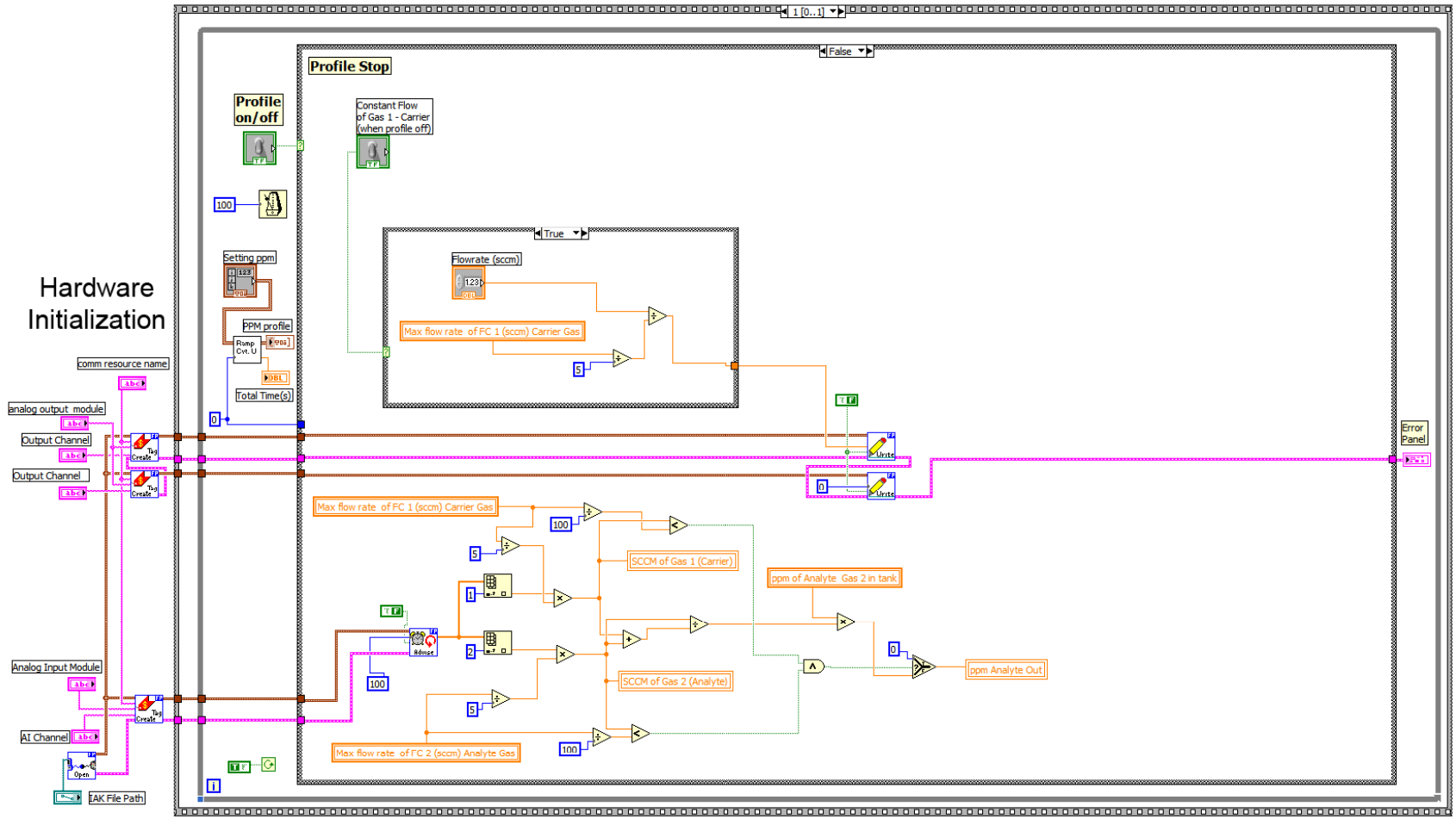

Figure F.3: Labview diagram B

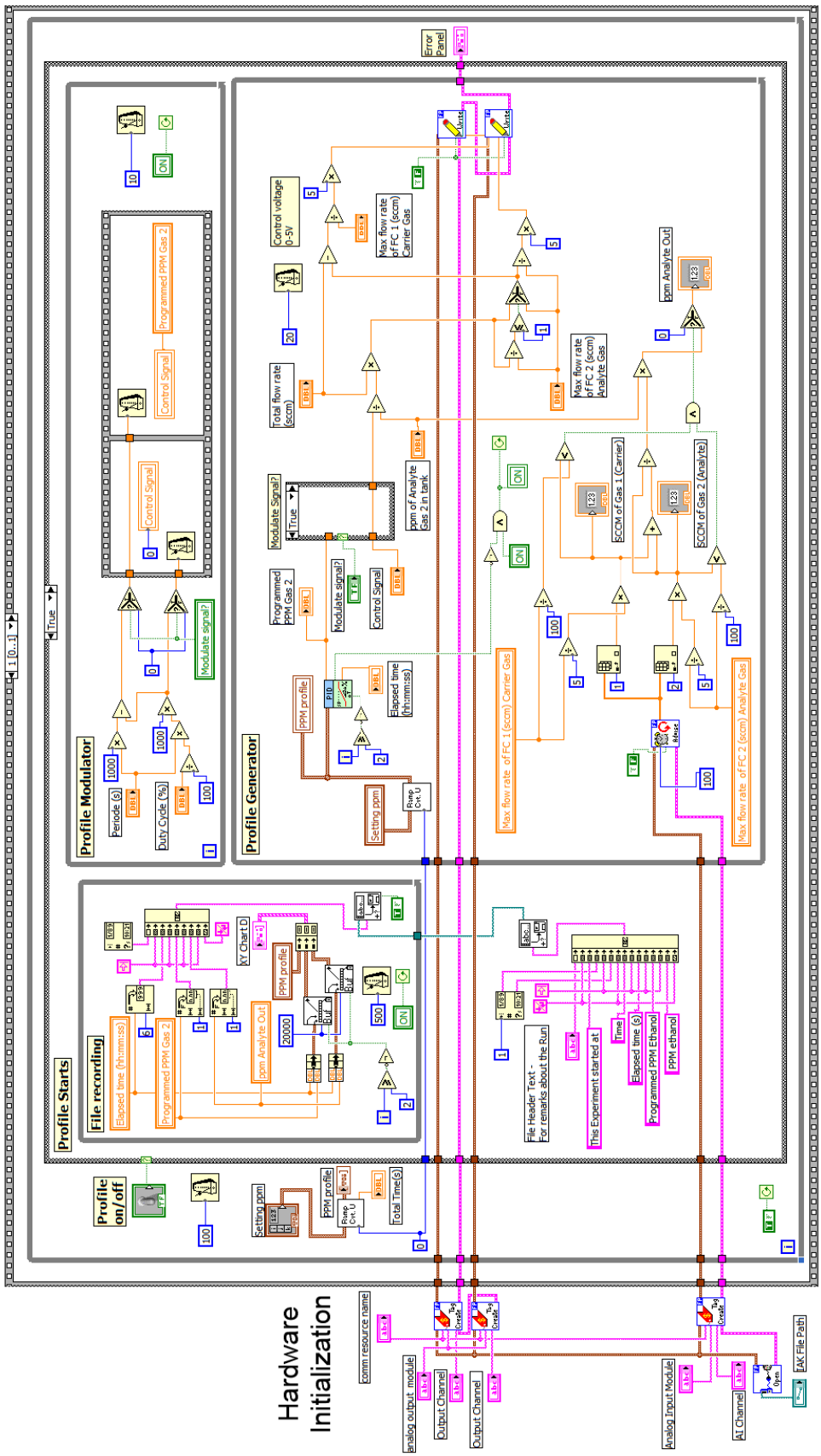

Figure F.4: Labview diagram C

APPENDIX G : Modification of the Carter Equation for Chemical Reaction Control at the Product/Gas Interface[144]

Consider the following gas solid reaction:

$$A(g) + bB(s) \rightarrow cC(s) \quad (1)$$

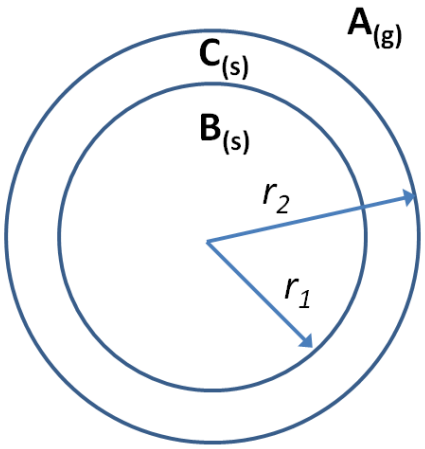

Figure G.1: Illustration of a reacting sphere that undergoes gas-solid reaction.

For chemical reaction control at the A(g)/C(s) interface and assuming a steady-state condition, the molar rate of reaction of solid B (dN_B/dt) at any given time during the reaction is proportional to its total reacting surface ($4\pi r_2^2$), the chemical reaction rate constant (K_{Rxn}), and the n-th order of reaction (C_i^n):

$$\frac{dN_B}{dt} = -4\pi r_2^2 K_{Rxn} C_i^n \quad (2)$$

The rate of molar change of B (dN_B/dt) is related to its rate of volume change (dQ_B/dt) according to the following equation:

$$\frac{dN_B}{dt} = \frac{\rho_B}{M_B}\frac{dQ_B}{dt} = \frac{\rho_B}{M_B}\frac{d\left(\frac{4}{3}\pi r_1^3\right)}{dt} = \frac{\rho_B}{M_B}4\pi r_1^2\frac{dr_1}{dt} \tag{3}$$

where ρ_B and M_B are the mass density and the molecular weight of B, respectively. If z is defined as volume of C formed per volume of B consumed, the relation between r_1 and r_2 can be written as:

$$\frac{4}{3}\pi r_2^3 = \frac{4}{3}\pi\left[r_1^3 + z\left(r_o^3 - r_1^3\right)\right] \text{ or } \quad r_2^3 = r_1^3 + z\left(r_o^3 - r_1^3\right) \tag{4}$$

where r_o is the radius of the initial sphere before the reaction began. Substituting Equation (3) and (4) into Equation (2), and rearranging for integration:

$$\frac{\rho_B}{M_B}4\pi r_1^2\frac{dr_1}{dt} = -4\pi\left[r_1^3 + z\left(r_o^3 - r_1^3\right)\right]K_{Rxn}C_i^n \tag{5}$$

$$\int_{r_2}^{r_1}\frac{r_1^2}{\left[r_1^3 + z\left(r_o^3 - r_1^3\right)\right]^{2/3}}dr_1 = -\int_0^t\frac{M_B}{\rho_B}K_{Rxn}C_i^n dt \tag{6}$$

The left hand side of the above equation can be integrated by using the following substitution method:

$$y^3 = r_1^3 + z\left(r_o^3 - r_1^3\right) = (1-z)r_1^3 + zr_o^3 \tag{7}$$

$$3y^2 dy = (1-z)3r_1^2 dr_1 \tag{8}$$

Or $$\frac{y^2}{(1-z)}dy = r_1^2 dr_1 \tag{9}$$

Substituting Equation (7) and (9) into the left side of Equation (6) and followed by integration:

$$\frac{1}{(1-z)}\int_{r_2}^{r_1} dy = -\int_0^t \frac{M_B}{\rho_B} K_{Rxn} C_i^n dt \tag{10}$$

$$\frac{1}{(1-z)}\left[r_1^3 + z\left(r_o^3 - r_1^3\right)\right]^{1/3}\Big|_{r_o}^{r_1} = -\frac{M_B}{\rho_B} K_{Rxn} C_i^n t \tag{11}$$

$$\left[r_1^3 + z\left(r_o^3 - r_1^3\right)\right]^{1/3} - r_o = -(1-z)\frac{M_B}{\rho_B} K_{Rxn} C_i^n t \tag{12}$$

If X is the extent of reaction which is defined by $X = 1 - \frac{r_1^3}{r_o^3}$ or $r_1 = (1-X)^{1/3} r_o$ then the above equation become:

$$\left[(1-X)r_o^3 + z\left(r_o^3 - (1-X)r_o^3\right)\right]^{1/3} - r_o = -(1-z)\frac{M_B}{\rho_B} K_{Rxn} C_i^n t \tag{13}$$

$$\left[1-(z-1)X\right]^{1/3} - 1 = (z-1)\frac{M_B}{\rho_B} K_{Rxn} C_i^n \frac{1}{r_o} t \tag{14}$$

The total time, τ, required for complete of the reaction (X = 1) is:

$$\tau = \left[\frac{z^{1/3}-1}{z-1}\right]\frac{\rho_B}{M_B}\frac{1}{K_{Rxn}}\frac{1}{C_i^n} r_o \tag{15}$$

Thus, Equation (14) can be simplified into a dimensionless form:

$$\frac{t}{\tau} = \frac{\left[1+(z-1)X\right]^{1/3} - 1}{z^{1/3} - 1} \tag{16}$$

Note: this equation is shown as Equation (13) in Chapter 8.

REFERENCES

[1] Hull, W. Q.; Keel, H.; Kenney, J., Jr.; Gamson, B. W.; *Diatomaceous earth*, Journal of Industrial and Engineering Chemistry (Washington, D. C.) **1953**, *45*, 256-69.

[2] Bennett, K.; *Precoat filtration*, Filtration & Separation **2000**, *37*, 32-33.

[3] Schuler, P. F.; Ghosh, M. M.; Gopalan, P.; *Slow sand and diatomaceous earth filtration of cysts and other particulates*, Water Research **1991**, *25*, 995-1005.

[4] Ross, T. E.; *Diatomaceous earth as a possible alternative to chemical insecticides*, Agriculture and Environment **1981**, *6*, 43-51.

[5] Yamanaka, T.; *Effects of supports in metallic catalysts. III*, Kagaku Kogyo **1977**, *28*, 1299-302.

[6] Ghebregzabher, M.; Rufini, S.; Monaldi, B.; Lato, M.; *Thin-layer chromatography of carbohydrates*, Journal of Chromatography **1976**, *127*, 133-62.

[7] Gomes, U. U.; Acchar, W.; Tavares, E. C. S.; Silva, N. F.; *Development of dielectric ceramics based on diatomite-titania and diatomite-niobia*, Materials Science Forum **1999**, *299-300*, 115-120.

[8] Parkinson, J.; Gordon, R.; *Beyond micromachining: the potential of diatoms*, Trends in Biotechnology **1999**, *17*, 190-196.

[9] Armbrust, E. V.; Berges, J. A.; Bowler, C.; Green, B. R.; Martinez, D.; Putnam, N. H.; Zhou, S.; Allen, A. E.; Apt, K. E.; Bechner, M.; Brzezinski, M. A.; Chaal, B. K.; Chiovitti, A.; Davis, A. K.; Demarest, M. S.; Detter, J. C.; Glavina, T.; Goodstein, D.; Hadi, M. Z.; Hellsten, U.; Hildebrand, M.; Jenkins, B. D.; Jurka, J.; Kapitonov, V. V.; Kroeger, N.; Lau, W. W. Y.; Lane, T. W.; Larimer, F. W.; Lippmeier, J. C.; Lucas, S.; Medina, M.; Montsant, A.; Obornik, M.; Parker, M. S.; Palenik, B.; Pazour, G. J.; Richardson, P. M.; Rynearson, T. A.; Saito, M. A.; Schwartz, D. C.; Thamatrakoln, K.; Valentin, K.; Vardi, A.; Wilkerson, F. P.; Rokhsar, D. S.; *The genome of the diatom Thalassiosira pseudonana: Ecology, evolution, and metabolism*, Science **2004**, *306*, 79-86.

[10] Sandhage, K. H.; Dickerson, M. B.; Huseman, P. M.; Zalar, F. M.; Carrol, M. C.; Rondon, M. R.; Sandhage, E. C.; *A Novel Hybrid Route to Chemically-Tailored, Three-Dimensional Oxide Nanostructures: The Basic (Bioclastic and Shape-Preserving Inorganic Conversion) Process*, Ceramic Engineering and Science Proceedings **2002**, *24*, 653-664.

[11] Sandhage, K. H.; Dickerson, M. B.; Huseman, P. M.; Caranna, M. A.; Clifton, J. D.; Bull, T. A.; Heibel, T. J.; Overton, W. R.; Schoenwaelder, M. E. A.; *Novel, bioclastic route to*

self-assembled, 3D, chemically tailored meso/nanostructures: shape-preserving reactive conversion of biosilica (diatom) microshells, Advanced Materials **2002**, *14*, 429-433.

[12] Unocic, R. R.; Zalar, F. M.; Sarosi, P. M.; Cai, Y.; Sandhage, K. H.; *Anatase assemblies from algae: coupling biological self-assembly of 3-D nanoparticle structures with synthetic reaction chemistry*, Chemical Communications **2004**, *7*, 796-7.

[13] Zhao, J.; Gaddis, C. S.; Cai, Y.; Sandhage, K. H.; *Free-standing microscale structures of nanocrystalline zirconia with biologically replicable three-dimensional shapes*, Journal of Materials Research **2005**, *20*, 282-287.

[14] Gaddis, C. S.; Sandhage, K. H.; *Freestanding microscale 3D polymeric structures with biologically-derived shapes and nanoscale features*, Journal of Materials Research **2004**, *19*, 2541-2545.

[15] Weatherspoon, M. R.; Allan, S. M.; Hunt, E.; Cai, Y.; Sandhage, K. H.; *Sol-gel synthesis on self-replicating single-cell scaffolds: applying complex chemistries to nature's 3-D nanostructured templates*, Chemical Communications (Cambridge, United Kingdom) **2005**, 651-653.

[16] Bao, Z.; Weatherspoon, M. R.; Shian, S.; Cai, Y.; Graham, P. D.; Allan, S. M.; Ahmad, G.; Dickerson, M. B.; Church, B. C.; Kang, Z.; Abernathy, H. W., III; Summers, C. J.; Liu, M.; Sandhage, K. H.; *Chemical reduction of three-dimensional silica micro-assemblies into microporous silicon replicas*, Nature **2007**, *446*, 172-175.

[17] Kusari, U.; Bao, Z.; Ye, C.; Ahmad, G.; Sandhage, K. H.; Sneddon, L. G.; *Template Routes to Non-Oxide Ceramic Nano- and Micro-Structures*, Materials Research Society Symposium Proceedings **2006**, *921E*, No pp given, Paper #: 0921-T04-10.

[18] Lee, S.-J.; Huang, C.-H.; Shian, S.; Sandhage, K. H.; *Rapid hydrolysis of organophosphorous esters induced by nanostructured, fluorine-doped titania replicas of diatom frustules*, Journal of the American Ceramic Society **2007**, *90*, 1632-1636.

[19] Round, F. E.; Crawford, R. M.; Mann, D. G. *The Diatoms: Biology & Morphology of the Genera*; Cambridge University Press: Cambridge, England, 1990.

[20] Werner, D. *The Biology of Diatoms*; Blackwell Scientific: Oxford, England, 1997.

[21] Birkby, I.; Stevens, R.; *Applications of zirconia ceramics*, Key Engineering Materials **1996**, *122-124*, 527-551.

[22] Anthony, A. M.; *High temperature refractory applications of zirconia*, Advances in Ceramics **1981**, *3*, 437-54.

[23] Schwank, J. W.; DiBattista, M.; *Oxygen sensors: materials and applications*, MRS Bulletin **1999**, *24*, 44-48.

[24] Armendariz, H.; Coq, B.; Tichit, D.; Dutartre, R.; Figueras, F.; *Influences of some synthesis parameters and activation procedures on the one-step sol-gel synthesis of*

sulfated-zirconia catalysts, followed by TG-DSC and mass spectrometry, Journal of Catalysis **1998**, *173*, 345-354.

[25] Burkhard, D. J. M.; Hanson, B.; Ulmer, G. C.; *Zirconia oxygen sensors: an evaluation of behavior at temperatures as low as 300 DegC*, Solid State Ionics **1991**, *47*, 169-75.

[26] Catledge, S. A.; Cook, M.; Vohra, Y. K.; Santos, E. M.; McClenny, M. D.; Moore, K. D.; *Surface crystalline phases and nanoindentation hardness of explanted zirconia femoral heads*, Journal of Materials Science: Materials in Medicine **2003**, *14*, 863-867.

[27] Denry, I.; Kelly, J. R.; *State of the art of zirconia for dental applications*, Dental Materials **2008**, *24*, 299-307.

[28] Zadesky, S. P.; Lynch, S. B.; Office, U. S. P. a. T., Ed.; Apple Computer, Inc.: USA, 2006.

[29] Shevchenko, A. V.; Dudnik, E. V.; Ruban, A. K.; Red'ko, V. P.; Vereschaka, V. M.; Lopato, L. M.; *Nanocrystalline Powders Based on ZrO2 for Biomedical Applications and Power Engineering*, Poroshkovaya Metallurgiya **2002**, *41*, 558-563.

[30] Vasylkiv, O.; Sakka, Y.; Skorokhod, V. V.; *Low-temperature processing and mechanical properties of zirconia and zirconia-alumina nanoceramics*, Journal of the American Ceramic Society **2003**, *86*, 299-304.

[31] Boaro, M.; Trovarelli, A.; Hwang, J.-H.; Mason, T. O.; *Electrical and oxygen storage/release properties of nanocrystalline ceria-zirconia solid solutions*, Solid State Ionics **2002**, *147*, 85-95.

[32] Mamak, M.; Coombs, N.; Ozin, G.; *Self-Assembling Solid Oxide Fuel Cell Materials: Mesoporous Yttria-Zirconia and Metal-Yttria-Zirconia Solid Solutions*, Journal of the American Chemical Society **2000**, *122*, 8932-8939.

[33] Pang, G.; Chen, S.; Zhu, Y.; Palchik, O.; Koltypin, Y.; Zaban, A.; Gedanken, A.; *Preparation and Characterization of Monodispersed YSZ Nanocrystals*, Journal of Physical Chemistry B **2001**, *105*, 4647-4652.

[34] Crepaldi, E. L.; Soler-Illia, G. J. d. A. A.; Bouchara, A.; Grosso, D.; Durand, D.; Sanchez, C.; *Controlled formation of highly ordered cubic and hexagonal mesoporous nanocrystalline yttria-zirconia and ceria-zirconia thin films exhibiting high thermal stability*, Angewandte Chemie, International Edition **2003**, *42*, 347-351.

[35] Soyez, G.; Eastman, J. A.; Thompson, L. J.; Bai, G. R.; Baldo, P. M.; McCormick, A. W.; DiMelfi, R. J.; Elmustafa, A. A.; Tambwe, M. F.; Stone, D. S.; *Grain-size-dependent thermal conductivity of nanocrystalline yttria-stabilized zirconia films grown by metal-organic chemical vapor deposition*, Applied Physics Letters **2000**, *77*, 1155-1157.

[36] Zhang, X.; Jiang, X. N.; Sun, C.; *Micro-stereolithography of polymeric and ceramic microstructures*, Sensors and Actuators, A: Physical **1999**, *A77*, 149-156.

[37] Cima, M. J.; Oliveira, M.; Wang, H. R.; Sachs, E.; Holman, R.; *Slurry-based 3DP and fine ceramic components*, Solid Freeform Fabrication Symposium Proceedings **2001**, 216-223.

[38] Vojak, B. A.; Park, S. J.; Wagner, C. J.; Eden, J. G.; Koripella, R.; Burdon, J.; Zenhausern, F.; Wilcox, D. L.; *Multistage, monolithic ceramic microdischarge device having an active length of .apprx.0.27 mm*, Applied Physics Letters **2001**, *78*, 1340-1342.

[39] Zhao, X.; Evans, J. R. G.; Edirisinghe, M. J.; Song, J.-H.; *Direct ceramic ink-jet printing of vertical walls*, Journal of the American Ceramic Society **2002**, *85*, 2113-2115.

[40] Smay, J. E.; Gratson, G. M.; Shepherd, R. F.; Cesarano, J., III; Lewis, J. A.; *Directed colloidal assembly of 3D periodic structures*, Advanced Materials **2002**, *14*, 1279-1283.

[41] Martin-Jezequel, V.; Hildebrand, M.; Brzezinski, M. A.; *Silicon metabolism in diatoms: Implications for growth*, Journal of Phycology **2000**, *36*, 821-840.

[42] Lebeau, T.; Robert, J.-M.; *Diatom cultivation and biotechnologically relevant products. Part I: Cultivation at various scales*, Applied Microbiology and Biotechnology **2003**, *60*, 612-623.

[43] Joubert, P.; Gaudreau, B.; *Zirconium(IV) oxyfluorides*, Revue de Chimie Minerale **1975**, *12*, 289-302.

[44] Sandhage, K. H.; Allan, S. M.; Dickerson, M. B.; Ernst, E. M.; Gaddis, C. S.; Shian, S.; Weatherspoon, M. R.; Ahmad, G.; Cai, Y.; Haluska, M. S.; Snyder, R. L.; Unocic, R. R.; Zalar, F. M., Inorganic preforms of biological origin: shape-preserving reactive conversion of biosilica microshells (diatoms), In *Handbook of Biomineralization: Biomimetic and Bioinspired Chemistry* 2007, p 235-253.

[45] Barin, I. *Thermochemical data of Pure Substances, 3rd edition*; VCH Verlagsgesellschaft mbH: Weinheim, Germany, 1995; Vol. I and II.

[46] Gourishankar, K. V.; Ranjbar, M. K.; St. Pierre, G. R.; *Revision of the enthalpies and Gibbs energies of formation of calcium oxide and magnesium oxide*, Journal of Phase Equilibria **1993**, *14*, 601-11.

[47] Tverskov, V. A.; Morozov, I. S. *System $ZrCl_4$-$MgCl_2$-KCl*; The American Ceramic Society: Westerville, OH, 1985; Vol. II.

[48] Cullity, B. D. *Elements of X-ray Diffraction*; 2 ed.; Addison-Wesley: Reading, MA, 1976.

[49] Karapetrova, E.; Platzer, R.; Gardner, J. A.; Torne, E.; Sommers, J. A.; Evenson, W. E.; *Oxygen vacancies in pure tetragonal zirconia powders: dependence on the presence of chlorine during processing*, Journal of the American Ceramic Society **2001**, *84*, 65-70.

[50] Pasquevich, D. M.; Lovey, F.; Caneiro, A.; *Structural and microstructural changes in zirconia in dilute chlorine atmosphere*, Journal of the American Ceramic Society **1989**, *72*, 1664-7.

[51] Birkefeld, L. D.; Azad, A. M.; Akbar, S. A.; *Carbon Monoxide and Hydrogen Detection by Anatase Modification of Titanium Dioxide*, Journal of the American Ceramic Society **1992**, *75*, 2964-2968.

[52] Maira, A. J.; Yeung, K. L.; Soria, J.; Coronado, J. M.; Belver, C.; Lee, C. Y.; Augugliaro, V.; *Gas-Phase Photo-Oxidation of Toluene Using Nanometer-Size TiO_2 Catalysts*, Applied Catalysis, B: Environmental **2001**, *29*, 327-336.

[53] Gratzel, M.; *Photoelectrochemical Cells*, Nature **2001**, *414*, 338-344.

[54] Yuan, Z. Y.; Su, B. L.; *Titanium Oxide Nanotubes, Nanofibers and Nanowires*, Col. Surf. A **2004**, *241*, 173-183.

[55] Yoo, S.; Akbar, S. A.; Sandhage, K. H.; *Nanocarving of Bulk Titania Crystal into Oriented Arrays of Single-Crystal Nanofibers via Reaction with Hydrogen-Bearing Gas*, Adv. Mater. **2004**, *16*, 260-264.

[56] Liu, S. M.; Gan, L. M.; Liu, L. H.; Zhang, W. D.; Zeng, H. C.; *Synthesis of Single-Crystalline TiO_2 Nanotubes*, Chem. Mater. **2002**, *14*, 1391-1397.

[57] Imai, H.; Matsuta, M.; Shimizu, K.; Hirashima, H.; Negishi, N.; *Preparation of TiO_2 Fibers With Well-Organized Structures*, J. Mater. Chem. **2000**, *10*, 2005-2006.

[58] Oota, T.; Yamai, I.; *Vapor Phase Growth of Titania Whiskers by Hydrolysis of Titanium Fluoride*, J. Crys. Gro. **1984**, *66*, 262-268.

[59] Gratson, G. M.; Xu, M.; Lewis, J. A.; *Microperiodic structures: Direct writing of three-dimensional webs*, Nature **2004**, *428*, 386.

[60] Xu, M.; Gratson, G. M.; Duoss, E. B.; Shepherd, R. F.; Lewis, J. A.; *Biomimetic silicification of 3D polyamine-rich scaffolds assembled by direct ink writing*, Soft Matter **2006**, *2*, 205-209.

[61] Droop, M. R.; *A procedure for routine purification of algal cultures with antibiotics*, British Phycological Bulletin **1967**, *3*, 295-297.

[62] Anderson, R. A.; Jacobson, D. M.; Sexton, J. P. *Provasoli–Guillard Center for Culture of Marine Phytoplankton: Catalogue of Strains*; Provasoli–Guillard Center for Culture of Marine Phytoplankton: West Boothbay Harbor, ME, 1991.

[63] Guillard, R. R. L. In *Culture of Marine Invertebrate Animals* 1975, p 29-60.

[64] Smetacek, V.; Klaas, C.; Menden-Deuer, S.; Rynearson, T. A.; *Mesoscale distribution of dominant diatom species relative to the hydrographical field along the Antarctic Polar Front*, Deep Sea Research Part II: Topical Studies in Oceanography **2002**, *49*, 3835-3848.

[65] Sozuer, H. S.; Dowling, J. P.; *Photonic band calculations for woodpile structures*, Journal of Modern Optics **1994**, *41*, 231-9.

[66] Schwartz, B. T.; Piestun, R.; *Dynamic properties of photonic crystals and their effective refractive index*, Journal of the Optical Society of America B: Optical Physics **2005**, *22*, 2018-2026.

[67] Eranna, G.; Joshi, B.; Runthala, D.; Gupta, R.; *Oxide materials for development of integrated gas sensors. A comprehensive review*, Critical Reviews in Solid State and Materials Sciences **2004**, *29*, 111-188.

[68] Capone, S.; Epifani, M.; Quaranta, F.; Siciliano, P.; Taurino, A.; Vasanelli, L.; *Monitoring of rancidity of milk by means of an electronic nose and a dynamic PCA analysis*, Sensors and Actuators, B: Chemical **2001**, *B78*, 174-179.

[69] Rossi, V.; Garcia, C.; Talon, R.; Denoyer, C.; Berdague, J. L.; *Rapid discrimination of meat products and bacterial strains using semiconductor gas sensors*, Colloques - Institut National de la Recherche Agronomique **1995**, *75*, 85-9.

[70] Capone, S.; Epifani, M.; Quaranta, F.; Siciliano, P.; Vasanelli, L.; *Application of a semiconductor sol-gel sensor array to the discrimination of pollutants in air*, Thin Solid Films **2001**, *391*, 314-319.

[71] Heule, M.; Gauckler, L. J.; *Gas sensors fabricated from ceramic suspensions by micromolding in capillaries*, Advanced Materials (Weinheim, Germany) **2001**, *13*, 1790-1793.

[72] Yamazoe, N.; *New approaches for improving semiconductor gas sensors*, Sensors and Actuators, B: Chemical **1991**, *B5*, 7-19.

[73] Comini, E.; Faglia, G.; Sberveglieri, G.; Li, Y. X.; Wlodarski, W.; Ghantasala, M. K.; *Sensitivity enhancement towards ethanol and methanol of TiO2 films doped with Pt and Nb*, Sensors and Actuators B-Chemical **2000**, *64*, 169-174.

[74] Lewin, J. C.; Guillard, R. R. L.; *Diatoms*, Annual review of microbiology **1963**, *17*, 373-414.

[75] Hildebrand, M.; Wetherbee, R.; *Components and control of silicification in diatoms*, Progress in Molecular and Subcellular Biology **2003**, *33*, 11-57.

[76] Sberveglieri, G.; Comini, E.; Faglia, G.; Atashbar, M. Z.; Wlodarski, W.; *Titanium dioxide thin films prepared for alcohol microsensor applications*, Sensors and Actuators, B: Chemical **2000**, *B66*, 139-141.

[77] Micocci, G.; Serra, A.; Tepore, A.; Capone, S.; Rella, R.; Siciliano, P.; *Properties of vanadium oxide thin films for ethanol sensor*, Journal of Vacuum Science & Technology, A: Vacuum, Surfaces, and Films **1997**, *15*, 34-38.

[78] Neri, G.; Bonavita, A.; Rizzo, G.; Galvagno, S.; Capone, S.; Siciliano, P.; *Methanol gas-sensing properties of CeO2-Fe2O3 thin films*, Sensors and Actuators B-Chemical **2006**, *114*, 687-695.

[79] Garzella, C.; Comini, E.; Bontempi, E.; Depero, L. E.; Frigeri, C.; Sberveglieri, G.; *Sol-gel TiO2 and W/TiO2 nanostructured thin films for control of drunken driving*, Sensors and Actuators B-Chemical **2002**, *83*, 230-237.

[80] Liu, J.; Wang, X.; Peng, Q.; Li, Y.; *Vanadium pentoxide nanobelts: highly selective and stable ethanol sensor materials*, Advanced Materials **2005**, *17*, 764-767.

[81] Sun, F.; Cai, W.; Li, Y.; Jia, L.; Lu, F.; *Direct growth of mono- and multilayer nanostructured porous films on curved surfaces and their application as gas sensors*, Advanced Materials **2005**, *17*, 2872-2877.

[82] Akbar, S. A.; Younkman, L. B.; *Sensing mechanism of a carbon monoxide sensor based on anatase titania*, Journal of the Electrochemical Society **1997**, *144*, 1750-1753.

[83] Morrison, S. R. *The Chemical Physics of Surfaces*; Plenum: New York, 1977.

[84] http://www.iihs.org/laws/state_laws/dui.html.

[85] Tang, H.; Prasad, K.; Sanjines, R.; Levy, F.; *Tio2 Anatase Thin-Films as Gas Sensors*, Sensors and Actuators B-Chemical **1995**, *26*, 71-75.

[86] Li, P.; Miser, D. E.; Rabiei, S.; Yadav, R. T.; Hajaligol, M. R.; *The removal of carbon monoxide by iron oxide nanoparticles*, Applied Catalysis, B: Environmental **2003**, *43*, 151-162.

[87] Yu, J. C.; Yu, J.; Zhang, L.; Ho, W.; *Enhancing effects of water content and ultrasonic irradiation on the photocatalytic activity of nanosized TiO2 powders*, Journal of Photochemistry and Photobiology, A: Chemistry **2002**, *148*, 263-271.

[88] Kominami, H.; Kumamoto, H.; Kera, Y.; Ohtani, B.; *Photocatalytic decolorization and mineralization of malachite green in an aqueous suspension of titanium(IV) oxide nano-particles under aerated conditions: correlation between some physical properties and their photocatalytic activity*, Journal of Photochemistry and Photobiology, A: Chemistry **2003**, *160*, 99-104.

[89] Kontos, A. I.; Arabatzis, I. M.; Tsoukleris, D. S.; Kontos, A. G.; Bernard, M. C.; Petrakis, D. E.; Falaras, P.; *Efficient photocatalysts by hydrothermal treatment of TiO2*, Catalysis Today **2005**, *101*, 275-281.

[90] Gao, L.; *Developing new routes for preparation of nanostructured TiO as highly efficient photocatalysts*, Materials Integration **2004**, *17*, 43-49.

[91] Burniston, N.; Bygott, C.; Stratton, J.; *Nano technology meets titanium dioxide*, Surface Coatings International, Part A: Coatings Journal **2004**, *87*, 179-184.

[92] Tomkiewicz, M.; Kelly, S.; *Morphology-dependent photocatalysis with nanoparticle aggregates*, Nanoparticles and Nanostructured Films **1998**, 263-274.

[93] Serpone, N.; Khairutdinov, R. F.; *Application of nanoparticles in the photocatalytic degradation of water pollutants*, Studies in Surface Science and Catalysis **1997**, *103*, 417-444.

[94] Hoffmann, M. R.; Martin, S. T.; Choi, W.; Bahnemann, D. W.; *Environmental Applications of Semiconductor Photocatalysis*, Chemical Reviews **1995**, *95*, 69-96.

[95] Fox, M. A.; Dulay, M. T.; *Heterogeneous photocatalysis*, Chemical Reviews **1993**, *93*, 341-57.

[96] Green, M. B.; Hartley, G. S.; West, T. F. *Chemicals for Crop Improvement and Pest Management*; 3rd ed.; Pergamon Press: Oxford, England, 1987.

[97] Ohno, T.; Sarukawa, K.; Tokieda, K.; Matsumura, M.; *Morphology of a TiO2 Photocatalyst (Degussa, P 25) Consisting of Anatase and Rutile Crystalline Phases*, Journal of Catalysis **2001**, *203*, 82-86.

[98] ASTM, Annual Book of ASTM Standards; ASTM International: West Conshohocken, PA, 2002; Vol. 12.01, p 1502-01.

[99] Minh, D. P.; Gallezot, P.; Besson, M.; *Degradation of olive oil mill effluents by catalytic wet air oxidation*, Applied Catalysis, B: Environmental **2006**, *63*, 68-75.

[100] Torrents, A.; Stone, A. T.; *Hydrolysis of phenyl picolinate at the mineral/water interface*, Environmental Science and Technology **1991**, *25*, 143-9.

[101] Huang, C.-H.; Stone, A. T.; *Synergistic Catalysis of Dimetilan Hydrolysis by Metal Ions and Organic Ligands*, Environmental Science and Technology **2000**, *34*, 4117-4122.

[102] Smolen, J. M.; Stone, A. T.; *Divalent metal ion-catalyzed hydrolysis of phosphorothionate ester pesticides and their corresponding oxonates*, Environmental Science and Technology **1997**, *31*, 1664-1673.

[103] Herrmann, J. M.; Guillard, C.; Arguello, M.; Aguera, A.; Tejedor, A.; Piedra, L.; Fernandez-Alba, A.; *Photocatalytic degradation of pesticide pirimiphos-methyl. Determination of the reaction pathway and identification of intermediate products by various analytical methods*, Catalysis Today **1999**, *54*, 353-367.

[104] Smolen, J. M.; Stone, A. T.; *Metal (hydr)oxide surface-catalyzed hydrolysis of chlorpyrifos-methyl, chlorpyrifos-methyl oxon, and paraoxon*, Soil Science Society of America Journal **1998**, *62*, 636-643.

[105] Huang, C.-H.; Stone, A. T.; *Hydrolysis of naptalam and structurally related amides: inhibition by dissolved metal ions and metal (hydr)oxide surfaces*, Journal of Agricultural and Food Chemistry **1999**, *47*, 4425-4434.

[106] Torrents, A.; Stone, A. T.; *Oxide surface-catalyzed hydrolysis of carboxylate esters and phosphorothioate esters*, Soil Science Society of America Journal **1994**, *58*, 738-45.

[107] Seo, G.; Kim, N.-H.; Lee, Y.-H.; Kim, J.-H.; *Influence of the fluorine loading level on the skeletal isomerization of 1-butene over fluorine-modified alumina*, Catalysis Letters **1998**, *51*, 101-107.

[108] Ghosh, A. K.; Kydd, R. A.; *Fluorine-promoted catalysts*, Catalysis Reviews - Science and Engineering **1985**, *27*, 539-89.

[109] Huheey, J. E.; Keiter, E. A.; Keiter, R. L. *Inorganic Chemistry*; 4th ed.; Hapers Collins College Publishers: New York, NY, 1993.

[110] Fulton, G. P. *Diatomaceous Earth Filtration for Safe Drinking Water*; American Society of Civil Engineers: Reston, VA, 2000.

[111] Lytle, J. C.; Yan, H.; Turgeon, R. T.; Stein, A.; *Multistep, Low-Temperature Pseudomorphic Transformations of Nanostructured Silica to Titania via a Titanium Oxyfluoride Intermediate*, Chemistry of Materials **2004**, *16*, 3829-3837.

[112] Vorres, K. S.; Donohue, J.; *The Structure of Titanium Oxydifluoride*, Acta Crystallographica **1955**, *8*, 25-26.

[113] Hayward, S. A.; Morrison, F. D.; Redfern, S. A. T.; Salje, E. K. H.; Scott, J. F.; Knight, K. S.; Tarantino, S.; Glazer, A. M.; Shuvaeva, V.; Daniel, P.; Zhang, M.; Carpenter, M. A.; *Transformation processes in LaAlO3: Neutron diffraction, dielectric, thermal, optical, and Raman studies*, Physical Review B: Condensed Matter and Materials Physics **2005**, *72*, 054110/1-054110/17.

[114] Glazer, A. M.; *Classification of tilted octahedra in perovskites*, Acta Crystallographica, Section B: Structural Crystallography and Crystal Chemistry **1972**, *28*, 3384-92.

[115] Dudley, S.; Kalem, T.; Akinc, M.; *Conversion of SiO2 diatom frustules to BaTiO3 and SrTiO3*, Journal of the American Ceramic Society **2006**, *89*, 2434-2439.

[116] Fujimori, H.; Yashima, M.; Kakihana, M.; Yoshimura, M.; *The b-cubic phase transition of scandia-doped zirconia solid solution: Calorimetry, x-ray diffraction, and Raman scattering***2002**, *91*, 6493-6498.

[117] Kennedy, B. J.; Vogt, T.; *Powder x-ray diffraction study of the rhombohedral to cubic phase transition in TiF3*, Materials Research Bulletin **2002**, *37*, 77-83.

[118] Shannon, R. D.; *Revised effective ionic radii and systematic studies of interatomic distances in halides and chalcogenides*, Acta Crystallographica, Section A: Crystal Physics, Diffraction, Theoretical and General Crystallography **1976**, *A32*, 751-67.

[119] Howard, C. J.; Kennedy, B. J.; Chakoumakos, B. C.; *Neutron powder diffraction study of rhombohedral rare-earth aluminates and the rhombohedral to cubic phase transition*, Journal of Physics: Condensed Matter **2000**, *12*, 349-365.

[120] Chen, B. J.; Rodriguez, M. A.; Misture, S. T.; Snyder, R. L.; *Effect of undercooling temperature on the solidification kinetics and morphology of Y-Ba-Cu-O during melt texturing*, Physica C: Superconductivity and Its Applications **1993**, *217*, 367-75.

[121] Lind, C.; Wilkinson, A. P.; Rawn, C. J.; Payzant, E. A.; *Kinetics of the cubic to trigonal transformation in ZrMo2O8 and their dependence on precursor chemistry*, Journal of Materials Chemistry **2002**, *12*, 990-994.

[122] Sheridan, A. K.; Anwar, J.; *Kinetics of the Solid-State Phase Transformation of Form b to g of Sulfanilamide Using Time-Resolved Energy-Dispersive X-ray Diffraction*, Chemistry of Materials **1996**, *8*, 1042-51.

[123] Wilkinson, A. P.; Speck, J. S.; Cheetham, A. K.; Natarajan, S.; Thomas, J. M.; *In situ x-ray diffraction study of crystallization kinetics in PbZr1-xTixO3, (PZT, x = 0.0, 0.55, 1.0)*, Chemistry of Materials **1994**, *6*, 750-4.

[124] Norby, P.; Christensen, A. N.; Hanson, J. C.; *Crystallization in Nonaqueous Media of Co- and Mn-Substituted Microporous Aluminophosphates Investigated by in Situ Synchrotron X-ray Powder Diffraction*, Inorganic Chemistry **1999**, *38*, 1216-1221.

[125] Dolan, M. D.; Misture, S. T.; *A high-temperature diffraction study of reduction and reoxidation of nickel oxide*, Rigaku Journal **2004**, *21*, 12-16.

[126] Ozawa, M.; Loong, C. K.; *In situ X-ray and neutron powder diffraction studies of redox behavior in CeO2-containing oxide catalysts*, Catalysis Today **1999**, *50*, 329-342.

[127] Wakiya, N.; Chun, S.-Y.; Shinozaki, K.; Mizutani, N.; *Redox reaction of praseodymium oxide in the ZnO sintered ceramics*, Journal of Solid State Chemistry **2000**, *149*, 349-353.

[128] Haluska, M. S.; Snyder, R. L.; Sandhage, K. H.; Misture, S. T.; *Closed, heated reaction chamber design for dynamic high-temperature x-ray-diffraction analyses of gas/solid displacement reactions*, Review of Scientific Instruments **2005**, *76*, 126101/1-126101/4.

[129] Lide, D. R. *CRC Handbook of Chemistry and Physics*; 77th ed.; CRC Press, Inc.: Roca Baton, 1996.

[130] Kyun, V. A.; Roslik, G. T.; *Selection of material for the window of the radiation chamber during the x-ray spectral analysis of slurries and solutions*, Zavodskaya Laboratoriya **1976**, *42*, 948-9.

[131] Almtoft, K. P.; Bottiger, J.; Chevallier, J.; Schell, N.; Martins, R. M. S.; *Influence of the substrate bias on the size and thermal stability of grains in magnetron-sputtered nanocrystalline Ag films*, Journal of Materials Research **2005**, *20*, 1071-1080.

[132] Hubbell, J. H.; Seltzer, S. M. *Tables of x-ray mass attenuation coefficients and mass energy-absorption coefficients 1 keV to 20 MeV for elements Z = 1 to 92 and 48 additional substances of dosimetric interest*, Ionizing Radiation Div.,National Inst. of Standards and Technology,Gaithersburg,MD,USA., 1995.

[133] Drews, A. R.; *Calibration of a high temperature X-ray diffraction stage by differential thermal expansion*, Advances in X-Ray Analysis **2001**, *44*, 44-49.

[134] Szekely, J.; Evans, J.; Sohn, H. Y. *Gas Solid Reactions*; Academic Press: London, 1976.

[135] Bhatia, S. K.; Perlmutter, D. D.; *A Random Pore Model for Fluid-Solid Reactions: I. Isothermal, Kinetic Control*, AIChE Journal **1980**, *26*, 379-386.

[136] Karatepe, N.; Erdogan, N.; Ersoy-Mericboyu, A.; Kucukbayrak, S.; *Preparation of diatomite/Ca(OH)$_2$ sorbents and modelling their sulphation reaction*, Chem. Eng. Sci. **2004**, *59*, 3883-3889.

[137] Levenspiel, O. *Chemical Reaction Engineering*; 3rd ed.; John Wiley & Sons: New York, 1999.

[138] Ramachandran, P. A.; Doraiswamy, L. K.; *Modeling of noncatalytic gas-solid reactions*, AIChE Journal **1982**, *28*, 881-900.

[139] Park, J. Y.; Levenspiel, O.; *Crackling core model for the reaction of solid particles*, Chemical Engineering Science **1975**, *30*, 1207-14.

[140] Schulmeyer; *Mechanisms of The Hydrogen Reduction of Molybdenum Oxides*, INT J REFRACT MET H **2002**, *20*, 261-269.

[141] Carter, R. E.; *Kinetic model for solid-state reactions*, Journal of Chemical Physics **1961**, *35*, 1137-8.

[142] Wen, C. Y.; *Noncatalytic heterogeneous solid-fluid reaction models*, Industrial and Engineering Chemistry **1968**, *60*, 34-54.

[143] Ishida, M.; Wen, C. Y.; *Comparison of zone-reaction model and unreacted-core shrinking model in solid-gas reactions. I. Isothermal analysis*, Chemical Engineering Science **1971**, *26*, 1031-41.

[144] Sandhage, K. H.; *Unpublished Work*.

[145] Young, R. A. *The Rietveld Method*; Oxford University Press: Oxford, 1993.

[146] Lowell, S.; Shields, J. E.; Thomas, M. A.; Thommes, M. *Characterization of Porous Solids and Powder; Surface Area, Pore Size, and Density* Kluwer Academic Publisher: Dordrecht, 2004.

[147] Ravikovitch, P. I.; Neimark, A. V.; *Characterization of nanoporous materials from adsorption and desorption isotherms*, Colloids And Surfaces A-Physicochemical And Engineering Aspects **2001**, *187*, 11-21.

[148] Badley, R. D.; Ford, W. T.; McEnroe, F. J.; Assink, R. A.; *Surface modification of colloidal silica*, Langmuir **1990**, *6*, 792-801.

[149] Lecloux, A. J.; Bronckart, J.; Noville, F.; Dodet, C.; Marchot, P.; Pirard, J. P.; *Study of the texture of monodisperse silica sphere samples in the nanometer size range*, Colloids and Surfaces **1986**, *19*, 359-74.

[150] Khalil, K. M. S.; Elsamahy, A. A.; Elanany, M. S.; *Formation and Characterization of High Surface Area Thermally Stabilized Titania/Silica Composite Materials via*

Hydrolysis of Titanium(IV) tetra-Isopropoxide in Sols of Spherical Silica Particles, Journal of Colloid and Interface Science **2002**, *249*, 359-365.

[151] Shinmei, M.; Imai, T.; Yokokawa, T.; *Thermodynamics study of Si_2OF_6(g) from 723 to 1288 K by mass spectrometry*, Journal of Chemical Thermodynamics **1986**, *18*, 241-246.

[152] *ICDD PDF-4*; International Center for Diffraction Data: Newton Square, PA, 2004.

[153] Welty, J. R.; Wicks, C. E.; Wilson, R. E.; Rorrer, G. *Fundamentals of Momentum, Heat, and Mass Transfer*; 4th ed.; John Wiley and Sons: New York, 2001.

[154] Peters, B.; *Classification of combustion regimes in a packed bed of particles based on the relevant time and length scales*, Combustion and Flame **1998**, *116*, 297-301.

[155] Ruthven, D. M. *Principles of Adsorption and Adsorption Process*; John Wiley and Sons, Inc.: New York, 1984.

[156] Shelby, J. E. *Handbook of Gas Diffusion in Solids and Melts*; ASM International: Materials Park, OH, 1996.

[157] Shian, S.; Cai, Y.; Weatherspoon, M. R.; Allan, S. M.; Sandhage, K. H.; *Three-dimensional assemblies of zirconia nanocrystals via shape-preserving reactive conversion of diatom microshells*, Journal of the American Ceramic Society **2006**, *89*, 694-698.

[158] Weatherspoon, M. R.; Haluska, M. S.; Cai, Y.; King, J. S.; Summers, C. J.; Snyder, R. L.; Sandhage, K. H.; *Phosphor Microparticles of Controlled Three-Dimensional Shape from Phytoplankton*, Journal of the Electrochemical Society **2006**, *153*, H34-H37.

[159] Weatherspoon, M. R.; Dickerson, M. B.; Wang, G.; Cai, Y.; Shian, S.; Jones, S. C.; Marder, S. R.; Sandhage, K. H.; *Thin, conformal, and continuous SnO2 coatings on three-dimensional biosilica templates through hydroxy-group amplification and layer-by-layer alkoxide deposition*, Angewandte Chemie, International Edition **2007**, *46*, 5724-5727.

[160] Ernst, E. M.; Church, B. C.; Gaddis, C. S.; Snyder, R. L.; Sandhage, K. H.; *Enhanced hydrothermal conversion of surfactant-modified diatom microshells into barium titanate replicas*, Journal of Materials Research **2007**, *22*, 1121-1127.

[161] Cai, Y.; Dickerson, M. B.; Haluska, M. S.; Kang, Z.; Summers, C. J.; Sandhage, K. H.; *Manganese-doped zinc orthosilicate-bearing phosphor microparticles with controlled three-dimensional shapes derived from diatom frustules*, Journal of the American Ceramic Society **2007**, *90*, 1304-1308.

[162] Li, D.; Haneda, H.; Hishita, S.; Ohashi, N.; *Visible-Light-Driven N-F-Codoped TiO2 Photocatalysts. 1. Synthesis by Spray Pyrolysis and Surface Characterization*, Chemistry of Materials **2005**, *17*, 2588-2595.

[163] Park, H.; Choi, W.; *Effects of TiO_2 Surface Fluorination on Photocatalytic Reactions and Photoelectrochemical Behaviors*, Journal of Physical Chemistry B **2004**, *108*, 4086-4093.

[164] Yu, J. C.; Yu, J. G.; Ho, W. K.; Jiang, Z. T.; Zhang, L. Z.; *Effects of F- Doping on the Photocatalytic Activity and Microstructures of Nanocrystalline TiO2 Powders*, Chemistry of Materials **2002**, *14*, 3808-3816.

[165] Lowenstam, H. A.; Weiner, S.; *Mineralization by organisms and the evolution of biomineralization*, Biomineralization and Biological Metal Accumulation **1983**, 191-203.

[166] Perry, C. C.; Mann, S.; Williams, R. J. P.; Watt, F.; Grime, G. W.; Takacs, J.; *A scanning proton microprobe study of macrohairs from the lemma of the grass Phalaris canariensis L*, Proceedings of the Royal Society of London, Series B: Biological Sciences **1984**, *222*, 439-45, 2 plates.

[167] Mann, S.; Ozin, G.; *Synthesis of inorganic materials with complex form*, Nature **1996**, *382*, 313-318.

[168] Aizenberg, J.; Tkachenko, A.; Weiner, S.; Addadi, L.; Hendler, G.; *Calcitic microlenses as part of the photoreceptor system in brittlestars*, Nature **2001**, *412*, 819-22.

[169] Weaver, J. C.; Pietrasanta, L. I.; Hedin, N.; Chmelka, B. F.; Hansma, P. K.; Morse, D. E.; *Nanostructural features of demosponge biosilica*, Journal of Structural Biology **2003**, *144*, 271-281.

[170] Sundar, V. C.; Yablon, A. D.; Grazul, J. L.; Ilan, M.; Aizenberg, J.; *Fiber-optical features of a glass sponge*, Nature **2003**, *424*, 899-900.

[171] Bauerlein, E.; *Biomineralization of unicellular organisms: An unusual membrane biochemistry for the production of inorganic nano- and microstructures*, Angewandte Chemie, International Edition **2003**, *42*, 614-641.

[172] Crawford, S. A.; Higgins, M. J.; Mulvaney, P.; Wetherbee, R.; *Nanostructure of the diatom frustule as revealed by atomic force and scanning electron microscopy*, Journal of Phycology **2001**, *37*, 543-54.

[173] Zaslavskaia, L. A.; Lippmeier, J. C.; Kroth, P. G.; Grossman, A. R.; Apt, K. E.; *Transformation of the diatom Phaeodactylum tricornutum (Bacillariophyceae) with a variety of selectable marker and reporter genes*, Journal of Phycology **2000**, *36*, 379-386.